Nanoparticle Coatings for Surface Morphology Control and Superhydrophobicity

by

Jie Zhong

A dissertation submitted to the Graduate Faculty of
Auburn University
in partial fulfillment of the
requirements for the Degree of
Doctor of Philosophy

Auburn, Alabama
December 10, 2016

Keywords: nanoparticles, gas expanded liquid, surface morphology, coatings, superhydrophobicity

Committee Members:

W. Robert Ashurst, Co-Chair, Associate Professor of Chemical Engineering
Christopher B. Roberts, Co-Chair, Dean of Engineering
Allan E. David, Assistant Professor of Chemical Engineering
Robert Dean, Professor of Electrical and Computer Engineering

Abstract

Surface modifications with nanoparticles are major concerns in the realization of the full potential of nanoscale devices. Currently, no single surface treatment technology can solve all problems of reliability. Further, precise control of nanoparticle coatings is still lacking. Therefore, the goal of this research was to obtain a fundamental understanding of the way in which the surface chemistry and deposition conditions of the nanoparticles affect the films achieved. With such an improved understanding, it will be possible to achieve well-controlled nanoparticle coatings with the properties desired.

Various self-assembled monolayers have been deposited in liquid phase onto substrates prior to nanoparticle deposition to combine the SAM and GXL technologies by providing both a low energy surface and a rough nanoparticle coating. Self-assembled monolayers are synthesized on Si substrates and characterized. Because film growth is affected by the critical surface tension of the SAMs, it alternates between layer-by-layer deposition and agglomeration formation, which also changes the surface roughness. On the other hand, the surface chemistry of the AuNPs, which is affected by stabilizing ligands on the nanoparticles, also has some effect on film deposition. By using a combination of dodecanethiol-stabilized AuNPs and APhTS-coated Si substrates, it has been confirmed that the nanoparticle films deposited follow the Stranski-Krastanov mechanism. The changes in morphology induced by the concentration of nanoparticle solution emphasize the importance of the number of nanoparticles involved in film deposition and demonstrate the potential to achieve better control of the films formed.

A calculation based on the GW model was applied to the surface topographies from AFM data presented as a quantitative assessment method to compare various coatings. Varied concentrations of the initial nanoparticle solution help visualize the growth process, and demonstrate that a change in concentration has a major effect on the long-range roughness parameters, such as the root-mean-square (rms) surface roughness and standard deviation of summit height distribution. Average size of nanoparticles affects short-range roughness parameters, including autocorrelation length and roughness exponents. The size variation of the nanoparticles facilitates better control of several important surface parameters, such as the ratio of true to apparent contact area, which is critical in minimizing adhesion and friction in real applications.

By using size-varied iron oxide nanoparticles and a GXL deposition technology, the surfaces of MEMS devices can be coated uniformly with these nanoparticles. Based on the experimental results and theoretical calculations, the increase in plane separation reduced the retarded van der Waals interaction, diminishing the contribution of the non-contacting portion in adhesion. On the other hand, normal van der Waals interactions between contacting asperities were affected by the combination of average summit density and summit radius, which plays the dominant role in adhesion. Changes in these parameters influence the total effects of normal and retarded van der Waals interactions between contacting asperities, leading to reduced adhesion.

The size effect of the nanoparticles on the reduced adhesion still exists; however, the contribution of adhesion now derives primarily from the van der Waals interaction between nanoparticle monolayers. Based on the experimental results and theoretical calculations, the surface coverage increases as the initial concentration increases, while the surface film growth is

limited at the sub-monolayer level; this leads to an increase in the apparent work of adhesion, which derives from the greater area of interaction when two surfaces are in close proximity. This proves that under different surface topographical conditions, reduction of the total contact area is essential to reduce adhesion while achieving sufficient long-range roughness.

Attempts also have been made to coat MEMS devices with gold nanorods via GXL deposition technology. However, rather than the uniform nanocoatings obtained with nanoparticles, only isolated aggregates exist on the surface. Test results showed that gold nanorods cannot be deposited well as uniform films on various substrates and the expected good reduction in adhesion cannot be achieved. To understand this effect further, a total interaction energy model to correlate the solvent-ligand interaction with the maximum size of a ligand-stabilized nanoparticle that can be dispersed within a given solvent system was introduced to simulate the interactions between various nanoshapes. The results indicated that larger nanoshapes become unstable more easily when the particle-solvent and particle-particle interaction are affected. For gold nanorods, a side-to-side (SS) configuration is more favorable when the nanorods become unstable and precipitate from the solution, leading to aggregation even in a very dilute concentration. Therefore, it is still possible to coat nanoshapes, but a better design based on the surface chemistry of the nanostructures is required.

VPD-based, durable, superhydrophobic nanoparticle coatings were obtained and applied to actual boards, and the fundamental material characterizations for an optimal target structure and morphology were developed. Because different application environments emphasize corresponding film properties, VPD-coated substrates were characterized by their durability,

water-resistance, electrical and thermal properties, and other functions based on customers' requirements.

The coatings were subjected to a water erosion test to determine the durability of superhydrophobicity. The results showed that our coating offered good protection against water erosion. The mechanism of superhydrophobicity occurs through the transition from a Cassie-Baxter to a Wenzel state. The increased spacing on the surface resulted in decreased surface roughness and density of structures with peak height.

Self-assembly monolayers were applied to our coatings to enable them to withstand higher temperatures. Samples were heated in either a furnace or by TGA and corresponding results were used to analyze their heat stability. The application of SAMs increased the temperature at which the film began to fail and the contact angle value dropped. The differences between furnace and TGA results were attributable to the desorption mechanism of monolayers. XPS results of DDMS-coated substrate before and after heat treatment showed that the thermal decomposition of DDMS coating derives from the oxidation of the methyl chain and the conversion from silane to SiO_2-like structures. Quantitative analysis showed that polymerized DDMS, or PDMS oligomer, may exist on the surface of a rough commercial substrate and can contribute to the stable silane structures. This explains the difference in thermal stability of the DDMS-coated Si substrate and the commercial nanocomposite substrate. The rough morphology of the substrate plays an important role and could have potential in future applications.

VPD nanoparticle coatings were applied to electric boards and tested under water to ensure that they are applicable in the commercial market. One of the main problems in actual

devices is electromigration, which derives from the migration of metal ions in solution and the reduction of ions into metal deposition. The superhydrophobic coating plays an important role here by preventing water from contacting the metal wire directly, which reduces the hydrolysis and solvation of metal ions into solution. Another possibility is that some of the VPD nanoparticle layers dissolve into the solution and form metal hydroxides integrated with the dendrites, making the dendrite bridge less conductive and reducing the current flow.

Overall, the work presented here demonstrated the possibility that the surface morphology of GXL-deposited nanoparticle films can be controlled during synthesis by changing the surface chemistry of the nanoparticles or substrates. By using VPD, durable, superhydrophobic nanoparticle coatings can be applied to commercial devices and their chemical and physical properties specified. This work has the potential to make nanoparticle coatings more attractive for realistic applications and market consumers.

Acknowledgments

Throughout my Ph.D. studies, I have received considerable support, advice, and help from many people, all of whom deserve my sincere thanks. First, I would like to thank my advisors, Dr. W. Robert Ashurst and Dr. Christopher B. Roberts, for providing me with the opportunity to join their research groups at Auburn University, and for their continued support and guidance during my pursuit of this degree. The insightful discussions we have had, as well as the advice they have given have led me to discover my independent ability to achieve my ultimate goal. The conversations that we have had provided not only academic guidance, but also honest criticism and help related to issues in my personal life, which definitely will be useful to me in future. I also gratefully thank all of the committee members and the university reader, Dr. Allan E. David, Dr. Robert Dean and Dr. Bart Prorok for offering their time, assistance, and good will throughout the preparation and review of this document. I would like to thank Dr. Jeff Chin from IST for providing me the opportunity to participate in commercial projects, and for expanding my experience significantly with practical applications.

I acknowledge all of the predecessors on my research project gratefully, especially Dr. Kendall Hurst and Dr. Naveed Ansari, who provided a solid foundation and intellectual insights on this research. I also would like to thank Dr. Michael Miller for his assistance with SEM/TEM characterizations, and Mr. Brian Schweiker for his assistance in maintaining the lab equipment. I would also like to thank Ms. Karen Cochran, Ms. Elaine Manning, Ms. Jennifer Harris, Ms. Georgetta Dennis, and Ms. Sue Ellen Abner for their help in various matters over the years.

Thanks are also due to current and past members of Dr. Ashurst's and Roberts' research groups, including, but not limited to, Dr. Steven Saunders, Dr. Rui Xu, Dr. Sihe Zhang, Dr. Rajeshwar Chinnawar, as well as Charlotte Stewart and David Roe. In particular, I gratefully acknowledge Dr. Pranav Vengsarkar for his help in the synthesis and size fractionation of various metal nanoparticles. I would like to thank Dr. John Tatarchuk from the Department of Electrical and Computer Engineering for discussions and help with the fabrication of MEMS chips. I would like to thank Dr. Alexander Haywood and Mahesh Parit for their help with TGA data acquisition. I also thank Mingyang Chi from Dr. Tatarchuk's research group for his help with the XPS analysis.

I gratefully acknowledge Auburn University, the Department of Energy, and the National Science Foundation for providing me with financial support for all of the research efforts. There are many fellow graduates and friends who have made my life at Auburn enjoyable and memorable, and I would like to thank them again for their friendship.

Finally, and most importantly, I must thank my parents for their continuous support and inspiration during these years of my study. I would not be here without their unconditional love and guidance, and I dedicate this dissertation to them.

Table of Contents

List of Tables

List of Figures

List of Symbols and Abbreviations

a, b, c, L	Lengths of corresponding shapes
A, $A_{S\text{-}NP}$, $A_{NP\text{-}NP}$	Hamaker constant of corresponding systems
A_0	Apparent contact area
A_c	True contact area
A_m	Expected mean contact area
d, D, D_{ave}	Mean plane separation distance
d_b	Length of beam interacted
d_{co}	Cutoff separation
D_{SUM}	Average surface summit density
E, E_1, E_2	Young's moduli of corresponding components
F, F_t, F_e, F_v	Applied forces from various sources
$g_e(D)$	Correction function describing the retardation of van der Waals force
$H(\tau_x)$	Height-height correlation function
h	Roughness exponent
h_0	Free standing height
h_1, h_2, h_n	Thickness values of corresponding finite films
h(x)	Vertical beam position
k_B	Boltzmann constant
L	Length of the cantilever beam

l	Ligand length
M	Number of columns of the data field
M_{Au}	Molar mass of gold
MW	Molecular weight of the ligand
m_0	Zeroth spectral moment of the profile
m_2	Second spectral moment of the profile
m_4	Fourth spectral moment of the profile
N	Total number of summits
N_A	Avogadro's constant
N_{Au}	Average number of gold atoms in each gold nanoparticle
N_T	Total number of gold atoms
n	Total number of summits in contact
R, R_1, R_2	Radii of corresponding shapes
R_i	Ideal gas constant
s	Crack length
T	Autocorrelation length
T_e	Temperature
t	Thickness of the cantilever beam
U_E	Elastic energy in a deformed cantilever beam
U_S	Interfacial surface energy that promotes adhesion
U_T	Total mechanical energy
$u(x)$	Deflection of the beam
V	Volume of the solution

V_A	Applied voltage
v_{solv}	Molar volume of the solvent
w	Width of the cantilever beam
w_s	Surface coverage
z	Summit height
α	Bandwidh parameter
Γ	Ligand surface coverage
γ	Apparent work of adhesion
γ_L	Liquid surface energy
γ_S	Solid surface energy
γ_{SL}	Interfacial energy between the solid and liquid
Δx	Sampling interval
δ	Indentation distance
δ_{solv}	Hildebrand solubility parameter of the solvent
δ_{lig}	Hildebrand solubility parameter of the ligand
ε_0	Permittivity of free space
θ	Contact angle
κ_m	Mean summit curvature
λ_0	London characteristic wavelength
ν, ν_1, ν_2	Poisson's ratios of corresponding components
ρ	Density of the ligand
ρ_{Au}	Density of fcc gold
σ, σ_1, σ_2, R_q	RMS roughness values of corresponding surfaces

τ_x	Sampling length
σ_s	Standard deviation of summit height distribution
$\Phi elas$	Elastic repulsive potential
Φosm	Osmotic repulsive potential
$\Phi total$	Total interaction potential
Φvdw	Van der Waals attractive potential
φ	Ligand volume fraction
$\varphi(z)$	Height distribution function
χ	Flory-Huggins interaction parameter

ADC	Analog-to-digital converter
AFM	Atomic force microscopy
ALD	Atomic layer deposition
APhTS	p-Aminophenyltrimethoxysilane
AuNP	Gold nanoparticle
BOE	Buffered oxide etch
C8-OTS	Octyltrichlorosilane
CBA	Cantilever beam array
CCD	Charge-coupled device
CVD	Chemical vapor deposition
DAQ	Data acquisition
DDMS	Dimethyldichlorosilane
DIUF	Deionized ultra filtered
DRIE	Deep reactive ion etching
FDTS	H,1H,2H,2H-Perfluorodecyltrichlorosilane
FeNP	Iron oxide nanoparticle
FOTS	(Tridecafluoro-1,1,2,2-tetrahydrooctyl)trichlorosilane
GW	Greenwood-Williamson
GXL	Gas-expanded liquid
HHCF	Height-height correlation function
HMDS	Hexamethylene disilazane
LDDMS	Liquid-deposited dimethyldichlorosilane film
LLLSM	Limited ligand length solvation model

LSPR	localized surface plasmon resonance
MEMS	Microelectromechanical system
MPTS	3-Mercaptopropyltrimethoxysilane
OTS	n-Octadecyltrichlorosilane
PDF	probability density function
PDMS	Polydimethylsiloxane
RF	Radio frequency
RH	Relative humidity
RMS	Root-mean-square
RTD	Resistive temperature detector
SAM	Self-assembled monolayer
SEM	Scanning electron microscopy
SOI	Silicon on insulator
SPR	Surface plasmon resonance
SPRB	Surface plasmon resonance band
TEM	Transmission electron microscopy
TGA	Thermogravimetric analysis
TMA	Trimethylaluminium
TP	Test platform
VDDMS	Vapor-deposited dimethyldichlorosilane film
VPD	Vapor phase deposition
XPS	X-ray photoelectron spectroscopy

Chapter 1

Introduction

1.1 Surface and tribology

1.1.1 Chemistry of surface

Science today is concerned with determining the structures of matter, such as solids, liquids, and gases. In the chemical industry and technology, and natural biological phenomena, we need a much more comprehensive picture of the structures involved in all types of processes. It has been accepted widely that when researchers deal with various types of matter, the molecules positioned at the interfaces of the material may behave differently than those in the bulk. This concept has led to a new research area: surface chemistry.

The way in which the molecules near or at the interface interact with each other derives from intramolecular forces. Thus, all reactions that occur near any interface will depend on these molecular orientations and interactions. Furthermore, it has been found that for dense matter, the forces that dominate the molecular structure are of primary importance. Within the bulk, the primary effect of the interacting forces is to provide a uniform potential so that the molecules remain in a relatively stable environment. However, the molecules at the interface are subject to an asymmetrical force field, which gives rise to so-called surface tension or interfacial tension (Birdi, 2013).

Because of the molecules' movement, the force acting on them will vary according to time and location. The closer the molecule is to the surface, the greater the asymmetric force. This kind of asymmetry plays a very important role. Thus, when the surface area of a form of matter changes, some molecules must move from the interior of the continuous phase to the interface; this is the source of the surface tension (Figure 1.1).

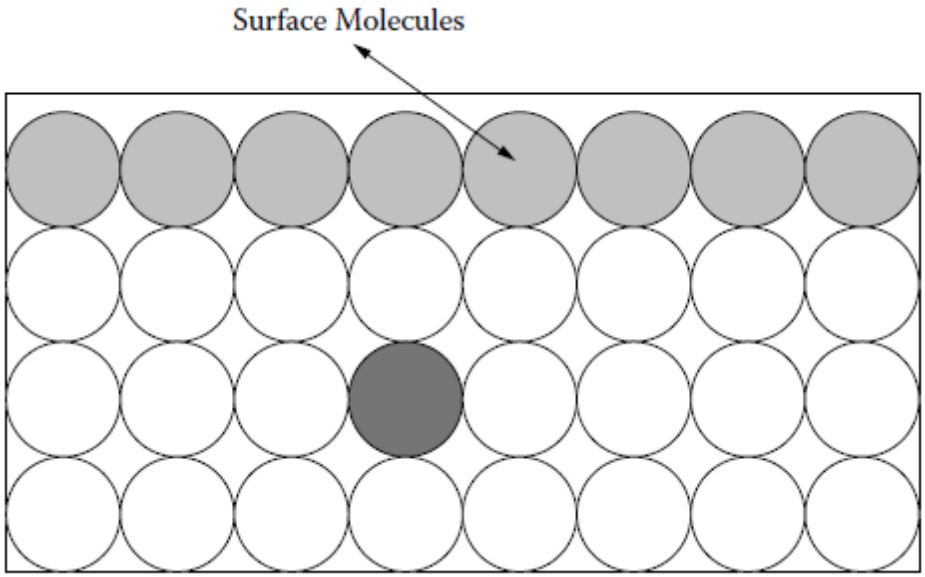

Figure 1.1. Molecules in the bulk liquid (dark) and on the surface (light: Birdi, 2013).

Surface tension is defined as the differential change of free energy associated with a change in surface area. An increase in surface area requires molecules to move from the bulk phase to the surface area. This process takes place for all kinds of surfaces, but it is very typical and of great importance in liquids, in which it is also called interfacial tension. A liquid molecule attracts the molecules that surround it and is attracted by them. For the molecules within a liquid, all these forces result in a neutral environment in which all are in equilibrium during their interaction with each other. When these molecules move to the surface, the molecules in the bulk below, but not from the outside, attract them. The result is a force directed into the liquid.

Moreover, the cohesion among the molecules supplies a force tangential to the surface. Therefore, a fluid surface acts like a membrane that keeps the liquid below the surface stable. The surface tension indicates the force with which the surface molecules attract each other.

Surface energy is very important because it leads to certain macroscopic phenomena, such as hydrophobicity and hydrophilicity. Figure 1.2 shows the contact angle of a water droplet on both hydrophobic and hydrophilic substrates. Hydrophobicity is defined as the physical property of a molecule that is repelled by water molecules, while hydrophilicity is defined as the tendency of a molecule to be attracted to other water molecules. These terms describe the apparent attraction or repulsion between water and nonpolar substances.

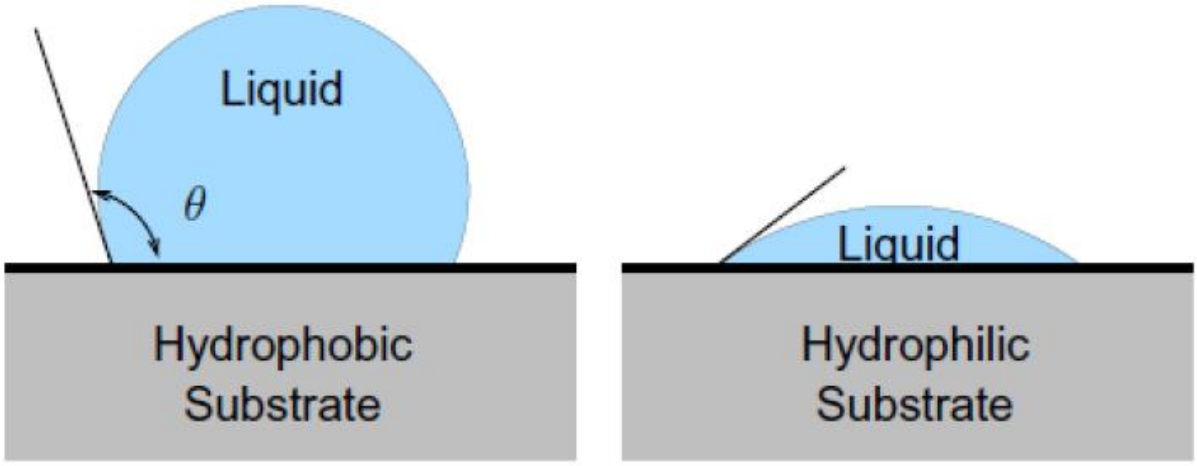

Figure 1.2. Contact angle of a water droplet on hydrophobic and hydrophilic substrates.

The hydrophobicity of a surface is related directly to the interfacial surface energy following Young's equation (Adamson et al., 1990; Doms et al., 2008):

$$\gamma_L \cos\theta = \gamma_S - \gamma_{SL} \quad (1.1)$$

In Equation 1.1, θ is the contact angle of the fluid on the surface, γ_L is the liquid surface energy, γ_S is the solid surface energy, and γ_{SL} is the interfacial energy between the solid and liquid. Physically, γ_{SL} is the energy required to pull the two surfaces apart to create two distinct surfaces.

Based on Equation 1.1, when the solid surface energy is higher than the solid-liquid interfacial energy ($\gamma_S > \gamma_{SL}$), the contact angle will be less than 90° and the solid surface is said to be hydrophilic. In contrast, if the solid surface energy is lower than the solid-liquid interfacial energy ($\gamma_S < \gamma_{SL}$), the surface of the solid becomes hydrophilic. In the case of silicon-based surfaces, the surface energy is extremely high and yields a very hydrophilic surface. For the self-assembled layer-coated, silicon-based surface, the surface energy can be so low that the contact angle with the water will exceed 150°, which yields a very hydrophobic surface usually defined as superhydrophobicity. Superhydrophobic surfaces play a vital role in many applications. Therefore, an effective way to control the hydrophobicity is to control the surface energy by changing the surfaces, either chemically or physically.

1.1.2 Tribology

The word tribology is derived from the Greek word “tribos” which means “rubbing”. Literally, tribology refers to “the science of rubbing”. Tribology is accepted widely today as a research area that includes adhesion, friction, wear, lubrication, and other topics. Tribology is defined scientifically as the science and technology of interacting surfaces in relative motion and of related subjects and practices. Phenomena and processes related to tribology are of great

economic significance. Surface interactions in a tribological interface are very complex, and a better understanding of tribology requires knowledge of various disciplines, including physics, chemistry, fluid mechanics, thermodynamics, material science, and so on (Jost, 2006).

The purpose of research in tribology is to minimize, and if possible, eliminate the losses that result from friction and wear in all levels of technology in which complex interactions of surfaces are involved. Current research in tribology leads to higher efficiency, better performance, and significant savings.

1.1.2.1 Adhesion

When two solid surfaces are in contact, adhesion or bonding across the interface will occur, which requires a finite normal force, adhesive force, to pull the two solids apart (Figure 1.3). Adhesion and cohesion are distinct phenomena. Cohesion refers to the bulk bonding forces within a material. Thus, cohesion derives from the forces that exist within the bulk of the material and bond one atom or molecule to another. However, when two similar or different materials are brought together and steady contact with an interface occurs, the bonding of the surface of one solid to that of another results instead in the formation of adhesive bonds.

Adhesion occurs in either solid-solid or solid-liquid contacts. If all of the chemical contaminants are removed from two solid surfaces, and they are kept clean, strong adhesion or bonding generally occurs between the two. Surface contaminants or thin films reduce adhesion; however, in some cases, the opposite may be true.

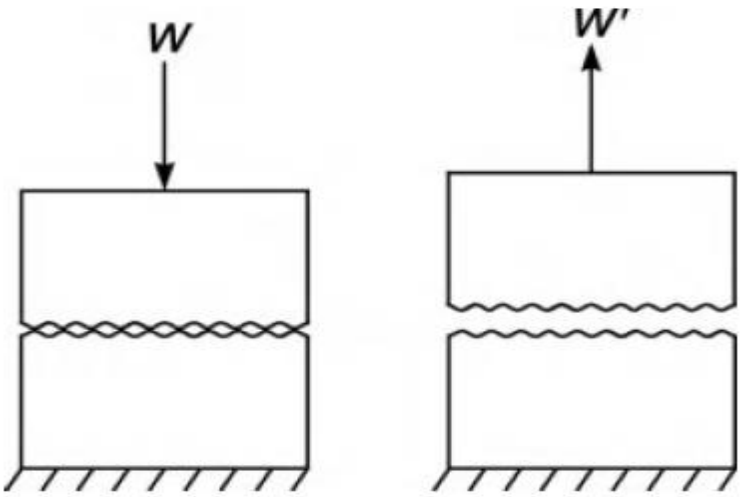

Figure 1.3. Normal pull or separation of two solid bodies; W is the load force applied for a certain duration and W' is the force needed to separate the surfaces (Bhushan, 2002).

Adhesion can be either desirable or undesirable, depending on the actual application. Strong adhesion is essential to bond two surfaces together. However, in many engineering applications, such as machinery systems with small components, adhesion is highly undesirable, because it results in friction and wear. Therefore, controlled adhesion typically is required.

1.1.2.2 Friction

Friction is the resistance to motion when a solid body slides or rolls over another with which it is in contact. The resistive force that acts in direct opposition to the direction of motion is called the friction force.

Friction is not an intrinsic property of a material, but is instead a response to applied force. If two solid surfaces are free of chemical contaminants, high friction occurs. Surface contaminants or thin films affect friction in a similar way as adhesion. With well-lubricated surfaces, weak adhesion and friction can be achieved. However, a small quantity of liquid present at the interface results in liquid-mediated adhesion, which may produce high friction, especially between two smooth surfaces.

Like adhesion, friction forces can be either essential or undesirable. Without friction, it would be impossible to walk, drive on a roadway, or pick up objects. Even in some machine applications, such as vehicle brakes, friction must be maximized. However, for many sliding and rotating components, friction is undesirable. Friction causes energy loss and wear of the moving surfaces in contact. In these cases, it is mandatory to minimize friction (Bhushan, 2002).

1.1.2.3 Stiction

When solids are loaded together and a force is applied, then the value of the repulsive force required to initiate motion is the static friction force. If the force applied is lower than this value, the solids will not move. This kind of static friction is defined sometimes as stiction. Usually it refers to unintentional and undesirable adhesion of compliant structures in the current micromachining industry, because it is a significant phenomenon for a system running at the micro or nanoscale.

Because microsystem structures have lateral dimensions that range typically from 50-500 μm and thicknesses that range typically from 0.1-10 μm, they have very large surface area-to-volume ratios, which increase the influence of interfacial forces on their tribological behavior significantly. In particular, the interfacial forces experienced by the surfaces of a microdevice, the microstructures of which have hydrophilic surfaces, are several orders of magnitude greater than the forces required to bring and keep them in contact. Essentially, the interfacial forces that exist on the scale of these small devices is relatively significant. The nature of these structures and the small internal forces that typically are generated by most devices make the surfaces of nanostructures extremely susceptible to stiction. Stiction occurs in two situations: during the release procedure, which is classified as release stiction, and after it, which is classified as in-use stiction (Maboudian et al., 1997; Friedrich et al., 2009). Figure 1.4 shows some typical lateral and vertical stiction on cantilevers.

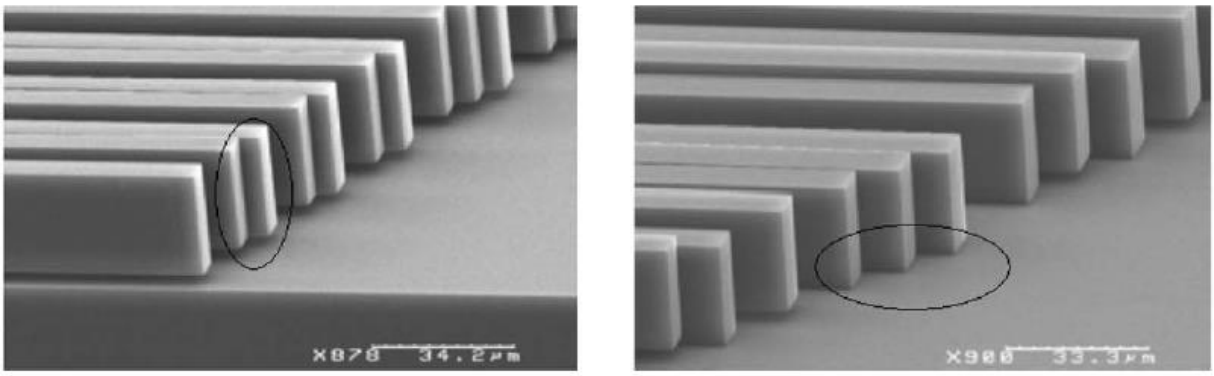

Figure 1.4. Example of lateral and vertical stiction on cantilevers (Huang et al., 2012).

Practically, most micro- and nanodevices are susceptible to either release and/or in-use stiction, which can be reduced by modifying their structural stiffness, interfacial topography, and surface chemistry. There have been many major approaches to prevent stiction in devices,

including the use of rough surfaces or hydrophobic surfaces, deposition of an anti-stiction coating, and design of strong structures (Huang et al., 2012).

1.1.2.4 Wear

Wear is a phenomenon associated with surfaces that rub or experience impact that can be a concern with sliding parts. Wear is defined as the removal of material from a solid surface through mechanical action (Huang et al., 2012). Figure 1.5 shows severe wear on a pad. Based on the mechanism, wear can have several main causes: adhesion, abrasion, corrosion, surface fatigue, erosion and percussion, and electrical-induced (Bhushan, 2002). Because there are so many wear mechanisms, one or more may affect a particular piece of machinery. In many cases, wear is initiated by one mechanism and then may proceed to another, which makes failure analysis more complicated. The types of wear mechanisms responsible for actual failure cannot be determined until the surfaces are examined carefully.

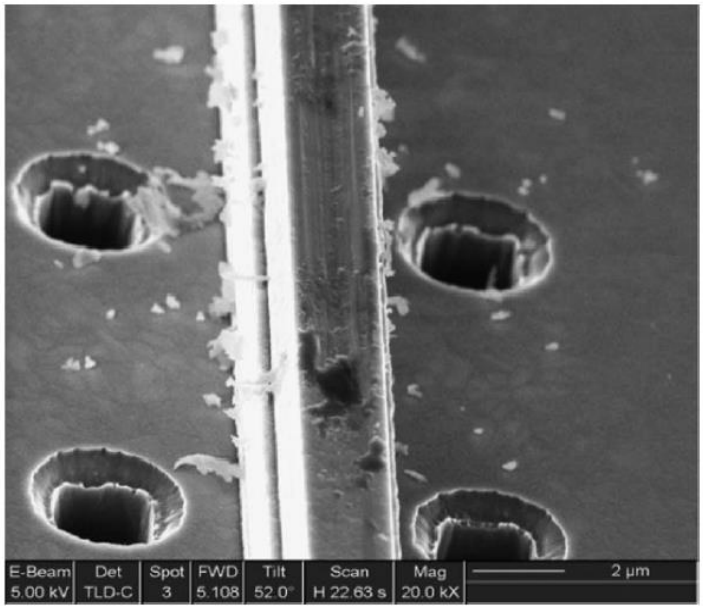

Figure 1.5. Severe wear on a friction pad that caused device failure (Huang et al., 2012).

1.2 Nanoparticle films

1.2.1 Nanoparticles

1.2.1.1 An introduction to nanoparticles

The application of nanoscale particles and structures is an emerging aspect of nanoscience and nanotechnology. Nanoparticles usually refer to those with a diameter that ranges from 1 to 100 nanometers. Appropriate control of the properties of nanometer-scale structures will lead to novel scientific discoveries, as well as new devices and technologies. Feynman indicated the importance of nanotechnology as early as 1959 in his widely cited paper entitled, "There is plenty of room at the bottom" (Feynman, 1959). Since then, and particularly

in the last several decades, nanoscience and technology have witnessed explosive growth. These fields are motivated by the application of new strategies for the synthesis of nanomaterials and new tools needed to characterize them in detail.

Why are nanoparticles so important and attractive? The key is size effects, which are the most important feature of such materials. These size effects are associated with the evolution of structural, thermodynamic, electronic, spectroscopic, electromagnetic, and chemical features of varying systems. The size effects of nanoparticles can be classified into two types, one related to individual size effects, such as the number of atoms in metal clusters and quantum mechanical effects at small scales, while the other includes scaling effects that are applicable to relatively larger nanostructures, including nanoaggregates and nano-assembly layers. In the former case, new features appear in the electronic structure. The electronic structures of metal and semiconductor nanocrystals differ from those of bulk materials (Rao et al., 2002). In addition, the energy gap between nanostructures and the effective percentage of surface atoms changes with particle diameter, which changes the bulk properties. Figure 1.6 shows an example, the size dependence of the melting temperature of CdS nanocrystals.

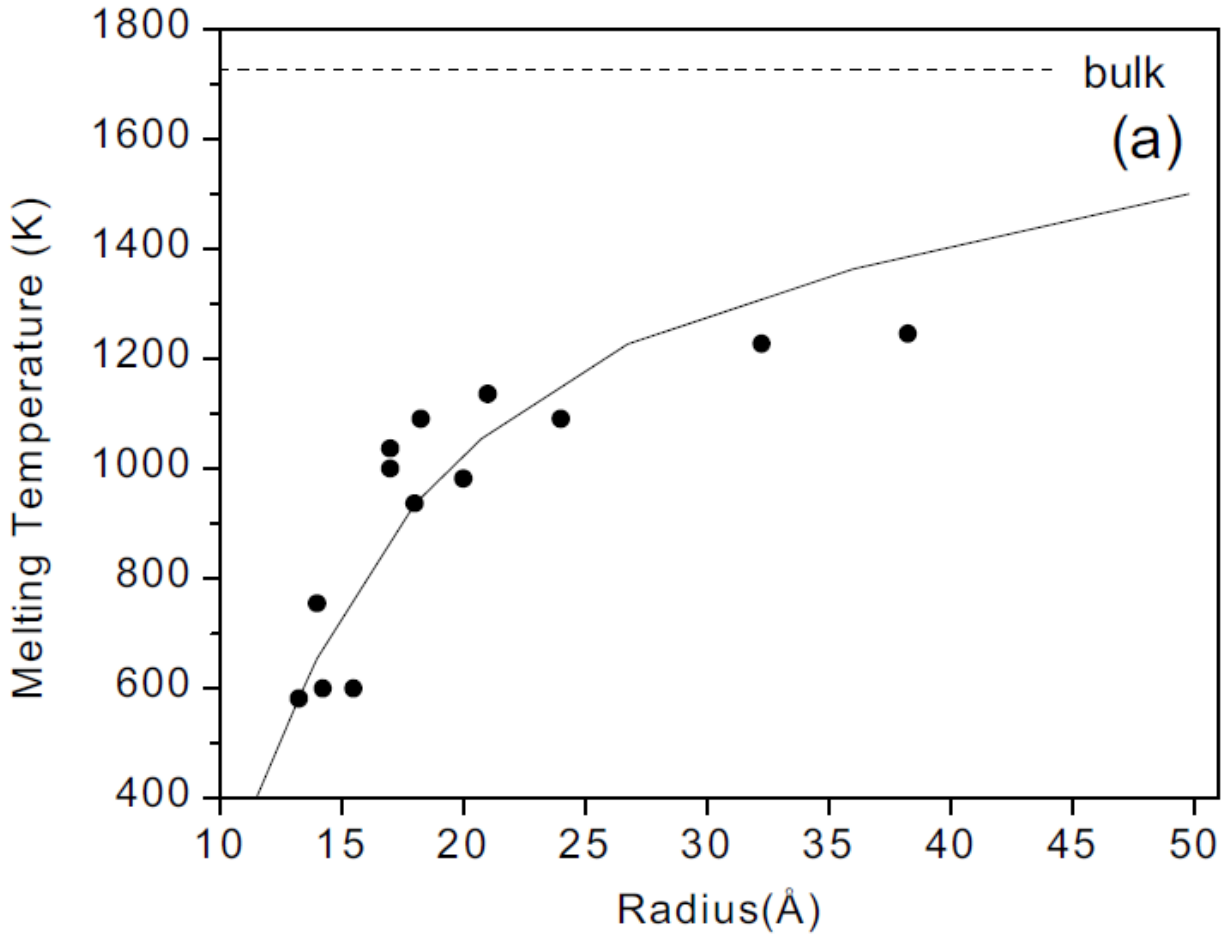

Figure 1.6. Size dependence of the melting temperature of CdS nanocrystals (Alivisatos, 1996).

Research on nanoparticles is vital and offers enormous opportunities. It is an interdisciplinary topic that involves chemistry, physics, biology, materials, and related aspects of engineering. Collaborative work on nanoparticles amongst scientists with different backgrounds definitely will create new scientific fields, and in particular, new materials that offer surprising technological possibilities. What is noteworthy is that nanotechnology is likely to benefit from not only the electronics industry, but also the chemical industry, as well as medicine and healthcare. Nanoparticles may provide ways to solve environmental and social challenges related to such applied research topics as solar energy, catalysis, biomedicine, and wastewater treatment, among others.

1.2.1.2 Synthesis of nanoparticles

Conventionally, nanoparticles can be prepared by both "top down" and "bottom up" processes (Zhao et al., 2013). In "top down" procedures, a bulk state metal is broken down to generate nanoparticles at the scales desired. In this case, a pattern or matrix controls particle assembly and formation. However, the "top down" method is limited in its ability to control the size and shape of particles, as well as their further function. In contrast, in the "bottom up" strategy, the formation of nanoparticles originates from individual molecules, and involves a chemical or biological reaction. This method usually includes two steps: nucleation followed by particle growth. When nucleation and growth are completed in the same process, it is called in situ synthesis; otherwise, it is referred to as the seed-growth method. The focus in in situ synthesis is the preparation of spherical or quasi-spherical nanoparticles. In contrast, the seed-growth method can generate nanoparticles of various sizes and shapes.

In general, the preparation of nanoparticles by chemical reduction consists of two major steps: reduction, using agents such as borohydrides, aminoboranes, hydrazine, and so on, stabilizing agents such as trisodium citrate dihydrate, sulfur ligands polymers, and surfactants (cetyltrimethylammonium bromide in particular). Nanoparticles synthesized in situ also can be used for seed-growth or further functionalization (Zhao et al., 2013).

For example, Faraday first reported the synthesis of gold nanoparticles (AuNP) in 1857, where he used the reduction of a tetrachloroaurate solution by phosphorus in carbon disulfide (a biphasic reaction). During the second half of the 20^{th} century, the preparation of nanoparticles with controlled sizes and shapes has drawn increased attention (Rao et al., 2004).

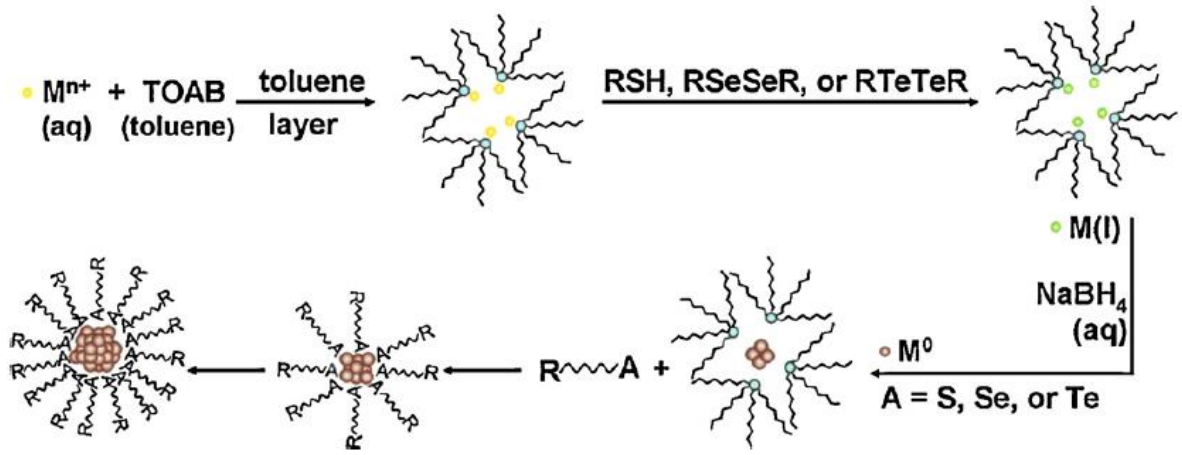

Figure 1.7. Mechanism for organo-chalcogenate-protected metal NP synthesis by the Brust-Schiffrin method (Zhao et al., 2013).

Other scientists have achieved breakthroughs with different reducing agents. In the 1980s, metal clusters and quantum dots were used. After several years' improvement, synthesis and stabilization of nanoparticles has been achieved by many sophisticated, but convenient methods. Figure 1.7 shows a typical metal nanoparticle synthesis method, the Brust-Schiffrin method (Zhao et al., 2013). During the last decade, many novel synthesis methods, especially seed-growth synthesis, have led to a variety of applications.

Synthesizing nanoparticles through chemical or biological reactions uses various solvents, such as water or organic solvents, all of which have certain advantages and disadvantages.

The water-based synthesis method usually is referred to as environmentally friendly synthesis or "green" synthesis. Water is a good solvent for a number of metal ions, as well as

many capping agents. The procedure includes preparation of an aqueous salt solution followed by reduction of the metal ions in a single step, and thus usually is considered a simpler protocol. After synthesis, the nanoparticles can be dispersed stably in water without further post-processing, which makes it easy for biological applications in conjugation with DNA, enzymes, and proteins. However, because of the ionic environment of a water solution, the concentration of nanoparticles is limited by ionic interactions in the aqueous phase, even at very dilute concentrations. Further, those nanoparticles do not assemble spontaneously into a close-packed arrangement with solvent evaporation. This limits its application to other fields, such as the semiconductor industry (Cliffel et al., 2000; Shon et al., 2001).

In contrast, organic solvent-based synthesis provides a high degree of control. It may be exercised over the monodispersity and nanoparticle size and chemical nature of the nanoparticle surface area via capping with different agents, including terminally functionalized thiols, amines, and so on. The nanoparticles assemble spontaneously into close-packed, hexagonal monolayers upon solvent evaporation. Therefore, the bulk properties of the nanoparticle assembly may be controlled by changing the interparticle separation via capping with different ligands. However, it is also clear that this process involves organic solvents that could pose a risk to the environment, especially in industrial processes (Rao et al., 2002).

In the synthesis of gold nanoparticles, both methods have specific advantages and disadvantages. Depending on the particular application of the nanoparticles, the ideal condition is to combine two methods and maximize their advantages. This may be accomplished by a process called phase transfer. This process transfers gold nanoparticles synthesized in one medium, either water or organic solvent, to another medium. Figure 1.8 shows an example of phase transfer of

Pt nanoparticles. The ability to move nanoparticles across liquid interfaces also makes it possible to probe certain applications. For example, variation in the optical properties of the nanoparticle solution is an attractive feature of phase-transfer protocols (Underwood et al., 1994).

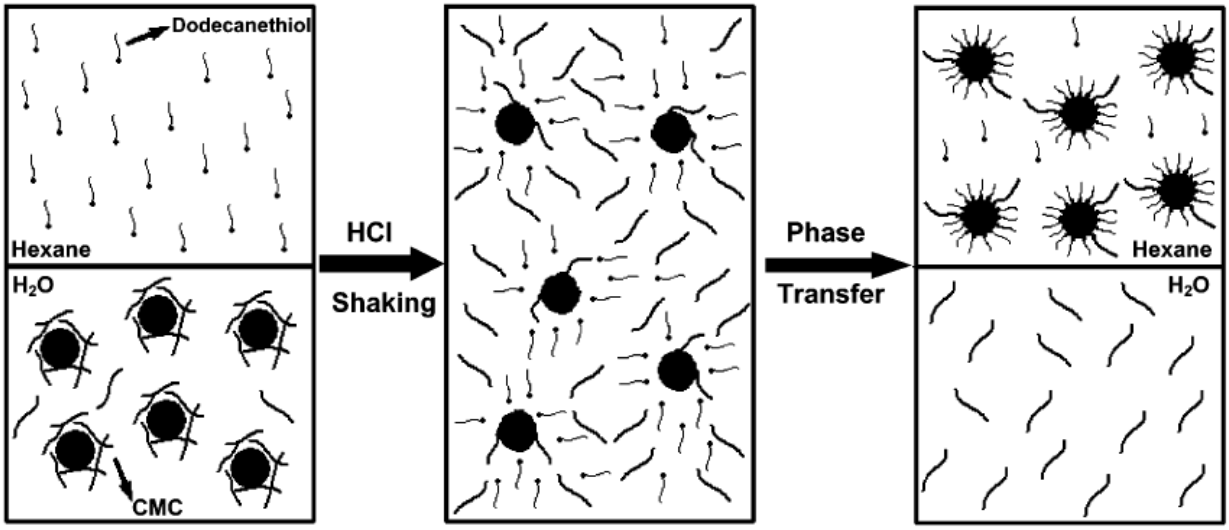

Figure 1.8 Illustration of the mechanism of the phase transfer of CMC-stabilized Pt nanoparticles from the aqueous solution to the hexane phase (Liu et al., 2007a).

Chemical Vapor Deposition (CVD) is a very mature technology. However, we have achieved an in-depth understanding of the process and developed increasing applications of CVD to nanoparticle synthesis only in the past 40 years. CVD involves the dissociation or chemical reactions of gaseous reactants in an activated environment, followed by the formation of a stable solid product. This process includes homogeneous gas phase reactions that occur in the gas phase, or heterogeneous chemical reactions that occur near the local area of certain surfaces and lead to the formation of powders or films. The CVD process has been used widely to produce ultrafine metal powder materials. Figure 1.9 shows a typical schematic of the CVD process.

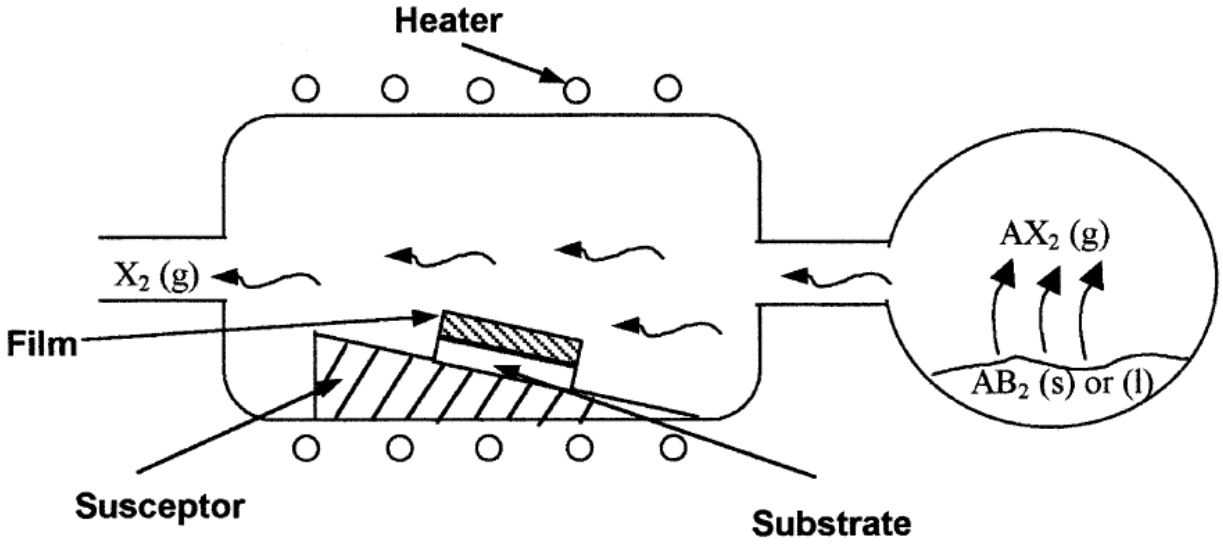

Figure 1.9. A typical schematic of the CVD process (Choy, 2003).

Typically, CVD is a complex chemical system, but it is still used widely because it has certain unique advantages. It can produce highly dense, pure materials and uniform films with good reproducibility at reasonably high deposition rates. CVD is a systematic process, and can be used to coat complex shaped components uniformly and deposit films according to industrial standards. It also has the ability to control crystal structure, surface morphology, and orientation of the products by controlling the process parameters.

1.2.2 Nanoparticle-deposited films

To use nanoparticles in actual applications, it is necessary to integrate them into bulk materials. During the past several decades, increased understanding of nanoparticles has led scientists to focus on specific films and coatings based on assemblies of nanoparticles. These new materials are designed to make use of nanoparticles on the macroscale. One fascinating

attempt is to bring nanoparticles into proximity at distances where they can interact with one another without aggregating.

1.2.2.1 Nanoparticle deposition technology: GXL and CVD

There have been many reports of major methods to produce nanoparticle-deposited structures. These include linker-assisted synthesis, in which a molecule is introduced between the nanoparticles and kept in the final film; the template-assisted method, in which the nanoparticles are forced to form certain structures and the template is removed at the end of the synthesis, and direct deposition of nanoparticles, in which the interaction between the nanoparticles and the surface helps organize the nanoparticle assembly (Neouze, 2013). Figure 1.10 shows a typical nanoparticle coating method: Langmuir layer-by-layer deposition. These technologies can be categorized in two ways: post-deposition, in which the nanoparticles are synthesized before the deposition process, and in-situ deposition, in which the nanoparticles are formed as soon as they are deposited on certain assembly templates.

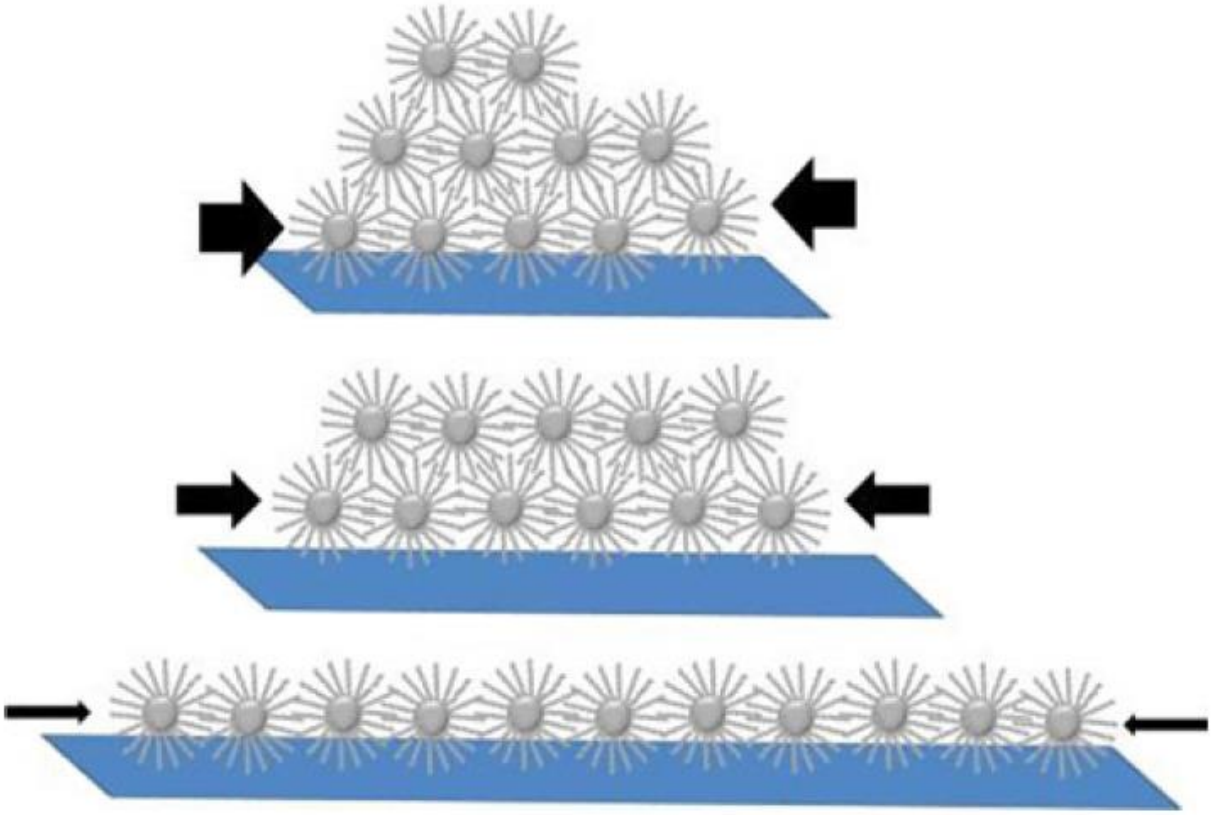

Figure 1.10. Langmuir–Blodgett deposition of mono-, di-, or tri-layers of gold nanoparticles (Neouze, 2013).

One special technology in post-deposition is the Gas-Expanded Liquid (GXL). Several research groups have demonstrated the use of gas-expanded liquids as another new choice of solvent. Gas-expanded liquids are mixtures of compressible gases dissolved in an organic solvent (Jessop et al., 2007). When CO_2 (or other compressible gas) dissolves in an organic solvent, the liquid volume expands. Organic solvents' ability to dissolve gases differs considerably. Certain organic liquids, such as methanol and hexane, dissolve a large amount of CO_2 and expand greatly. Figure 1.11 illustrates the volume expansion of n-hexane by CO_2, showing that when the pressure of compressed CO_2 is increased from 100 to 700 psi, the volume of n-hexane expands to

almost 200% of its original volume. This expansion causes noteworthy changes in almost every physical property of the original solvent, including density, solubility, and viscosity.

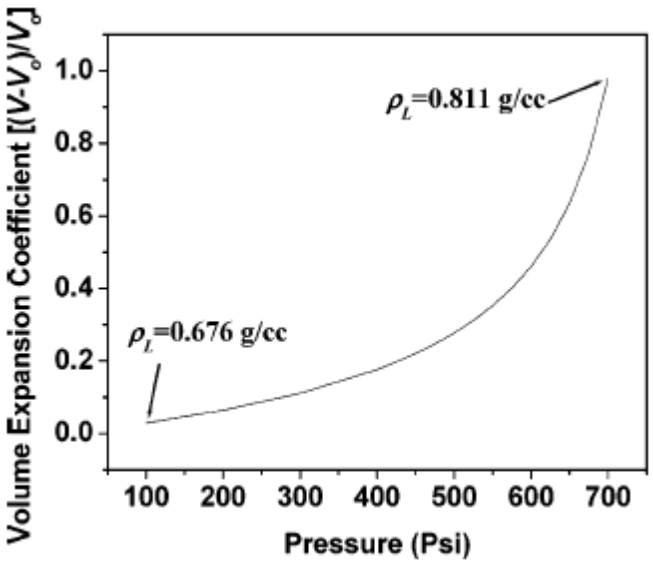

Figure 1.11. Volume expansion coefficient of liquid n-hexane with increasing CO_2 pressure (Anand et al., 2005).

Many methods have been employed to produce a deposition layer of certain polymers ororganic and inorganic nanoparticles, based on technologies that use the CO_2 expansion of a solution, including precipitation with a compressed antisolvent, supercritical antisolvent precipitation, and depressurization of a nanoparticle solution. Because typical nanoparticle processing methods are usually very solvent consuming and time intensive, the use of GXL as a precipitation technology for nanoparticle solutions has received great attention over the last several years. Several groups have been able to precipitate silver and gold nanoparticles in fractions of different sizes in supercritical ethane by tuning the density of the medium (Clarke et al., 2001; Shah et al., 2002; Williams et al., 2009).

The mechanism of GXL nanoparticle deposition can be described as follows. When an organic dispersion of nanoparticles is pressurized with CO_2, the CO_2 dissolves into the organic phase and acts as an antisolvent. At low CO_2 pressures, the gas does not dissolve well in the liquid solvent, but as the pressure increases, the solubility of the gas increases significantly, allowing a large amount of CO_2 to dissolve into the liquid phase. When the CO_2 becomes the main portion of the mixture solvent, the stabilization provided by the interaction between the ligand tails and the solvent is reduced, which causes the nanoparticles to begin to precipitate from the dispersion. By increasing the pressure of CO_2 slowly, nanoparticles can be precipitated slowly from the dispersion to achieve uniform nanoparticle films. Figure 1.12 shows the mechanism of nanoparticle precipitation in GXL. To make the final nanoparticle film smooth, a supercritical drying stage must be introduced that removes the solvent and creates thin films of good quality.

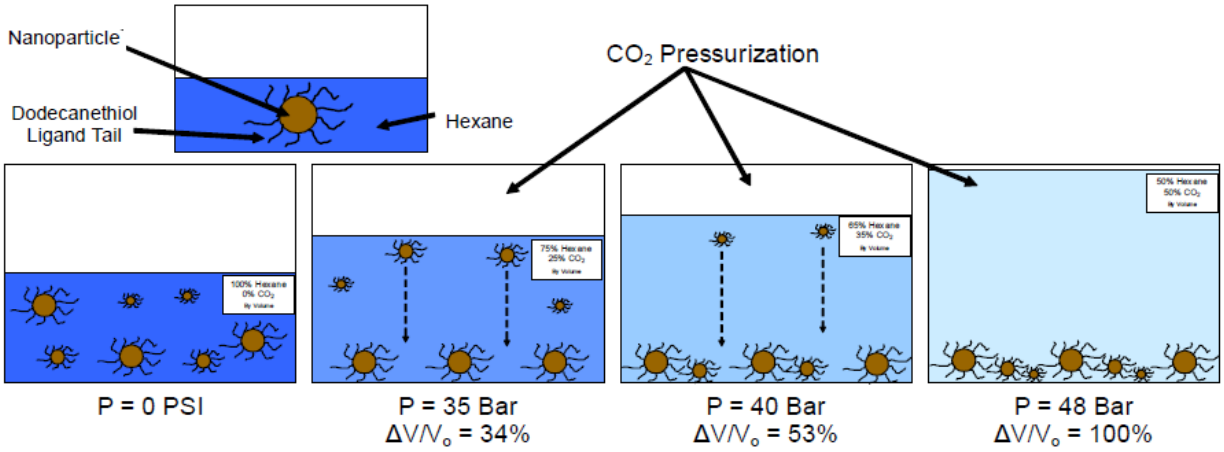

Figure 1.12. Mechanism of nanoparticle precipitation in GXL (Saunders, 2011a).

As mentioned in Section 1.2.1.2, CVD is a promising method for simultaneous nanoparticle film synthesis and coating. However, conventional CVD technology still has some

disadvantages. To increase the efficiency of the process, the use of toxic, corrosive, flammable, or explosive precursor chemicals is inevitable, and the amount used is usually relatively high. This may cause potential safety hazards. In addition, when complex reactions are required for certain multicomponent nanoparticle systems, it is difficult to deposit such materials under well-controlled conditions, as different precursors have different vaporization rates; therefore, to overcome those problems, a deposition system with better control must be used.

Suntola invented Atomic Layer Deposition (ALD) to enable nanoparticle film deposition with good uniformity and precise control (Kim et al., 2009). A typical ALD process consists of four essential steps: precursor exposure, evacuation or purging of the precursors and unwanted products from the chamber, exposure of the reactant species, and evacuation or purging of the chamber. This procedure is illustrated in Figure 1.13. ALD is very similar to CVD, and in fact, they follow the same mechanism. However, the most important feature of ALD is the limitation of precursor adsorption and the sequential exposure of precursors and reactants. The ALD reaction occurs in such a way that it breaks the CVD reaction into half-reactions, keeping the precursor materials separate during the reaction. This results in the unique characteristics of ALD.

One of the most significant advantages of ALD is its excellent uniformity. As ALD is based on self-limited adsorption of the precursors, the amount of the reactant can be controlled precisely. This excellent characteristic of ALD has enabled the synthesis of nanoscale particles of exact sizes. Thickness and composition control is feasible at the atomic level as well. Thus, ALD is not only a good method of synthesis, but also is an ideal deposition technique to form thin nanoparticle films and nanostructures. There have been early reports of multilayer film

formation using ALD. The ability to construct thin films on the nanoscale is very important in many applications (Kim et al., 2009).

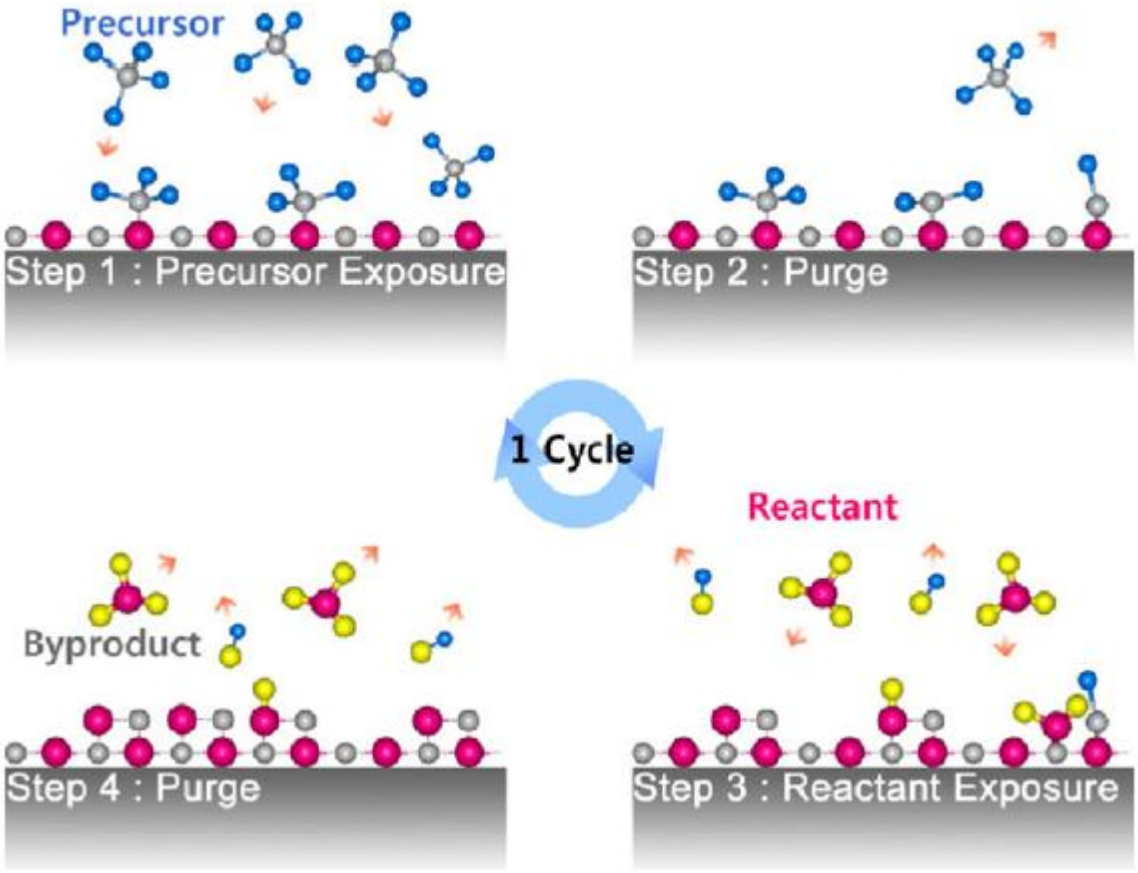

Figure 1.13. Schematic of the ALD process (Kim et al., 2009).

Another key feature of ALD is its ability to synthesize high quality nanoparticles and deposit them at low temperatures. In conventional deposition technology, the temperature of the reaction is sometimes very crucial, and may require high temperatures. Because the adsorbed precursor molecules will react with reactants directly, the level of impurities and the amount of unwanted chemical during the ALD process are expected to be low compared to conventional methods, even at low growth temperatures. However, as most precursor molecules are injected

into the ALD system, a heating system for the precursor or substrate typically is required. This can be achieved easily and modified during actual production. A Al_2O_3 ALD using TMA and water is a typical low-temperature ALD process, and can be conducted even at a temperature lower than 40 °C (Groner et al., 2004). The resulting film deposited also is very smooth (Figure 1.14).

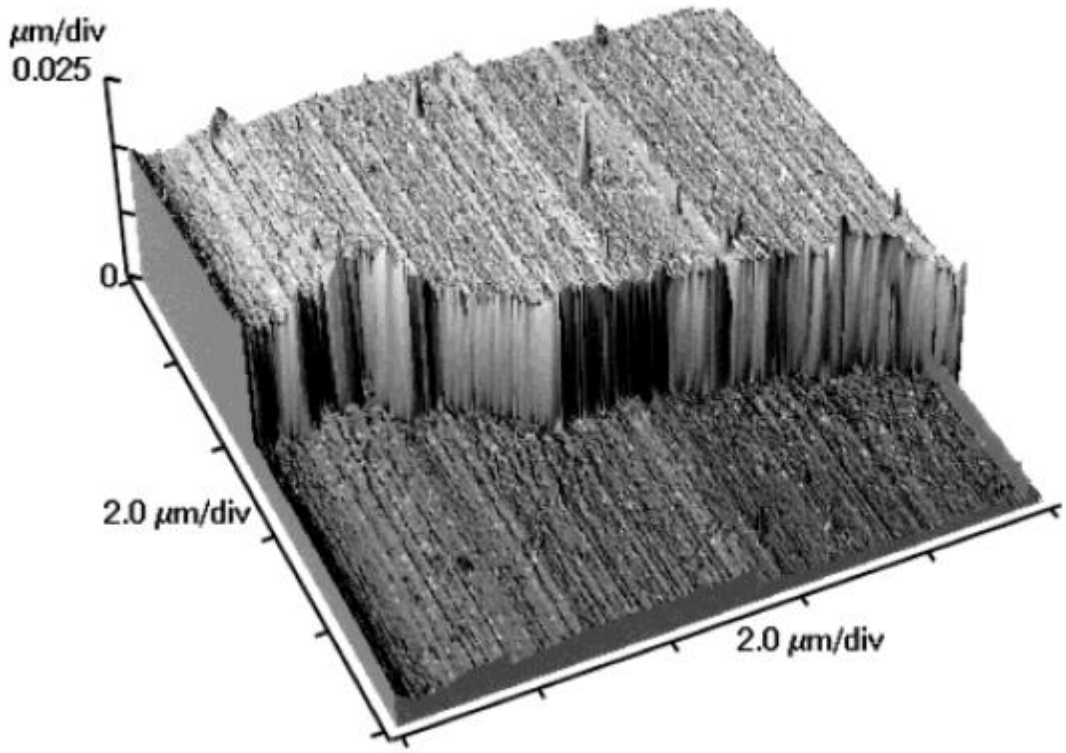

Figure 1.14. AFM of an Al_2O_3 ALD film with a thickness of 50nm (Groner et al., 2004).

1.2.2.2 GXL-deposited nanoparticle films

After nanoparticles are deposited on surfaces, the morphology and tribology of the original surfaces changes. Usually, nanoparticles are used to roughen the surfaces, although contrasting situations exist. A smooth surface indicates a high quality substrate, but it may introduce other problems during applications. Interfacial forces that exist between two relatively smooth interfaces could cause adhesion and stiction in all types of devices. These interfacial forces depend highly on the distance between surfaces, which makes applied force very sensitive to surface contamination (DelRio et al., 2006). Therefore, it is essential to treat the surface of the devices.

One of the most effective treatments employs a chemical modification approach that addresses adhesion and stiction successfully, and involves deposition of a thin molecular film onto microstructure surfaces. The molecular films deposited are referred to as self-assembled monolayers (SAMs). During deposition, the precursor molecules attach themselves first to the nanostructure surfaces and then align and orient with each other, forming a thin film at the molecular level with a degree of order (Figure 1.15). Typically, the molecules used to form SAMs on surfaces have a polar head, which binds to the surface chemically, and a non-polar tail that points away from the surface.

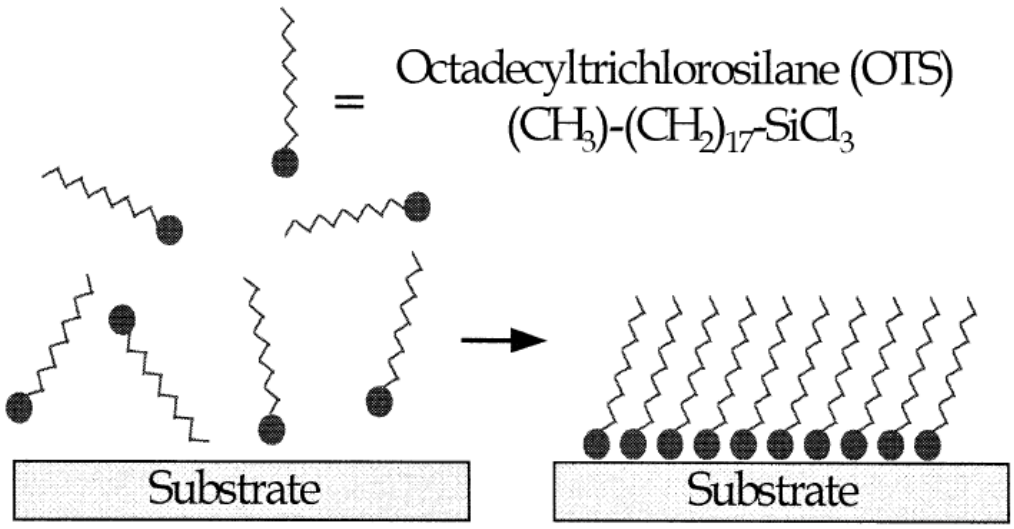

Figure 1.15. Schematic of the SAM formation process (Maboudian et al., 2000).

However, SAM has its limitations. The SAM precursors used most commonly are silanes, which produce one HCl molecule when the Si-Cl bond is hydrolyzed. This could pose a hazard for any metal component in the device. Another limitation derives from the sensitivity of precursor polymerization to ambient moisture and water concentration, which are usually difficult to control. Moreover, SAM technology does not change the surface roughness greatly, and the interaction problem related to the distance between surfaces remains. To go further, attention has focused on assembling and immobilizing nanoparticles onto solid surfaces (Yamanoi et al., 2004; Yonezawa et al., 2001), and following this research approach, strategies have been developed that allow nanoparticles to be immobilized. Over the last several decades, reports have been published about immobilizing nanoparticles on surfaces, typically through interactions between particles and SAMs.

Our group has demonstrated that dispersed metallic nanoparticles can be precipitated from a solution and deposited as uniform, thin films via GXLs (McLeod et al., 2005; Liu et al.,

2006). During this process, CO_2 is introduced to induce dispersed nanoparticles to precipitate. Following particle precipitation, the mixture is brought to the supercritical state to eliminate the liquid-vapor interface before it is dried. By using supercritical drying, nanoparticle-coated samples can be recovered without experiencing detrimental dewetting effects. The coated nanoparticle films reduce the real contact surface area effectively, and change the chemical constituents of the contacting areas as well. When this type of nanoparticle film is applied to actual polysilicon microstructures, it has been shown to achieve a uniform nanoparticle coating (Figure 1.16), and reduce the apparent adhesion energy that occurs ordinarily due to dominant interfacial surface forces (Hurst et al., 2009).

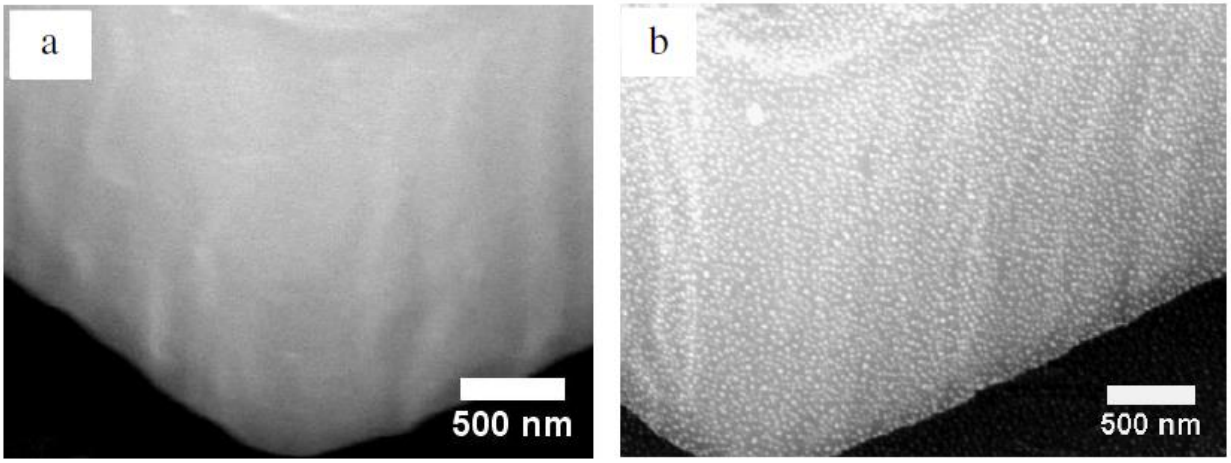

Figure 1.16. SEM image of polysilicon cantilever beam tip (a) uncoated and (b) coated with nanoparticles (Hurst et al., 2009).

1.2.2.3 CVD-based nanoparticle coatings

The fabrication of nanoparticle coatings is among the key requirements in the development of nanotechnology. To construct nanoparticle coatings by CVD, a way to confine the dimensions of the nanostructured materials prepared must exist. While CVD can be used in various aspects of nanofabrication, the combination of CVD with other technologies, such as the self-assembly process, crosslinking, and monolayer coating, is particularly attractive.

In conventional nanoparticle deposition technology, metal nanoparticles must be synthesized before they are deposited onto certain surfaces. The metal nanoparticles are stabilized with different ligands, which may have certain negative effects on the coated surface. A novel vapor phase deposition (VPD) apparatus developed by Integrated Surface Technologies (Menlo Park, CA, USA) has been used to solve such problems. This VPD process includes depositions of elemental metals, metal nitrides, and metal oxides. The VPD reaction results in conformal, metallic thin film nanoparticle depositions with precise thickness control.

For example, Al_2O_3 nanofilms have been used widely as protective coatings for microelectromechanical system (MEMS) devices (Figure 1.17, Hoivika et al., 2003). Another example of environmental applications involves applying a TiO_2 coating on glass using titanium tetramethoxide and water to remove deinococus geothermalis cells effectively through photocatalytic effects (Kim et al., 2009).

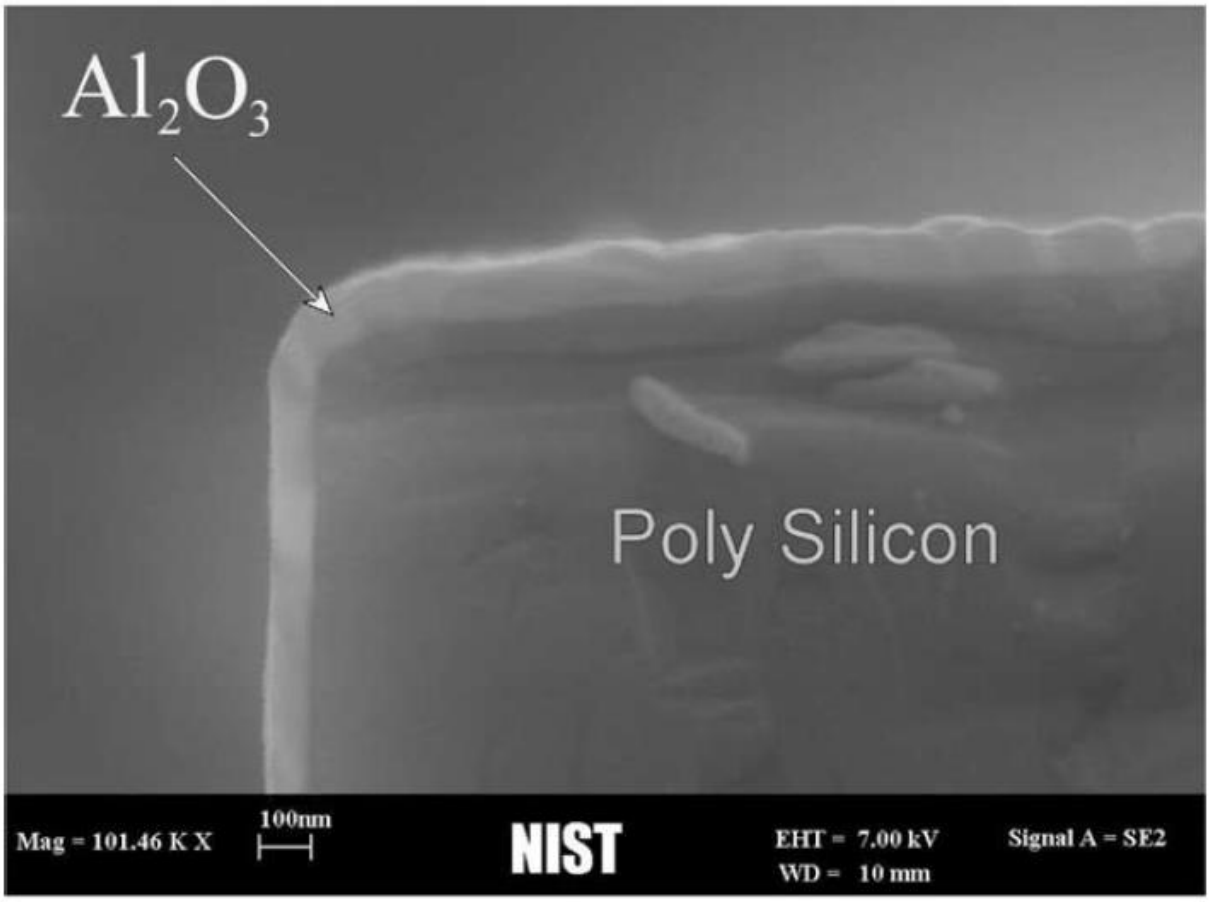

Figure 1.17. SEM image showing the tip of a cantilever beam coated with Al_2O_3 (Hoivika et al., 2003).

When CVD/VPD technology is associated with other processes, such as self-assembled monolayer formation, new applications can be achieved, such as superhydrophobic nanoparticle coatings. This is because VPD nanoparticle films are particularly favorable for the growth of a wide variety of chemical absorbents. Currently, many companies use such technology to apply water-resistant coatings on commercial electronic devices. A research group from the University of Colorado deposited an Al_2O_3 nanoparticle film as a seed layer for the subsequent attachment of hydrophobic chemicals. This deposition technique resulted in a solid hydrophobic film with a water contact angle of 108 ± 2^{o} (Herrmann et al., 2005).

The superhydrophobic coatings deposited also can be applied on biomaterials. ALD of aluminum oxide and zinc oxide onto natural cotton cellulose produces a transition from hydrophilic to hydrophobic, then from hydrophobic back to hydrophilic (Figure 1.18, Lee et al., 2012).

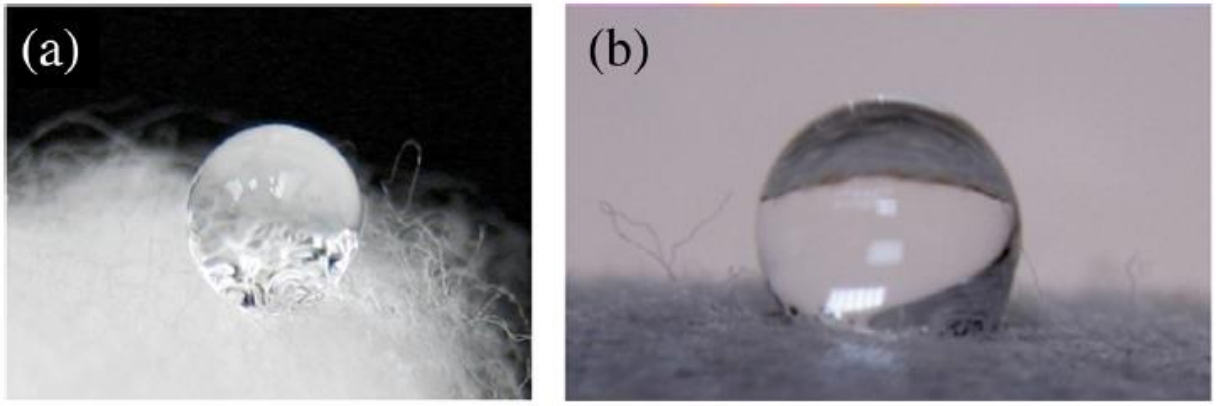

Figure 1.18. Pictures of a water drop on a cotton ball (a) before and (b) after Al_2O_3 ALD process (Lee et al., 2012).

1.3 Objectives of this work

Surface modifications with nanoparticles are major concerns in the realization of the full potential of microdevices. Previous attempts have shown that wear and stiction can be decreased and surface properties, such as hydrophobicity, can be improved. Currently however, no single surface treatment technology can solve all problems of reliability at once. Further, more precise control of the nanoparticle coatings is still lacking. Therefore, the goal of this research was to achieve a fundamental understanding of the way in which the surface chemistry and deposition

conditions of the nanoparticles affect the films achieved. On that basis, we can synthesize and apply well-controlled nanoparticle coatings with the properties desired to actual devices.

Because of our group's previous work on the deposition of nanoparticles by GXL technology and supercritical fluid drying, the use of deposited nanoparticles as coatings has been explored. However, the intentional deposition of particles onto different kinds of surfaces and the control of film formation are new concepts. Therefore, a number of fundamental studies has been conducted. Through the effects of the critical surface tension of the SAMs, the film growth alternates between layer-by-layer deposition and island formation and changes the surface topography as well. The surface topography of the deposited film also is influenced by the concentration of the nanoparticle solution, the average size and size distribution of the nanoparticles, and the nature of the nanoparticle surface chemistry. Therefore, an evaluation model was applied to the surface topographies from AFM data as a quantitative assessment method for the coatings obtained.

After investigating plain Si surfaces coated with films formed by nanoparticles of varying sizes and concentrations, a number of nanoshapes, including larger nanoparticles and nanorods were applied to MEMS devices via our GXL deposition technique. Lab-made MEMS chips were fabricated and used to evaluate performance by the imaging technique of phase shifting interferometry. The effect of nanostructure shape on surface coverage, real contact area, and the apparent work of adhesion was investigated. These tuning effects achieved better tribology control and the theoretical analysis of the contribution of adhesion is discussed.

In the current scheme, the processing time and final durability of VPD-based nanoparticle films still limit their wide commercial application. The primary scientific merits of this work included improving the efficiency of the process while maintaining film quality. Further, the chemical stability and failure mechanism must be determined. To do so requires fundamental material characterizations for an optimal target structure and morphology. VPD coated substrates were characterized for their durability, water-resistance, and electrical and thermal properties. Atomic force microscopy, Fourier transform infrared spectroscopy, and other analytic techniques were used to check the fundamental mechanism of film formation and failure. The results will satisfy the commercial use of, and economic interest in such coatings in the market.

Chapter 2

Modeling and analysis of surface topographical parameters from experimental data

2.1 Introduction

Scientists realized long ago that rough surfaces on a microscopic scale result in an actual area of contact that is extremely small compared to the nominal area. The calculation of the area of contact, or even the prediction of how this varies with load, is very difficult, especially when various shapes are introduced. To obtain a better understanding of the way in which contact behaviors are affected by different surface topologies, certain models of the surface contact must be constructed. These models are used to estimate fundamental parameters of rough surfaces and ensure that a fair comparison can be made among films deposited by various nanomaterials.

The rms surface roughness value has been used widely as a key parameter for rough surfaces. However, for two surfaces in contact, rms surface roughness sometimes does not provide enough information. Some AFM data may have similar rms surface roughness, but they clearly show contact behaviors that differ significantly based on their apparent morphologies, such as higher separation distance and a smaller number of touching asperities, leading to a possible lower real contact area. A fair comparison of the contact effect between these surfaces should be demonstrated as well.

2.2 Modeling of surface contact

Until now, nanospheres, nanocubes, and nanorods have been the nanomaterial shapes used most commonly. The modeling process begins with one shape contacting a flat surface. Assume that a simple shape is in contact with a flat surface and a load is applied normally to the surface. Some deformation will occur at the contact point and one can calculate those changes, including stress distribution, contact area, and normal displacement.

The fundamental calculations are based on the Hertzian contact model, the classical theory of contact that focuses primarily on non-adhesive contacts. However, the Herzian contact model is an ideal model and has several assumptions: the surfaces are continuous and non-conforming; the strains are small; each solid surface in contact can be considered an elastic half-space, and the surfaces are frictionless (Johnson, 2003). Additional complications arise when some or all of these assumptions are violated, which usually occurs in practical problems and are referred to as non-Hertzian contacts. However, with further improvements, the Hertzian model can still be applied. Therefore, the following calculations are necessary, even for more complex models.

For a sphere on a flat plate:

The radius of the contact area:

$$a = \sqrt[3]{\frac{3F\left[\frac{1-v_1^2}{E_1} + \frac{1-v_2^2}{E_2}\right]}{\frac{4}{R_1}}} \qquad (2.1)$$

Contact area:

$$S_a = \pi a^2 \tag{2.2}$$

Normal displacement:

$$\delta_a = 1.04 \sqrt[3]{\frac{F^2 \left[\frac{1-v_1^2}{E_1} + \frac{1-v_2^2}{E_2}\right]^2}{2R_1}} \tag{2.3}$$

For a cylinder on a flat plate:

The half-width of the rectangular contact area:

$$b = \sqrt{\frac{4F\left[\frac{1-v_1^2}{E_1} + \frac{1-v_2^2}{E_2}\right]}{\frac{\pi L}{R_1}}} \tag{2.4}$$

Contact area:

$$S_b = 2bL \tag{2.5}$$

Normal displacement:

$$\delta_b = \frac{F}{L}\left(\frac{1-v_1^2}{\pi E_1}+\frac{1-v_2^2}{\pi E_2}\right)\left[1+ln\frac{L^3}{\left(\frac{1-v_1^2}{\pi E_1}+\frac{1-v_2^2}{\pi E_2}\right)FR_1}\right] \quad (2.6)$$

For a cube on a flat plate (Persson, 2001):

The edge length of the cube:

$$c \quad (2.7)$$

Contact area:

$$S_c = c^2 \quad (2.8)$$

Normal displacement:

$$\delta_c = \frac{F}{c}\left[\frac{1-v_1^2}{E_1}+\frac{1-v_2^2}{E_2}\right] \quad (2.9)$$

where F is the applied force, v_1 and v_2 are Poisson's ratio of metal and silicon, E_1 and E_2 are Young's modulus of metal and silicon, R_1 is the radius of sphere or circular end of cylinder, and L is the length of cylinder.

The simplest model of a randomly rough, but nominal flat surface, consists of a regular array of nanospheres, nanorods, or nanocubes with equal dimension parameters and equal height. If such a surface is pressed against an elastic solid with a flat surface, the Hertz contact theory can be applied approximately to each asperity contact region and the total effect can be taken into account.

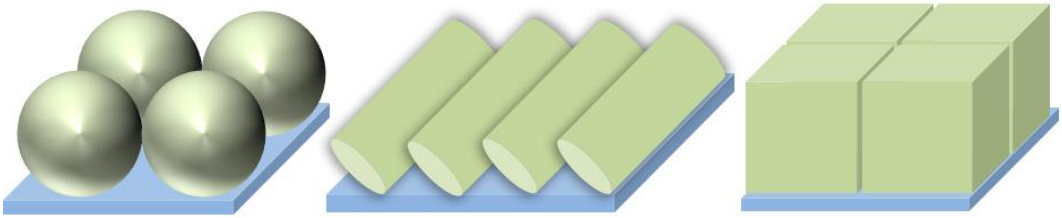

Figure 2.1. Illustration of regularly deposited nanoshapes.

An area of 20nm x 20nm was defined for the nanofilm deposition. All of the nanoshapes are deposited regularly on this surface (Figure 2.1). The dimensions and the depositing patterns of the nanoshapes are:

Nanospheres: Radius = 5nm. Single layer dense packing.

Nanorods: Radius of circular area = 2.5nm. Length = 20nm. Single layer dense packing.

Nanocubes: Edge length = 10nm. Single layer dense packing.

By using these dimension parameters, this fixed area now contains the same number of nanostructure asperities (4 for each) for different nanofilms. It can be seen that different shapes have certain effects on the final contact area and the displacement of contacting asperities.

However, these ideal calculations cannot be applied to actual surface contact, as it is almost impossible to obtain nanostructures deposited in such regular patterns. A realistic surface is more like a set of randomly distributed spherical or non-spherical asperities. When the Hertzian theory is applied directly to the contact between rough surfaces, two difficulties arise. One is that the area of the contact spot depends on the radius of the asperity, which is not usually known until it is measured directly; another is that the predicted variation in the area with load is usually incorrect. Therefore, Greenwood and Williamson presented a more detailed model of elastic contact between nominally flat surfaces (Greenwood et al., 1966). Nominally, flat surfaces may be defined as those in which the area of nominal apparent contact is large, such that the individual contacts are dispersed and the forces acting on neighboring areas do not influence each other.

Now, the contact between two nominally flat surfaces with an rms roughness of σ_1 and σ_2, respectively, will be our concern. To simplify it, the contact of one flat smooth surface and another rough surface of equivalent rms surface roughness σ was considered:

$$\sigma = \sqrt{(\sigma_1^2 + \sigma_2^2)} \tag{2.10}$$

It is assumed that all asperity summits have similar structures, and that their heights vary randomly: the probability that a particular asperity has a height between z and z+dz above some reference plane will be φ(z)dz, where φ(z) is the height distribution function.

When two surfaces are pressed together and come in contact, the separation distance is d. Any summit for which the height, z, is greater than d will be compressed by δ=z-d. If there are N summits in a unit area, the total number of contact asperities, n, will be:

$$n = N \int_d^\infty \varphi(z) dz \tag{2.11}$$

For each summit, the contact area A_0 is determined by Equations 2.2, 2.5, or 2.8, where A_0 should be a function of F. As δ is determined by F, A_0 can be related to δ as well.

$$A_0 = f(\delta) = f(z - d) \tag{2.12}$$

The expected mean contact area is:

$$A_m = \int_d^\infty A_0 \varphi(z) dz = \int_d^\infty f(z - d) \varphi(z) dz \tag{2.13}$$

Therefore, the total real contact area, A_c, is:

$$A_c = N A_m = N \int_d^\infty f(z - d) \varphi(z) dz \tag{2.14}$$

From Equation 2.14, it can be seen that the separation distance of the two surfaces and the density of the number of contacting asperities affects the total contact area (Greenwood et al., 1966). In addition, the height distribution of the rough surface must be taken into account, and these parameters must be discussed to make fair comparisons between nanofilms deposited by different shapes.

The height distribution function, $\varphi(z)$, derives from the actual experimental data. Existing reports have concluded that for many common rough surfaces, a Gaussian distribution is a good approximation of the actual height distribution function (Greenwood et al., 1966).

2.3 Analysis of surface contact model and roughness parameters

The rms surface roughness value is used widely as a key parameter for rough surfaces. However, for two surfaces in contact, rms surface roughness sometimes does not provide sufficient information. For example, as Figure 2.2 shows, these two line profiles have the same rms surface roughness, but it is clear that their contact behaviors differ significantly. The second surface has a higher separation distance and smaller number of touching asperities, which leads to a possible lower real contact area. Thus, a fair comparison between these surfaces on the contact effect should be demonstrated.

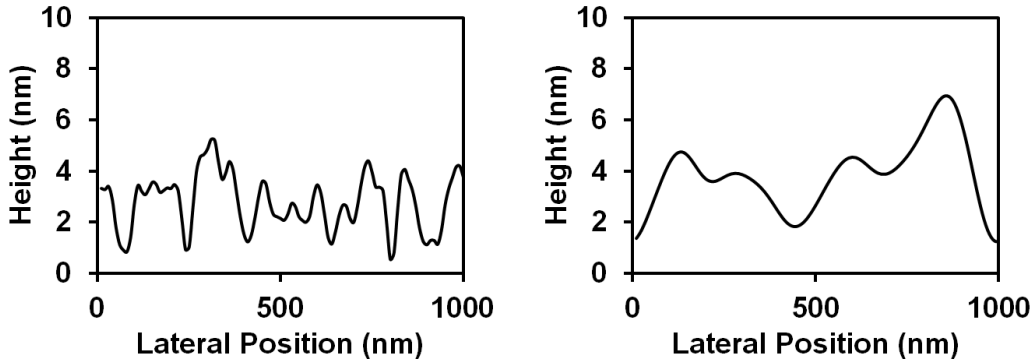

Figure 2.2. Two line profiles with the same rms surface roughness but different mean heights and contact asperities.

Roughness is a key issue in contact modeling, as even a small change in roughness in the surface coating may result in significantly different true and apparent contact areas at an interface. Therefore, dependable models of surface roughness require knowledge of the number of contact asperities, the true contact area, and local contact pressures at the interfaces (Greenwood, 1992; Johnson, 2003). Some fundamental analytic approaches have been introduced to develop sophisticated models of surface contact for the evaluation of interfacial properties. The first such approach was the Greenwood-Williamson (GW) model (Greenwood et al., 1966). Later, this analysis was carried out by McCool (McCool, 1986), who demonstrated a method to extract appropriate characteristic parameters for the GW model from surface topographic measurements. The analytic method was modified further by Nayak (Nayak, 1973), which who provided a model that takes into account some corrections to the GW model. Based on this modeling work and calculations, the general contact properties of MEMS interfaces were generated by de Boer et al. through a simple, yet reasonable analytic model (Carpick et al., 2002).

Here we provide a calculation based on the GW model and applied to the surface topographies from AFM data presented as a quantitative assessment method for the comparison between different coatings. To carry out this analysis, we followed the treatment of de Boer (Carpick et al., 2002) and McCool (McCool, 1986).

The basic assumption of the GW model is that the surface has a large number of spherical summits with a random distribution of summit heights, but the same radius (Greenwood et al., 1966). A contact between the rough surface and a rigid, flat surface is engaged and the number of summits in contact, the real contact area, and total load are calculated.

The quantitative analysis begins with calculation of three spectral moments of the surface topography: m_0, m_2, and m_4, known as the zeroth, second, and fourth spectral moments of the profile, respectively. These numbers are equivalent to the mean square height, slope, and second derivative of a profile in an arbitrary direction from the surface topography, which are defined as follows:

$$m_0 = \langle z^2 \rangle, m_2 = \langle (dz/dx)^2 \rangle, m_4 = \langle (d^2z/dx^2)^2 \rangle \tag{2.15}$$

where z is a profile in an arbitrary direction, x and < > denotes a statistical average, and m_0 is the mean square surface height; thus, the RMS roughness, R_q, can be related to m_0: $m_0 = R_q^2$. The spectral moments, m_2 and m_4, cannot be measured directly; therefore, these two parameters can evaluated using the procedure provided by de Boer (Carpick et al., 2002). AFM images were obtained and exported as raw ASCII data file, and the first and second numerical derivatives of z height with respect to the fast scan direction were calculated from the exported

data. The data calculated were imported back to Gwyddion as images and the RMS values of these derivative images were evaluated. The square of the RMS values from these two data images provides the values of m_2 and m_4, respectively.

The bandwidth parameter, α, can now be calculated as $\alpha = m_0 m_4 / m_2^2$. α is a key parameter in McCool's analysis, as it is related to the density of summits, the distribution of curvature and height, and the mean plane distance (McCool, 1986).

Based on these numbers, surface characteristic parameters can be calculated. The average surface summit density, D_{SUM}, is given by:

$$D_{SUM} = m_4/(6\sqrt{3}\pi m_2) \tag{2.16}$$

The mean summit curvature averaged over all summit heights, κ_m, is given by:

$$\kappa_m = 8\sqrt{m_4}/(3\sqrt{\pi}) \tag{2.17}$$

The mean summit radius averaged over all summit heights, R, is then given by the reciprocal of κ_m.

The standard deviation of summit height distribution σ_s was calculated by Bush et al. (Bush et al., 1976):

$$\sigma_s = \sqrt{(1 - 0.8968/\alpha)m_0} \tag{2.18}$$

The expected average number of summits in contact, n, is given by:

$$n = D_{SUM} F_0(d/\sigma_s) \tag{2.19}$$

where d is the separation between the summit's mean height and the approaching surface.

The ratio of true to apparent contact area, A_c/A_0, is given by:

$$A_c/A_0 = \pi R \sigma_s D_{SUM} F_1(d/\sigma_s) \tag{2.20}$$

Combining all the parameter expressions above, this ratio can be rewritten as:

$$A_c/A_0 = \sqrt{\pi(\alpha - 0.8968)/768} \cdot F_1(d/\sigma_s) \tag{2.21}$$

The function $F_n(t)$ is given by:

$$F_n(t) = \frac{1}{\sqrt{2\pi}} \int_t^{\infty} (x - t)^n e^{-x^2/2} dx \tag{2.22}$$

which is from the original GW model and integrates quantities using the Hertz theory of contact with an assumption of a Gaussian summit height distribution (Greenwood et al., 1966).

For the calculation, the surface separation, d, is chosen to be equal to one standard deviation of the summit height distribution, σ_s, which indicates that d/σ_s is 1. This ensures that the calculations represent a substantial, but not severe interaction between the surfaces.

Another function that we used for surface analysis is the HHCF (height-height correlation function). For AFM measurements, the height-height correlation function based on profiles along the fast scanning axis can be evaluated from the discrete AFM data values as:

$$H(\tau_x) = \frac{1}{N(M-m)} \sum_{l=1}^{N} \sum_{n=1}^{M-m} (z_{n+m,l} - z_{n,l})^2 \tag{2.23}$$

where $m = \tau_x/\Delta x$, τ_x is the sampling length, Δx is the sampling interval, N and M are the number of rows and columns of the data field, respectively, and z is the value of the height at the corresponding point.

For practical modeling, a specific function form for the height-height correlation function H(x) was proposed by Sinha et al. (Sinha et al., 1988):

$$H(x) = 2\sigma^2(1 - e^{-(x/T)^{2h}}) \tag{2.24}$$

where σ is the rms roughness, T is the autocorrelation length, and h is the roughness exponent.

The asymptotic behavior of this height-height correlation function can be described as:

$$H(x) \approx \begin{cases} \sigma^2(x/T)^{2h} & for\ x \ll T \\ 2\sigma^2 & for\ x \gg T \end{cases} \tag{2.25}$$

Therefore, the short- and long-range roughness properties can be characterized using H(x).

A linear fit on a log-log plot of HHCF at short lateral length ranges was used to extract the roughness exponent, h, which can be obtained from the slope of the linear fit. h is between 0 and 1 and is used to characterize short-range surface roughness, which indicates whether the surface is smooth or jagged within a small area (subjectively speaking). A small value of h produces extremely "jagged" surfaces, while values of h that approach 1 appear to have "smooth" surface patterns (Krim et al., 1993). It should be noted that h is not an indicator of the roughness overall, but can be used to quantify the way in which the roughness changes with the length scale within a short-range. At long-range, H(x) will converge to $2\sigma^2$, determined by the rms surface roughness.

The autocorrelation length, T, can be used to determine the special variation along the lateral direction. A higher T value indicates a larger average hill or valley grain size, and the surface variations are correlated within this length range.

2.4 Conclusion

Surface roughness is an important parameter that affects the properties of interfaces of bulk materials. Although roughness parameters from surfaces have been discussed to some extent, a detailed study must be conducted that integrates experimental topography measurements of various surfaces.

Statistical surface descriptors, such as rms roughness and maximum peak-to-valley height, are useful in describing height variations in the vertical direction, but contain no information about spatial variations in the lateral direction. Therefore, surface parameters of both height and spatial scale are required to describe surface topography variations sufficiently. In this chapter, an analytical model based on the Greenwood-Williamson is introduced to model experimental AFM data to characterize surface topography. Height-height correlation functions (HHCF) were used for data analysis, and provided quantitative metrics related to the spatial variation and scaling of surface roughness at multiple length scales. This theoretical investigation can be used as a general method and applied on most surfaces to make fair comparisons between them. The effect of these parameters will be discussed further with nanoparticle coatings obtained experimentally.

Chapter 3

Synthesis and characterization of films of size-varied gold nanoparticles on silicon substrates via a GXL deposition process

3.1 Introduction

Nanoparticles cannot be precipitated and evaporated well from stable solutions onto silicon substrates or microdevices because of the strong interfacial forces and the dewetting effect during the drying process. Therefore, we used the GXL deposition technique to solve these problems.

Our group has studied the deposition of stabilized nanoparticles onto a silicon substrate via gas-expanded liquids previously. However, not too much is known yet about the way in which the deposition conditions affect film formation and how better control can be achieved in the surface chemistry and morphology of the film deposited. The opportunity exists to deposit various self-assembled monolayers in liquid phase onto substrates prior to nanoparticle deposition to combine the SAM and GXL technologies by providing both a low energy surface and a rough nanoparticle coating. Before the deposition of nanoparticle films becomes a practical option for actual devices, the behavior of GXL-deposited nanoparticles on such surfaces must be characterized. Another important factor is the size of the original nanoparticles, which is also the key point in nanotechnology. The surface morphology of the deposited film is influenced by the concentration of the nanoparticle solution, the average size, and size distribution of the

nanoparticles, and the nature of the nanoparticle's surface chemistry. Therefore, we investigated the manner in which the surface roughness is affected using nanoparticles of different sizes.

3.2 Experimental section

3.2.1 Synthesis of thiol-stabilized gold nanoparticles

Thiol-capped gold nanoparticles (AuNPs) were synthesized by a two-phase reducing precipitation process, the Brust method (Brust et al., 1994). All chemicals used for gold nanoparticle synthesis were purchased from Alfa Aesar and used as received. The synthesis procedure was as follows. A 36 ml aqueous solution containing 0.38 g hydrogen tetrachloroaurate was mixed with a solution of 2.7 g of the phase transfer catalyst tetraoctylammonium bromide in 24.5 ml toluene. After stirring the mixture for 1 h, the aqueous phase was removed and discarded, leaving a bright orange organic phase containing gold ions. The organic solution was then combined with a 30 ml aqueous solution containing 0.5 g $NaBH_4$ to begin to reduce the gold ions to their ground state. The mixture was stirred for 8-10 h to allow particle growth before the aqueous phase was discarded. 240 µl of thiol with the carbon chain structure desired was then added to the organic solution and stirred for 4 h to cap and stabilize the gold nanoparticles. The nanoparticle dispersion was then centrifuged with ethanol at 4500 rpm for 5 min to rinse the particles of excess thiol and reducing agent molecules. After repeating the centrifugation several times, the nanoparticles were dispersed and stored in n-hexane.

The synthesized nanoparticles were analyzed by evaporating a few drops of the dispersion onto a carbon-coated transmission electron microscopy grid, and TEM images were taken using a Zeiss EM 10CR transmission electron microscope.

3.2.2 Preparation of Si substrates

Small Si wafers were prepared by cutting large wafers into 1cm×1cm squares with a dicing blade. The Si wafers were ultrasonicated in acetone for 10 min, followed by isopropanol for 10 min, and then dried under a stream of nitrogen. The wafers were etched for 10 min in concentrated HF to remove the native oxide layer, rinsed in excess deionized water, and then dried under a stream of nitrogen. Thereafter, the wafers were placed into a Novascan PSD-UVT UV Ozone Cleaner and cleaned by exposure to ultraviolet light and ozone for 15 min. The wafers were loaded into a custom-built vacuum deposition system, the design of which can be found in our previous report (Poda et al., 2010). The vacuum deposition system consists of a rotary vane pump connected to a glass reaction chamber that contains electrodes to create in-situ, capacitively-coupled radio frequency (RF) plasma (13.56 MHz), which is necessary for plasma cleaning.

Surface treatment of the wafers included two steps: air and water plasma. The air plasma treatment is used to rebuild the surface oxide layer and water plasma treatment is known to leave the surface's hydroxyl group (-OH) terminated. The wafers were placed in the chamber on an aluminum sample holder placed beneath the lower (ground) perforated electrode. First, the vacuum system was pumped down to a pressure of less than 30 mTorr. A background of air gas

in the chamber was created by performing purge cycles with air. Then, air was allowed to flow into the chamber. When the pressure of the chamber reached 1000 mTorr, the airflow was cut off and the vacuum system was pumped down to approximately 300 mTorr. Next, plasma was struck by applying a dc bias to the perforated electrodes for 10 min. After the air plasma treatment was completed, the entire system was pumped down to base pressure and water gas was introduced into the chamber from the vapor delivery system to replace the air. A similar water plasma treatment was performed for 10 min. Treating wafers by plasma results in a clean, flat surface without organic contaminants. This cleaning method was repeated until inspection by contact angle measurement indicated that the water contact angle was lower than 5°.

3.2.3 Coating of self-assembled monolayers

SAMs were deposited onto the cleaned Si substrates following similar liquid-phase procedures. An n-octadecyltrichlorosilane (OTS) monolayer was formed by making a 1 mmol/L solution in n-hexane. After allowing the OTS molecules to hydrolyze for 45 min, the Si substrate was immersed in the OTS solution for 45 min, then taken out and rinsed in n-hexane. A 1H,1H,2H,2H-perfluorodecyltrichlorosilane (FDTS) monolayer was formed following a similar procedure with a 1 mmol/L solution in n-hexane. Next, a 3-mercaptopropyltrimethoxysilane (MPTS) monolayer was formed following the method reported method (Hurst et al., 2011). The Si substrate was immersed in a solution of 20 mL of 2-propanol, 400 μL of DIUF water, and 400 μL of MPTS heated to 70 ºC for 30 min. The substrate was then rinsed consecutively with 2-propanol, water, and n-hexane to remove any excess molecules. A p-

aminophenyltrimethoxysilane (APhTS) monolayer was synthesized as follows. The substrate was rinsed first in methanol, a 1:1 (v/v) mixture of methanol and toluene, and pure toluene. Then the substrate was immersed in a 3 mmol/L APhTS solution in toluene for 30 min. After coating, the substrate was ultrasonicated in toluene for 10 min to remove excess surface molecules, and then rinsed in n-hexane. All the SAM-coated substrates were dried under a stream of nitrogen, and then annealed by heating at 120 °C for about 1 h in ambient atmosphere. SAM coating was confirmed by contact angle measurements on a Rame-Hart Model 200 Standard Contact Angle Goniometer and ellipsometry analysis on a Ruldoph Research AutoEL5 Ellipsometer.

3.2.4 Nanoparticle deposition by the GXL technique

The SAM-coated Si substrate was placed carefully upside-down on top of a stainless steel washer inside a glass vial. The substrate was placed upside-down to avoid the deposition of large particle agglomerations that do not stay well dispersed and fall onto the sample surface by gravity (Figure 3.1). 200 µL of a AuNP solution in hexane at a certain concentration was added to the vial and stirred. The sample vial was then placed in a stainless steel high-pressure vessel equipped with a quartz viewing window, a resistive temperature detector (RTD), heating rope, and pressure gauge. To prevent rapid evaporation of the hexane, approximately 400 µl of pure hexane was added beneath the sample vial in the high-pressure vessel to saturate the headspace with organic vapor before the vessel faceplate and the quartz windows were sealed with Teflon o-rings. Figure 3.2 shows the complete GXL nanoparticle deposition experimental apparatus.

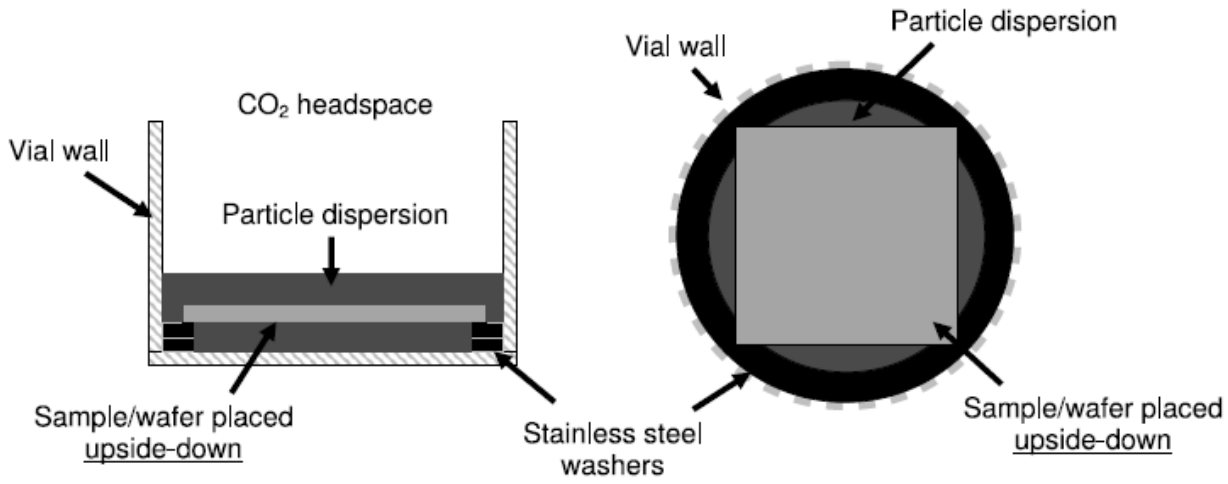

Figure 3.1. Side and top views of the glass sample vial used for GXL particle deposition.

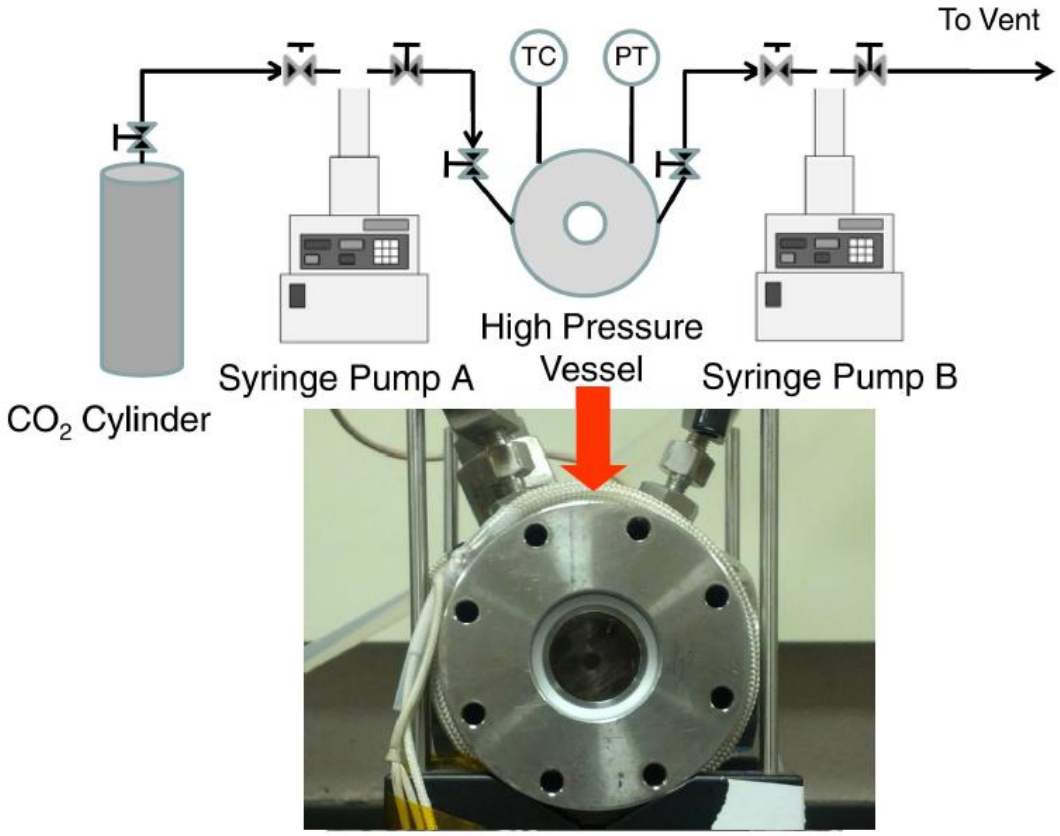

Figure 3.2. Schematic of the GXL particle deposition experimental setup.

After the high-pressure vessel was sealed, the chamber was pressurized with CO_2 to approximately 330 psi at room temperature (25 °C), in equilibrium with a 500-ml Teledyne ISCO piston syringe pump. The chamber was then pressurized slowly by setting the pump flow rate at a typical value of 0.4 ml/min, up to approximately 900 psi, which is approximately the vapor pressure of hexane at room temperature. During pressurization, CO_2 was dissolved in hexane, expanding the volume of the liquid mixture effectively and reducing the strength of the organic solvent. This reduction in solvent strength reduces the stabilization effect of the ligands on nanoparticles. Once the solvent strength was weakened below the stabilization threshold, the particles began to precipitate. For example, dodecanethiol-stabilized gold nanoparticles in the size range of 3 to 7 nm precipitate typically within a pressure range of 500 to 800 psi (McLeod et al., 2005).

The entire vessel chamber was pressurized until it was filled with liquid CO_2 that dissolved the organic solvent. The liquid mixture was heated to 40 °C to induce a supercritical state. The chamber was then flushed with pure supercritical CO_2 (at 40°C and approximately 1200 psi) at a rate of approximately 1 ml/min to ensure the removal of the organic solvent and prevent any dewetting effect. Following the purge of the pure supercritical CO_2, the chamber was depressurized slowly by venting to the atmosphere through a water bubbling system, and the dry, nanoparticle-coated sample was kept for further characterizations, mainly with a Pacific Nanotechnology Atomic Force Microscope.

3.3 Results and discussions

3.3.1 Synthesis of thiol-stabilized gold nanoparticles and SAM-coated Si substrates

3.3.1.1 Thiol-stabilized gold nanoparticles

A TEM image and photo showing the thiol-stabilized AuNP solution are shown in Figure 3.3. The nanoparticle solution was very stable, and the typical average diameter of the AuNP was 4.5±1.4 nm.

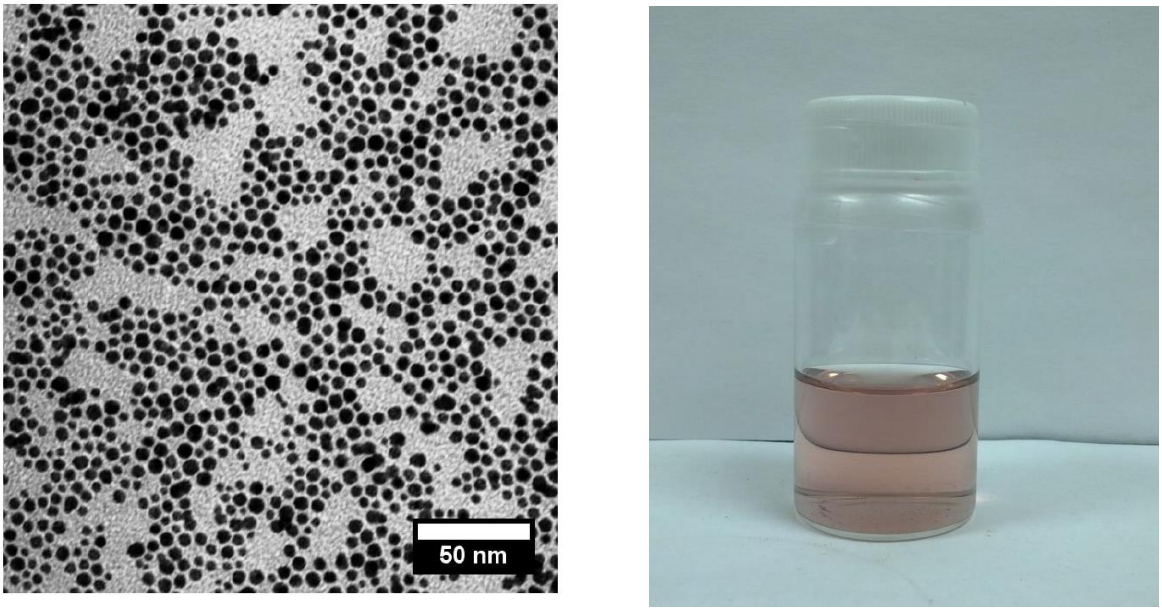

Figure 3.3. TEM image of AuNPs and photo showing the dodecanethiol-stabilized AuNP solution.

The concentration of the original AuNP solution can be estimated quantitatively using physical parameters (Liu et al., 2007b). Assuming the nanoparticle is spherical and has a fcc structure, the average number of gold atoms in each AuNP (N_{Au}) is calculated by Equation 3.1,

where D is the typical average diameter, ρ_{Au} is the density of fcc gold (19.3 g/cm^3), and M_{Au} is the molar mass of gold (197 g/mol).

$$N_{Au} = \pi \rho_{Au} D^3 / 6 M_{Au} \quad (3.1)$$

The molar concentration of the original AuNP solution was calculated by Equation 3.2, where N_T is the total number of gold atoms that derive from the initial amount of gold salt in the solution, V is the volume of the solution, and N_A is Avogadro's constant (6.022×10^{23}/mol):

$$C = N_T / (N_{Au} V N_A) = 6 M_{Au} N_T / (\pi \rho_{Au} D^3 V N_A) \quad (3.2)$$

The concentration of diluted AuNP solution can be calculated based on the volume ratio of the diluting solvent and original solution.

AuNPs stabilized with thiol ligands with straight chains, but different lengths and branched chains, were synthesized as well. They have a similar average size and stability after synthesis. It has been demonstrated that the stability of alkanethiol-stabilized gold nanoparticles is strongly dependent on the method of synthesis (Bellino et al., 2004). Because throughout this dissertation, the synthesis method and conditions remained unchanged, the apparent stability of those nanoparticles should not have changed much. However, with respect to the GXL deposition process, the steric effect of the ligands cannot be neglected, which will be discussed in the following sections.

3.3.1.2 SAM-coated Si substrates

The contact angle of sessile water droplets on SAM is a convenient method to confirm SAM coating on Si substrates. The contact angle values of water on pure SiO_2, OTS, FDTS, MPTS, and APhTS SAMs on Si substrate are listed in Table 3.1. These values are consistent with those reported in the literature (Hurst et al., 2011), and indicates that the coverage of the SAMs on the Si substrate was sufficient. From the results, it can be seen that clean SiO_2 is very hydrophilic, and is very oleophilic for nearly all types of organic solvents as well. After the SAMs were coated on the Si substrate, they increased its hydrophobicity.

	Pure SiO_2	OTS	FDTS	MPTS	APhTS
Contact angle of water (^{o})	<5	108 ± 3	114 ± 3	70 ± 2	63 ± 2
Film thickness (Å)	–	26.3 ± 2.2	14.7 ± 1.3	11.2 ± 1.0	18.5 ± 1.6
Surface tension (dyn/cm)	140	21.8	3.61	25.2	22.0

Table 3.1. Contact angle values of water, film thickness, and surface tension of SiO_2 and SAMs on Si substrate.

Another important parameter is the SAMs' thickness. A change in the value of the water contact angle indicates that the surface has been coated with the SAMs. Usually, the contact angle increases as the coverage of the SAMs increases. However, after the surface is covered nearly fully, bulk polymerization of the precursor molecules will result in particulates or thicker

layers on the substrate that may or may not reduce the contact angle (Kim et al., 2008). A film thickness measurement is required to ensure that a good monolayer was formed rather than multi-layers. The thickness of these SAMS on Si substrate were collected using the ellipsometer and are shown in Table 3.1. The thickness values were in agreement with the values calculated in other reports, and proved that a monolayer was formed on the Si substrate (Gandhi et al., 2007; Choi et al., 2004). A smooth and uniform monolayer formation is very important for the deposition of nanoparticles (Figure 3.4).

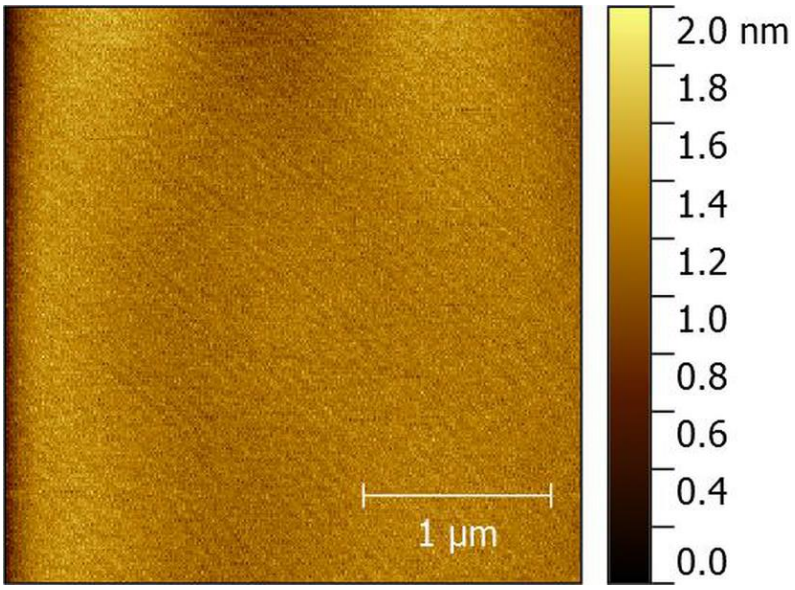

Figure 3.4. AFM image showing a good coating of APhTS SAM on Si substrate.

The surface tension values of different Sam-coated substrates were calculated by Zisman plots using contact angle measurements of various solvents of known surface tension. The results are shown in Table 3.1. Our group's previous work demonstrated that when the surface tension of the substrate is much greater than that of the film, such as SiO_2 with a surface tension of 140 dyn/cm, the nanoparticle film formation will follow the Frank-van der Merwe mode. Layer-by-

layer film formation is preferred. In contrast, if the surface tension of the substrate is much lower than that of the film, such as FDTS SAM with a surface tension of only 3.61 dyn/cm, the Volmer-Weber mode takes control, and many aggregates will appear on the final film. When the surface tension of the substrate is on the same order as that of the film, such as OTS or APhTS, the film formation follows the Stranski-Krastanov mode (Hurst et al., 2011). This is very interesting, as it allows the opportunity to engineer the nanoparticle films to achieve the roughness and surface morphology desired, given that the surface chemistry of the substrate and the nanoparticle capping agent is known. In this work, APhTS was chosen as the target SAM coating because the surface tension of APhTS SAM is neither too high nor too low, making it possible to observe the Stranski-Krastanov growth mode with the application of appropriate ligand-capped nanoparticles.

3.3.2 GXL-deposited films of AuNPs onto SAMs with varying surface energies

The nanoparticle deposition process involves the interaction between the nanoparticles and the substrate surface. In this section, the surface chemistry of the substrate, which is affected by the coated SAMs, was investigated.

Figure 3.5 shows AFM scans and rms roughness values of AuNPs deposited onto SiO_2, OTS, and FDTS. The images show that there are island-like structures on the surface, and the layer height from the AFM line profile is approximately 5 nm, which indicates the formation of partial monolayers. On the other hand, the AuNPs formed much larger agglomerates on the FDTS-coated Si substrates. The AuNP films formed on the OTS-coated Si substrate also were

uniform, but still had some larger three-dimensional structures. Therefore, SAMs played an important role here in the formation of AuNP films.

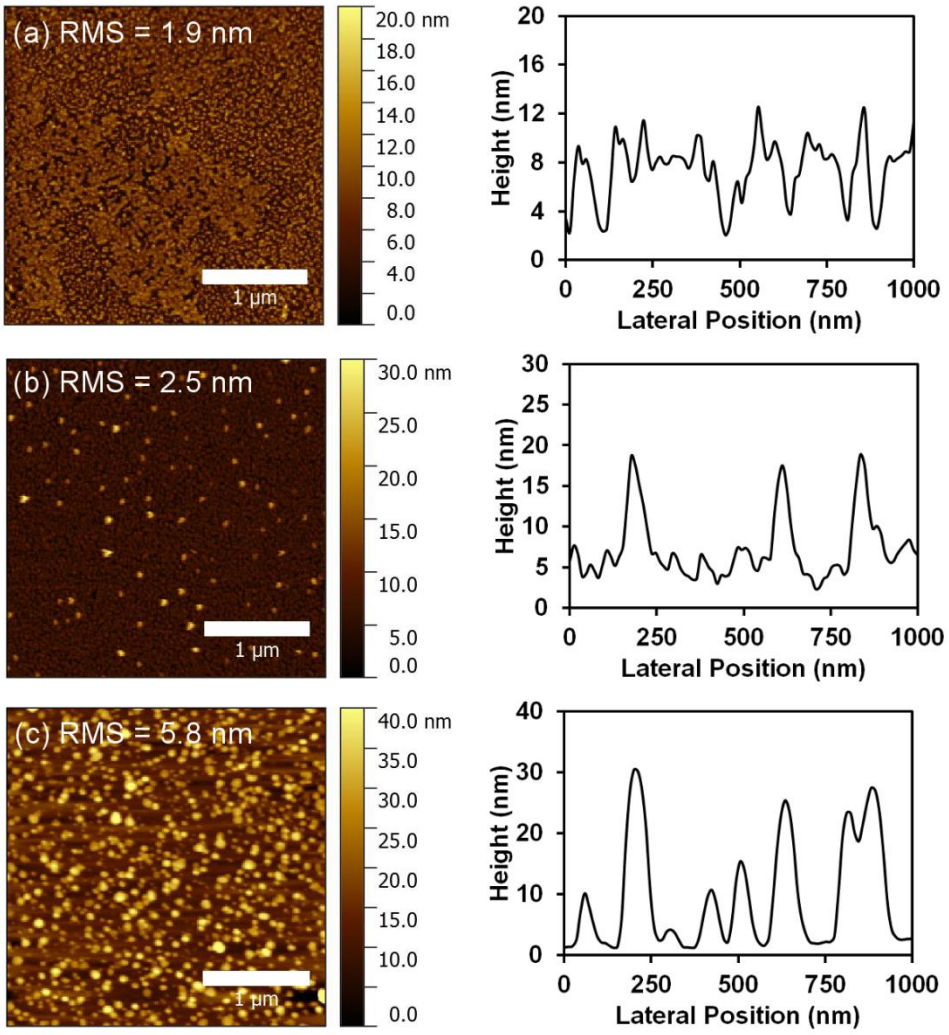

Figure 3.5. AFM scans and rms roughness values of AuNPs deposited onto (a) SiO_2, (b) OTS, and (c) FDTS.

The surface chemistry of SAMs is determined by surface energy, or critical surface tension. It is accepted generally that there are three possible modes of particle film growth on

surfaces (Figure 3.6): the island mode, or Volmer-Weber mode, in which some small clusters are nucleated directly on the substrate surface and then grow into islands of the condensed phase. This occurs when the small particles of the deposit are bound more strongly to each other than to the substrate; the layer or Frank-van der Merwe mode, which has characteristics opposite to those in the Volmer-Weber mode. The interactions between the particles and substrate are so strong that the particles tend to bind to the substrate rather than each other, and the layer plus island, or Stranski-Krastanov growth mode prevails, which is an interesting intermediate situation. After forming the first or several monolayers, subsequent layer growth is unfavourable, and islands form on top of existing layers (Venables et al., 1984).

The mechanism by which the nanoparticle films form on the substrate is determined by the surface tension of both the nanoparticles and substrate. In this procedure, dodecanethiol-capped AuNP was used for film deposition. From experimental data reported, the critical surface tension of a dodecanethiol monolayer on gold was estimated to be 19.3 dyn/cm (Hurst et al., 2011). Zisman plots using contact angle measurements of various solvents of known surface tension were used to calculate the surface tension values of different SAM-coated substrates. The results are listed in Table 3.1.

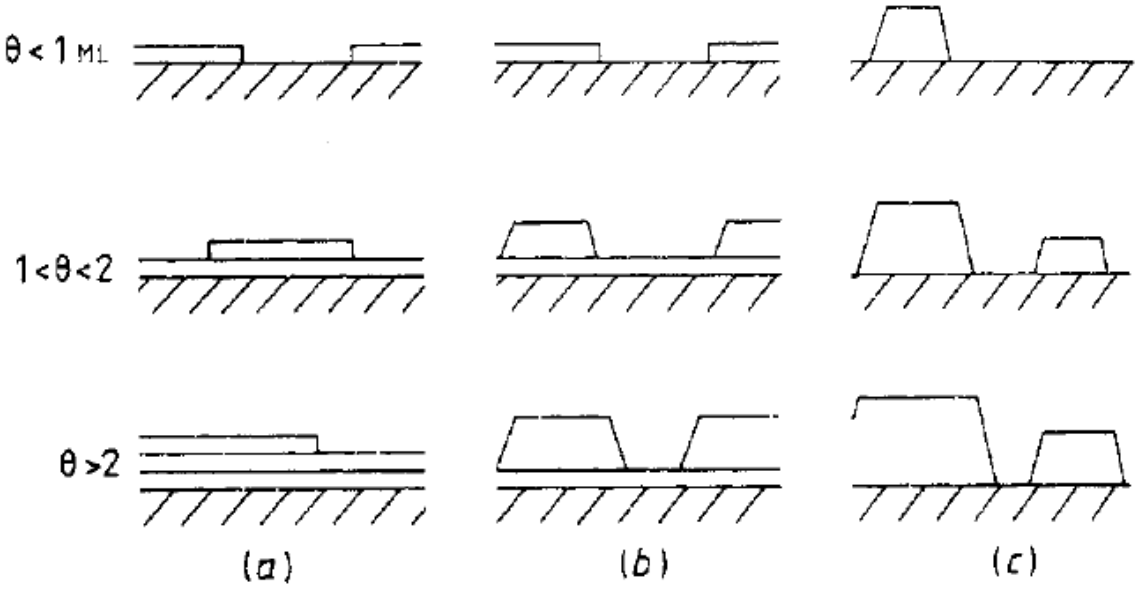

Figure 3.6. Schematic representation of the three growth modes: (a) layer or Frank-van der Merwe mode, (b) layer plus island or Stranski-Krastanov, and (c) island or Volmer-Weber. θ represents the number of monolayers (Venables et al., 1984).

When the surface tension of the substrate is much greater than that of the film, such as SiO_2 with a surface tension of 140 dyn/cm, the nanoparticle film formation will follow the Frank-van der Merwe mode. A layer-by-layer film formation is preferred. In opposite, if the surface tension of the substrate is much lowerer than that of the film, like FDTS SAM with a surface tension of only 3.61 dyn/cm, the Volmer-Weber mode takes control. Many aggregates will appear on the final film. When the surface tension of the substrate is at the same order of that of the film, such as OTS or APhTS, the film formation goes with Stranski-Krastanov mode. This is very interesting since it enables the opportunity that nanoparticle films can be engineered to achieve desired roughness and surface morphology given that surface chemistry is known about the substrate and the nanoparticle capping agent.

3.3.3 GXL-deposited films of AuNPs with different capping ligands

The previous section discussed the way in which the surface chemistry of the substrate affects the film deposition mechanism. Because the SAM coating interacts with the surface of nanoparticles, the interfacial properties of the nanoparticles should also play an important role in the film deposition, which is determined by the ligands. The typical ligand used for AuNP synthesis is dodecanethiol, which is a thiol with a 12-carbon straight alkyl chain. In order to make comparisons, octanethiol (8 carbons, straight), pentadecanethiol (15 carbons, straight), and t-dodecanethiol (12 carbons, branched), were used during the synthesis of AuNPs as different stabilizing agents. Figure 3.7 shows the chemical structures of these thiols. The synthesized AuNPs from different ligands disperse well in hexane and have similar morphologies and average diameters. During nanoparticle synthesis, thiols were added after the gold ion reduction and nanoparticle formation, which were used as stabilizing agents only. Therefore, the size distribution was unaffected by the different thiols.

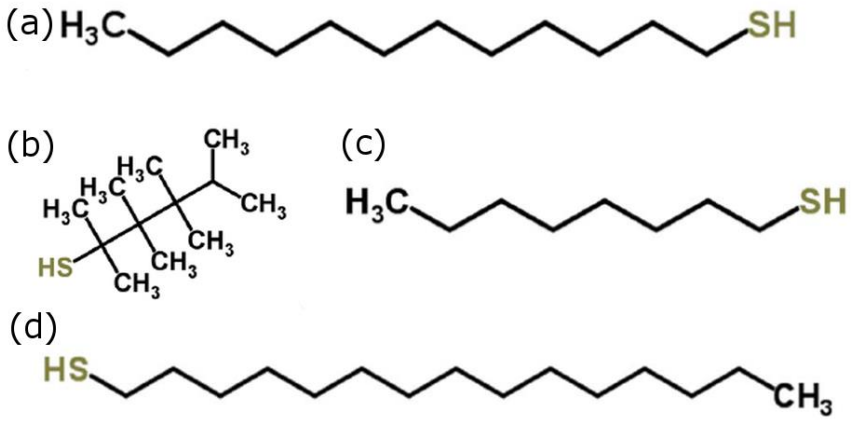

Figure 3.7. Structures of thiols: (a) dodecanethiol, (b) t-dodecanethiol, (c) octanethiol, and (d) pentadecanethiol.

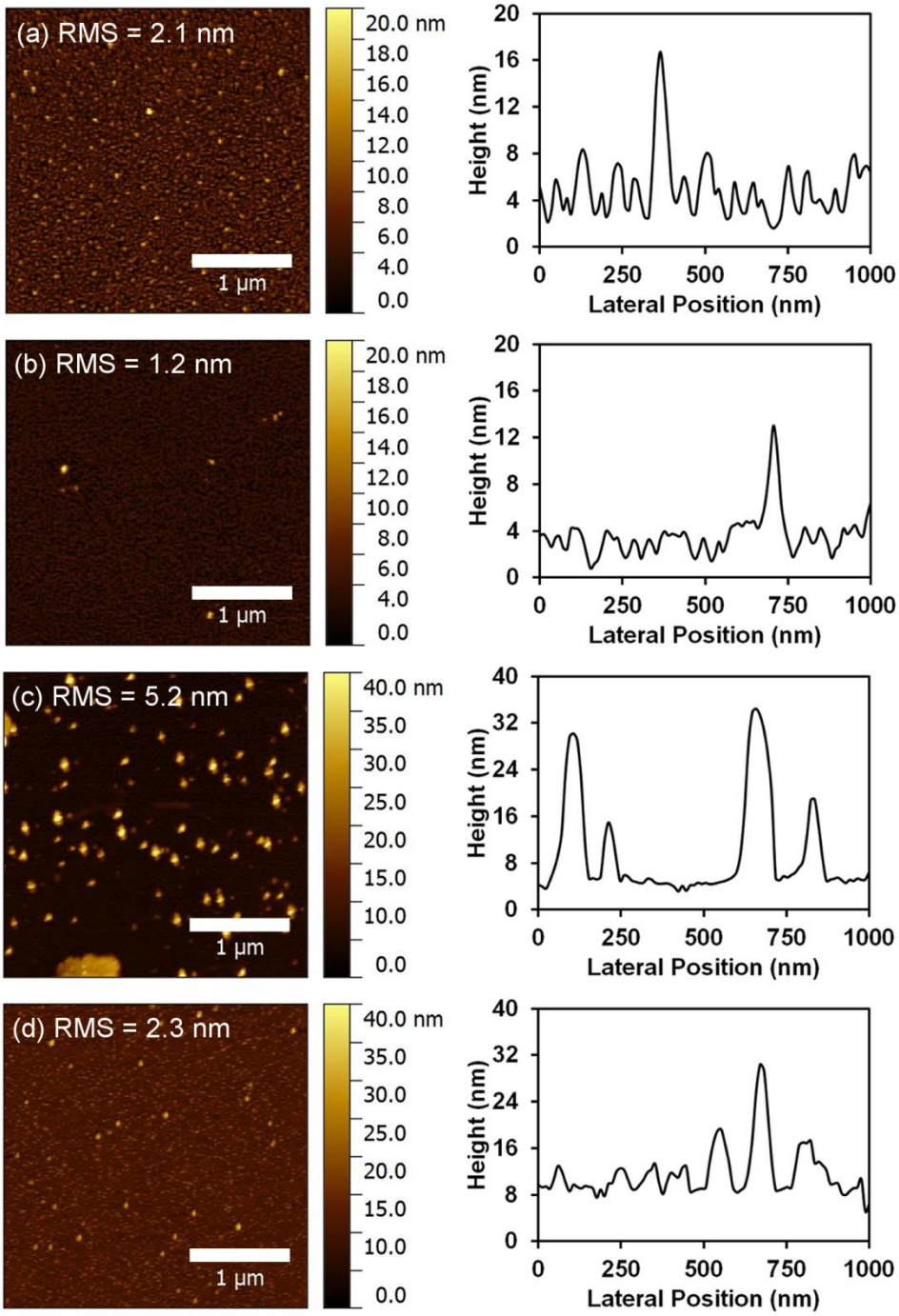

Figure 3.8 AFM scans of GXL-deposited AuNP films on APhTS-coated Si substrate. The AuNPs were stabilized with (a) dodecanethiol, (b) octanethiol, (c) pentadecanethiol, and (d) t-dodacanethiol.

	Dodecanethiol	Octanethiol	Pentadecanethiol	t-Dodecanethiol
Average summit density (/μm^2)	223.2 ± 21.5	233.3 ± 22.7	86.7 ± 8.4	230.6 ± 23.3
Average summit radius (x10^{-3} μm)	74.2 ± 4.5	113 ± 6.9	95.6 ± 5.9	58.5 ± 3.6
σ_s, standard deviation of summit height distribution (x10^{-3} μm)	1.74 ± 0.26	0.95 ± 0.14	4.70 ± 0.71	1.81 ± 0.28
Average number of summits in contact (/μm^2)	35.4 ± 3.4	37.2 ± 3.8	13.8 ± 1.3	36.6 ± 3.9
Ratio of true to apparent contact area (%)	0.75 ± 0.12	0.65 ± 0.12	1.02 ± 0.19	0.64 ± 0.14
α, bandwidth parameter	2.90 ± 0.36	2.41 ± 0.31	4.55 ± 0.58	2.38 ± 0.32
m_0 (x10^{-6} μm^2)	4.41 ± 0.37	1.44 ± 0.19	27.5 ± 2.11	5.29 ± 0.44
m_2 (x10^{-3})	11.1 ± 0.8	4.57 ± 0.33	17.2 ± 1.27	17.1 ± 1.36
m_4 (/μm^2)	80.8 ± 5.1	34.8 ± 2.1	48.6 ± 2.9	128.8 ± 8.0

Table 3.2. Surface parameters calculated for coatings of nanoparticles stabilized with different ligands.

The films formed after these AuNPs were deposited on APhTS-coated Si substrate are shown in Fig 3.8. According to previous reports, the critical surface tension values for alkyl thiols are within a certain range if the length of the alkyl chain is neither too long nor too short. For example, the surface tension of octanethiol is approximately 21.6 dyn/cm (Comeau et al.,

2012), and that of dodecanethiol is approximately 19.3 dyn/cm (Hurst et al., 2011). The surface tensions of these thiols are similar to that of the APhTS SAM (22.0 dyn/cm). Figure 3.8 shows clearly that the AuNP films deposited had mixed morphologies. Layers of AuNP coating can be seen in the background, and large aggregates formed on top of the smooth layers.

The surface parameters calculated for coatings of nanoparticles stabilized with different ligands are summarized in Table 3.2. Coatings of nanoparticles stabilized with dodecanethiol, octanethiol, and t-dodecanethiol showed similar surface characteristics. Layers of AuNP coating can be seen in the background, as well as a certain amount of aggregates formed on top of the smooth layers. The only exception was the coating of nanoparticles stabilized with pentadecanethiol, where much larger aggregates can be seen on the surface, leading to a lower summit density, but higher ratio of true to apparent contact area.

The experimental HHCF curves from AFM data and corresponding HHCF curves with model fitting are plotted in Figure 3.9. The rms roughness, autocorrelation lengths, and roughness component values from the HHCF model are summarized in Table 3.3. Similar results can be seen in the curves, in that the autocorrelation lengths and roughness component values from coatings of nanoparticles stabilized with dodecanethiol, octanethiol, and t-dodecanethiol were within the same range, while the coating of nanoparticles stabilized with pentadecanethiol had a longer autocorrelation length and higher roughness component value. This again confirmed that coatings of nanoparticles stabilized with dodecanethiol, octanethiol, and t-dodecanethiol have comparable surface characteristics.

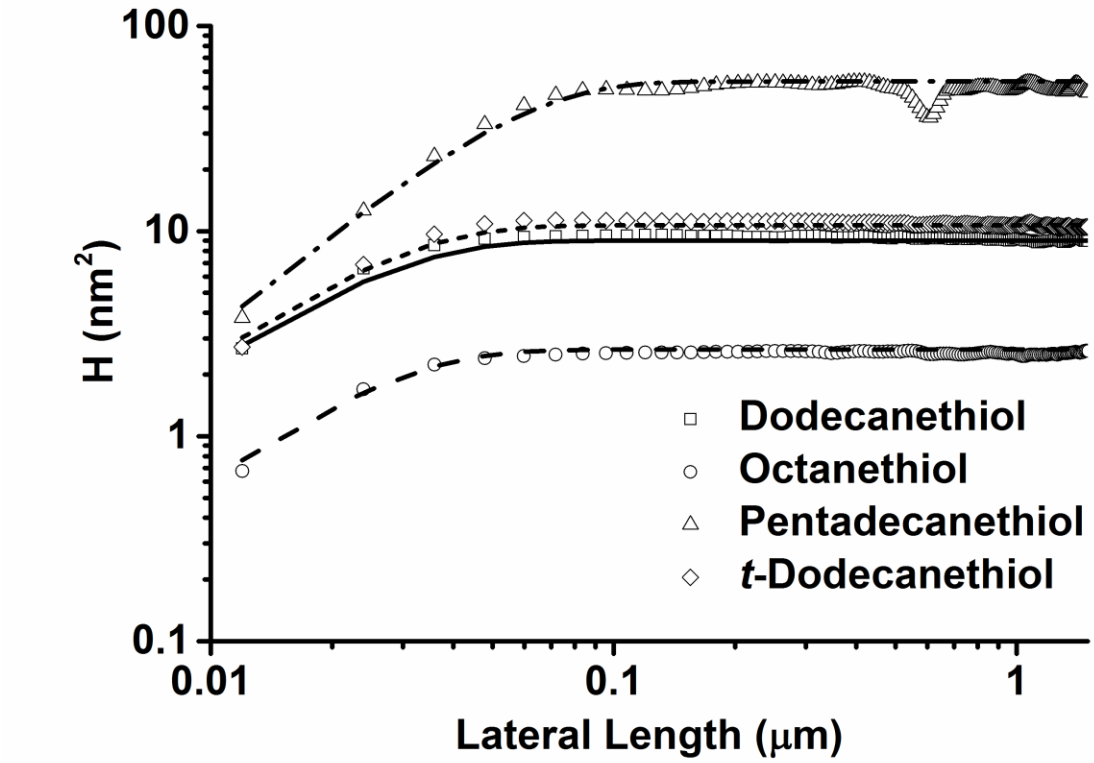

Figure 3.9. Experimental HHCF data for coatings of nanoparticles stabilized with different ligands. Lines are the corresponding HHCF curves calculated using the proposed HHCF model fitting.

Size of NPs (nm)	rms roughness (nm)	Autocorrelation length (nm)	Roughness exponent
Dodecanethiol	2.12 ± 0.17	24.0 ± 1.8	0.721 ± 0.035
Octanethiol	1.26 ± 0.15	24.6 ± 2.3	0.748 ± 0.037
Pentadecanethiol	5.18 ± 0.40	53.8 ± 3.2	0.826 ± 0.064
t-Dodecanethiol	2.31 ± 0.19	25.2 ± 1.4	0.734 ± 0.045

Table 3.3. Surface parameters calculated from HHCF model for coatings of nanoparticles stabilized with different ligands.

The GXL deposition is based on the change in stability of the nanoparticles. When the stabilization provided by the interaction between the ligand tails and the solvent is reduced, it causes the nanoparticles to begin to precipitate from the dispersion. The stability of nanoparticles in the solution requires the attraction force to be controlled well so that it is balanced with the osmotic repulsive force, and the solvation effect generated by the interaction between the solvent and the alkyl chain of ligands.

Previous work by our group has shown that the length of the alkyl chain in thiol ligands has some effect on the precipitation process (Anand et al., 2005). The shorter tail length in octanethiol and hexanethiol ligands causes the nanoparticles to precipitate at a relatively lower CO_2 pressure compared to dodecanethiol ligand-stabilized nanoparticles (Figure 3.10). This effect occurs because the shorter length ligands have a smaller effective ligand alkyl chain length for solvation interactions with the solvent compared to ligands of longer lengths. On the other hand, nanoparticles stabilized with thiols having longer alkyl chains than those of dodecanethiol

also require less CO_2 pressure for nanoparticle precipitation. A possible explanation for this is that there is a decrease in particle-particle attraction energy with an increase in the thiol hydrocarbon chain length when it is under the effect of solvation, which leads to a decrease in the stability of nanoparticle dispersions.

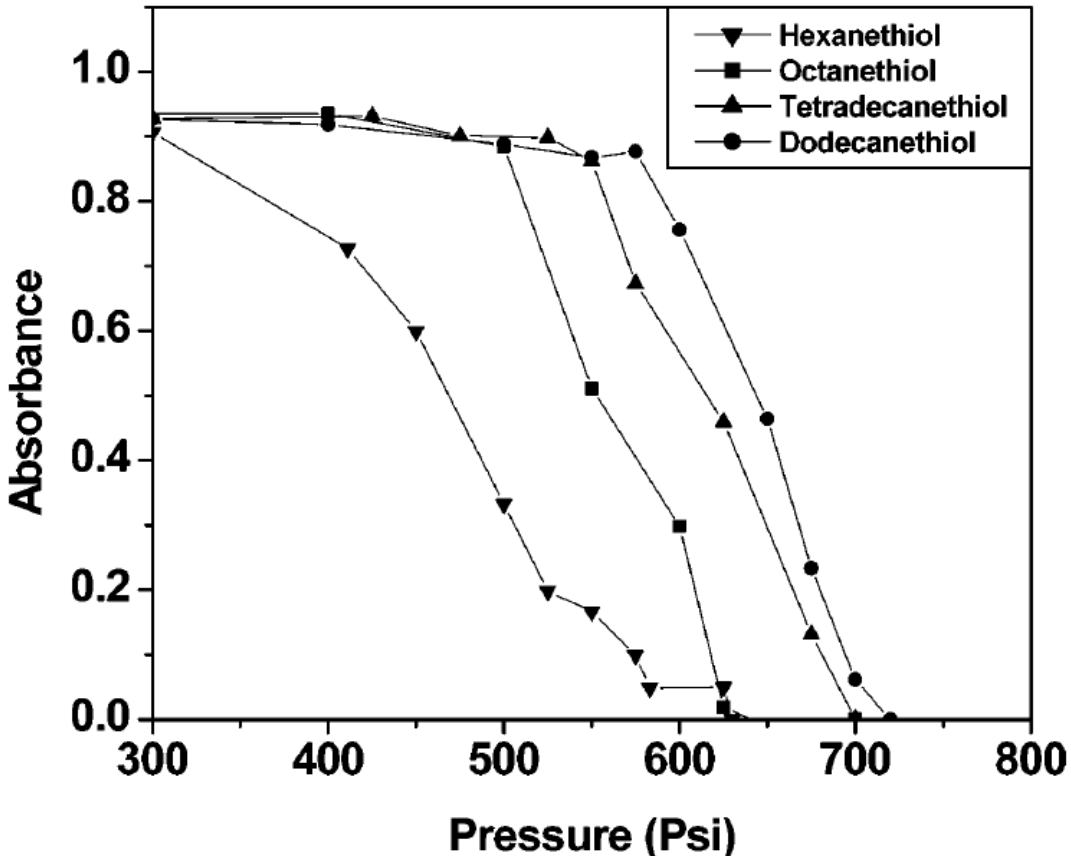

Figure 3.10. Maximum UV-visible absorbance values for AuNPs coated with different thiol length molecules dispersed in liquid hexane/CO_2 mixtures at increasing CO_2 pressure (Anand et al., 2005).

When AuNPs become unstable and begin to precipitate from the solution, they are deposited on the substrate and form thin films as well as larger aggregates. The lower the stability of the precipitated nanoparticles, the greater the tendency for particle-to-particle

attraction during deposition. When the surface of the substrate has been covered with several layers of AuNPs, the interaction between nanoparticles and the substrate weakens and the particle-to-particle attraction strengthens. The driving force in this process is that larger particles are favored energetically to a greater degree than are smaller particles. A similar phenomenon, referred to as Ostwald ripening, has been reported, in which metallic species form islands rather than monolayers when deposited onto ceramic or semiconductor substrates (Ohring, 2002). Because of the low operating pressures from the solvent mixture, more time is required to allow the nanoparticles to precipitate once destabilized. The lower operating pressure causes the solvent mixture to be more liquid-like, with a higher viscosity and lower diffusivities through the medium. The fluid properties make the precipitation process more similar to traditional liquid-liquid solvent precipitation, which usually results in large aggregate precipitation (Saunders et al., 2011c). Therefore, a proper choice of ligand-SAM surface chemistry system (dodecanethiol-APhTS) is essential to achieve a stable coating process.

3.3.4 GXL-deposited films of AuNPs at different concentrations

When the dodecanethiol-stabilized AuNPs are deposited on APhTS-coated Si substrate, the process is affected by the total number of nanoparticles deposited on the substrate surface, which is related to the concentration of the nanoparticle solutions used during GXL.

AuNP films were deposited by GXL on APhTS-coated substrate by starting with different AuNP concentrations. The concentration of the AuNP solutions was determined qualitatively by the maximum peak intensity of UV-Vis spectra at around 510 nm. Our group's

previous work showed that the peak intensity at this wavelength decreases when the concentration of the nanoparticle solution is lower because of the pressure applied (Figure 3.11, Saunders et al., 2012).

The AFM scans and rms roughness values of dodecanethiol-capped AuNP films deposited onto APhTS-coated silicon substrate at different concentrations are shown in Figure 3.12. Qualitatively, the concentrations of the nanoparticle solution increased from very low to high.

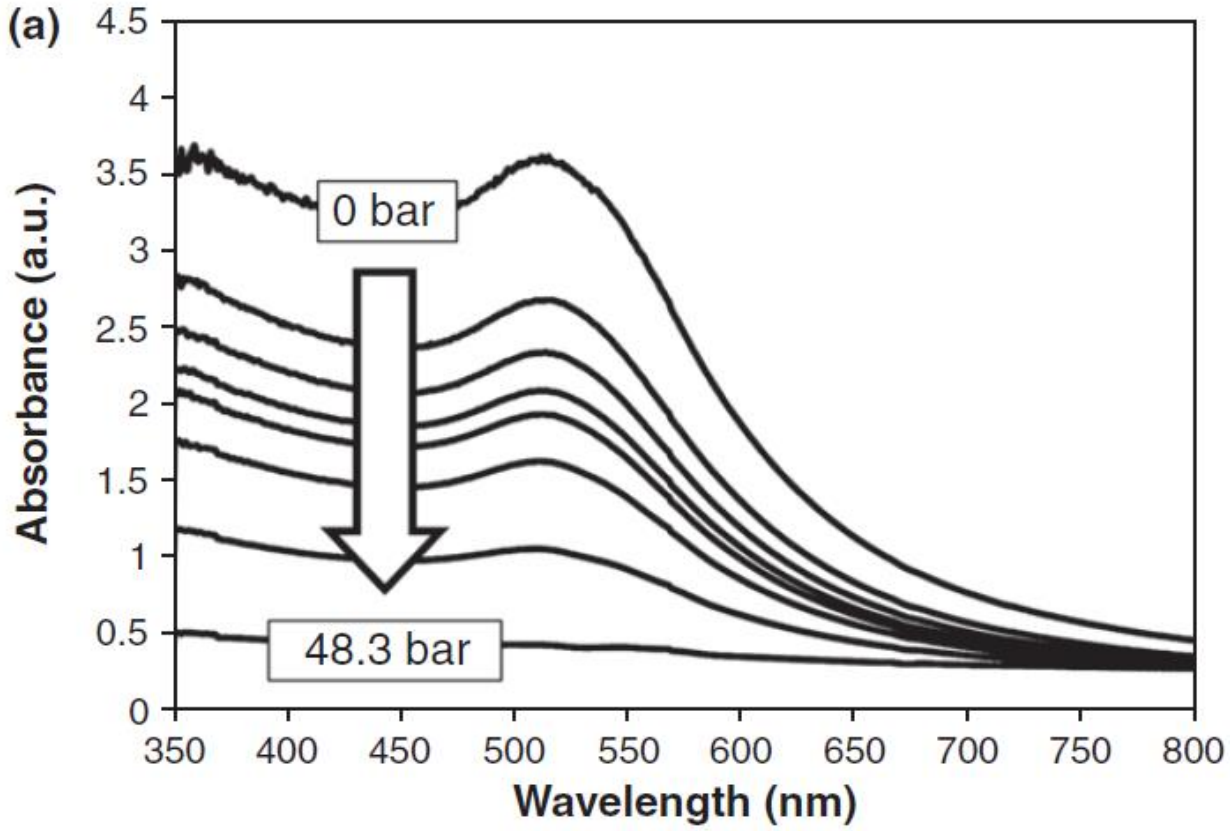

Figure 3.11. UV–vis spectra of GXL precipitation of dodecanethiol-stabilized gold nanoparticles from hexane at various CO_2 pressures applied (Saunders et al., 2012).

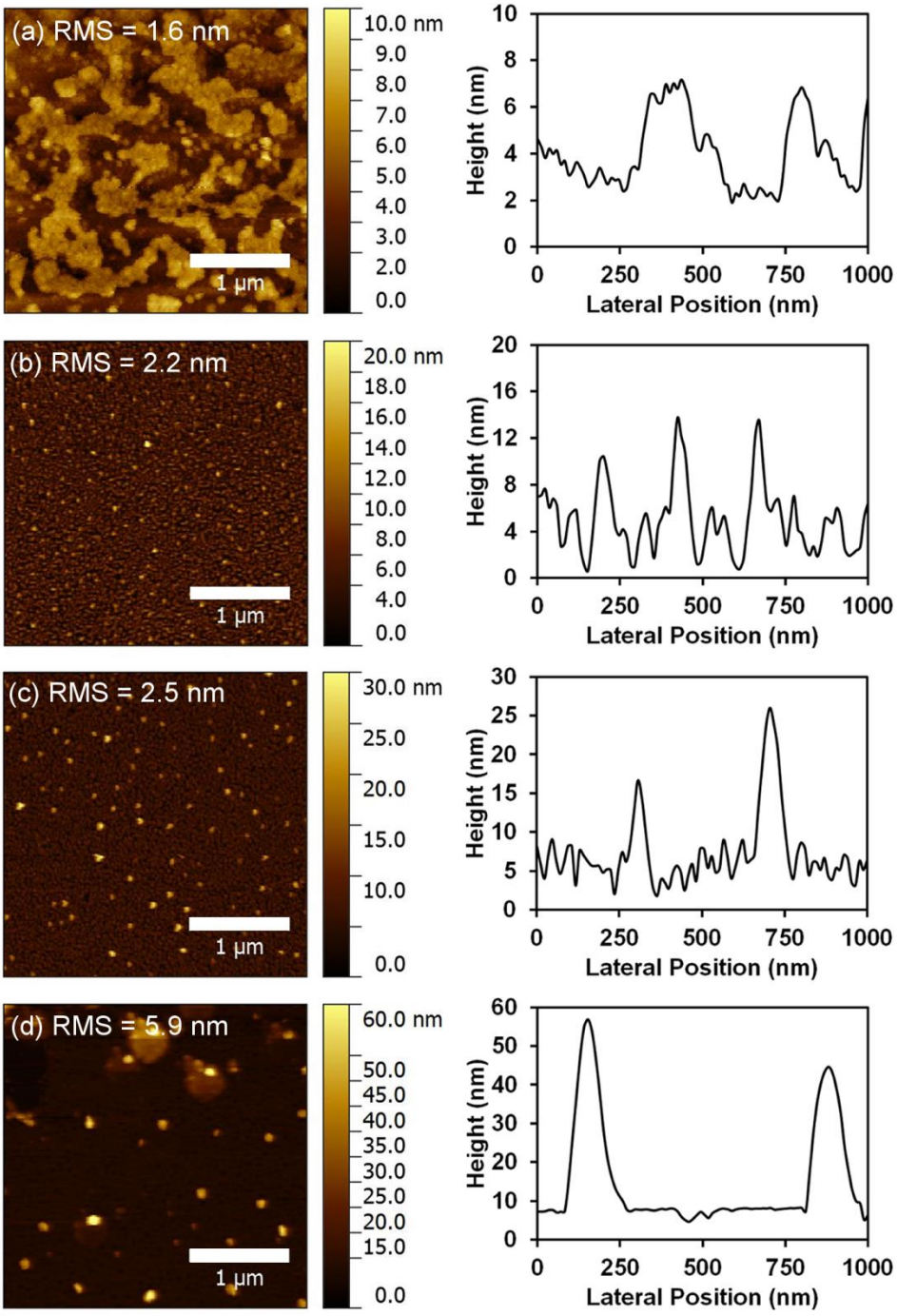

Figure 3.12. AFM scans and rms roughness values of dodecanethiol-capped AuNP films deposited onto APhTS-coated silicon substrate at different concentrations. The concentrations are (a) very low, (b) low, (c) medium, and (d) high.

	Very Low	Low	Medium	High
Average summit density (/μm^2)	90.4 ± 8.7	225.3 ± 22.5	163.2 ± 15.8	79.4 ± 8.9
Average summit radius (x10^{-3} μm)	328.9 ± 20.4	73.9 ± 4.6	74.6 ± 4.9	101.9 ± 8.4
σ_s, standard deviation of summit height distribution (x10^{-3} μm)	1.46 ± 0.22	1.81 ± 0.27	1.98 ± 0.25	5.43 ± 0.81
Average number of summits in contact (/μm^2)	14.3 ± 1.4	35.7 ± 3.4	25.9 ± 2.4	12.6 ± 1.4
Ratio of true to apparent contact area (%)	1.14 ± 0.21	0.77 ± 0.15	0.61 ± 0.11	1.14 ± 0.27
α, bandwidth parameter	5.45 ± 0.69	2.99 ± 0.41	2.23 ± 0.25	5.48 ± 0.73
m_0 (x10^{-6} μm^2)	2.56 ± 0.21	4.49 ± 0.37	6.16 ± 0.39	34.7 ± 2.5
m_2 (x10^{-3})	1.38 ± 0.10	11.2 ± 0.8	14.9 ± 1.1	16.4 ± 1.2
m_4 (/μm^2)	4.08 ± 0.25	81.6 ± 5.5	79.4 ± 4.9	42.5 ± 3.3

Table 3.4. Surface parameters calculated for coatings at different initial nanoparticle concentrations.

The surface parameters calculated for coatings from different initial concentrations are summarized in Table 3.4. All values here were calculated from the previous modified GW model analysis. Differences between the surfaces can be summarized as follows. At very low concentrations, many gaps on the surface can be seen clearly, but the surface height and

roughness are still low, which indicates partially formed monolayers. There are slightly fewer summits per unit area, which is likely a result of the increased size of the grain boundaries. This can be confirmed from the average summit radius, which was highest among all the coatings.

For the coatings at low and medium concentrations, the average summit density increased while the average summit radius decreased. This indicates that there were more summits in contact per unit area, but the contact area for each summit may have been smaller. The ratio of true to apparent contact area was only 50–70% of the value for the coating at the very low concentration, indicating that the actual contact area was smaller.

The coating at the high concentration showed a lower summit density, again with a small average summit radius. However, the average summit radius is the average of all summits across the whole surface. From the AFM image, it can be seen that there are some very large aggregates and many small asperities in the background. Therefore, it is likely that this average value may underestimate the contribution of larger asperities. The ratio of true to apparent contact area was still high, which derives from these larger structures with higher surface height.

The experimental HHCF curves from the AFM data and corresponding HHCF curves by model fitting are plotted in Figure 3.13. The fitting curves and the experimental data matched well, which indicates that the surfaces obtained can be quantified using parameters from the HHCF analysis. The rms roughness, autocorrelation lengths, and roughness component values from the HHCF model are summarized in Table 3.5. All values here were calculated from the previous HHCF analysis.

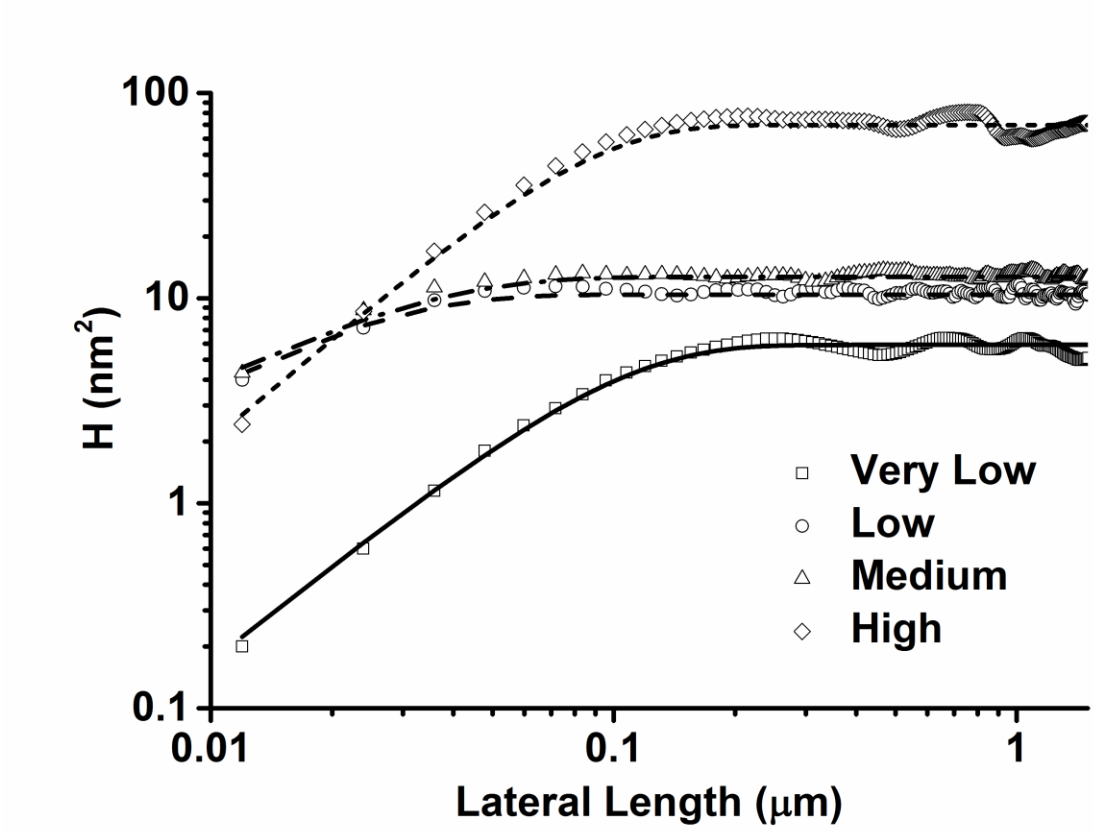

Figure 3.13. Experimental HHCF data for coatings at different initial nanoparticle concentrations. Lines are the corresponding HHCF curves calculated using the HHCF model fitting proposed.

Concentration	rms roughness (nm)	Autocorrelation length (nm)	Roughness exponent
Very Low	1.62 ± 0.13	94.5 ± 3.2	0.788 ± 0.062
Low	2.24 ± 0.17	20.1 ± 1.9	0.607 ± 0.044
Medium	2.52 ± 0.16	24.7 ± 2.1	0.653 ± 0.038
High	5.91 ± 0.42	90.5 ± 3.6	0.850 ± 0.053

Table 3.5. Surface parameters calculated from the HHCF model for coatings at different initial nanoparticle concentrations.

The autocorrelation length was used to determine the spatial variation in the lateral direction. A higher T value indicates a larger average hill or valley grain size, and the surface variations were correlated within this length range. It can be seen that the coating with a very low concentration had higher correlation lengths, while the rms surface roughness was low. This is related to the larger grain structures on the surface, which can be confirmed from the AFM images. As the initial concentration of the nanoparticle solution was low, the number of nanoparticles provided by the solution was insufficient to form complete surface coverage and one or more incomplete monolayers may cover the surface of the substrate in part, as can be seen in Figure 3.12 (a). Many gaps can be seen clearly on the surface, but the surface height and roughness are still low, indicating partially formed monolayers rather than large aggregates.

As the concentration increased, the nanoparticles deposited began to form complete layers with more uniform characteristics. As shown in Figure 3.12 (b), the surface layers were relatively uniform, with some medium-sized aggregates on the surface. The surface roughness values were within the same magnitude, but the top surface height in Figure 3.12 (c) was 10 nm higher than that in Figure 7 (b), which may derive from several monolayers underneath. The HHCF parameters were very similar for both coatings, with lower autocorrelation lengths. This was due to the smaller grain size on the complete surface layers.

The roughness exponent values of coatings at very low and high concentrations were much higher than were those of coatings at low and medium concentrations. From the linear profiles in Figure 3.12, it is clear that there were many small, but jagged structures on the line profiles of coatings at low and medium concentrations, while the surface texture was relatively smooth for coatings at very low and high concentrations.

It has been shown that the largest nanoparticles in the nanoparticle dispersion will precipitate onto the substrate first upon progressive introduction of CO_2. As the pressure of CO_2 increases and the solvent strength becomes weaker, smaller particles begin to precipitate (Anand et al., 2005; Saunders et al., 2012). Thus, not all nanoparticles in the initial dispersion are deposited onto the substrate and the smaller particles will remain dispersed in the mixture depending on the pressure applied throughout the GXL process. The intensity of the surface plasmon resonance band (SPRB) for the precipitation of 1-dodecanethiol stabilized nanoparticles from n-hexane was measured experimentally and is presented in Figure 3.14 as a function of the CO_2 pressure applied. As the CO_2 pressure increased, progressive precipitation of large nanoparticles occured first as the solvent conditions worsened, and correspondingly reduced the

SPRB intensity of the dispersed smaller nanoparticles. The calculated intensity of the SPRB as a function of the threshold nanoparticle size is presented in Figure 3.14 and related to the experimental intensity.

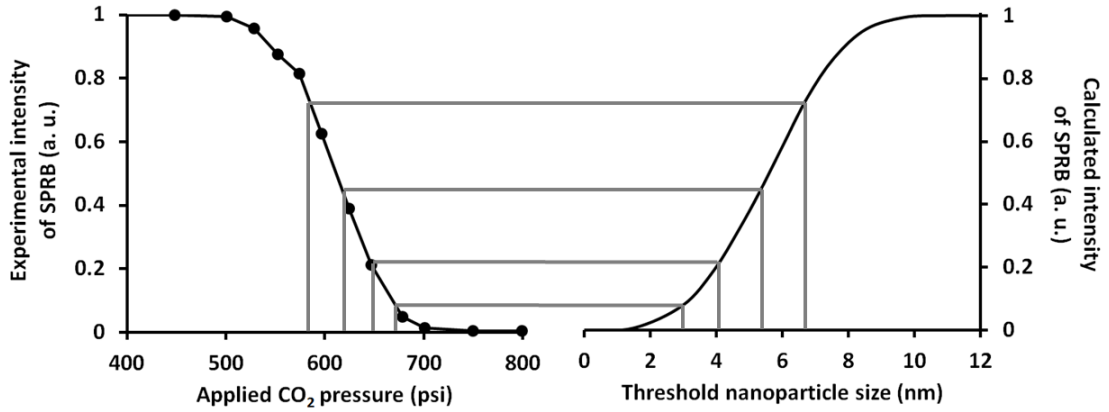

Figure 3.14. Experimental intensity of SPRB as a function of applied CO_2 pressure applied and calculated intensity from the contributions of nanoparticles at a given threshold nanoparticle size. Gray lines indicate how the nanoparticle threshold size can be determined from the CO_2 pressure applied (Saunders et al., 2011c).

Because of the miniscule size of the nanoparticles, attractive van der Waals forces dominate over gravitational forces, and cause particles at the equilibrium of precipitation to be attracted to any surface submerged in the dispersion. On the other hand, as the nanoparticles are made of a different material than the surface, attraction between particles is also important. The attractive force between nanoparticles can be approximated as the non-retarded van der Waals force between two spherical particles in solution. Therefore, when the solvent strength is reduced because of the addition of CO_2, the precipitation of nanoparticles has to achieve equilibrium

between the particle-particle interaction, which forms larger aggregates, and the particle-substrate interaction, which forms deposited nanoparticle layers.

As mentioned earlier, in this case, the film growth followed the Stranski-Krastanov mechanism, or layer plus aggregation mode. The Stranski-Krastanov mechanism is affected thermodynamically by the experimental conditions (Santalla et al., 2003). According to the thermodynamic model, the surface energy of the substrate plays an important role in the surface-particle interactions. As the surface energy of the substrate, which is determined by the critical surface tension (Table 3.1), approaches that of the particles, monolayers form, with some three-dimensional aggregate growth on top. In addition to the thermodynamic view, there is also a suggestion that other processes are involved in the aggregate formation in the Stranski-Krastanov mechanism. These processes usually include particle aggregation and diffusion during the deposition (Santalla et al., 2003).

In our system, the critical surface tension of the SAM (21.8 dyn/cm) was higher than that of the gold nanoparticles (19.3 dyn/cm) deposited, but was still close. As the nanoparticles began to precipitate from the solution, initial deposition led to the formation of one, or in some instances more, stressed monolayers, the structure of which is influenced strongly by the surface energy of the substrate. If the number of nanoparticles provided by the solution is insufficient, the surface of the substrate may be covered by one or more incomplete monolayers, as can be seen in Figure 3.12 (a). Many gaps can be seen clearly on the surface, but the surface height and roughness remained low, which indicated partially formed monolayers rather than large aggregates. In this stage, observation of the film shows a layer of growth in various areas: the substrate, an intermixing layer, and the film. As the layer-by-layer formation finished and the

layers of film increased, when the film thickness exceeded an apparent critical thickness, film growth shifted to small island growth, which produced small aggregates on top of the relatively smooth films (Figure 3.12 (b) and (c)). This resulted from the change in surface energy with film coverage. As the layers of nanoparticles accumulated on the substrate, the interaction between the SAM-coated substrate and the deposited nanoparticles that followed became weaker. The particle-substrate interaction then became a particle-deposited film interaction, which occurred within the same range as the particle-particle interaction in the solution. In this case, the existing small islands on the surface acted as the nucleation points for further island growth and led to larger aggregates. This was confirmed by the AFM image and line scan profile in Figure 3.12 (d), where there are visible large structures on the surface while the background still shows smooth films. Therefore, the difference in surface energies between the film and substrate is a crucial condition for the Stranski-Krastanov growth mechanism.

Growth stages of the Stranski-Krastanov mechanism were observed by depositing different numbers of nanoparticles on the surface. The concentration of the nanoparticle solution affects the particle aggregation during the deposition from the liquid phase. The tendency for nanoparticles to aggregate is affected by two factors: the size of the nanoparticles and the concentration of the nanoparticle solution. The size of the nanoparticles affects the non-retarded van der Waals force, while the concentration of the nanoparticle solution determines how frequently the nanoparticles interact with each other. When the initial concentration of the nanoparticle solution was very low, the particle-particle interaction was suppressed and the nanoparticles precipitated and were deposited on the substrate, demonstrating initial film formation from Stranski-Krastanov growth. Because there are not enough nanoparticles to cover the whole surface, the substrate may be covered in part by incomplete layers with medium-sized

grains (Figure 3.12 (a)). As the concentration increased, after the large nanoparticles were deposited, small nanoparticles precipitated under higher pressure filled in the valleys of the incomplete surface layers and produced a relatively smooth topographical appearance that indicated layer-by-layer growth. As the number of nanoparticles was higher, the film formation completed and the particle-particle interaction became more significant, but was still unable to form many large agglomerates (Figure 3.12 (b) and (c)). When the initial concentration was high, nanoparticle aggregation became dominant, which resulted in larger asperities (Figure 3.12 (d)). The aggregation results from the combined effect of stronger particle-particle interaction with a large number of nanoparticles during the GXL process and the weak particle-substrate interaction after the layer-by-layer film formation. The strong particle-particle interaction was confirmed by the results of deposited films of AuNPs with different capping ligands, where the film deposited by pentadecanethiol-stabilized AuNPs showed many large aggregates even at normal concentrations (Figure 3.8 (c)), indicating that destabilization of nanoparticles during the GXL process is a main source of nanoparticle aggregation in addition to the variation in surface energy.

Quantitative study of surface morphological properties usually begins with the rms roughness, which is the square root of the arithmetic mean of the square of the deviation from the average height and can be obtained easily. Nonetheless, the rms roughness cannot describe the surface topography completely. Thus, the height-height correlation function (HHCF) was introduced to support the statistical analysis of a surface. The key parameters of the quantitative surface analysis results are summarized in Table 3.6. Here, rms roughness and the standard deviation of summit height were treated as the long-range or overall surface roughness

parameters, while the autocorrelation length and roughness exponent were used as the short-range roughness indicators.

Concentration	Rms roughness (nm)	Standard deviation of summit height distribution (nm)	Autocorrelation length (nm)	Roughness exponent
Very Low	1.62 ± 0.13	1.46 ± 0.22	94.5 ± 3.2	0.788 ± 0.062
Low	2.24 ± 0.17	1.81 ± 0.27	20.1 ± 1.9	0.607 ± 0.044
Medium	2.52 ± 0.16	1.98 ± 0.25	24.7 ± 2.1	0.653 ± 0.038
High	5.91 ± 0.42	5.43 ± 0.81	90.5 ± 3.6	0.850 ± 0.053

Table 3.6. Key parameters based on quantitative surface analysis of coatings at different initial nanoparticle concentrations.

As the initial concentration increased, the rms roughness and standard deviation of the summit height values increased as well. This indicated that the concentration changes affected the long-range roughness significantly, and the result of the overall topographic variation was caused by the various structures formed on the surface. However, the autocorrelation length and the roughness exponent values did not follow the same increasing trend. These short-range parameters showed that the roughness of the individual asperities was correlated within a certain range, beyond which the surface height fluctuations were no longer correlated. The short-range roughness was affected more by the particle aggregates formed, which precipitated from the solution at various cutoff radii as a function of the pressure and initial size distribution. The

absence of a trend in these short-range roughness parameters indicated that the general changes in surface topography according to the concentration, such as incomplete films (Figure 3.12 (a)) and large agglomerates (Figure 3.12 (d)), introduced larger structural shapes that might obscure the short-range details. Therefore, the concentration of the initial coating solution should be controlled well for the size effects of the nanoparticles.

By using the combination of dodecanethiol-stabilized AuNPs and APhTS-coated Si substrates, we confirmed that the deposition of nanoparticle films begins with layer-by-layer growth followed by aggregate formation. The variation in the concentration of the initial nanoparticle solution made it possible to observe the growth process. This again emphasizes the importance of the number of nanoparticles involved in film deposition and shows that it is possible to exert better control of film morphology.

3.3.5 GXL-deposited films of AuNPs with different sizes

The size effect is one of the key properties of nanoparticles, and size-dependent properties are often observed at the nanoscale. The properties of nanoparticles change as their size approaches the nanoscale. When nanoparticles are deposited onto substrates, the way in which their size affects the deposited film remains an interesting topic. Currently, many methods are used to achieve nanoparticles of varying sizes, either by direct synthesis parameter control or by using post-synthesis treatment. Our group has been using our GXL technology for precipitation and size fractionation of gold nanoparticles (Anand et al., 2005). The process is similar to GXL nanoparticle deposition, but now several high-pressure vessels (mounted

vertically in series) separated by valves that are isolated from each other were introduced. The whole process includes pressurization, nanoparticle precipitation, and solution transfer.

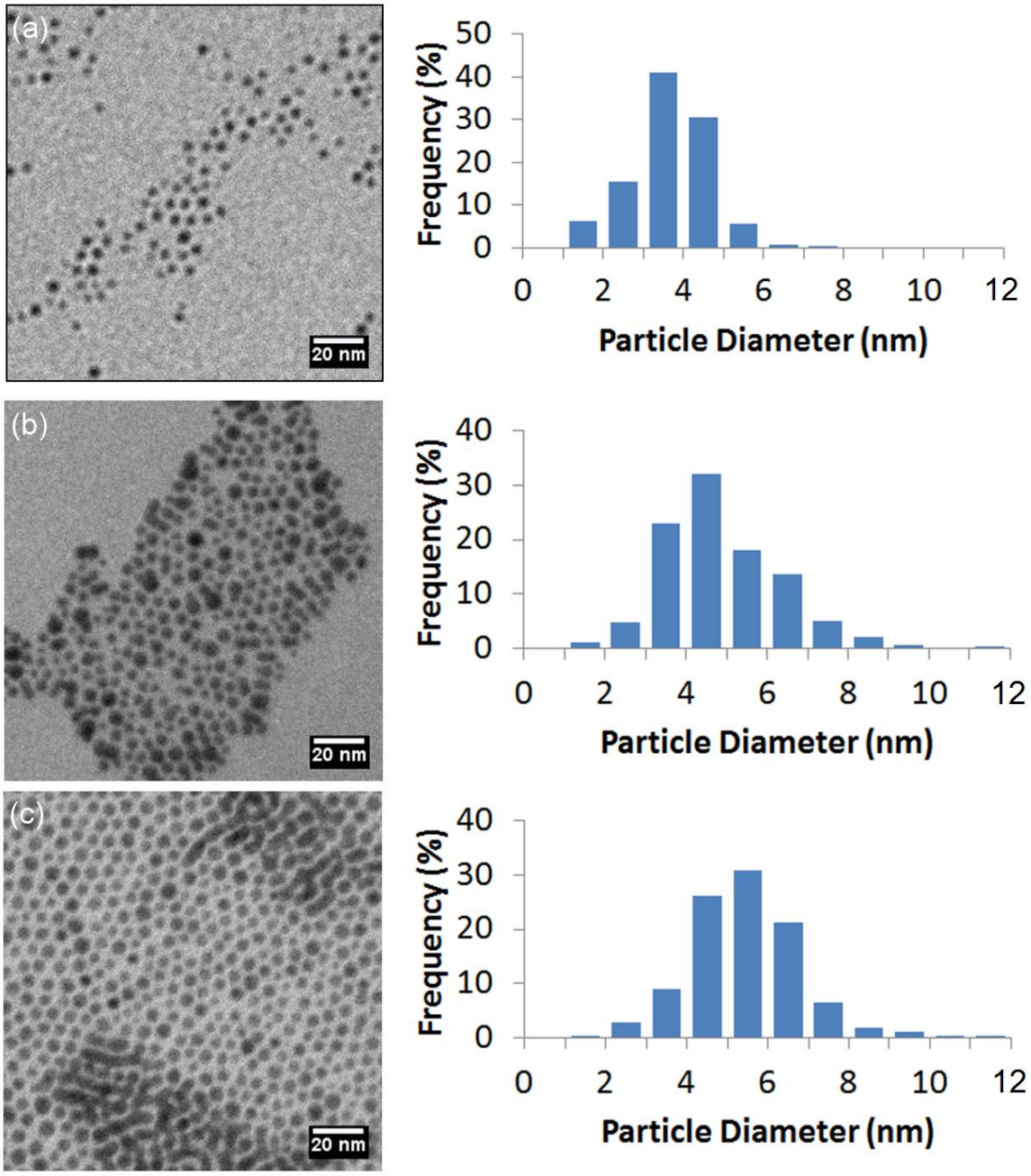

Figure 3.15. TEM images and size distribution of size-fractionized AuNPs. The size fractions are (a) small, (b) medium, and (c) large.

A series of AuNPs with different average diameters have been achieved via our GXL nanoparticle size fractionation process. The TEM images and corresponding size distribution are shown in Figure 3.15. The average size and size distribution of the AuNPs obtained were (a) 3.6 ± 0.9 nm, (b) 4.8 ± 1.4 nm, and (c) 5.4 ± 1.4 nm. These nanoparticles were used for GXL deposition to assess the effect of nanoparticle size on formed films.

AFM images with line profiles and rms surface roughness values of films formed by small nanoparticles are shown in Figure 3.16. It is clear that when using small particles, the surface roughness was relatively low, even at high concentrations. According to the line profiles, the increase in maximum height was approximately 3-5 nm, which is within the range of an AuNP monolayer. The surface parameters calculated for coatings from different initial concentrations are summarized in Table 3.7. The average summit densities at different concentrations were relatively high and the average summit radius values were high as well. It should be noted that the high summit radius value does not reflect the actual particle grain size, but it is affected by the long-range morphology characteristics, such as the large bumps that are visible. When combined, they lead to a higher ratio of true to apparent contact area. This can be verified by the smooth surface structure and lower standard deviation of summit height distribution.

The experimental HHCF curves from AFM data and corresponding HHCF curves by model fitting are plotted in Figure 3.17. The rms roughness, autocorrelation lengths, and roughness component values from HHCF model are summarized in Table 3.8. The autocorrelation lengths at low and medium concentrations were higher than those at the high concentration, indicating surfaces without many visible grains. Roughness components for these

two surfaces were higher as well, which can be seen from the line profiles, in that they have fewer tiny, jagged structures.

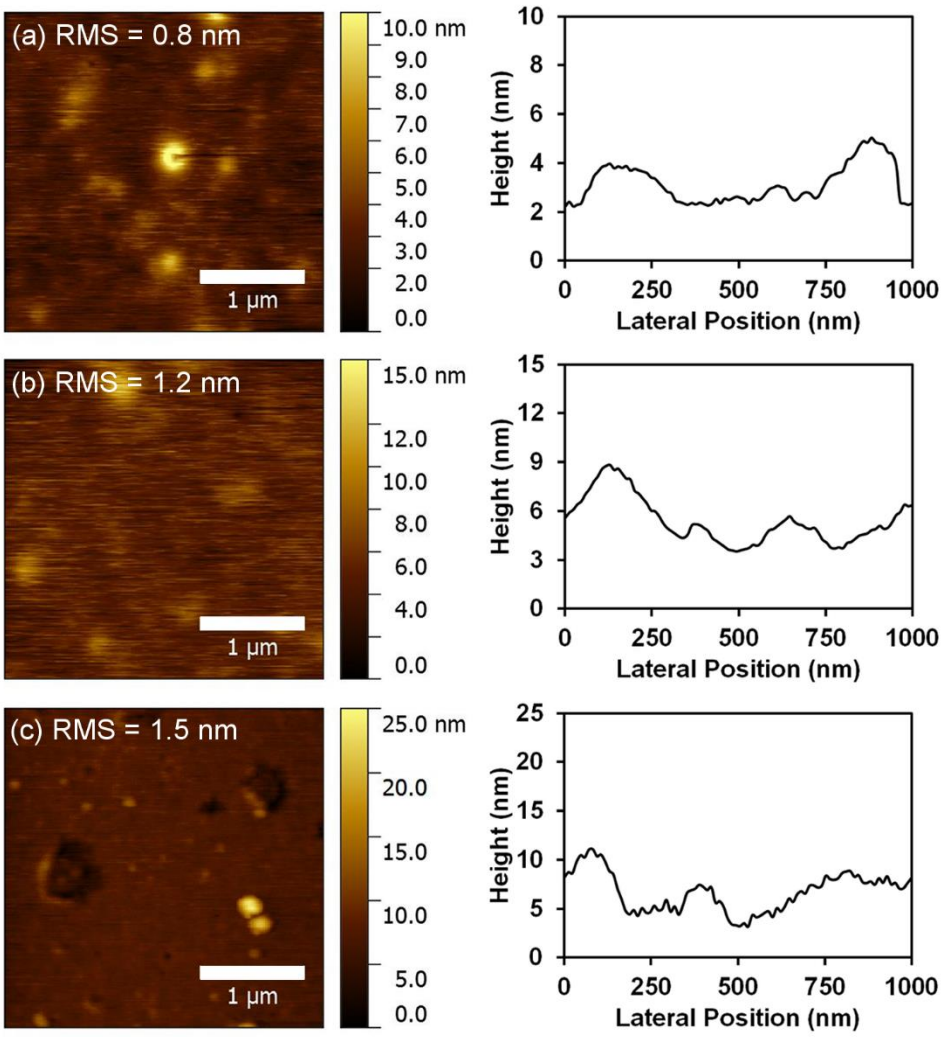

Figure 3.16. AFM images with line profiles and rms surface roughness values of small size AuNP films deposited onto APhTS-coated silicon substrate at different concentrations. The concentrations were (a) low, (b) medium, and (c) high.

	Low	Medium	High
Average summit density (/μm^2)	150.8 ± 13.9	144.3 ± 10.5	118.6 ± 13.7
Average summit radius (x10^{-3} μm)	344.3 ± 22.7	225.7 ± 10.8	303.5 ± 26.3
σ_s, standard deviation of summit height distribution (x10^{-3} μm)	0.71 ± 0.09	1.02 ± 0.11	1.41 ± 0.21
Average number of summits in contact (/μm^2)	23.9 ± 2.1	22.9 ± 1.6	18.8 ± 2.1
Ratio of true to apparent contact area (%)	0.96 ± 0.16	0.89 ± 0.14	1.32 ± 0.26
α, bandwidth parameter	4.17 ± 0.45	3.69 ± 0.37	7.03 ± 0.93
m_0 (x10^{-6} μm^2)	0.64 ± 0.04	1.44 ± 0.12	2.25 ± 0.17
m_2 (x10^{-3})	0.76 ± 0.05	1.84 ± 0.10	1.23 ± 0.09
m_4 (/μm^2)	3.72 ± 0.24	8.67 ± 0.42	4.79 ± 0.39

Table 3.7. Surface parameters calculated for coatings from small size AuNPs.

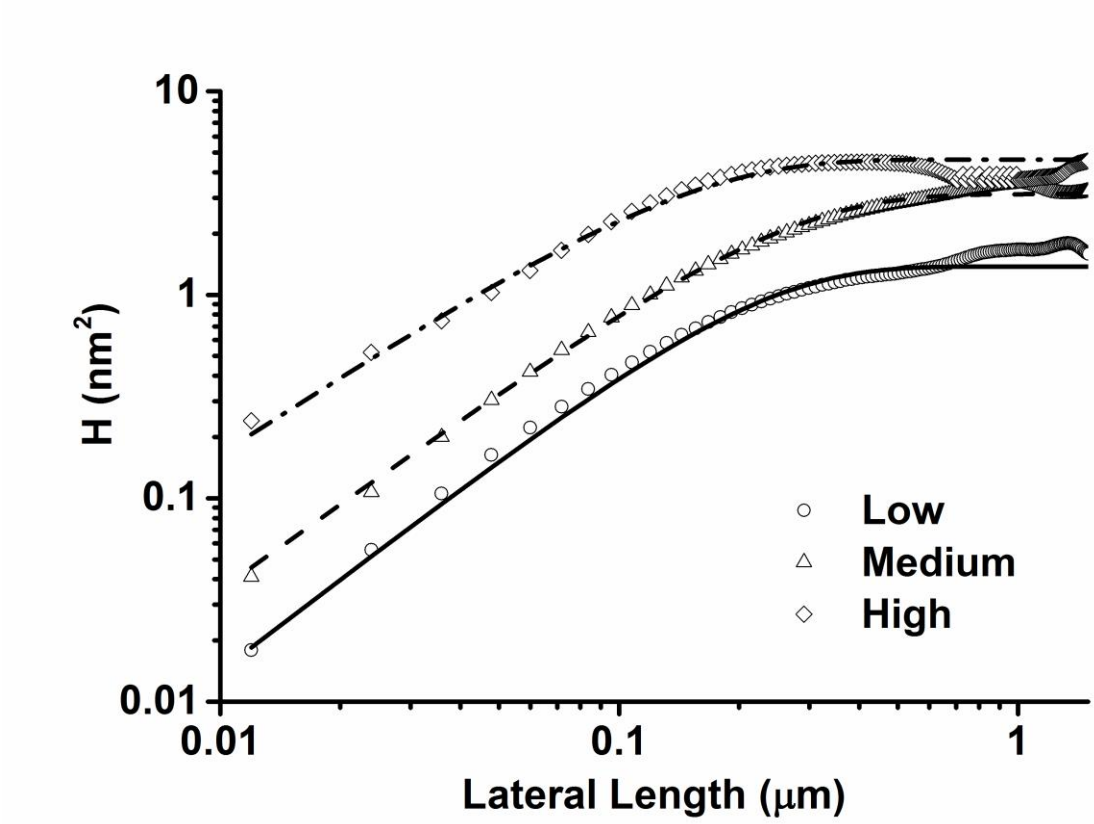

Figure 3.17. Experimental HHCF data for coatings from small size AuNPs. Lines are corresponding HHCF curves calculated using proposed HHCF model fitting.

Concentration	rms roughness (nm)	Autocorrelation length (nm)	Roughness exponent
Low	0.83 ± 0.05	210.1 ± 6.3	0.601 ± 0.090
Medium	1.21 ± 0.10	242.4 ± 8.6	0.608 ± 0.079
High	1.54 ± 0.12	133.6 ± 4.9	0.629 ± 0.047

Table 3.8. Surface parameters calculated from HHCF model for coatings from small size AuNPs.

AFM images with line profiles and rms surface roughness values of films formed by medium nanoparticles are shown in Figure 3.18. Because the average size was nearly the same as in the original AuNP solution, and the size distribution was narrower, the morphology of the deposited AuNP films also was very similar, showing a trend from smooth layer formation to aggregate structures. The surface parameters calculated for coatings at different initial concentrations are summarized in Table 3.9. The average summit densities at different concentrations decreased compared to those on the films formed by small nanoparticles and the average summit radius values decreased as well. Therefore, the ratio of true to apparent contact area decreased, which may be a positive trend for reduced adhesion applications.

The experimental HHCF curves from the AFM data and corresponding HHCF curves by model fitting are plotted in Figure 3.19, while the rms roughness, autocorrelation lengths, and roughness component values from HHCF model are summarized in Table 3.10. Both the autocorrelation lengths and the roughness components at various concentrations were within the

same range, indicating uniform surface morphology. At the high concentration, larger aggregates are visible on the surface, while the film underneath is still formed by uniform asperities.

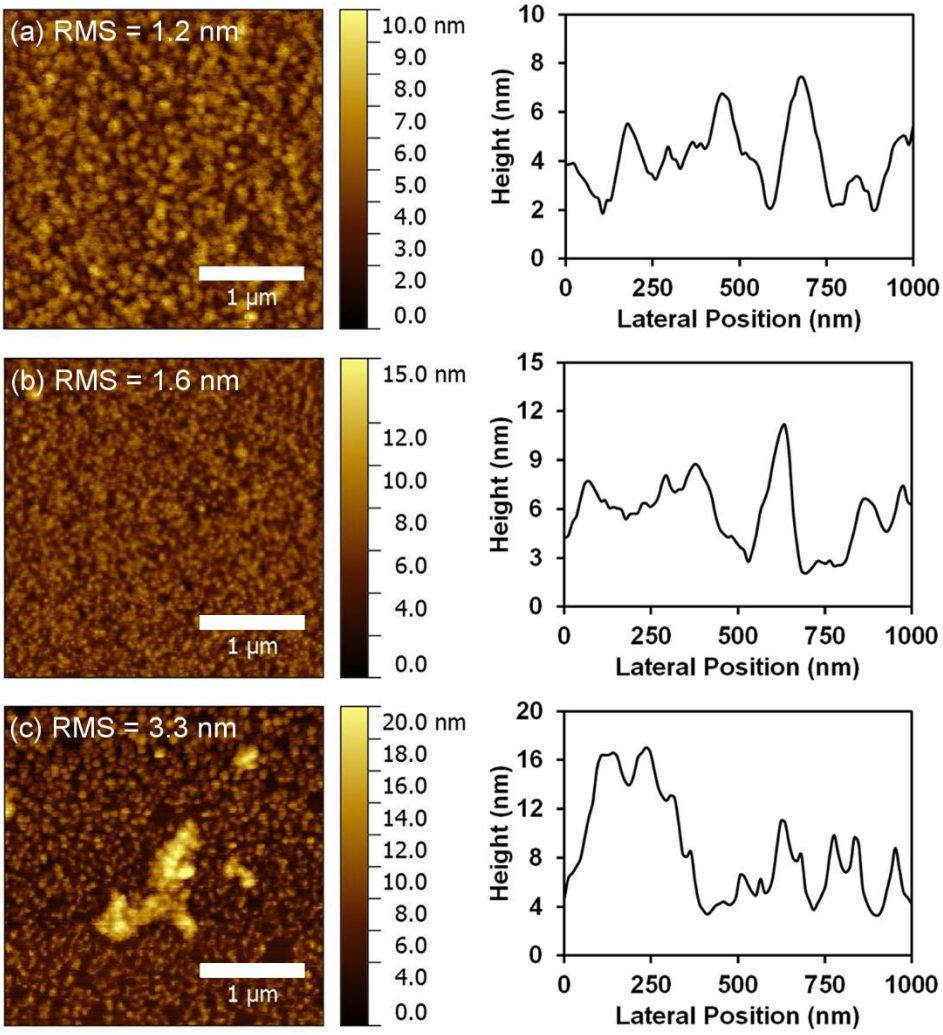

Figure 3.18. AFM images with line profiles and rms surface roughness values of medium size AuNP films deposited onto APhTS-coated silicon substrate at different concentrations. The concentrations were (a) low, (b) medium, and (c) high.

	Low	Medium	High
Average summit density (/μm^2)	90.5 ± 9.8	99.1 ± 9.4	101.4 ± 12.1
Average summit radius (x10^{-3} μm)	334.1 ± 26.0	239.9 ± 12.6	132.7 ± 11.6
σ_s, standard deviation of summit height distribution (x10^{-3} μm)	1.05 ± 0.15	1.38 ± 0.17	2.97 ± 0.48
Average number of summits in contact (/μm^2)	14.4 ± 1.5	15.7 ± 1.5	16.1 ± 2.0
Ratio of true to apparent contact area (%)	0.81 ± 0.16	0.86 ± 0.15	1.05 ± 0.24
α, bandwidth parameter	3.18 ± 0.41	3.49 ± 0.36	4.77 ± 0.68
m_0 (x10^{-6} μm^2)	1.44 ± 0.11	2.56 ± 0.16	10.9 ± 0.67
m_2 (x10^{-3})	1.34 ± 0.09	2.37 ± 0.18	7.55 ± 0.61
m_4 (/μm^2)	3.96 ± 0.32	7.67 ± 0.41	25.0 ± 2.2

Table 3.9. Surface parameters calculated for coatings from medium size AuNPs.

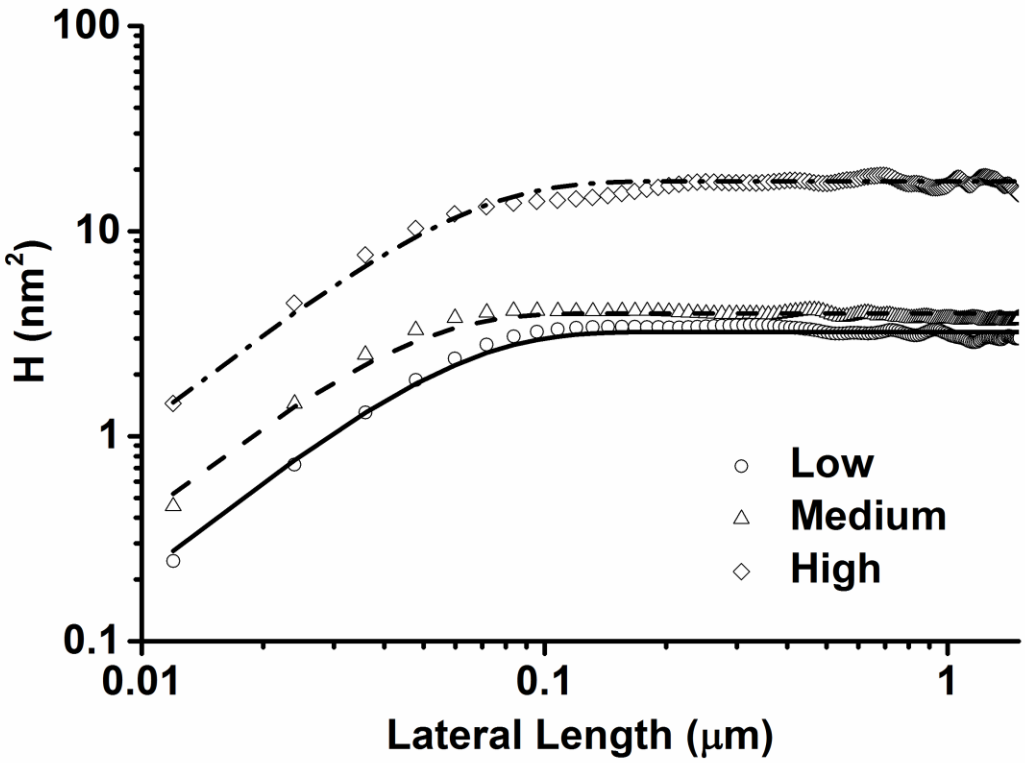

Figure 3.19. Experimental HHCF data for coatings from medium size AuNPs. Lines are corresponding HHCF curves calculated using proposed HHCF model fitting.

Concentration	rms roughness (nm)	Autocorrelation length (nm)	Roughness exponent
Low	1.23 ± 0.09	54.3 ± 3.4	0.748 ± 0.024
Medium	1.57 ± 0.11	40.3 ± 4.8	0.745 ± 0.037
High	3.26 ± 0.21	56.6 ± 4.3	0.765 ± 0.029

Table 3.10. Surface parameters calculated from HHCF model for coatings from medium size AuNPs.

AFM images with line profiles and rms surface roughness values of films formed by large nanoparticles are shown in Figure 3.20. The change in morphology showed a tendency similar to that in the previous films. The surface parameters calculated for coatings from different initial concentrations are summarized in Table 3.11. The average summit densities at different concentrations decreased compared to the films formed by medium nanoparticles, but the average summit radius values increased, which is attributable to the size effect. The ratio of true to apparent contact area was similar to the result from coatings at medium concentrations, but the variation between different values was more significant, indicating that the aggregates formed by larger nanoparticles have major effects on surface characteristics.

The experimental HHCF curves from AFM data and corresponding HHCF curves by model fitting are plotted in Figure 3.21 and the rms roughness, autocorrelation lengths, and roughness component values from HHCF model are summarized in Table 3.12. It should be

noted that at low concentrations, rough incomplete films with gaps appeared. The corresponding autocorrelation length for this surface was significantly higher than others, which derived from the pattern-like grains.

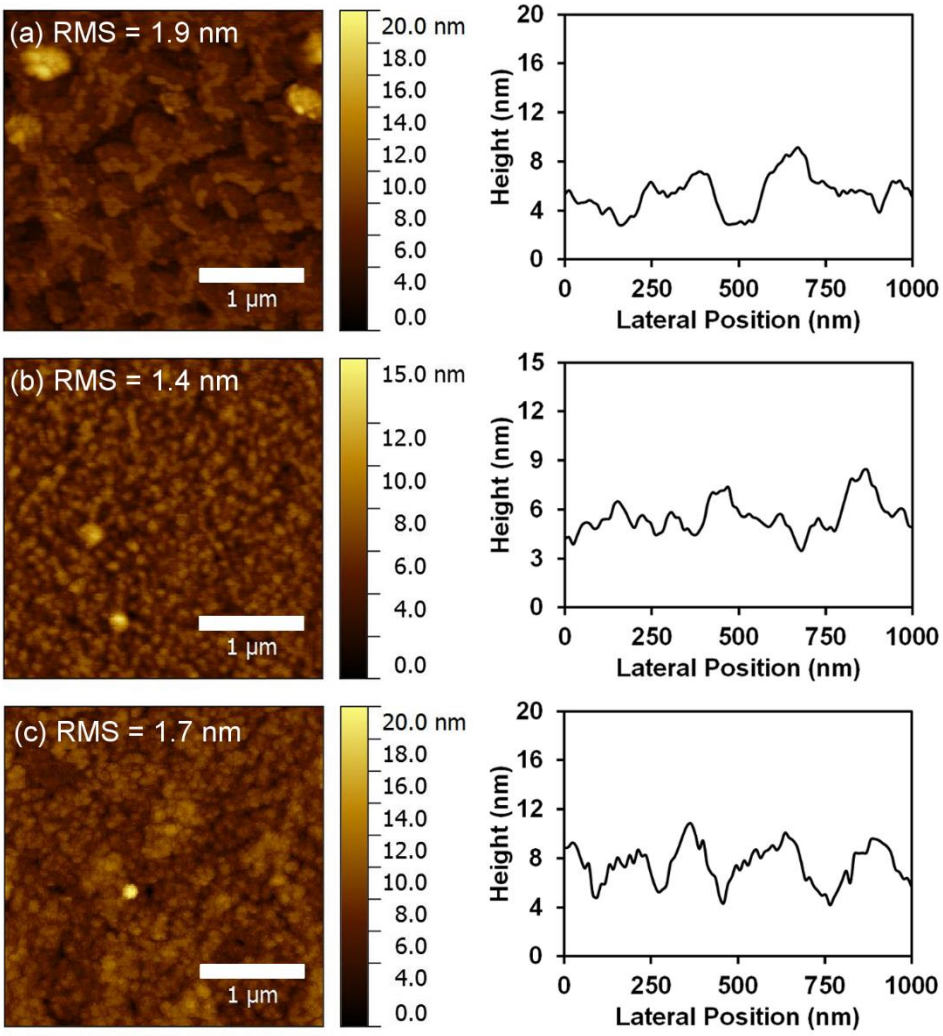

Figure 3.20. AFM images with line profiles and rms surface roughness values of large size AuNP films deposited onto APhTS-coated silicon substrate at different concentrations. The concentrations were (a) low, (b) medium, and (c) high.

	Low	Medium	High
Average summit density (/μm^2)	88.9 ± 10.1	81.7 ± 7.2	106.8 ± 12.4
Average summit radius (x10^{-3} μm)	299.4 ± 24.5	353.6 ± 21.2	223.8 ± 17.9
σ_s, standard deviation of summit height distribution (x10^{-3} μm)	1.76 ± 0.25	1.23 ± 0.16	1.49 ± 0.24
Average number of summits in contact (/μm^2)	14.1 ± 1.6	12.8 ± 1.1	16.9 ± 2.1
Ratio of true to apparent contact area (%)	1.22 ± 0.25	0.93 ± 0.16	0.94 ± 0.22
α, bandwidth parameter	6.17 ± 0.84	3.95 ± 0.46	3.98 ± 0.55
m_0 (x10^{-6} μm^2)	3.61 ± 0.23	1.96 ± 0.15	2.89 ± 0.21
m_2 (x10^{-3})	1.71 ± 0.13	1.32 ± 0.08	2.53 ± 0.25
m_4 (/μm^2)	4.93 ± 0.40	3.53 ± 0.21	8.82 ± 0.71

Table 3.11. Surface parameters calculated for coatings from large size AuNPs.

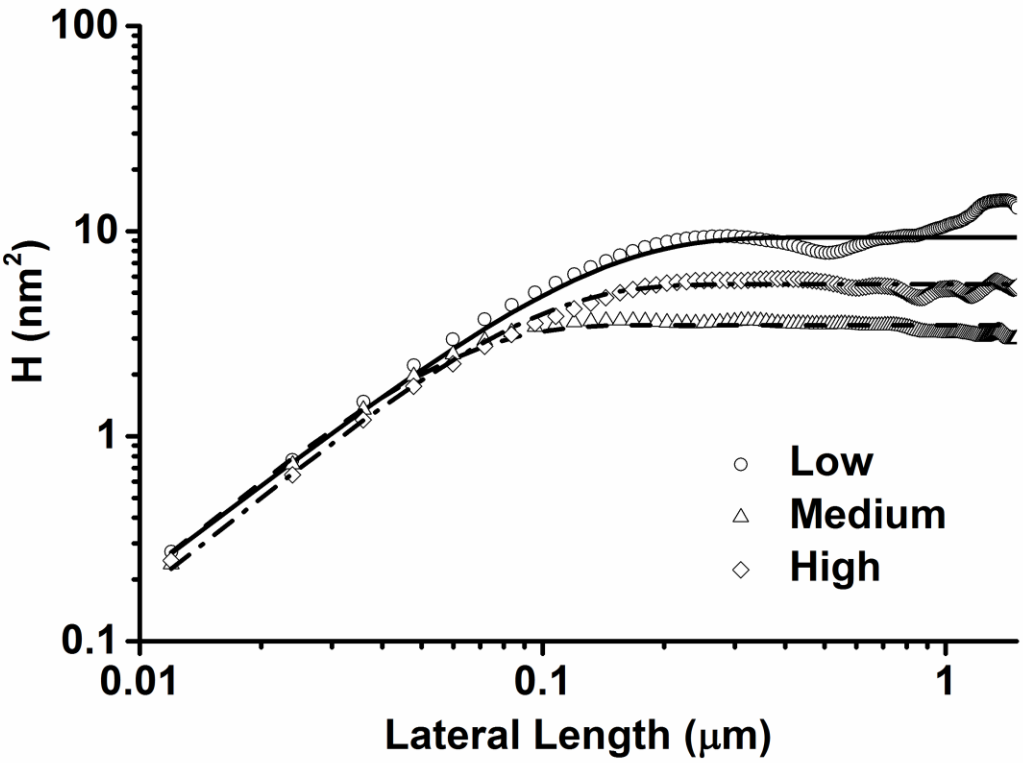

Figure 3.21. Experimental HHCF data for coatings from large size AuNPs. Lines are corresponding HHCF curves calculated using proposed HHCF model fitting.

Concentration	rms roughness (nm)	Autocorrelation length (nm)	Roughness exponent
Low	1.96 ± 0.12	86.4 ± 3.6	0.809 ± 0.041
Medium	1.41 ± 0.11	64.9 ± 1.7	0.824 ± 0.034
High	1.73 ± 0.12	78.4 ± 3.1	0.793 ± 0.040

Table 3.12. Surface parameters calculated from HHCF model for coatings from large size AuNPs.

As discussed before, the film formation mechanism is based on the surface energies of both nanoparticles and the substrate. Precipitation of nanoparticles achieves equilibrium between the particle-particle interaction and the particle-surface interaction. The size of the nanoparticles affects the non-retarded van der Waals force produced by these interactions. The non-retarded van der Waals attractive force to a flat silicon surface experienced by a gold nanoparticle can be estimated using Equation 3.3:

$$F_{S-NP} = A_{S-NP}R/6D^2 \tag{3.3}$$

where R is the radius of the nanoparticle, D is the separation distance between particle and surface, and $A_{S\text{-}NP}$ is an overall Hamaker constant for the particle-surface interaction (Israelachvili, 1992).

As the nanoparticles are made of a different material than the surface, the attraction between particles is also important. The non-retarded van der Waals force between two spherical particles in solution can be estimated by Equation 3.4:

$$F_{NP-NP} = A_{NP-NP} R_1 R_2 / 6(R_1 + R_2) D^2 \quad (3.4)$$

where R_1 and R_2 are radii of two interacting nanoparticles, and $A_{NP\text{-}NP}$ is an overall Hamaker constant for the particle-particle interaction (Israelachvili, 1992). Assuming the radius of every particle is approximately equal, the equation above can be reduced to:

$$F_{NP-NP} = A_{NP-NP} R / 12 D^2 \quad (3.5)$$

The difference in these two forces depends on the overall Hamaker constants. The overall Hamaker constant for the particle-surface interaction used in this study was estimated to be one magnitude lower than that for the particle-particle interaction. Therefore, the interaction between two gold particles of equal diameters is generally stronger than that between a gold particle of the same size and a large, flat silicon surface. Although this slight difference will not prevent the attraction of nanoparticles to the surface, other parameters, such as the particle radius, will affect the two interactions.

In a fixed system, the non-retarded van der Waals force is affected strongly by the particle radius. When the GXL process was applied to a nanoparticle solution with a broad size distribution, small nanoparticles precipitated under higher pressure and filled in the valleys of the incomplete surface layers formed by large nanoparticles, leading to a relatively smooth

topography. If the size distribution of the nanoparticle solution is narrowed, this phenomenon can be suppressed. The final morphology of films deposited by nanoparticles of different sizes is affected by competition between particle-particle and particle-surface attraction. For films formed by small nanoparticles, the particle-surface attraction was still strong enough to make the surface relatively uniform, while the size of the aggregates formed by particle-particle attraction was not large enough to change the surface roughness effectively. From the AFM images, it can be seen that smooth films formed at all concentrations. As the nanoparticle size increased, the particle-particle attraction became more significant than the particle-surface attraction, resulting in a morphology consisting of particle grains, which was confirmed by the AFM images. As shown in Tables 3.10 and 3.12, the average radius value of films formed by large nanoparticles was larger than that of films formed by medium nanoparticles, showing the size effect of nanoparticles.

The size effects on the surface roughness parameters are summarized in Table 3.13. The rms roughness and standard deviation of summit height values still showed an increasing trend for small and medium sized nanoparticle coatings. However, for surfaces coated with large nanoparticles, the overall roughness parameters varied, which derives from the incomplete coating at the low concentration. It is worth noting that the roughness exponent increased as the size of the nanoparticle increased, while it was not affected significantly by the concentration. The higher roughness exponent reflects lower local surface wiggles that are associated with a smoother short-range surface topography.

Size	Concentration	Rms roughness (nm)	Standard deviation of summit height distribution (nm)	Autocorrelation length (nm)	Roughness exponent
Small	Low	0.83 ± 0.05	0.71 ± 0.09	210.1 ± 6.3	0.601 ± 0.090
	Medium	1.21 ± 0.10	1.02 ± 0.11	242.4 ± 8.6	0.608 ± 0.079
	High	1.54 ± 0.12	1.41 ± 0.21	133.6 ± 4.9	0.629 ± 0.047
Medium	Low	1.23 ± 0.09	1.05 ± 0.15	54.3 ± 3.4	0.748 ± 0.024
	Medium	1.57 ± 0.11	1.38 ± 0.17	40.3 ± 4.8	0.745 ± 0.037
	High	3.26 ± 0.21	2.97 ± 0.48	56.6 ± 4.3	0.765 ± 0.029
Large	Low	1.96 ± 0.12	1.76 ± 0.25	86.4 ± 3.6	0.809 ± 0.041
	Medium	1.41 ± 0.11	1.23 ± 0.16	64.9 ± 1.7	0.824 ± 0.034
	High	1.73 ± 0.12	1.49 ± 0.24	78.4 ± 3.1	0.793 ± 0.040

Table 3.13. Key parameters based on quantitative surface analysis for coatings of different nanoparticle sizes.

For coatings of medium and large size nanoparticles, the roughness exponent values increased, as did the autocorrelation lengths, the size of which was on the same order as the grain size in the AFM images. This observation indicates that the grains formed by these size-controlled nanoparticles were visible on the surface and were described well by the surface roughness modeling. The dimensions of the particle grains were affected more by the particle size than the solution concentration. The average size of the grains was significantly larger than

that of the original average nanoparticle size, such that clustering of the nanoparticles during the GXL deposition process played an important role in the formation of the final morphology of the surface. However, although the roughness exponent of coatings of small size nanoparticles followed the same descending trend, the autocorrelation length was much higher than were the values of coatings formed by medium and large nanoparticles. From the AFM images, it can be observed that the tiny structures are unclear. The higher autocorrelation length suggests that for this kind of surface, heights of two points are correlated within a distance larger than the grain size, which cannot be observed. This is probably because the size of this batch of nanoparticles was too small to make elemental structural grains visible clearly, and the large local clustering on the surface overlapped the tiny structures during the deposition process.

Both the initial concentration of the nanoparticle solution and the average size of the nanoparticles affected the morphology characteristics of nanostructured surfaces. The change in concentrations had a major effect on the change in long-range roughness, such as the rms surface roughness and standard deviation of the summit height distribution. Clustering of the particles and grains resulted in local agglomerations, which can be characterized by short-range roughness parameters. The average size of the nanoparticles affected the autocorrelation length and roughness exponents and this effect was independent of the initial concentration or long-range roughness. It should be noted that the autocorrelation length was much larger for the coatings formed by very small nanoparticles, which indicates that morphological structures with a larger length-scale order than the fundamental particle clusters existed. For the coatings formed by medium and large nanoparticles, the correlation length and visible grain size were of the same order. All these results showed that control of the size variation of nanoparticles helps us achieve better observations of the surface roughness at different dimensional scales.

3.4 Conclusion

Various self-assembled monolayers were deposited in liquid phase on substrates prior to nanoparticle deposition to combine the SAM and GXL technologies by providing both a low energy surface and a rough nanoparticle coating.

Self-assembled monolayers were synthesized on Si substrates and characterized. The contact angle and thickness values of these SAMs were in agreement with the values measured and calculated in other reports, which proves that a monolayer formed on the Si substrate. A smooth and uniform monolayer formation is very important in the deposition of nanoparticles.

Because it was affected by the critical surface tension of the SAMs, the film growth alternated between layer-by-layer deposition and agglomeration formation, which also resulted in a change in the surface roughness. On the other hand, the surface chemistry of the AuNPs, which is affected by the stabilizing ligands on the nanoparticles, also had an effect on the film deposition. By using the combination of dodecanethiol-stabilized AuNPs and APhTS-coated Si substrates, we confirmed that the nanoparticle films deposited followed the Stranski-Krastanov mechanism. The changes in morphology induced by the concentration of the nanoparticle solution emphasize the importance of the number of nanoparticles involved in film deposition, and indicate the possibility to achieve better control of the films formed.

A calculation based on the GW model was applied to the surface topographies from AFM data presented as a quantitative assessment for the comparison of various coatings. The variation in concentration of the initial nanoparticle solution facilitated observation of the growth process. When nanoparticles of different sizes were deposited on a SAM-coated substrate at varying

concentrations, the surface morphology and roughness were affected at multiple length scales. Changes in concentration had a major effect on the long-range roughness parameters, such as the rms surface roughness and standard deviation of the summit height distribution. The average size of nanoparticles affected short-range roughness parameters, such as autocorrelation length and roughness exponents. Clustering of the particles and grains influenced the dimensions of local agglomerations and this effect was independent of the initial concentration. The variation in size of the nanoparticles allowed the opportunity to obtain better control of several important surface parameters, such as the ratio of true to apparent contact area, which is highly important in minimizing adhesion and friction in real applications.

The results discussed in this work indicated that the morphology of nanoparticle films can be engineered for specific surfaces and provide potential improvements for interfacial applications by altering certain deposition conditions.

Chapter 4

Nanoparticle films based on nanomaterials of different sizes and shapes and their effect on microtribology control for MEMS devices

4.1 Introduction

Our group's previous work proved that gold nanoparticles can be deposited successfully on cantilever beams using our GXL deposition technology with supercritical drying (Hurst et al., 2009). Using this technology resulted in reduced microstructure adhesion energy because the surfaces were roughened further and the real area of contact was reduced significantly. In contrast to traditional methods of surface roughening, the deposition of hydrophobic ligand-capped nanoparticles offers a new choice to control the chemical nature of contact, as well as the topographical benefits of reduced contact area. The GXL particle deposition technology is compatible with current fabrication requirements compared to conventional evaporation or drop casting of nanoparticles.

However, challenges still exist. One of the problems is the mobility of sphere nanoparticle-deposited films. Our previous work showed that after the actuation and contact of the cantilever beam with the substrate, the mechanical contact of the in-plane surfaces interacted and moved the weakly-bound nanoparticles from the organic monolayer films. This indicated that non-immobilized nanoparticles show regions of nanoparticle translation, which may result in decreased performance in applications because the top layer of spherical nanoparticles does not have a large enough contact area with lower nanoparticle films or self-assembled monolayers. A

potential solution is to apply a further enhancement layer on the surface, which requires additional processing. An alternative possibility is to use nanomaterials of various sizes. These size-controlled structures may produce stronger interactions between asperities and lead to improved stability. Application of these size-varied nanostructures also may produce films with different contact areas and morphology that affect the surface tribology.

Another reason to choose different sizes is their unique properties. The use of size-controlled nanomaterials has been reported as catalyst supports and in photovoltaic applications. It is believed that nanomaterials of different sizes function not only as supports, but also as electronic modulators, in addition to contributing asymmetric acting sites (Yamada et al., 2011). These materials have even greater potential for innovative surface structure design. The precise selection and control of size-based interfaces could lead to better applications for surface modification. Currently, there are few reports on the effect on devices of the integration of size-controlled nanomaterials with tribology control.

Based on these factors, the following hypothesis was proposed. If metal nanomaterials of different sizes are deposited on SAM-coated substrates, the effect of nanostructure shape on surface coverage, real contact area, and adhesion energy can be investigated. With these tuning effects, better tribology control can be achieved.

4.2 Experimental section

4.2.1 Iron oxide nanoparticles and gold nanorods

Synthesis of polydispersed iron oxide nanoparticles was accomplished with the help of our previous group member, Dr. Pranav Vengsarkar, who has synthesized iron oxide nanoparticles coated with oleic acid dispersed in hexane successfully and used our GXL technology to perform the particle size fractionation (Vengsarkar et al., 2015). Iron oxide nanoparticles coated with oleic acid (replaceable with other carboxylic acids) were synthesized based on a coprecipitation method described previously (Jain et al., 2005). Aqueous solutions of 0.1 M Fe (III) and 0.1 M Fe (II) were prepared using DIUF water. 30 mL of Fe (III) solution was mixed with 15 mL of Fe (II) solution in a three-necked flask with magnetic stirring. Under constant stirring in a nitrogen atmosphere, 3 mL of 5 M ammonium hydroxide was added to the solution to generate a black precipitate of iron oxide nanoparticles. The reaction solution was then heated to 80 °C and maintained for 30 min to evaporate the ammonia from the solution. While the temperature was increasing, 280μL of oleic acid was added to the mixture. The temperature was then cooled to 60 °C and maintained at that temperature for 1 h. Thereafter, the solution was allowed to cool to room temperature and was washed with water to remove any excess reagents and impurities. Then, 30 mL of ethanol was added, and the particles were centrifuged with ethanol twice. The particles were then dried using nitrogen and dispersed in n-hexane via sonication.

The particles synthesized using the method above have a broad size distribution. To obtain a better understanding of size effects, commercial, spherical, oleic acid-coated, iron oxide nanoparticles (average size 5 nm, 10 nm, and 20 nm) dispersed in toluene were purchased from

Sigma Aldrich. The concentration was 5 mg/mL for all nanoparticle dispersions, which also contained less than 1.0% oleic acid. The iron oxide nanoparticles were dried using nitrogen and redispersed in n-hexane for all experiments in this study.

To study the effect of nanoshapes, commercial gold nanorods were purchased from NanoPartz. The gold nanorods were stabilized with 1-dodecanethiol and dispersed in toluene at a concentration of 1 mg/mL. After the gold nanorod solution was made, it was redispersed in n-hexane and ready for GXL deposition.

4.2.2 Design of micromachine testing chips

To test the actual tribology effects of nanofilms formed by various shapes, it was necessary to design and fabricate certain test devices at micrometer scale. Historically, the test platforms that have been used to study the tribological properties of MEMS surfaces have had extremely complicated designs, and their fabrication has involved highly sophisticated processes that are not only expensive, but time consuming. However, the design of a test platform should be such that it can be fabricated easily, inexpensively, and in a reasonable amount of time. This is an important requirement because most university researchers are known to be short of two resources: time and money. Further, this also would make the design of the test platform portable among laboratories (Gad-el-Hak, 2006).

Naveed Ansari, a previous PhD student in our group, designed a test platform that can be fabricated using a silicon-on-insulator (SOI) wafer. The SOI wafer, which is used to fabricate the

microinstrument, consists of a 2 μm thick, n-type Si(100) layer, a 2 μm thick sacrificial layer, which is a buried-oxide (BOX) layer, and a substrate that is a 500 μm thick, n-type Si(100) wafer. To be able to investigate systematically, and establish a meaningful and reliable correlation between, the effects that a particular factor has on the different tribological properties of MEMS surfaces, several different types of microinstruments were included in the test platform. Their dimensions were determined keeping in mind that fabricating all of them on the same chip should not cause any issues during the release of the test platform. Fabricating all of the microinstruments used to determine the various properties of surfaces on the same chip ensured that the test surfaces examined each had identical surface characteristics, and were exposed to identical experimental conditions. Figure 4.1 shows a schematic of the complete chip design.

The test platform was designed to have multiple copies of the seven main microinstruments. The reason for including multiple copies of each microinstrument in the test platform was to obtain statistically significant experimental datasets. Further, the copies were distributed over the entire test platform to determine local variations in the experimental results. This enabled us to eliminate positional bias in the results. In addition, all of the microinstruments of the test platform were organized to make the most efficient use of the total area of the test platform. In summary, this test platform is a carefully designed and versatile tool that enables systematic and reliable studies of the tribology of MEMS interfaces.

The focus of this test platform is a microinstrument referred to as a Cantilever Beam Array (CBA), which can be used to study the adhesion characteristics of in-plane surfaces, and to determine the apparent work of adhesion of in-plane surfaces in contact. Although most of the

tribological studies reported to date have been conducted using in-plane surfaces, more surfaces come into contact during the operation of devices in several of the emerging classes of MEMS, such as microgears and microsliders. Information from the test data of in-plane surfaces still shows that it is critically important to understand tribology effects more thoroughly.

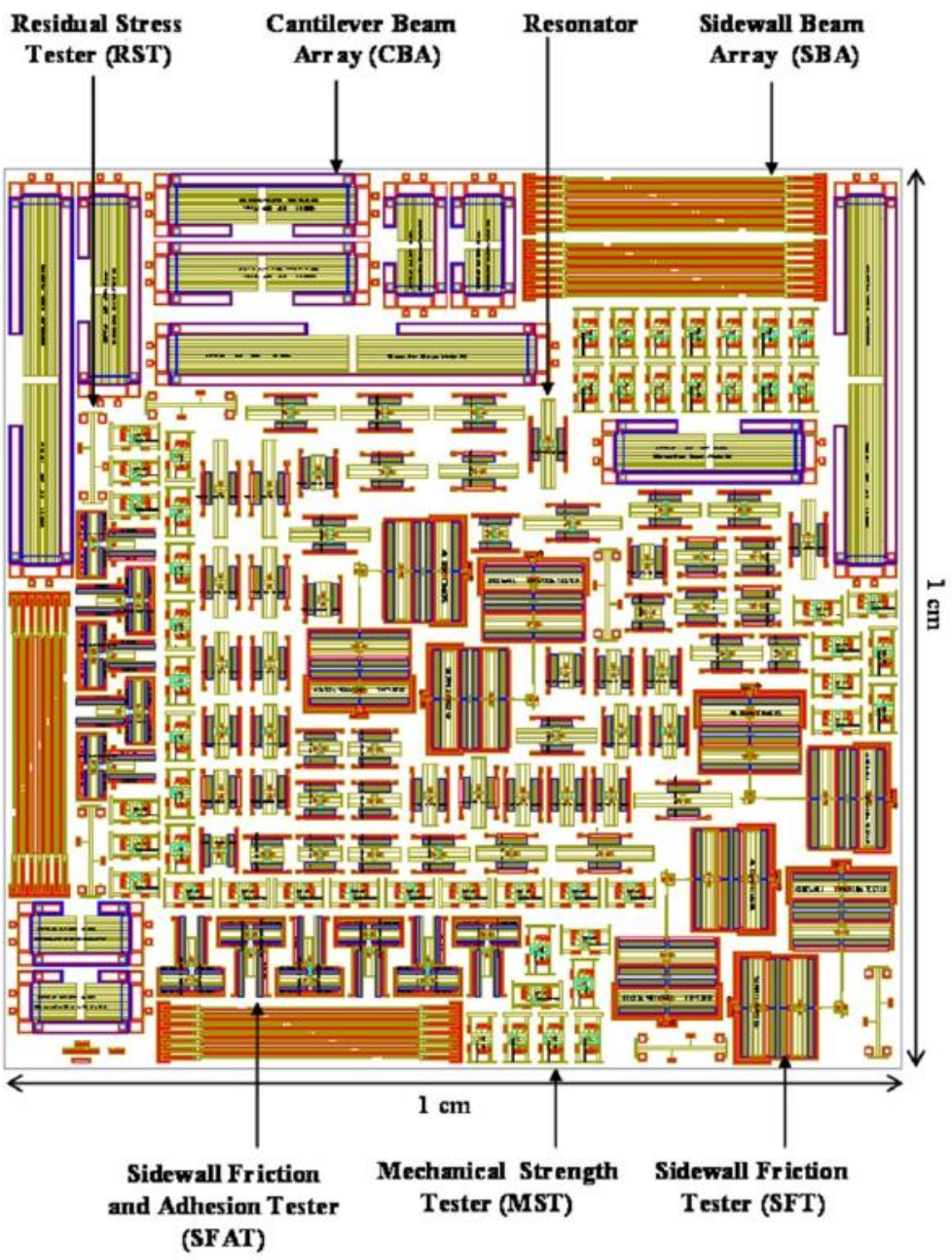

Figure 4.1. Schematic of the mask used to fabricate the test platform.

Cantilever beams were first used to determine the interfacial work of adhesion of in-plane surfaces by Mastrangelo (Mastrangelo et al., 1992). Since then, the CBA has been considered the standard test device for studying the stiction characteristics of in-plane surfaces, and has been

used widely to determine the mechanisms that underlie the stiction experienced by proximate MEMS surfaces, as well as to study the effects of different surface treatments. Historically, the CBAs that have been used to study stiction consisted of cantilever beams of increasing lengths. Later reports indicated that using cantilever beams that are adhered over long attachment lengths to determine the apparent work of adhesion of in-plane surfaces yielded significantly more accurate results. Using S-shaped beams to quantify adhesion and stiction is much less sensitive to variations in surface topography or to details of capillary drying than is the case when using arc-shaped beams (de Boer et al., 1999).

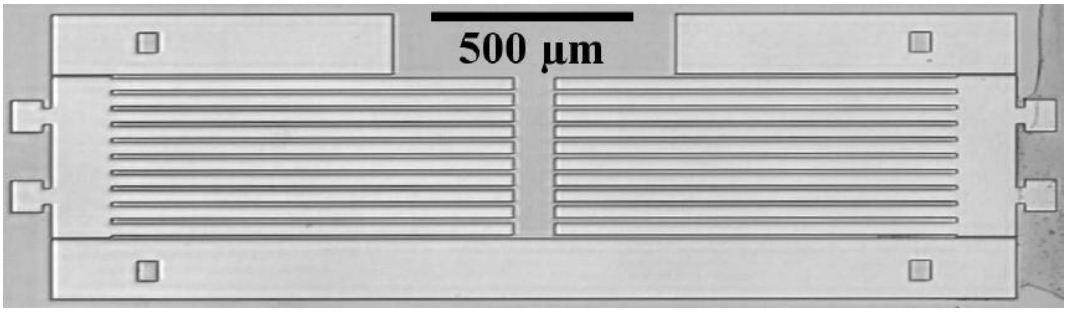

Figure 4.2. An optical image of two sets of Cantilever Beam Arrays.

To overcome the limitations of the CBA that consists of cantilever beams with increasing lengths, the CBAs that were included in the test chip were designed with 10 cantilever beams each, all of equal length. Figure 4.2 shows an optical image of the CBAs released. The crack length of each cantilever beam was determined using interferometry. Therefore, each cantilever beam of the CBA can be used to obtain a data point. Accordingly, each CBA in the TP can be used to obtain ten data points. This allowed not only the collection of a statistically significant dataset, but also enabled analysis of the local variation in the adhesion of the in-plane surfaces studied.

4.2.3 Fabrication of micromachine testing chips

To be able to fabricate the test chip using a simple, inexpensive, and less time consuming process, the microinstruments were designed in such a way that all can be fabricated in a single-mask scheme. The test chip was fabricated using standard surface micromachining tools with the help of John Tatarchuk, a PhD student in the Department of Electrical and Computer Engineering. The fabrication process began with cleaning the SOI wafer using a RCA1 solution (deionized $H_2O/NH_4OH/H_2O_2$ at a volume ratio of 5:1:1). The cleaned wafer was dried so that it could be primed with hexamethylene-disilazane (HMDS). Priming the device layer with HMDS ensured good adhesion between the device layer and the photoresist layer, which was used as a mask when patterning it. After priming, the device layer was spin-coated with a layer of positive photoresist, AZ 5214 E-IR. Next, the photoresist layer was patterned by exposing it through a hard (chrome on quartz) mask to the h-line of a mercury vapor lamp (radiation wavelength = 404.7 nm) and developing the exposed photoresist layer in an aqueous solution for 18 seconds (AZ400K/deionized H_2O at a volume ratio of 3:1). Patterning the photoresist layer transferred the layout of the test platform from the hard mask onto it. Next, the SOI wafer with the patterned photoresist layer was dipped in HF solution (concentrated 49% HF/deionized H_2O with a volume ratio of 50:1) for 10 seconds, which etched away the native oxide present on the exposed regions of the device layer. Using the patterned photoresist layer as the etch mask, the device layer was etched using the Bosch process in a deep reactive ion etching (DRIE) system. This anisotropic etching of the device layer defined the three dimensional geometries of the microinstruments of the test platform. Because the Bosch process etches the silicon relatively much faster than the SiO_2, the sacrificial layer can be used conveniently as an effective etch stop. Finally, after the

entire thickness of the device layer was etched, the wafer was diced carefully into individual test chips.

The Bosch process used to define the three dimensional geometries of the microinstruments of the test platform results in the formation of scallops on the sidewall surfaces (Rhee et al., 2008), because they are not masked during the etching process, as are the in-plane surfaces of the test platform. Therefore, a polishing process based on thermal oxidation was introduced to the fabrication to construct the sidewall surfaces of the test platform. The process began with cleaning the test platform in a piranha solution (concentrated H_2SO_4/30% H_2O_2 at a volume ratio of 2:1), for 2 min, after which the test platform was dried by a N_2 stream. A layer of thermal silicon oxide was grown on the exposed silicon surfaces of the test platform using the dry oxidation process at 1100 °C in laboratory air for 75 min. This formed a 120-140 nm thick layer of SiO_2 on the exposed surfaces of the microinstruments of the test platform. The thickness of the thermal oxide layer grown on the exposed silicon surfaces of the test platform was measured using ellipsometry on a Si(100) monitor chip processed simultaneously with the test platform. Next, the thermally-grown oxide layer was etched away completely from the surfaces of the test platform using BOE etching solution (concentrated HF/deionized H_2O at a volume ratio of 1:6). The thickness of the residual thermal oxide remaining on the surfaces of the test platform after this treatment was measured on the simultaneously processed Si(100) monitor chip using ellipsometry, to ensure that the timed etch was sufficient to remove the entire layer of thermally-grown oxide. This completed one cycle of polishing. The sidewall surfaces of the test platform used in this work were polished using two cycles.

4.2.4 Preparation of test platform chips

To study the tribology of MEMS instruments, the devices on the test platform first must be released before using them for testing. The microinstruments' release procedure began with cleaning the chip to remove the patterned photoresist layer. The chips were immersed in acetone and sonicated for 1 minute then dried by a N_2 stream. Next, the microinstruments were released by etching the sacrificial silicon oxide layer underlying the device layer in concentrated HF solution (49%) for approximately 10 minutes. This time depends on the thickness of the sacrificial layer and must be controlled precisely. After etching, the etchant was rinsed away thoroughly with DI water. The released microinstruments were then placed in hot H_2O_2 (80 °C) for 10 minutes to oxidize the microstructure surfaces. The oxidized chips were rinsed completely with isopropanol and further with anhydrous hexane. Care must be taken to ensure that the microinstruments are not exposed to the liquid-vapor interface while transferring the chip. The prepared chip was finally stored in anhydrous hexane for further testing.

4.2.5 Nanoparticle deposition on test platforms by the gas-expanded liquid technique

The process described in Section 3.2.4 was modified and used to deposit the iron oxide nanoparticles on the test surfaces of the chips. The released chip was stored in a glass vial kept in a large beaker filled with anhydrous hexane without exposing it to the liquid-vapor interface. To load the chip into the high-pressure vessel, the chip was first flipped and placed upside-down in the vial. The vial was then removed from the beaker, and the hexane removed from the vial

carefully to a level just above the chip. Next, 200 µL of diluted iron, oxide, gold nanoparticle dispersion in hexane was added to the vial and mixed carefully.

After mixing, the vial was placed in the stainless steel high-pressure vessel described previously. 400 µL of pure anhydrous hexane was added to the vessel to saturate the vapor space and prevent evaporation of the organic nanoparticle dispersion prior to sealing the vessel. After it was sealed, the chamber was pressurized with CO_2 to approximately 900 psi using a flow rate of 0.4 mL/min. During the pressurization, the CO_2 dissolves in the organic phase, effectively expanding the volume and reducing the solvent strength of the hexane/CO_2 mixture, which results in precipitation of the suspended iron oxide nanoparticles. Pressurization was continued until the entire chamber of the high-pressure vessel filled with liquid CO_2. The mixture of liquid CO_2 and hexane was then heated to 40 °C to bring it into supercritical state. Next, the chamber of the vessel was flushed with pure supercritical CO_2 (at 40 °C and 90 bar) at a rate of approximately 1 mL/min to ensure the removal of the organic solvent and prevent any dewetting effect. Finally, the chamber was depressurized to atmosphere slowly and the dried nanostructure-coated chip was removed and kept for further characterizations.

4.2.6 Actuation and analysis of nanoparticle-deposited test platform

The microinstruments on the test chip were actuated using a custom-built probing system (Probe Station). A photograph of the probing system is shown in Figure 4.3. The probing system is equipped with a long-working-distance, incoherent light interference, and a green LED that uses a monochromator as the illumination source. The probing system also is equipped with a

charge-coupled device (CCD)-IRIS camera to collect digital images. In addition, it has six probe modules used to establish mechanical and electrical contacts with the microinstruments. Lastly, it has an in-built vacuum pump that is used to generate the vacuum suction that holds the probe modules and chip in place during the actuation of the microinstruments. To automate the actuation of the various microinstruments, the testing procedures were executed using a scripting environment called MEMScript. The scripts used for testing the microinstruments not only actuate them, but also collect and store the data required.

The testing procedure was as follows. To actuate a cantilever beam, first, its tip was brought into contact with the substrate by pushing with the probe tip. Then, the cantilever beam was pushed along its length progressively at points closer to its anchor until it was in contact with the substrate over almost its entire length, as shown in Figure 4.4. At this point, the probe tip was retracted carefully and slowly, which allowed the cantilever beam to peel apart up to a certain characteristic length called the crack length under the interference of its restoring. The crack length exhibited by a cantilever beam depends on the interfacial properties of the two in-plane surfaces in contact, the bottom surface of the cantilever beam, and the top surface of the substrate. The crack length of each actuated cantilever beam was determined optically using phase shifting interferometry.

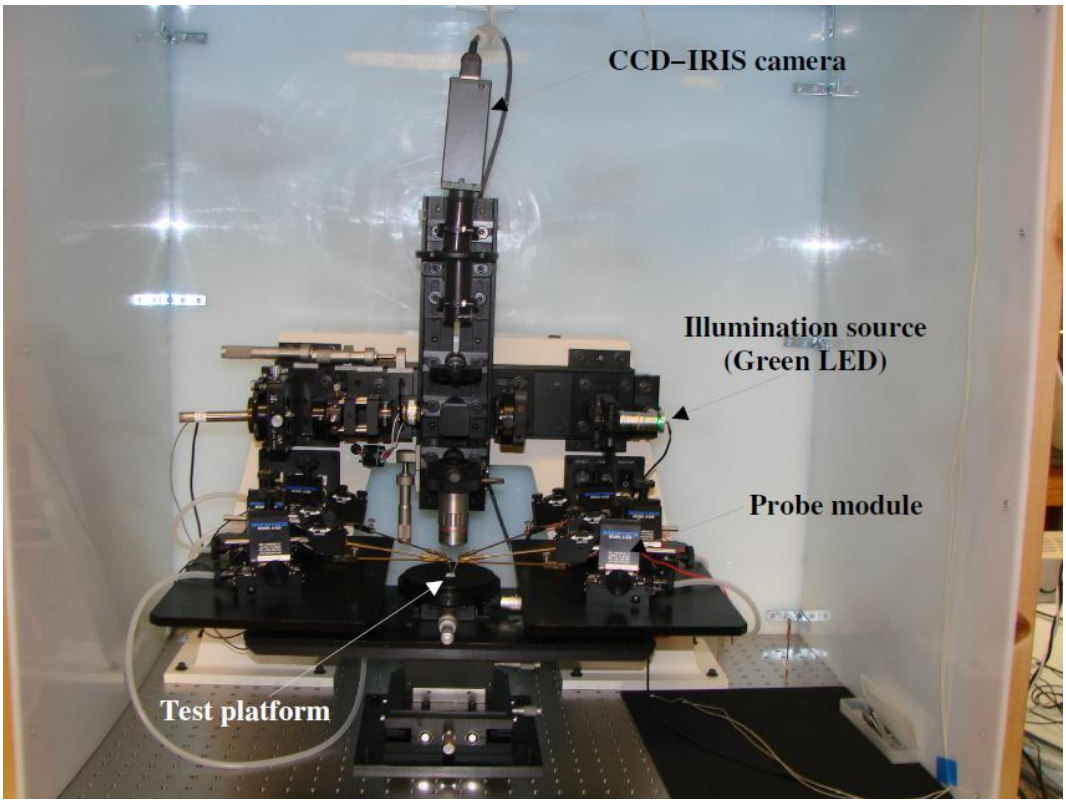

Figure 4.3. Photograph of the custom-built probing system used to actuate the microinstruments.

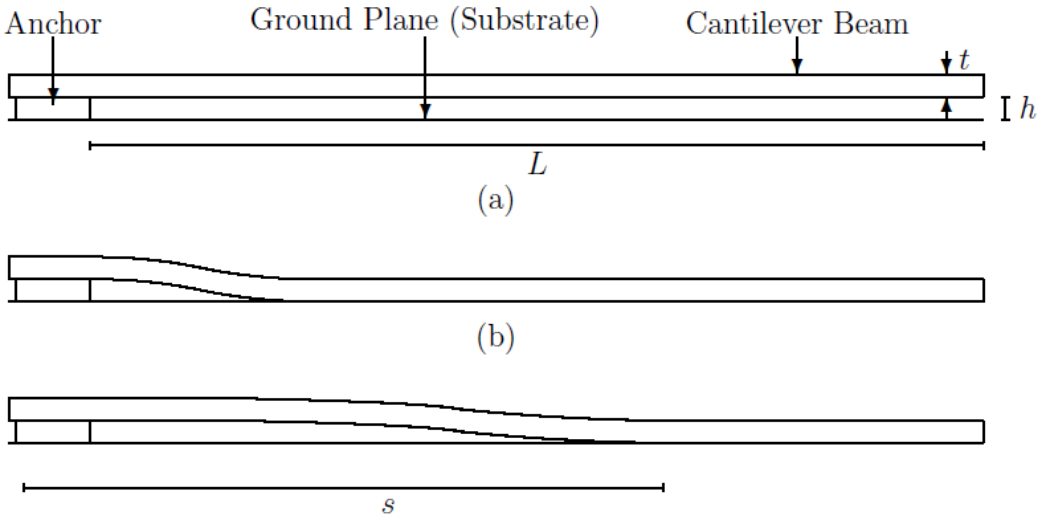

Figure 4.4. A schematic diagram illustrating the actuation procedure of a cantilever beam (Ansari, 2011).

Interferograms of the selected cantilever beam were collected at different phase increments. A five-point Hariharan phase shift calculation was performed using the interferograms to collect h(x) data (Hariharan et al., 1987). The experimental data were then fitted to a 3rd polynominal equation and normalized, giving the corresponding h(η) data. The apparent work of adhesion was calculated using coefficients from the polynomial, as well as material property and geometric information about the cantilever beam. The detailed modeling and calculation will be discussed in Section 4.3.2.

4.3 Results and discussions

4.3.1 Characterizations of nanoparticles and fabricated MEMS test chips

Iron oxide nanoparticles synthesized by the co-precipitation method were characterized using TEM. The TEM images and corresponding size distribution are shown in Figure 4.5 (a). From TEM image analysis via the ImageJ software, it can be seen that the particles synthesized were faceted and polydispersed significantly in size. The iron oxide nanoparticles obtained had an average size distribution of 5.8 ± 3.7 nm. The polydispersity and faceted nature of the synthesized iron oxide nanoparticles derived from the lack of control over the nucleation and growth stages of nanoparticle growth in the coprecipitation method (Laurent et al., 2008).

Commercial iron oxide nanoparticles of average sizes of 5 nm, 10 nm and 20 nm were also characterized using TEM. The TEM images and corresponding size distribution are shown in Figure 4.5 (b)-(d). These images show that all the commercial samples had monodispersed,

spherical, iron oxide nanoparticles. The average size distribution of these particles using the ImageJ software analysis showed that the iron oxide nanoparticle samples had average size distributions of 5.2 ± 1.7 nm, 10.5 ± 1.8 nm and 18.8 ± 1.2 nm, respectively, which was well within the range desired.

(a)

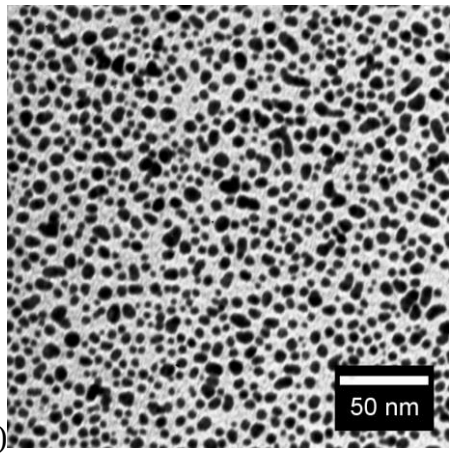

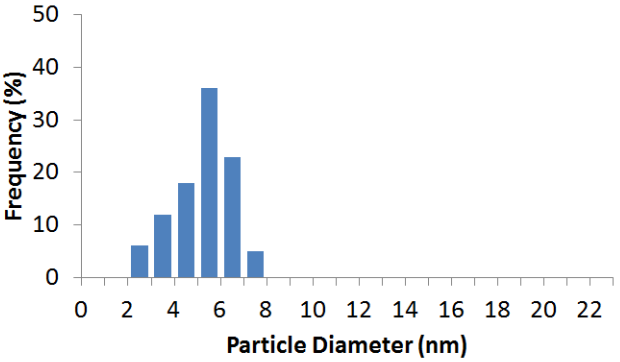

(b)

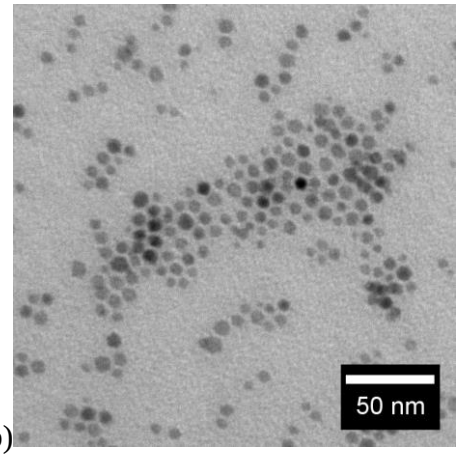

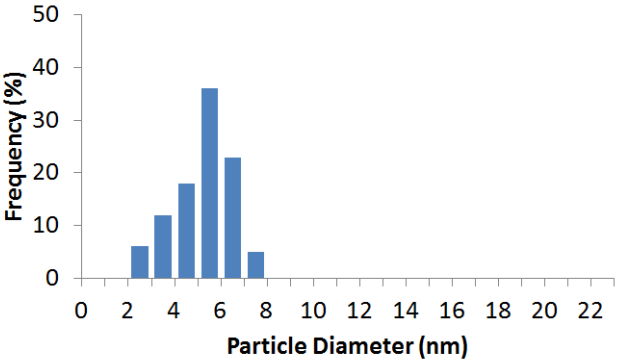

(c)

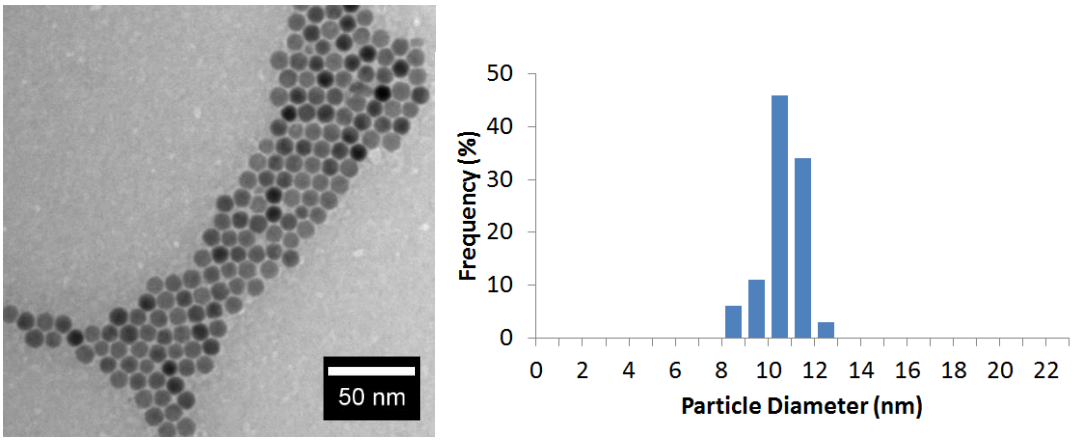

(d)

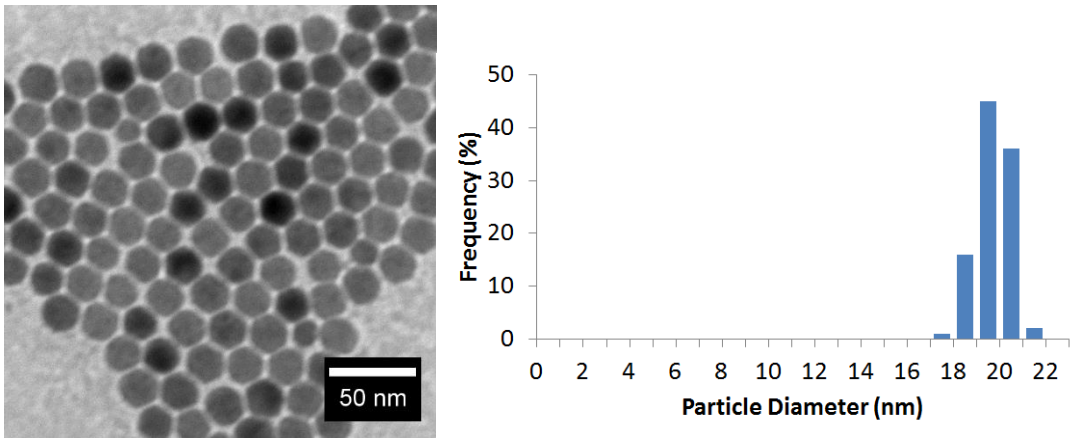

Figure 4.5. TEM images and size distribution of iron oxide nanoparticles: (a) synthesized polydispersed, (b) commercial monodispersed, 5 nm, (c) commercial monodispersed, 10 nm, and (d) commercial monodispersed, 20 nm.

After the fabricated chips were cleaned, released, and coated with various iron oxide nanoparticles, the microinstruments on the chip were checked first under the interferometer. Figure 4.6 shows a released cantilever beam array of the chip. It can be seen that the surface is clean. Only very few black bulk aggregates exist, which are wafer dust from the dicing process. The grey, scalloped shadow on the left side under the device layer is evidence that the HF

etching was sufficient to etch out the buried sacrificial oxide layer, but not so much that it caused any damage to the actual devices.

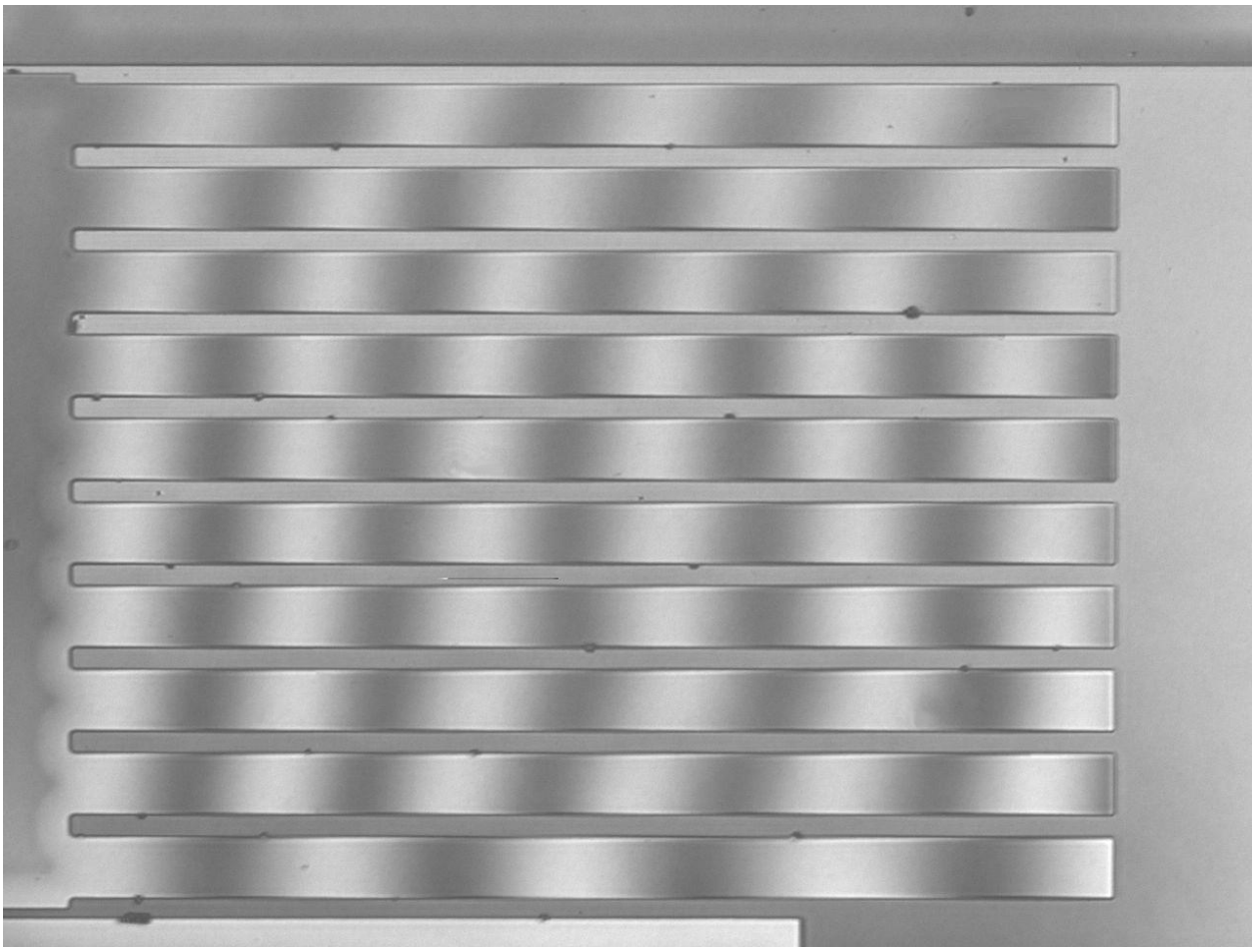

Figure 4.6. Interferogram showing a released cantilever beam array of the chip.

It should be noted that the presence of fringes on the cantilever beams shown in Figure 4.6 indicates clearly that they are not parallel to the substrate. The height profile of the cantilever beam was measured using interferometry, and is shown in Figure 4.7, which again, proves that the cantilever beams shown in Figure 4.6 are inclined upwards and slightly convex. This type of upward-inclined and curved height profile was observed in all the cantilever beams on the chip.

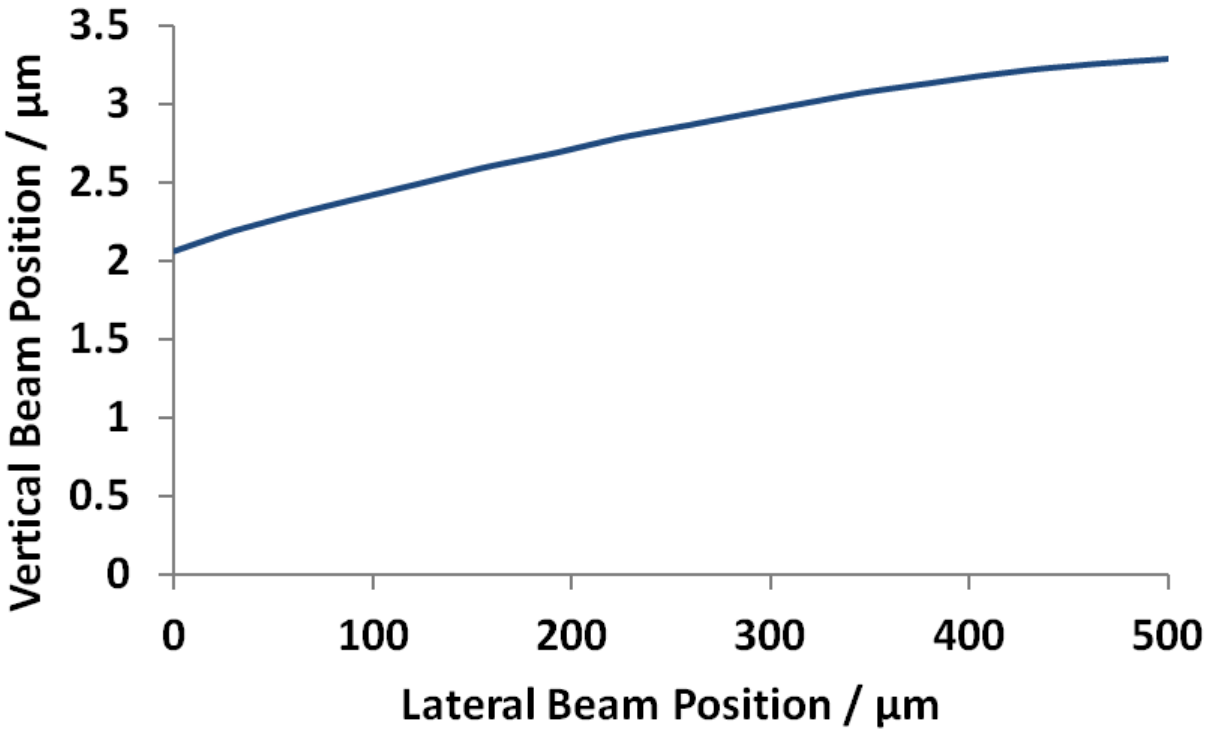

Figure 4.7. Height profile of the cantilever beam from Figure 4.6 obtained experimentally using phase shifting interferometry.

The upward inclination of the released cantilever beams on the chip developed in this study was a consequence of the stress-gradient present at the interface of the sacrificial oxide and device layers in their anchors. Their curved shape resulted from the internal moment induced in them by the stress gradient present in the device layer (Hoffman, 1981). The stress gradient that existed at the interface of the sacrificial oxide layer and device may have been induced by the high temperature cycling to which the fabricated chip was exposed when the scalloped sidewall test surfaces were polished. Therefore, to obtain an accurate estimate of the work of adhesion of the in-plane surfaces using the cantilever beams of the chip developed in this study, the effects

that the stress gradient present at the interface of the sacrificial oxide layer and device layer had on their initial (pre-actuated) height profiles had to be considered appropriately.

The upward inclination along the entire length of the cantilever beam range was approximately 1 μm, which is not a very large change compared to 500 μm, the length of the beam. However, as the cantilever beams were bent because of the additional height due to their upward inclination, they will store additional bending energy, as well as the work done to counter the resistance to bending of the stress gradient-induced internal moment present in them. Therefore, the additional work required to bring the tips of the upward-inclined cantilever beams in contact with the substrate must be included in the estimate of the work of adhesion of the in-plane surfaces. This will be discussed in the following section with the equations for the calculation of the apparent work of adhesion. The equation used in this study to estimate the apparent work of adhesion of the in-plane surfaces took into account the restoring energy required to counter the effects of the stress gradient.

4.3.2 Modeling of apparent work of adhesion from contacting beam surfaces

A typical MEMS switch is made of two conducting electrodes, one fixed, and the other movable. A voltage difference between the two electrodes causes the upper movable electrode to move downward to the ground electrode through electrostatic attraction. At a certain voltage, the movable electrode becomes unstable and pulls in onto the ground electrode, which decreases the distance between them. The reduced separation between the components requires MEMS designs to account for the intermolecular forces neglected when they are still far apart. For separations

less than 100 nm, the intermolecular force between two surfaces is simplified as the Van der Waals attraction, which is affected by material properties (Ramezani et al., 2008).

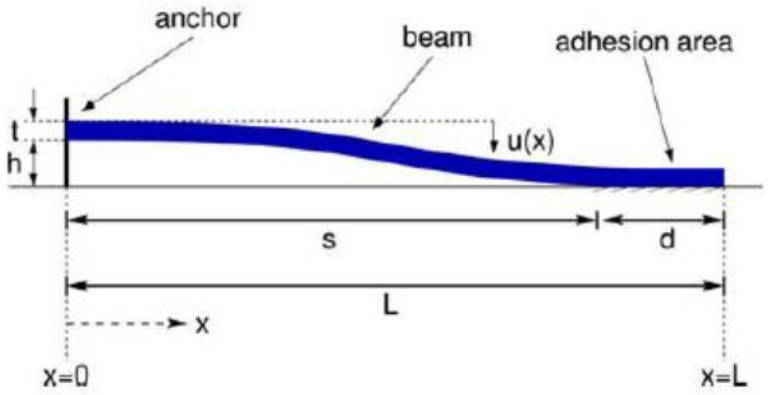

Figure 4.8. Illustration of cantilever beam adhered to the surface (Mastrangelo et al., 1992).

A typical cantilever beam in adhesion is shown in Figure 4.8. At a critical "pull-in" voltage, the cantilever beam becomes unstable and collapses or adheres to the ground plane spontaneously.

In the adhesion area, the total force applied per unit length is:

$$F_t = F_e + F_v \tag{4.1}$$

where F_t is the total force applied per unit length, F_e is the electrostatic force applied per unit length, and F_v is the Van der Waals force applied per unit length.

The electrostatic force of the beam F_e is:

$$F_e = \frac{\varepsilon_0 w d_b {V_A}^2}{2u^2}\left(1 + 0.65\frac{u}{w}\right) \tag{4.2}$$

The van der Waals force applied F_v is:

$$F_v = \frac{A w d_b}{6\pi u^3} \tag{4.3}$$

where V_A is the voltage applied, w is the width of the cantilever beam, u is the deflection of the beam between zero and the free-standing height, ε_0 is the permittivity of free space, d_b is the length of the beam interacted, and A is the Hamaker constant, either in a single pair or a combined relationship (Ramezani et al., 2008).

As explained in Section 4.2.6, the CBAs of the fabricated test platform developed in this study were brought into contact with the substrate manually by pushing them down using a sharp tungsten probe tip. No electrostatic force was introduced in the actuation and analysis procedure, and thus, a calculation method based on the force balance between elastic energy and adhesion energy should be developed. This test method first introduced by Mastrangelo as a theoretical method to measure the surface energy of micromachined cantilever beams by balancing mechanical forces (Mastrangelo et al., 1992). This measurement technique considers the equilibrium between the elastic energy in a deformed cantilever beam (U_E) and the interfacial surface energy that promotes adhesion (U_S), which yields the total mechanical energy balance:

$$U_T = U_E + U_S = \frac{E w t^3}{24}\int_0^s \left(\frac{d^2u}{dx^2}\right)^2 dx - \gamma w(L - s) \tag{4.4}$$

where E is the Young's modulus of the beam material, w and t are the beam width and thickness, respectively, L is beam length, s is the crack length, and u(x) is the deflection of the beam. The crack length, s, is defined as the distance between the beam anchor point and the point at which the beam comes into complete contact with the substrate.

Mastrangelo and Hsu developed the expression for u(x) (Mastrangelo et al., 1992) as follows:

$$u(x) = h_0 \left(\frac{x}{s}\right)^2 \left[\frac{(m-2)x}{s} + (3-m)\right] \tag{4.5}$$

where h_0 is the free standing height, and m is a non-dimensional number that describes the shape of a deflected beam, $0 < m < 3/2$.

At equilibrium:

$$\frac{dU_T}{ds} = 0 \tag{4.6}$$

Integrating Equation 4.4 into 4.5 and 4.6, the work of adhesion is determined as:

$$\gamma = \frac{3Et^3h_0^2}{2s^4}\left(1 - m + \frac{m^2}{3}\right) \tag{4.7}$$

The usefulness of this equation is limited, as m is not a fixed number and should be determined readily for any shape of the adhered beam. Therefore, an alternative mathematical method for u(x) should be derived.

Kendall developed an alternative mathematical expression by introducing the variation of the function u(x). It begins similarly to that of Mastrangelo and Hsu's in its total system energy equilibrium approach:

$$\gamma = \frac{Et^3}{24}\frac{d}{ds}\int_0^s \left(\frac{d^2u}{dx^2}\right)^2 dx \tag{4.8}$$

Because the shape of a cantilever beam is dependent on the value of s, the beam deflection function, u(x,s), is a function of both the lateral position, x, and crack length, s. The Leibniz integral rule is used to evaluate the derivative of u(x,s):

$$\frac{d}{ds}\int_{a(s)}^{b(s)} u(x,s)dx = \int_{a(s)}^{b(s)} \frac{\partial}{\partial s}u(x,s)dx + \frac{db(s)}{ds}u(x,s)|_{b(s)} - \frac{da(s)}{ds}u(x,s)|_{a(s)} \tag{4.9}$$

The height profile data collected using interferometry include the lateral beam position, x, and the vertical beam position, h(x). As the beam deflection function, $u(x) = h_0 - h(x)$, where h_0 is the free standing beam height, it is clear that:

$$\left(\frac{d^2u}{dx^2}\right)^2 = \left(\frac{d^2h}{dx^2}\right)^2 \tag{4.10}$$

The height profile data for the deflection expression can be collected directly from the interferometry profiles. A normalized, 3rd-order polynomial fit on h(s,x) was performed and yielded a function of the form:

$$h(\eta) = a_3\eta^3 + a_2\eta^2 + a_1\eta + a_0 \tag{4.11}$$

where η is a normalized dimensionless number:

$$\eta = \frac{x}{s}, 0 < \eta < 1$$

Combining 4.8, 4.9, 4.10, and 4.11, the apparent work of adhesion can be expressed as:

$$\gamma = \frac{3Et^3}{2s^4}\left(a_3^2 + a_2a_3 + \frac{1}{3}a_2^2\right) \tag{4.12}$$

This equation can be used directly to determine the apparent work of adhesion or surface energy for any adhered cantilever beam, regardless of its shape, as long as the coefficients a_3 and a_2 can be determined from experimental data that are scaled appropriately.

The large surface-to-volume ratio of MEMS devices requires consideration of various force sources in device performance. Most MEMS tests are conducted in air at a relative humidity (RH) of approximately 30%, a typical ambient RH. It has been observed that there is no significant effect of RH on adhesion test results up to 80% RH for surface-treated MEMS devices (de Boer et al., 2000). Scanning probe studies between a hydrophilic and hydrophobic

surface also have shown that the adhesion pull-off force is not dependent on RH for a hydrophobic surface (Xiao et al., 2000). Therefore, capillary condensation, which dominates the adhesion of hydrophilic surfaces, such as uncoated Si (100) surfaces, did not play a major role in our experiments. The actuation of the cantilever beam is based on a mechanical process, which indicates that electrostatic forces in the contact zone should be insignificant. van der Waals forces, however, had to be considered in the analysis of our results. In a nanoscale regime, the van der Waals contribution across contacting and non-contacting areas requires even more attention. The adhesion derives from the van der Waals interactions, which are contributed by interactions between contacting asperities and non-contacting van der Waals attractions. According to previous reports (DelRio et al., 2005), the fraction of the contribution to adhesion from these two sources will differ at different separation distances.

One of the adhesion sources is the van der Waals force from the non-contacting portion of the surfaces. The adhesion energy per area in this case follows the equation:

$$\gamma_{nc} = \frac{A g_e(D)}{12\pi}\left[\frac{1}{D^2} + \frac{1}{(D+h_1+h_2)^2} - \frac{1}{(D+h_1)^2} - \frac{1}{(D+h_2)^2}\right] \qquad (4.13)$$

where D is the mean separation distance between two rough surfaces, h_1 and h_2 are the thicknesses of the coated nanostructure films, and A is the Hamaker constant. $g_e(D)$ is a correction function based on separation distance that describes the retardation of van der Waals force (Anandarajah et al., 1995).

$$g_e(D) = 1 - \frac{4D}{p} - \frac{18D^2}{p^2} - \frac{12D^3}{p^3} + \frac{12D^2}{p^4}(D+p)^2 \ln\left(1+\frac{p}{D}\right) \qquad (4.14)$$

p is a constant which equals to $3\lambda_0/2\pi$, where λ_0 is defined as the London characteristic wavelength, often assumed to be approximately 100 nm. It is obvious that $g_e(D)$ approaches unity when D becomes very small, which indicates the non-retarded van der Waals interaction.

When the surfaces are rough and the non-contacting area of the surface is relatively distant, the van der Waals force from the dispersed contacting point now contributes more. In this case, the adhesion contribution can be expressed as follows:

$$\gamma_c = n\left[\frac{AR_1R_2}{6(R_1+R_2)d_{co}}\right] \tag{4.15}$$

where n is the average summit density in contact, A is the Hamaker constant, R_1 and R_2 are the curvature radii of the contacting asperities on both surfaces, and d_{co} is the cutoff separation with a typical value of 0.2 nm.

The total adhesion energy derives from van der Waals energy both from the area in contact and that not in contact. The non-contacting area, γ_{nc}, is affected primarily by the mean plane separation distance between two surfaces and decreases rapidly with increasing separation. The area in contact, γ_c, is affected more by the real contact area and the density of the contacting species. Therefore, when two different contacts occur, as in Fig 4.3, the contribution from the non-contacting and contacting parts can be calculated. By using experimental data, the contribution of the non-contacting part can be estimated and removed from the total adhesion energy, leaving only the contribution of the part in contact. Then, a fair comparison can be made

between these “corrected” adhesion energies based on the real surface contact area and surface asperity density.

4.3.3 Tribological effect of coatings based on size-varied nanoparticles

A systematic study of the morphological effect of varying the size of nanoparticles deposited on Si (100) wafers was conducted in Chapter 3. The morphology changes induced by the size of nanoparticles emphasized the importance of the size of the nanoparticles involved in film deposition and demonstrated the possibility of achieving better control of the films formed. Therefore, in this section, the size effect of nanoparticles on tribology was studied by depositing size-varied iron oxide nanoparticles on the Si (100) SOI wafers. As discussed previously, these new single crystalline devices are extremely smooth (ca. 0.2 nm). Therefore, it was postulated that nanoparticles should affect the device tribology by increasing the surface mean plane separation and reducing the real area of contact.

For reference, one uncoated, clean Si (100) SOI chip was tested just after releasing and surface oxidation, and the apparent work of adhesion was measured. The interferogram of the actuated cantilever beams on the uncoated, clean Si (100) SOI chip is shown in Figure 4.9. The AFM image and line profile of the scanned AFM image are shown in Figure 4.10. It is clear that the surface is very clean, with an rms surface roughness of only 0.2 nm. After the cantilever beam was actuated, the height profile of the actuated beam was obtained experimentally using phase shifting interferometry, and is shown in Figure 4.11. Most of the cantilever beam is stuck to the substrate and the crack length of the cantilever beam was measured to be 130 ± 15 μm.

This is very short, indicating an extremely high apparent work of adhesion. The apparent work of adhesion measured using the interferograms was 38520 ± 5300 $\mu J/m^2$, which is very close to the value reported (Ashurst et al., 2001a). This again proved that the release and actuation of the microinstruments was reliable and can be used as a good reference sample.

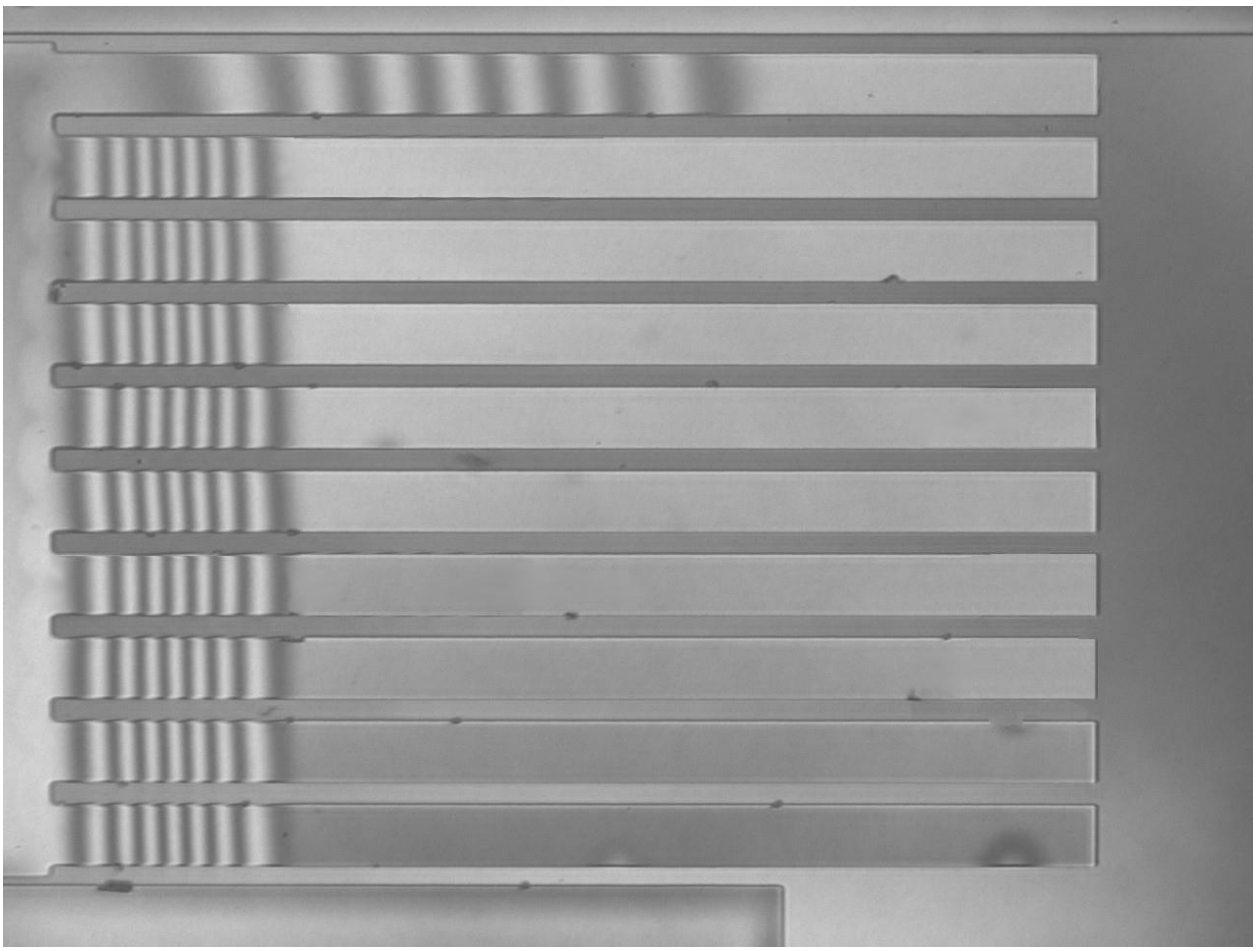

Figure 4.9. Interferogram showing an actuated cantilever beam array of the uncoated chip.

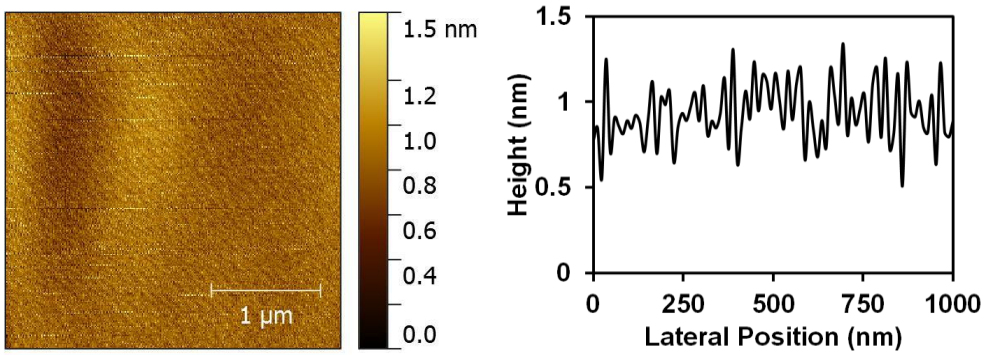

Figure 4.10. AFM scan and line profile of uncoated Si (100) SOI chip surface.

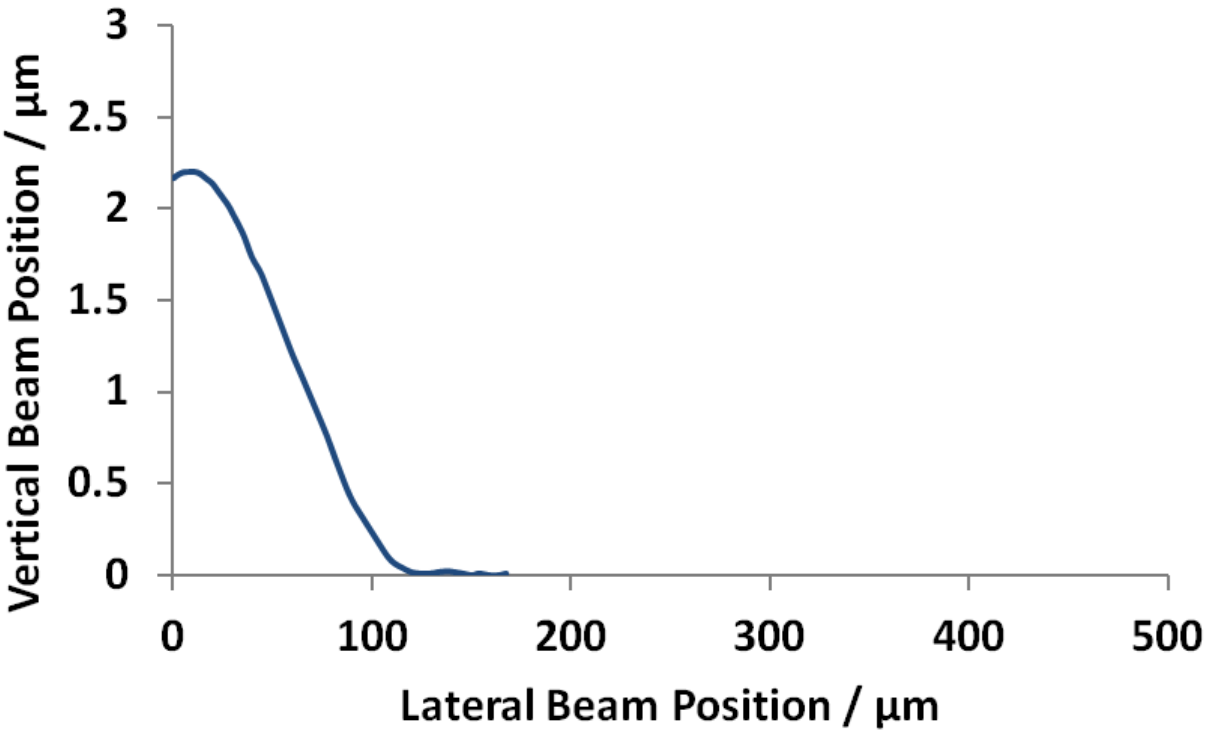

Figure 4.11. Height profile of the cantilever beam of uncoated Si (100) SOI chip surface after actuation obtained experimentally using phase shifting interferometry.

Next, iron oxide nanoparticles of different sizes were deposited on the released chip. Various iron oxide nanoparticles were used for the surface coatings, including polydispersed, and commercial monodispersed iron oxide nanoparticles of average sizes of 5 nm, 10 nm, and 20 nm. As an example, the interferogram of the actuated cantilever beam array on the chip coated by polydispersed iron oxide nanoparticles is shown in Figure 4.12. Now, the crack length is significantly longer than that of the uncoated chip, resulting in a lower apparent work of adhesion. All the actuated cantilever beams except the top one show cracks of similar lengths, which is probably due to the potential large particulates beneath the beam near the crack region, which prevented the beam from making contact and sticking. It is also worth noting that the surface is still relatively clean, without too many visible particle aggregates. This indicates that the concentration of the initial iron oxide nanoparticle solution was controlled well.

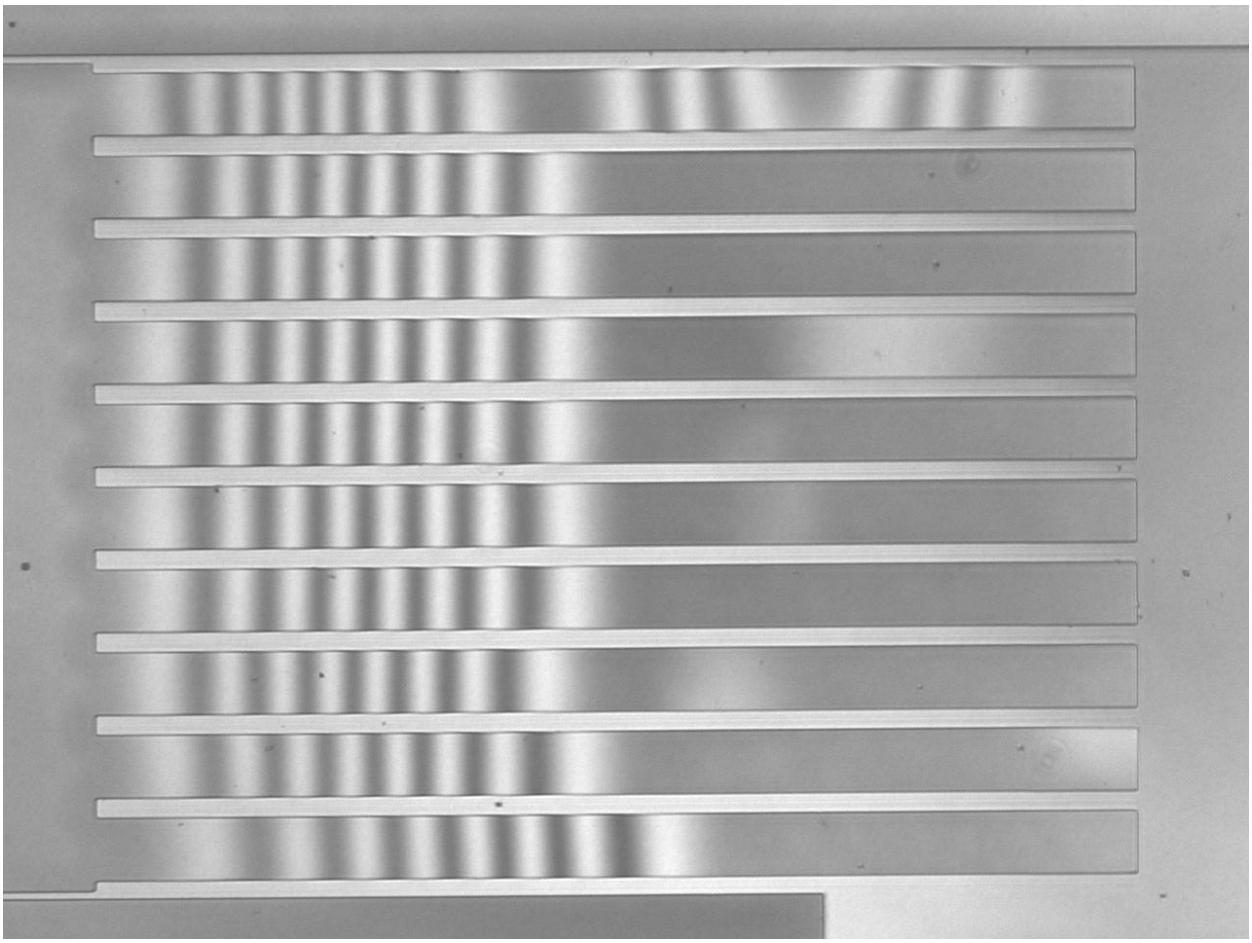

Figure 4.12. Interferogram showing an actuated cantilever beam array of the chip coated with polydispersed iron oxide nanoparticles.

The AFM scan, corresponding line profile and height profile of the cantilever beam after actuation from interferometry of chips coated with various iron oxide nanoparticles are shown in Figures 4.13 to 4.20. To coat iron oxide nanoparticles of 20 nm, the coating at a very low concentration is shown here. The concentration effect will be discussed later.

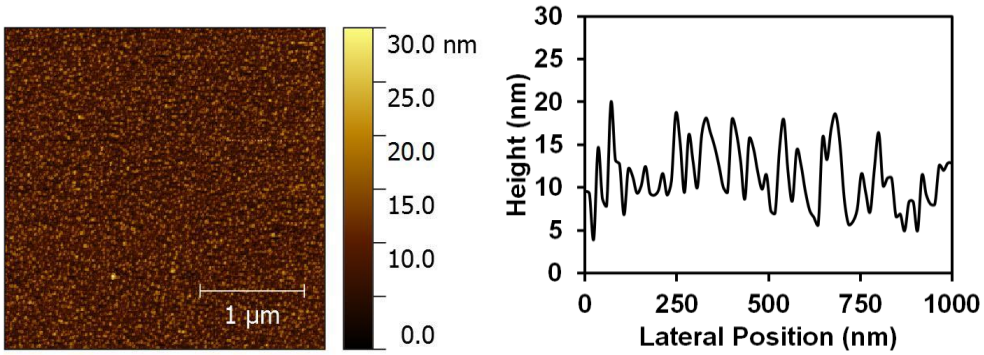

Figure 4.13. AFM scan and line profile of polydispersed iron oxide nanoparticle-coated chip surface.

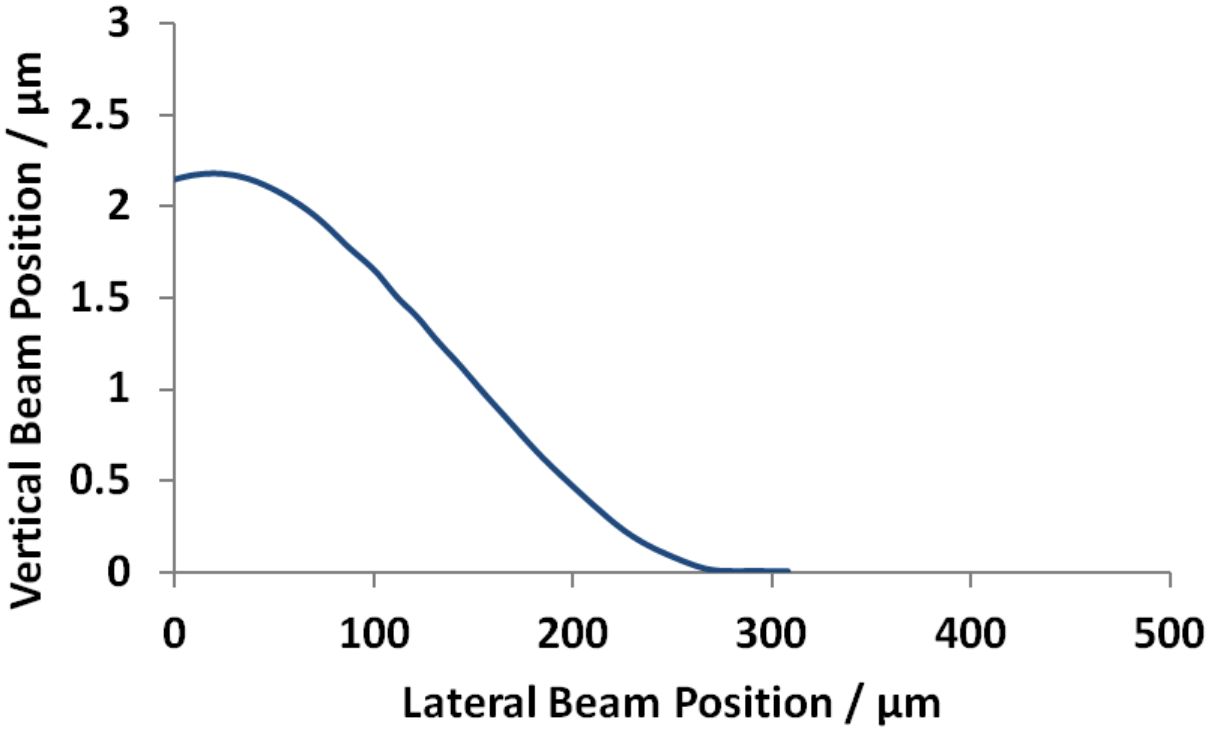

Figure 4.14. Height profile of the cantilever beam of a polydispersed iron oxide nanoparticle-coated chip surface after actuation obtained experimentally using phase shifting interferometry.

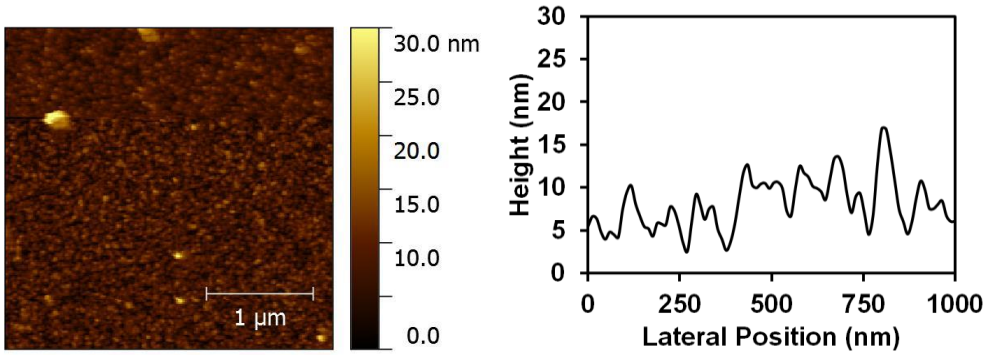

Figure 4.15. AFM scan and line profile of 5 nm monodispersed iron oxide nanoparticle-coated chip surface.

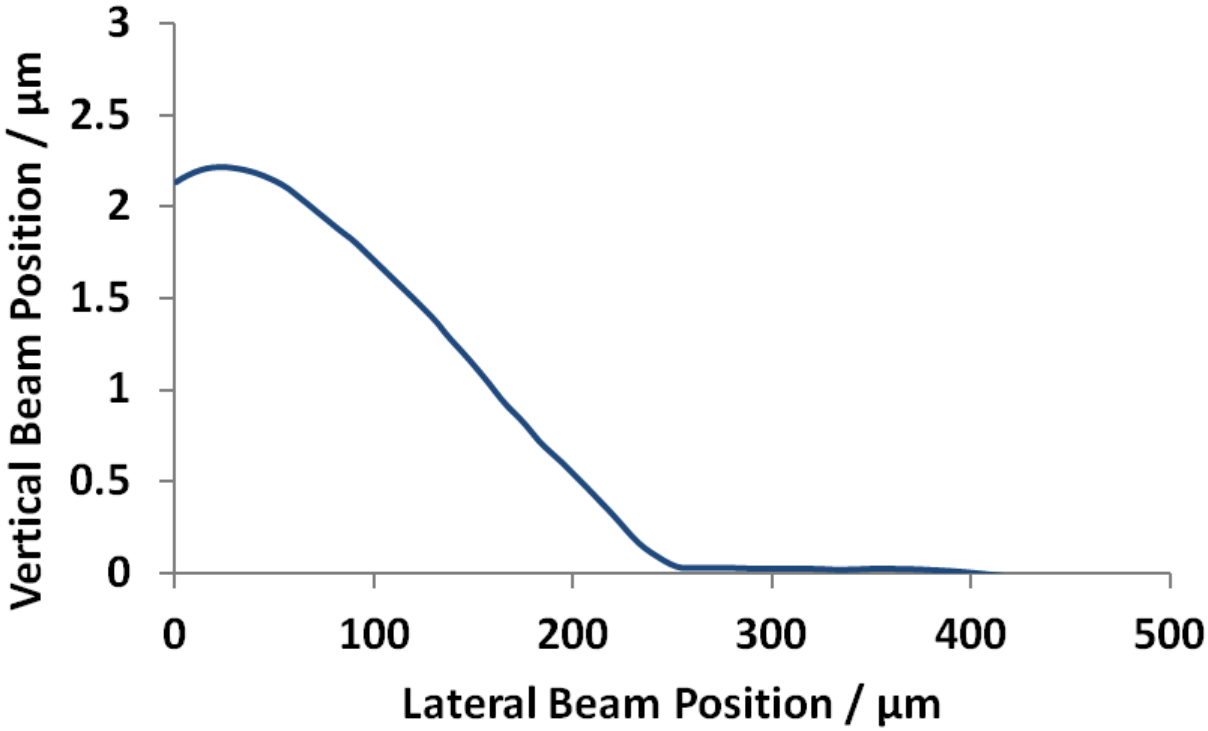

Figure 4.16. Height profile of the cantilever beam of 5 nm monodispersed iron oxide nanoparticle-coated chip surface after actuation obtained experimentally using phase shifting interferometry.

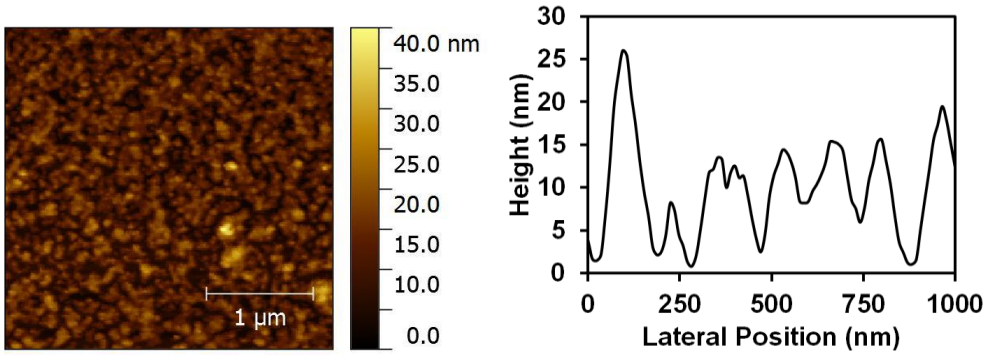

Figure 4.17. AFM scan and line profile of 10 nm monodispersed iron oxide nanoparticle-coated chip surface.

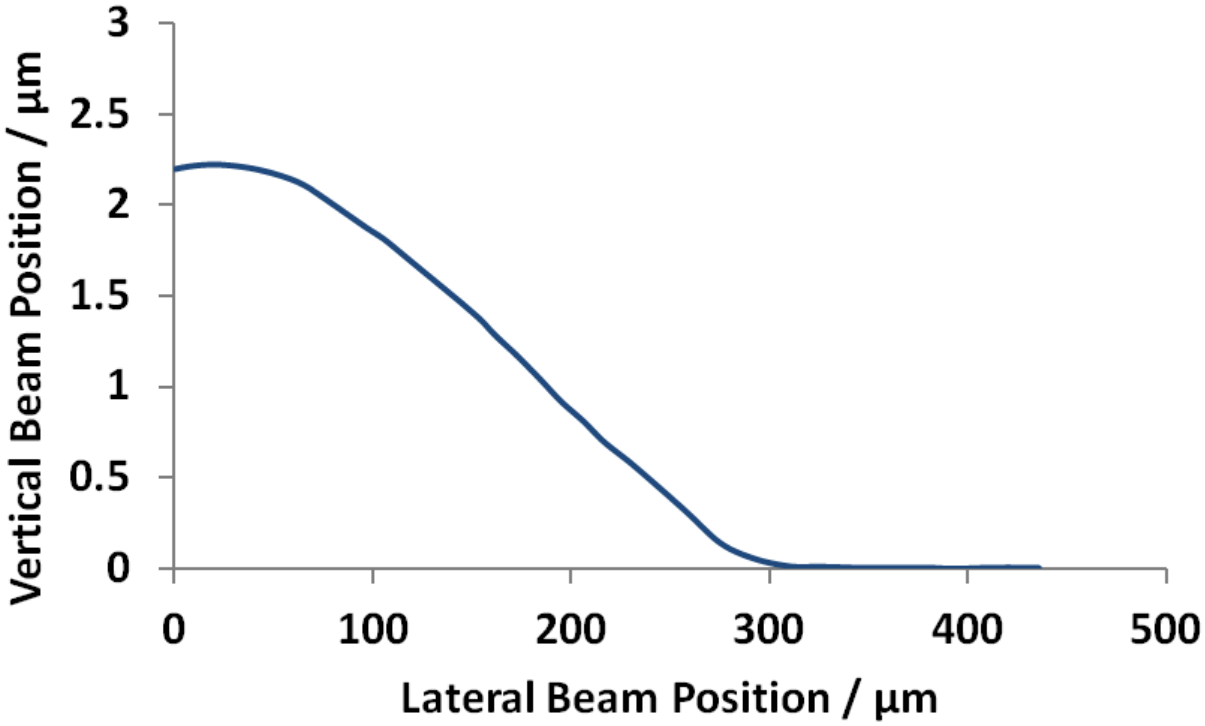

Figure 4.18. Height profile of the cantilever beam of 10 nm monodispersed iron oxide nanoparticle-coated chip surface after actuation obtained experimentally using phase shifting interferometry.

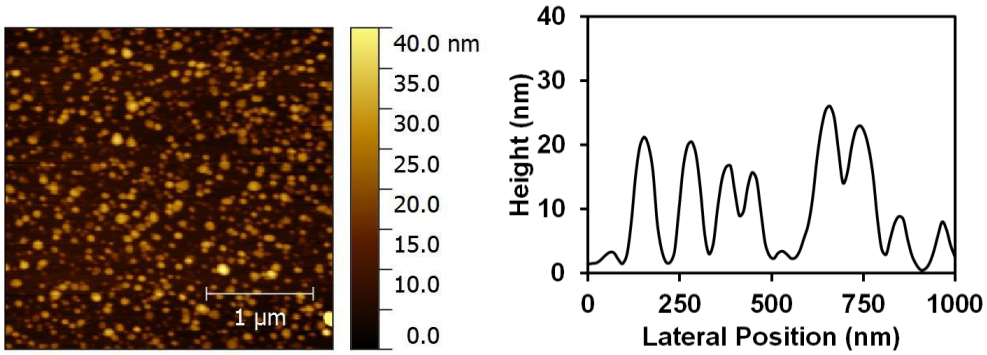

Figure 4.19. AFM scan and line profile of 20 nm monodispersed iron oxide nanoparticle-coated chip surface at very low initial concentration.

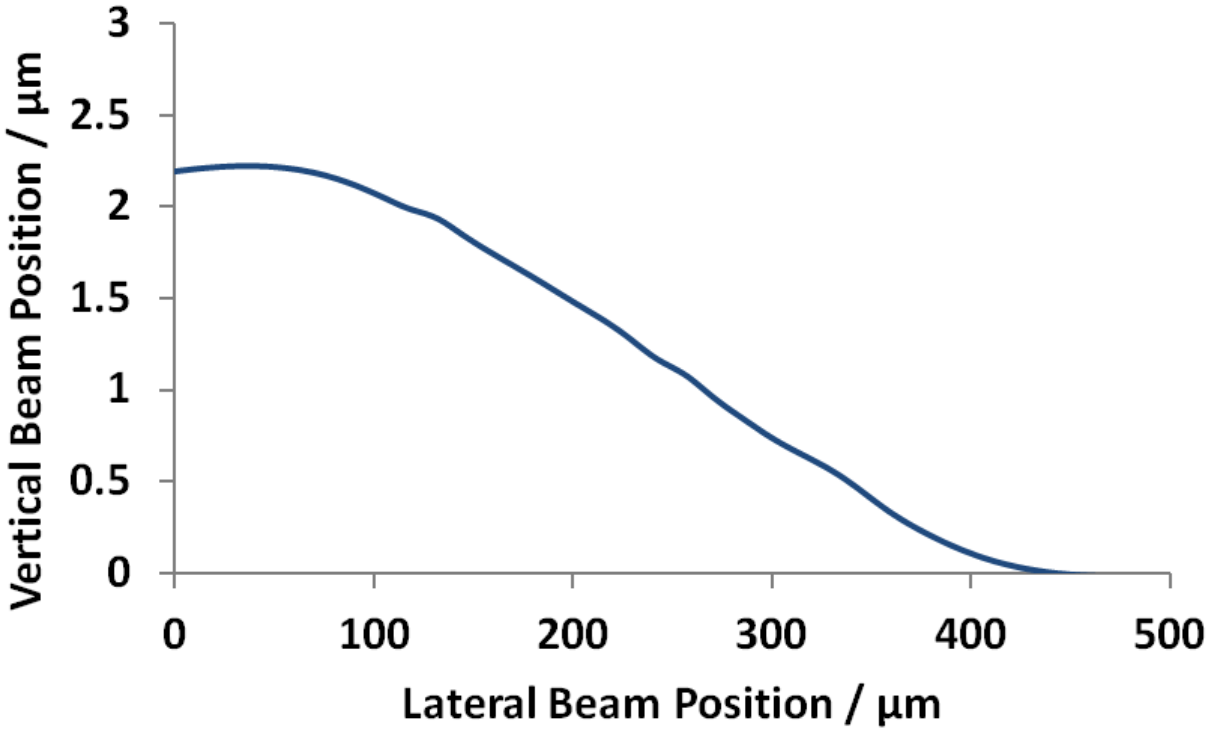

Figure 4.20. Height profile of the cantilever beam of 20 nm monodispersed iron oxide nanoparticle-coated chip surface at very low initial concentration after actuation obtained experimentally using phase shifting interferometry.

	rms surface roughness (nm)	Average crack length (μm)	Apparent work of adhesion (μJ/m^2)
Uncoated Si (100)	0.20 ± 0.04	130 ± 15	32520 ± 5300
Poly	3.42 ± 0.21	278 ± 23	1962 ± 127.5
Mono 5nm	2.83 ± 0.23	258 ± 27	1483 ± 296.9
Mono 10nm	4.82 ± 0.35	314 ± 36	788.3 ± 92.1
Mono 20nm Very Low	6.24 ± 0.51	432 ± 28	369.4 ± 77.2

Table 4.1. Rms surface roughness, average crack lengths, and the calculated apparent work of adhesion values obtained from size-varied iron oxide nanoparticle-coated cantilever beam arrays.

As discussed previously, nanoparticle films are sufficient to reduce this adhesion significantly by providing rough, low energy asperities. The typical apparent work of adhesion between uncoated Si (100) cantilever beams and the underlying substrates was approximately 37000 μJ/m^2 (Ashurst et al., 2001a). In Figures 4.13 to 4.20, the shortest adhered crack length among all the actuated cantilever beam arrays was approximately 250 μm, twice the crack length of the actuated, uncoated Si (100) cantilever beam. In their initial state, the Si (100) beams bent upwards slightly because of residual stress. However, this residual stress did not affect the actuation and analysis of the beam adhesion.

The rms surface roughness, average crack lengths, and the calculated apparent work of adhesion values after analyzing the cantilever beam arrays coated with sized-varied iron oxide nanoparticles are summarized in Table 4.1. The highest apparent work of adhesion derived from the cantilever beams coated with polydispersed iron oxide nanoparticles, the value of which was approximately 2000 $\mu J/m^2$. This value is 95% less than that of an actuated, uncoated Si (100) cantilever beam, suggesting that the nanoparticle coating reduced the adhesion between the cantilever beams and the substrate effectively. The lowest apparent work of adhesion was found in the cantilever beams coated with monodispersed 20 nm iron oxide nanoparticles at very low concentration, which reduced the adhesion by 99.5%. While this value was still higher than the apparent work of adhesion reported generally for polysilicon devices (Hurst et al., 2009), it is important to note that the lab-fabricated Si (100) in-plane surfaces are inherently smoother than are common polysilicon surfaces and, therefore, exhibit much higher adhesion energies.

The reduction in adhesion was related significantly to the topography of the coated surfaces, which was affected by the size of the nanoparticles. Figures 4.13 to 4.20 show topographic AFM images of chips coated with various iron oxide nanoparticles. Dark/bright areas correspond to low/high regions. It can be seen from all AFM images that the surface consists of grains of nanoparticles. Grain boundaries can be seen clearly and show that the grains ranged in size typically from 10 nm to 50 nm laterally, with sphere-like boundaries. The polydispersed nanoparticle-coated chip exhibited smaller grain boundaries, as expected, because of the existence and precipitation of smaller nanoparticles in the initial coating solution. The monodispersed nanoparticle-coated chips showed more distinct particle asperities on the surface, and similar results were demonstrated in Chapter 3. This result again proved that control of the nanoparticle size distribution and the average size affects the final morphology.

The height range of the topography was approximately 30 nm to 40 nm for all the coated chips. To characterize this more generally, the rms surface roughness was measured for all surfaces and is summarized in Table 4.1. One can see that the rms roughness values increased as the size of the monodispersed iron oxide nanoparticles increased, indicating the roughening effect of the larger size nanoparticles during the GXL process. However, it should be noted that the rms surface roughness value of a polydispersed nanoparticle-coated surface lay between the values of the surfaces coated with 5 and 10 nm monodispersed nanoparticles. There was no clear trend in the rms surface roughness that corresponded to the size of the nanoparticles here. Therefore, rms surface roughness is still a useful general surface parameter, although other parameters should be used for the adhesion analysis based on topography.

Rms surface roughness is a long-range parameter characteristic of surface roughness. However, when the rough surfaces are brought into contact, the highest structures obviously will be the ones that come into contact first with the counter surface, and friction, stiction, and wear will occur. Lower asperities eventually may come into contact if the surfaces are reduced further. Therefore, the rms roughness value takes into account all of the asperities at various height, while the surface adhesion may not be affected by all of them directly. From the AFM images, it can be concluded that asperities of various sizes were distributed randomly on the entire surface, and all of the surface had relatively non-distinguishable surface roughness structures at different scales.

Average crack lengths and the calculated apparent work of adhesion values are summarized in Table 4.1. Now, the trend shows that, as the average size of the nanoparticles increases, the apparent work of adhesion decreased. For the polydispersed iron oxide

nanoparticles, even the coated surface had a higher surface roughness, and still possessed the highest apparent work of adhesion among all the coated chips. Therefore, calculation based on Chapter 2 was introduced to all the surfaces here and the corresponding results are summarized in Table 4.2.

There are some clear trends here among surfaces coated with nanoparticles of different sizes. The deposition of polydispersed nanoparticles produced a rougher surface, which resulted in more summits per unit area. This was likely because of the smaller size of the particle asperities. The summit density decreased as the size of the nanoparticles increased. The average summit radius of this surface was the smallest compared to other particle-roughened surfaces. The average summit radius increased as the size of the nanoparticles increased as well. These values were averages of all summits, and were similar to the size of the visible particle asperities on the surface. The roughened surfaces also showed an ascending trend in the standard deviation in summit heights. This was confirmed by the average height of the AFM scans, or the height scale of the AFM images and the color contours. All of the results shown above indicated that the calculation for these coatings was a good estimation for realistic surfaces.

	Poly	Mono 5nm	Mono 10nm	Very Low
Average summit density (/μm^2)	296.9 ± 32.3	207.7 ± 24.9	89.2 ± 9.0	55.7 ± 5.3
Average summit radius (x10^{-3} μm)	42.1 ± 3.3	50.9 ± 3.5	80.1 ± 6.2	83.2 ± 5.1
σ_s, standard deviation of summit height distribution (x10^{-3} μm)	3.04 ± 0.42	3.51 ± 0.24	3.99 ± 0.53	5.30 ± 0.74
Average number of summits in contact (/μm^2)	47.1 ± 5.1	39.3 ± 4.0	14.1 ± 1.4	8.84 ± 0.84
Ratio of true to apparent contact area (%)	1.01 ± 0.19	0.87 ± 0.16	0.74 ± 0.14	0.64 ± 0.12
α, bandwidth parameter	4.42 ± 0.55	3.58 ± 0.44	2.86 ± 0.35	2.35 ± 0.28
m_0 (x10^{-6} μm^2)	11.7 ± 0.7	8.1 ± 0.6	23.2 ± 1.6	45.4 ± 3.4
m_2 (x10^{-3})	25.6 ± 1.8	18.1 ± 1.4	23.7 ± 1.9	35.0 ± 2.5
m_4 (/μm^2)	248.3 ± 19.7	146.4 ± 9.5	68.9 ± 5.4	63.7 ± 4.0

Table 4.2. Surface parameters calculated for coatings of size-varied iron oxide nanoparticles.

Significant contrast among the surfaces coated by iron oxide nanoparticles of different sizes can be analyzed now. From the perspective of the long-range roughness parameters, the size variation produced rougher surfaces, yet there were slightly fewer summits per unit area. This was likely because of the increased size of the grain boundaries. The average summit radius increased by a factor of 3 for the roughened surfaces. The ratio of true to apparent contact area was affected by the combination of summit density, the standard deviation in summit heights,

and the average summit radius. The standard deviation in summit heights also increased as the size of the iron oxide nanoparticles increased. In combination with the smaller summit density, this produced a descending trend in the average summit density in contact. The ratio of true to apparent contact area was small for all the surfaces, which is a typical and important result for rough surfaces. As expected, the apparent work of adhesion decreased as the ratio of true to apparent contact area decreased.

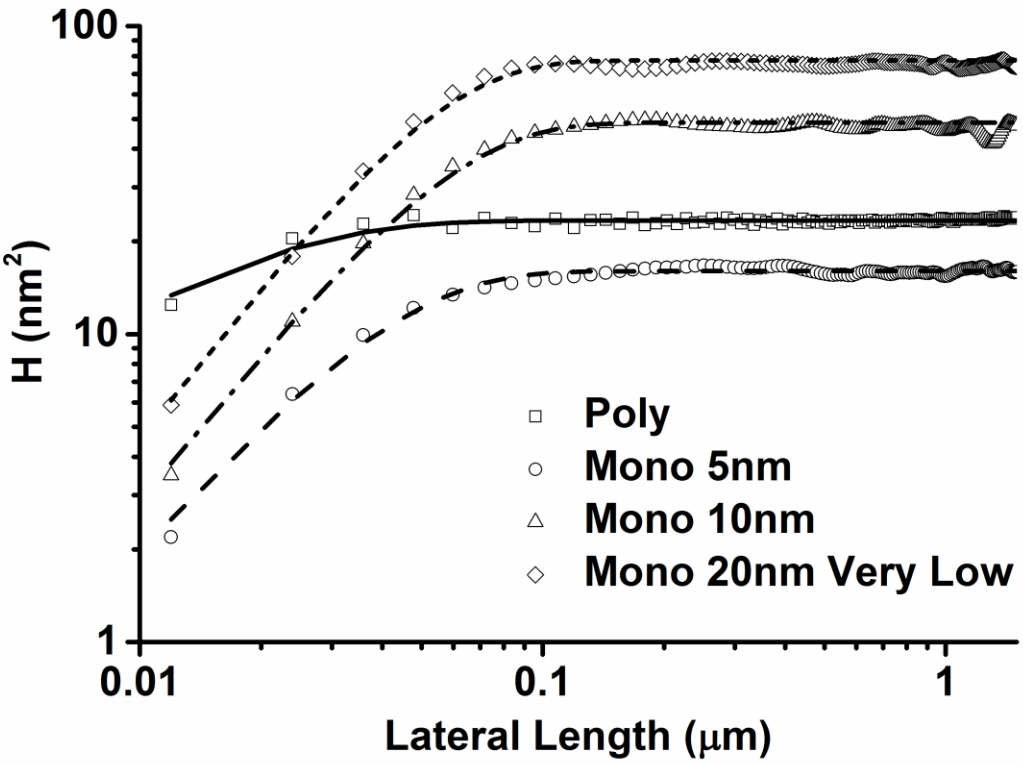

Figure 4.21. Experimental HHCF data for coatings of size-varied iron oxide nanoparticles. Lines are corresponding HHCF curves calculated using proposed HHCF model fitting.

The experimental HHCF curves from AFM data and corresponding HHCF curves by model fitting are plotted in Figure 4.21. The fitting curves and the experimental data matched well, which indicated that the surfaces obtained can be quantified using parameters from the HHCF analysis. The rms roughness, autocorrelation lengths, and roughness component values from the HHCF model are summarized in Table 4.3. All values here were calculated based on the previous HHCF analysis.

Size of NPs (nm)	rms roughness (nm)	Autocorrelation length (nm)	Roughness exponent
Poly	3.42 ± 0.21	14.5 ± 1.5	0.485 ± 0.039
Mono 5	2.83 ± 0.23	39.1 ± 2.7	0.747 ± 0.042
Mono 10	4.82 ± 0.35	54.8 ± 4.4	0.822 ± 0.048
Mono 20 Very Low	6.24 ± 0.51	50.8 ± 4.3	0.843 ± 0.056

Table 4.3. Surface parameters calculated from the HHCF model for coatings of size-varied iron oxide nanoparticles.

As discussed in Chapter 3, the autocorrelation length can be used to determine the spatial variation in the lateral direction. A higher T value indicates that the surface height variations are correlated within this length range. From Figure 4.21, it can be seen that film formed by polydispersed nanoparticles had the lowest autocorrelation length, which occurred because the small-sized particles on the top precipitated from the gas-expanded liquid under high pressure.

As the size of the iron oxide nanoparticles increased, the autocorrelation length and the roughness exponent increased. The autocorrelation length can be interpreted as the average grain size of the particle aggregates on the surface. This result indicated that the original particle size did affect the final particulate size on the surface, which derived from the particle-particle interactions during the GXL process. The values of the roughness component also showed an increasing trend. The higher roughness exponent reflects the lower local surface asperities, which are associated with smoother, short-range surface topography.

The size effect on the nanoparticle film formation was evaluated in Chapter 3. The film formation mechanism is determined thermodynamically by the experimental conditions. The critical surface tension of oleic acid, the ligand on the iron oxide nanoparticles, is 32.5 dyn/cm (Chumpitaz et al., 1999). This value is higher than that of the gold nanoparticles used previously. However, compared to the SAM-coated Si substrate used in Chapter 3, the MEMS device was coated with a native SiO_2 layer, the surface tension of which was approximately 140 dyn/cm. The surface energy of the substrate was much higher than that of the iron oxide nanoparticles, and therefore, the film formation here followed the layer-by-layer mode of growth, or the Frank-van der Merwe growth mechanism. Through this mechanism, because of the high surface energy of the native SiO_2 substrate, monolayers of particles formed layer-by-layer, the completeness of which was limited by the total number of particles available. Based on the experiments with gold nanoparticle coatings, it was concluded that the concentration of the initial nanoparticle solution should not be too high; otherwise, nanoparticle aggregation becomes dominant, which results in larger asperities. Larger structural shapes will affect the quantitative analysis of the surface, and the short-range details may not be visible. Therefore, the concentration of the initial coating

solution was controlled well in this chapter for the size effects of the nanoparticles to ensure that relatively smooth layers of nanoparticles were achieved.

Nanoparticles	Size of NPs (nm)	Average summit radius (nm)	Autocorrelation length (nm)
Poly	5.3 ± 3.7	42.1 ± 3.3	14.5 ± 1.5
Mono 5	5.2 ± 1.7	50.9 ± 3.5	39.1 ± 2.7
Mono 10	10.5 ± 1.8	80.1 ± 6.2	54.8 ± 4.4
Mono 20 Very Low	18.8 ± 1.2	83.2 ± 5.1	50.8 ± 4.3

Table 4.4. The original average size of iron oxide nanoparticles, the average summit radius, and the autocorrelation length values for coatings of size-varied iron oxide nanoparticles.

For the film deposited by nanoparticles of different sizes, the final morphology is affected by the competition between the particle-particle attraction and particle-surface attraction. As the nanoparticle size increases, the particle-particle attraction becomes more significant than the particle-surface attraction, which results in a morphology that consists of particle grains, the scale of which is affected by the size of the nanoparticles. Similar results were obtained here for films formed by iron oxide nanoparticles. The original average size of the iron oxide nanoparticles, the average summit radius, and the autocorrelation length values of various nanoparticle coatings are summarized in Table 4.4. There was a clear increasing trend in the average summit radius and the autocorrelation lengths as the original average size of the iron oxide nanoparticles increased. Values of the average summit radius typically are higher than are

those of the autocorrelation lengths. This is because the average summit radius is calculated based on the curvature of the surface asperities, while the autocorrelation length is analyzed directly in the 2-dimensional plane. Therefore, the radius will be higher than the apparent grain size because of the varied curvature of the asperities. It is worth noting that these quantitative parameters did not increase linearly with the original average particle size, but reached a maximum at approximately 80 nm and 50 nm for the average summit radius and autocorrelation length, respectively. This indicated that there is a size limit for the particle-particle interaction before the system becomes unstable. The size limit can be affected by two conditions in the process: the threshold nanoparticle size under different applied CO_2 pressures and the size of particle aggregates due to the non-retarded van der Waals attractive force between dispersed nanoparticles. When the size of the initial iron oxide nanoparticles is relatively small, the van der Waals attractive force between dispersed nanoparticles is weak, and the particle aggregates will remain dispersed in the GXL solution until the threshold precipitation size limit is reached. On the other hand, if the size of the initial iron oxide nanoparticles is large, the van der Waals attractive force between particles is strong enough to form larger aggregates, the size of which reaches the threshold precipitation size limit under lower CO_2 pressure and accelerates the GXL-based precipitation process.

It is known well that van der Waals forces cannot be eliminated and have a fundamental effect on the adhesion between MEMS surfaces. These forces can be reduced by several orders of magnitude because of microscale surface roughness, which is a consequence of the morphology of the structural materials deposited and processed subsequently. Several existing models of rough surface adhesion assume that only areas in direct contact contribute to adhesion because they deal normally with microscale roughness. However, surfaces that normally exhibit

nanoscale roughness usually have non-contacting portions of the interface that are separated by less than 100 nm. Within this separation range, one must consider the relevance of retarded van der Waals force. Calculations have been made regarding the relative role of normal and retarded van der Waals forces at adhered MEMS interfaces (DelRio et al., 2005).

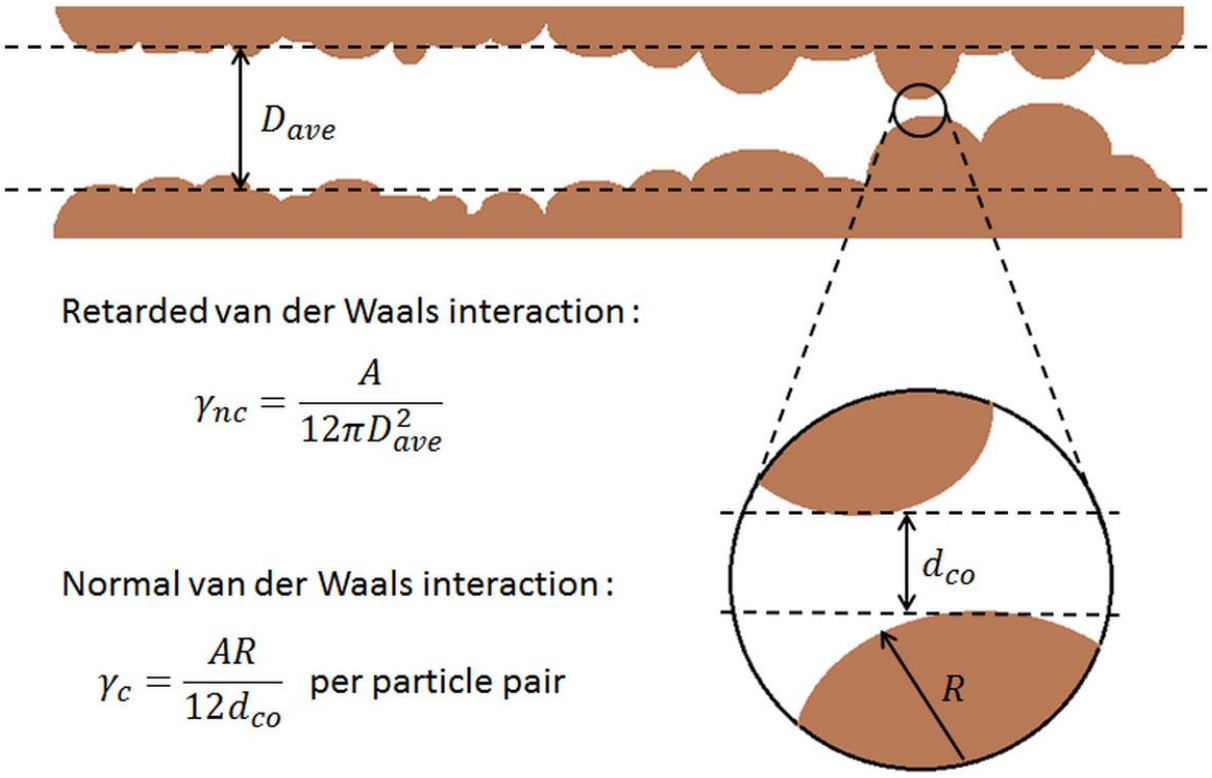

Figure 4.22. Contributions of adhesion from non-contacting portions and contacting asperities.

The adhesion derives from the van der Waals interactions that are contributed by interactions between contacting asperities and non-contacting van der Waals attractions. At different separation distances, the fraction of the contribution to adhesion from these two sources will differ. The retarded van der Waals force from the non-contacting portion of the surfaces is affected primarily by the mean separation distance between two non-contacting surfaces, while the shape of the asperities and the average summit density in contact affects the normal van der

Waals force from dispersed contacting asperities (Figure 4.22). With the assumption that the mean separation distance is less than 100 nm and the radii of the points in contact are the same, the total apparent work of adhesion can be expressed as the sum of the contributions from retarded and normal van der Waals interactions:

$$\gamma_T = \gamma_{nc} + \gamma_c = \frac{A}{12\pi D_{ave}^2} + n\frac{AR}{12d_{co}} \tag{4.16}$$

where D_{ave} is the mean separation distance between two rough surfaces, A is the Hamaker constant, n is the average summit density in contact, R is the curvature radius of the contacting asperities, and d_{co} is the cutoff separation with a typical value of 0.2 nm.

The parameters based on the surface quantitative analysis, and the apparent work of adhesion calculated based on retarded and normal van der Waals interactions are summarized in Table 4.5. Several previous reports have indicated that the adhesion energy decreases by $1/D_{ave}^2$ at small separation ranges if retarded van der Waals interaction plays the dominant role. However, the experimental results did not show this trend, and instead, the calculations showed that the contribution from the retarded van der Waals interaction was no longer significant, and instead, the contribution from normal van der Waals interaction between asperities in contact became the main source of the adhesion.

Surface	Retarded			Normal	
	D_{ave} (nm)	Apparent work of adhesion (calc.) (μJ/m^2)	Average summit radius (x10^{-3} μm)	Average summit density (/μm)	Apparent work of adhesion (calc.) (μJ/m^2)
Oxide	0.4 ± 0.1	22282 ± 4416	-	-	-
Poly	5.1 ± 0.5	214 ± 40	42.1 ± 3.3	296.9 ± 32.3	1544 ± 145
Mono 5	7.3 ± 0.8	113 ± 22	50.9 ± 3.5	207.7 ± 24.9	910 ± 106
Mono 10	10.1 ± 1.1	56.3 ± 12.1	80.1 ± 6.2	89.2 ± 9.0	623 ± 78
Mono 20 Very Low	10.7 ± 1.7	48.6 ± 15.2	83.2 ± 5.1	55.7 ± 5.3	406 ± 45

Table 4.5. Apparent work of adhesion calculated on the basis of retarded and normal van der Waals interactions.

The calculated and experimental values are plotted in Figure 4.23 for comparison. The apparent work of adhesion of the uncoated Si substrate was not plotted for clarity because of its high value. It has been proven that when the D_{ave} is lower than 5 nm, most of the adhesion derives from the non-contacting surfaces. The apparent work of adhesion calculated for the uncoated, smooth Si wafer using the retarded van der Waals interaction was the highest among all the samples. This calculated value was still lower than the experimental value, indicating that the actual separation distance may have been overestimated. For all of the surfaces coated with iron oxide nanoparticles, D_{ave} was increased significantly by the roughening effect. Now, the non-contacting portion of the surfaces was not the dominant contribution, and the model of the

adhesion can be simplified as rough surfaces with contacting asperities. Surface coated with polydispersed iron oxide nanoparticles which has a relatively smooth surface owes only 8.9% of its total adhesion to retarded van der Waals interactions. At large D_{ave}, surfaces in contact become the largest contributor. 94.5% of the total adhesion of the roughest surface, which was coated with monodispersed 20 nm iron oxide nanoparticles, is attributable to normal van der Waals interactions. Hence, at a larger mean plane separation, the adhesion of these surfaces began to fall within the scale of conventional adhesion models that take into account adhesion at points in contact.

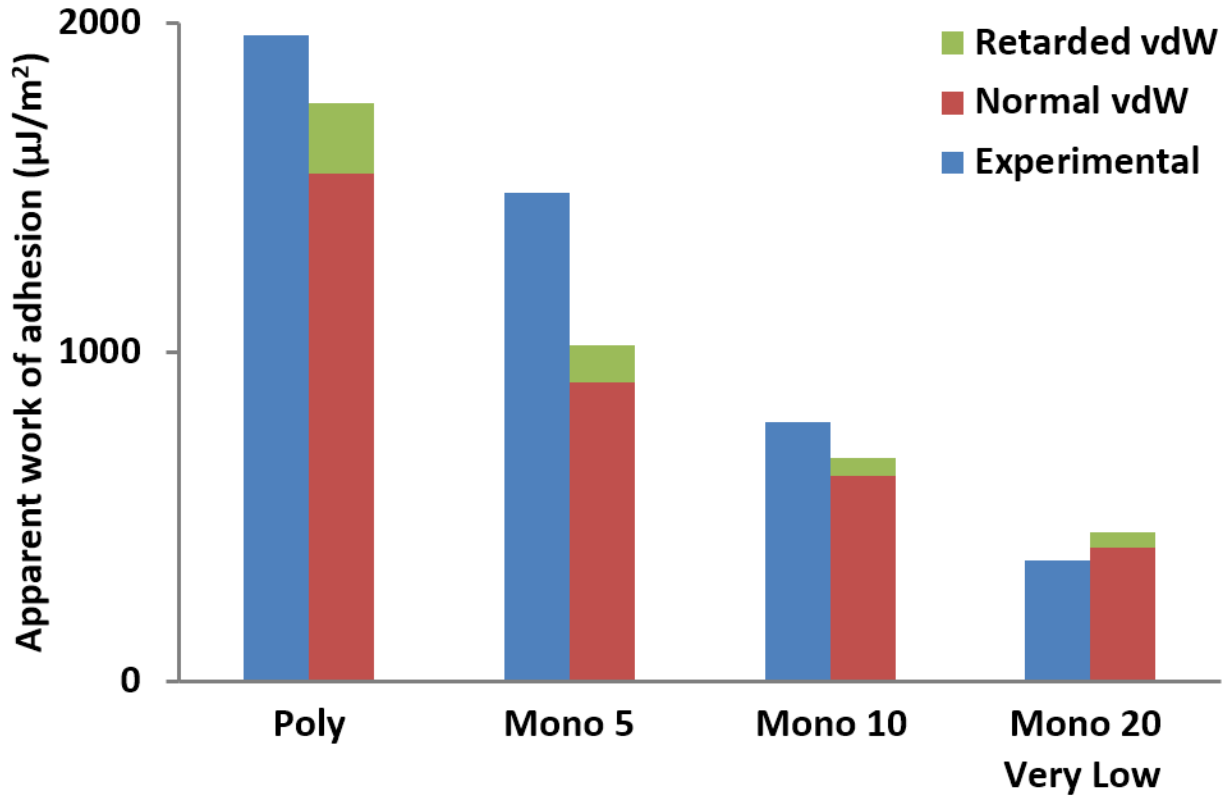

Figure 4.23. Calculated and experimental values of apparent work of adhesion for coatings of size-varied iron oxide nanoparticles.

Figure 4.23 shows that the experimental values were larger than the calculated values for most of the coatings. The explanation that we believe is the most probable is that the alignment between hills and valleys caused the actual surfaces to be in closer proximity than in the calculations. This phenomenon may have several effects on estimates of adhesion. First, closer contact between two surfaces may decrease the surface separations by certain amounts, which clearly would underestimate the adhesion measured. Moreover, both the average summit density and the summit radius affect the contact area in the calculations. When the surfaces are brought into closer proximity, asperities that are not aligned with valleys may come into contact and increase the actual summit density.

By using size-varied iron oxide nanoparticles via the GXL deposition technology, the surfaces of MEMS devices can be coated uniformly with these nanoparticles. The mean plane separation distance between two contacting surfaces can be increased, while the contact area is reduced by altering the summit density and radius, which are affected by the average size of the initial nanoparticles. Based on the experimental results and theoretical calculations, the decreased plane separation will reduce the retarded van der Waals interaction, thereby diminishing the contribution of the non-contacting portion to adhesion. On the other hand, normal van der Waals interactions between contacting asperities are affected by the combination of the average summit density and radius, which plays the dominant role in the adhesion. Changing these parameters will affect the total effects of normal and retarded van der Waals interactions between contacting asperities, leading to reduced adhesion.

4.3.4 Tribological effect of coatings based on monodispersed nanoparticles with varying initial concentrations

Based on the results obtained in the previous section, it was concluded that the apparent work of adhesion can be reduced by using iron oxide nanoparticles of larger average diameter. As discussed in Chapter 3, the effect of concentration is associated with the long-range roughness properties. It is worth varying the initial concentration of the monodispersed 20 nm iron oxide nanoparticles to determine whether the size and concentration effects can be combined to achieve greater reductions in adhesion. However, it has been proven that when the initial concentration is too high, the nanoparticle aggregation becomes dominant and produces larger asperities. These non-uniform aggregates have negative effects on the surface coating, such as eliminating short-range details and producing instability in surface structures. Therefore, during the GXL deposition process, the initial concentration range was controlled strictly to ensure that no large agglomerates existed on the final coatings.

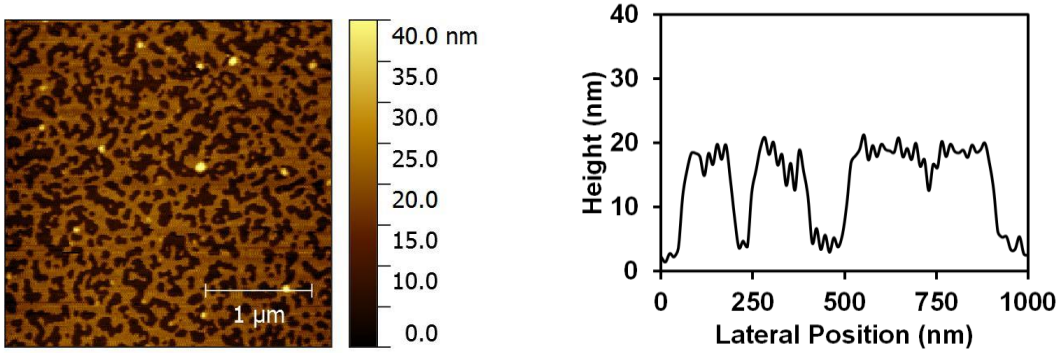

Figure 4.24. AFM scan and line profile of 20 nm iron oxide nanoparticle-coated chip surface at low concentration.

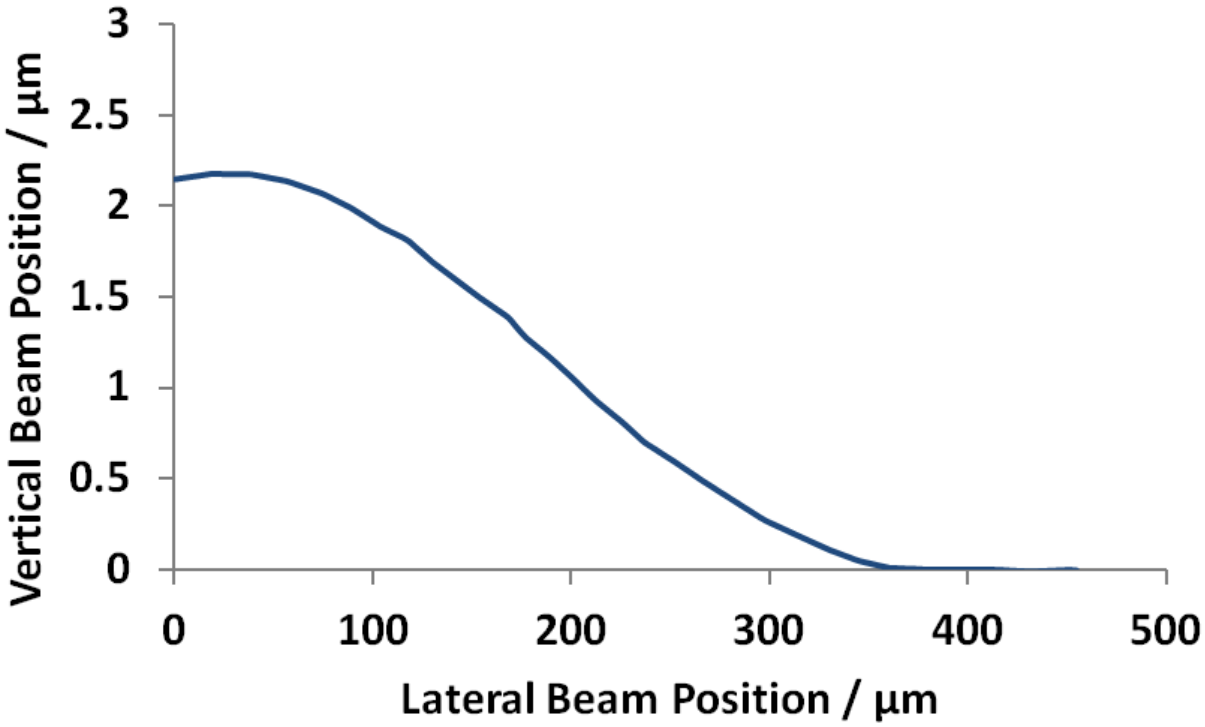

Figure 4.25. Height profile of the cantilever beam of 20 nm iron oxide nanoparticle-coated chip surface at low concentration after actuation obtained experimentally using phase shifting interferometry.

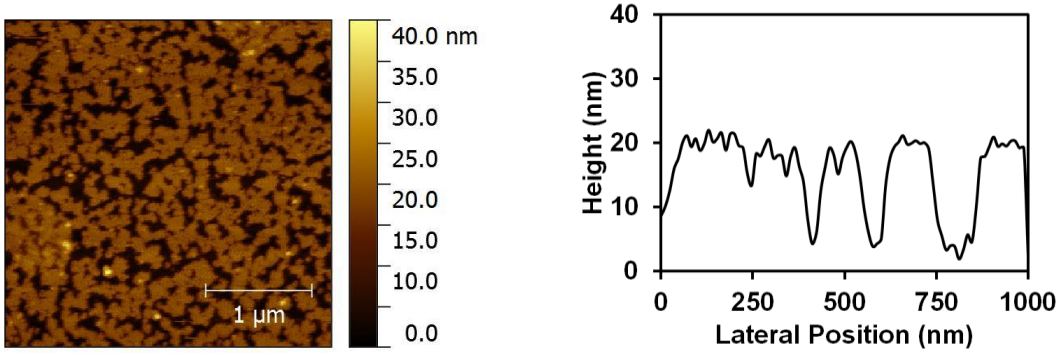

Figure 4.26. AFM scan and line profile of 20 nm iron oxide nanoparticle-coated chip surface at medium concentration.

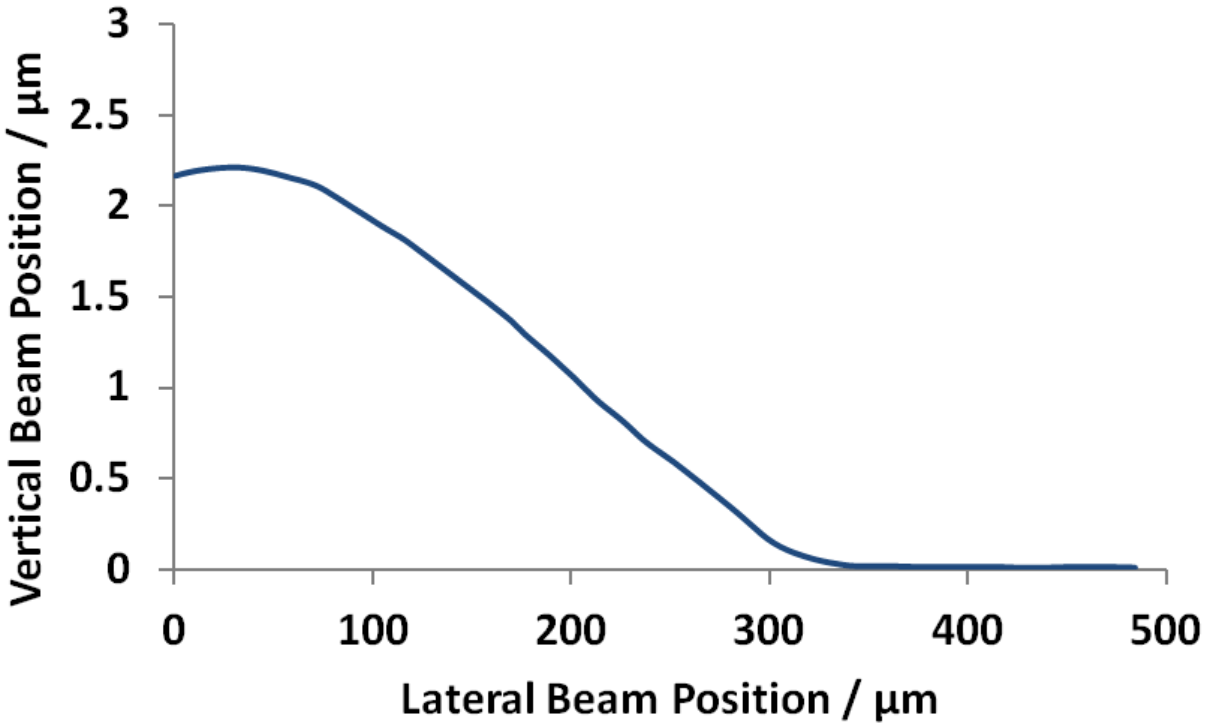

Figure 4.27. Height profile of the cantilever beam of a 20 nm iron oxide nanoparticle-coated chip surface at medium concentration after actuation obtained experimentally using phase shifting interferometry.

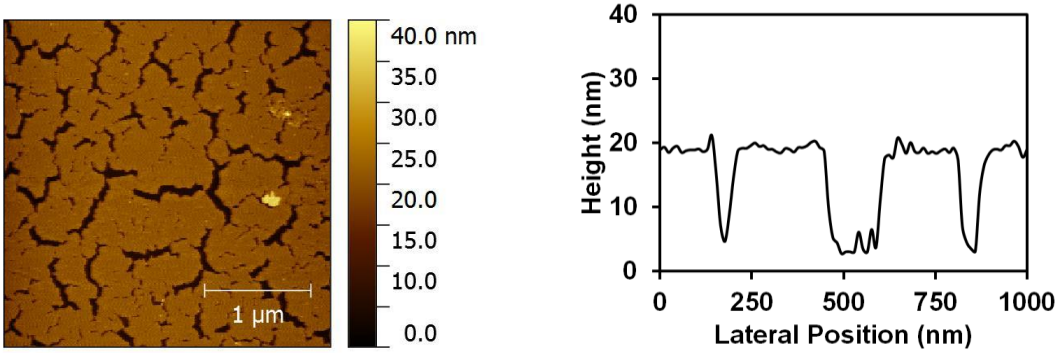

Figure 4.28. AFM scan and line profile of 20 nm iron oxide nanoparticle-coated chip surface at high concentration.

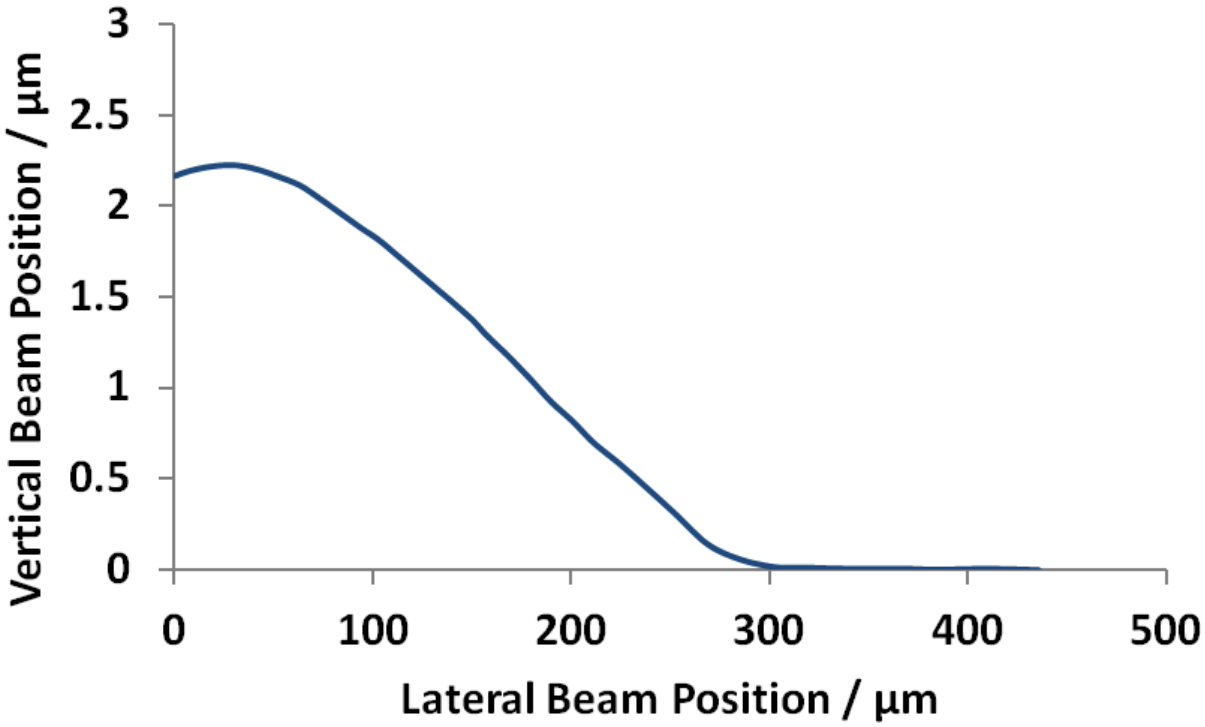

Figure 4.29. Height profile of the cantilever beam of a 20 nm iron oxide nanoparticle-coated chip surface at high concentration after actuation obtained experimentally using phase shifting interferometry.

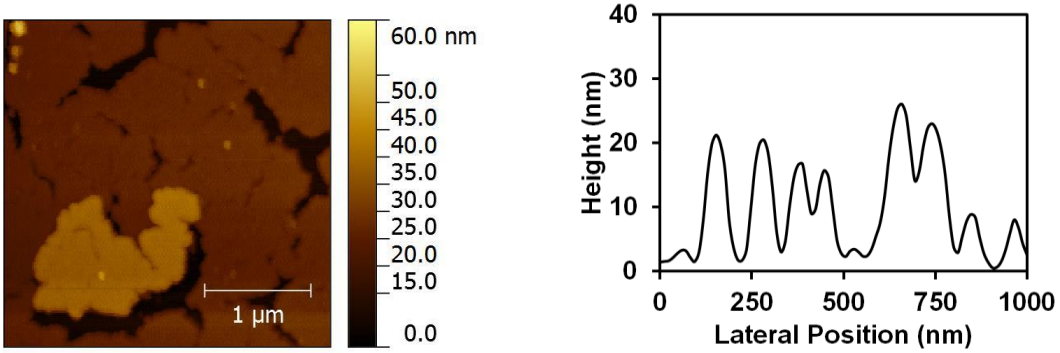

Figure 4.30. AFM scan and line profile of a 20 nm iron oxide nanoparticle-coated chip surface at very high concentration.

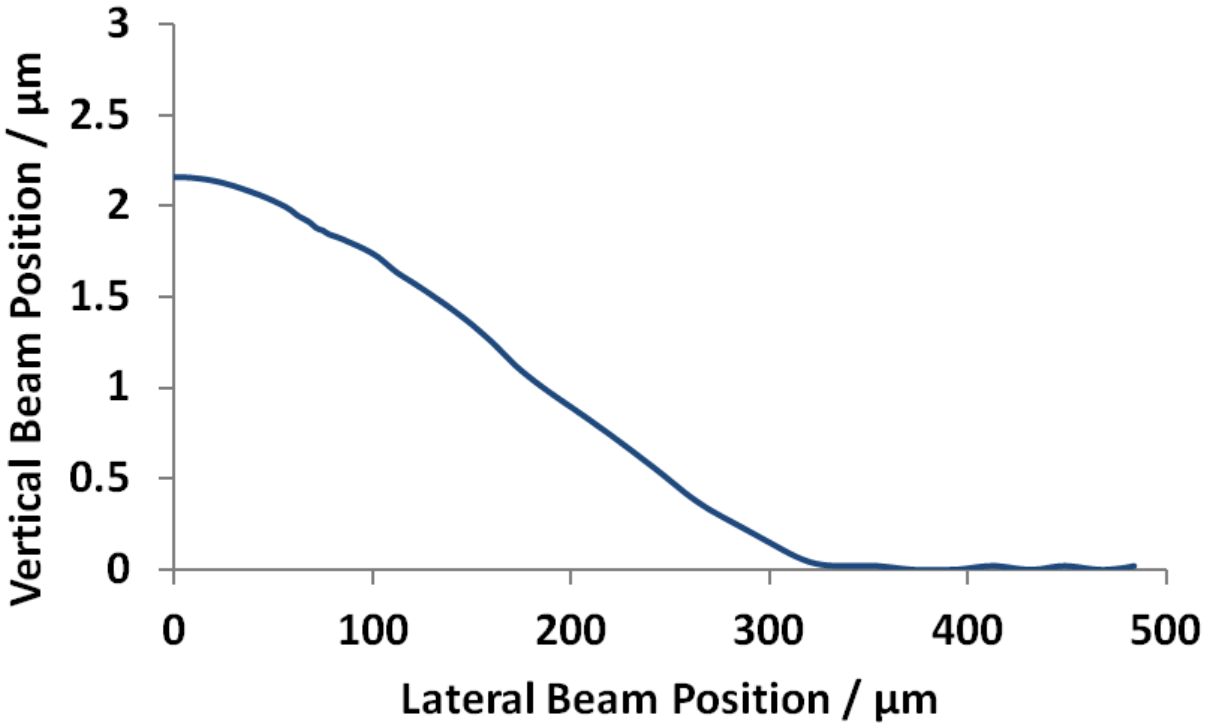

Figure 4.31. Height profile of the cantilever beam of a 20 nm iron oxide nanoparticle-coated chip surface at very high concentration after actuation obtained experimentally using phase shifting interferometry.

In the previous section, coating based on monodispersed, 20 nm iron oxide nanoparticles produced the greatest reduction in adhesion. Therefore, this set of nanoparticles and solutions of nanoparticles with varying initial concentrations was used in the GXL deposition process and deposited on the released chip. The AFM scan and corresponding line profile and height profiles from interferometry of the cantilever beam after actuation of chips coated with monodispersed 20 nm iron oxide nanoparticles at varying concentrations are shown in Figures 4.24 to 4.31. As expected, the shortest adhered crack length among all the actuated cantilever beam arrays was approximately 300 μm, indicating a good reduction in the adhesion.

Concentration	rms surface roughness (nm)	Average crack length (μm)	Apparent work of adhesion ($\mu J/m^2$)
Mono 20nm Low	7.65 ± 0.77	356 ± 53	533.1 ± 116.4
Mono 20nm Medium	5.98 ± 0.43	342 ± 54	570.7 ± 103.9
Mono 20nm High	4.47 ± 0.36	297 ± 26	923.6 ± 118.2
Mono 20nm Very High	6.49 ± 0.79	325 ± 89	382.5 ± 176.8

Table 4.6. Values of rms surface roughness, average crack lengths, and calculated apparent work of adhesion obtained from iron oxide nanoparticle coatings at various concentrations.

The values of rms surface roughness, average crack lengths, and the calculated apparent work of adhesion after analysis of the cantilever beam arrays are summarized in Table 4.6. Some of the results exceeded our expectations. A reduction in adhesion overall was achieved for all the coatings at varying concentrations, indicating that the size effect still operates here. However, the lowest apparent work of adhesion derived from the coating at very low concentration. As the concentration increased, the apparent work of adhesion also showed an increasing trend, except for the coating at very high concentration, which had an apparent work of adhesion similar to the coating at very low concentration.

The reduced adhesion was related to the topography of the coated surfaces, which was affected now by the initial concentration of the nanoparticle solution. As discussed, the variation in the concentration of the initial nanoparticle solution facilitates observation of the growth process, which is determined by the surface chemistry. In Chapter 3, the surface tension of the substrate was on the same order as that of the gold nanoparticle and the film formation followed the Stranski-Krastanov mode, where monolayers were formed with some three-dimensional aggregate growth on top. For the MEMS system investigated in this chapter, the surface tension of iron oxide nanoparticles was determined by the stabilizing ligands, which was 32.5 dyn/cm for oleic acid (Chumpitaz et al., 1999). This value is higher than that of the gold nanoparticles used in previous chapter. However, the substrate used in MEMS devices is an uncoated Si wafer with a thin oxide layer on top, the surface tension of which is around 140 dyn/cm. For this iron oxide nanoparticle-Si system, the surface tension of the substrate is much higher than that of the nanoparticles, leading to the Frank-van der Merwe film growth mechanism. In this mechanism, particles attach preferentially to the surface sites, resulting in layer-by-layer film formation. From the AFM images in Figures 4.24 to 4.31, it is clear that the surface was covered in part

with iron oxide nanoparticle films. Based on the line profiles, the average height of the nanoparticle island was approximately 20 nm. The AFM analysis confirmed that the thickness of the incomplete nanoparticle layer was relatively similar to the diameter of iron oxide nanoparticles, indicating that the nanoparticles formed a sub-monolayer on the substrate following the Frank-van der Merwe growth model. As the concentration increased, the monolayer coverage on the substrate increased, while the thickness remained the same. At a very high concentration, multilayers began to form on the surface, resulting in irregular structures.

In the topographical transition from the sub-monolayer to monolayer, the rms roughness values exhibited a direct correspondence with the numbers of nanoparticles deposited on them. As shown in Table 4.6, the rms surface roughness increased with an increase in the concentration of the initial nanoparticle solution, and the sub-monolayer surface coverage increased as well. When the concentration exceeded a certain level, the nanoparticles deposited began to fill the surface, thereby decreasing its rms roughness because of the surface smoothing effect. This transition is illustrated in Figure 4.32, where the red line indicates the actual surface line profile used to calculate rms surface roughness. Based on the diagrams in Figure 4.32, a simple analytical model was used to calculate the theoretical change in rms surface roughness vs. that in the surface coverage. The calculation began by placing monodispersed 20 nm nanoparticles on the surface one by one to fill the whole surface, after which the surface height profile was extracted and rms surface roughness was calculated after each particle was placed on the surface. The values calculated and the experimental results are plotted in Figure 4.33. It can be seen that the experimental values and their trends were similar to the calculated curve, proving the growth of monolayer nanoparticle films.

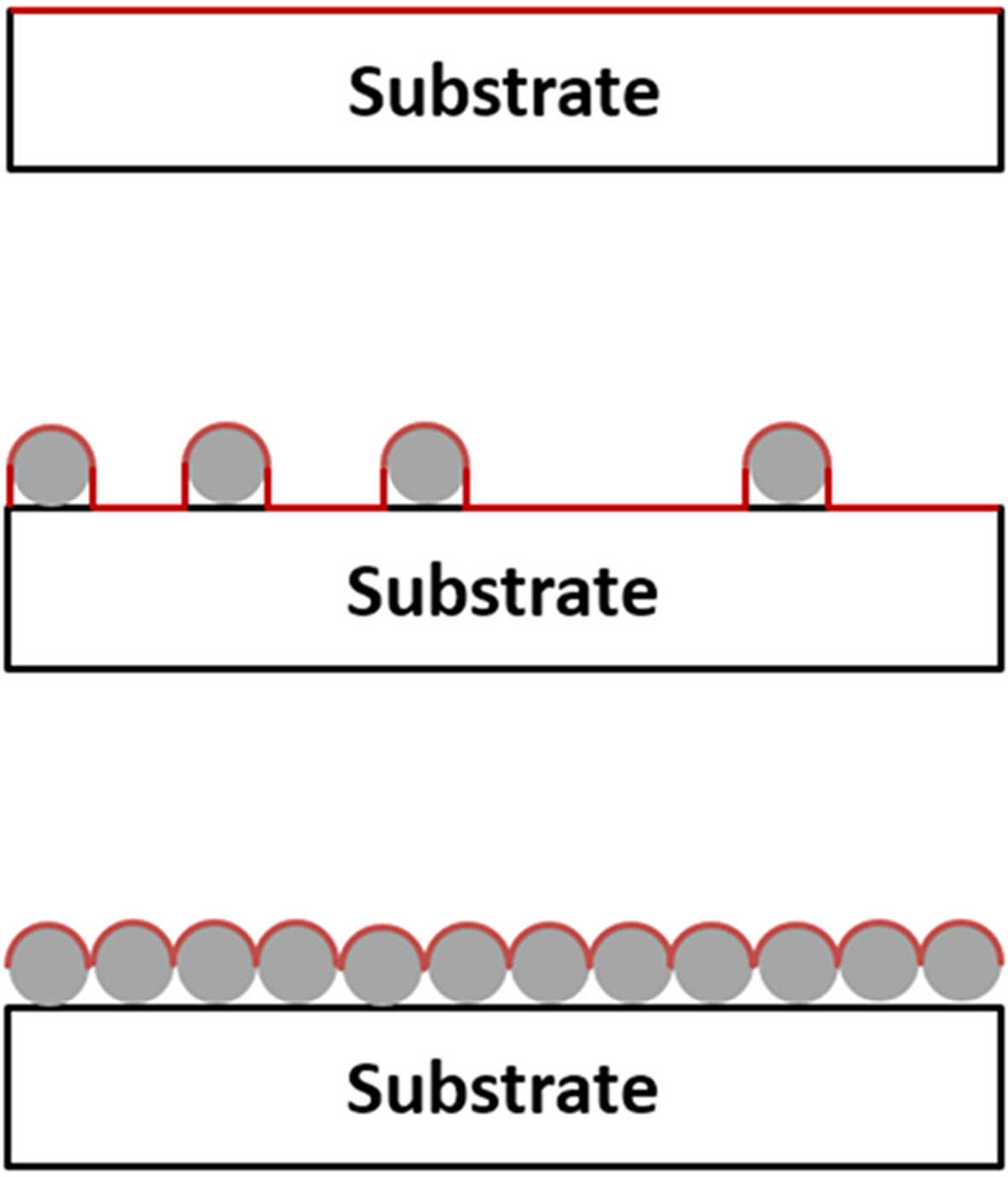

Figure 4.32. A schematic explanation of the roughness of the nanoparticle monolayer. The red lines shown in all the diagrams represents the surface profile obtained from AFM data.

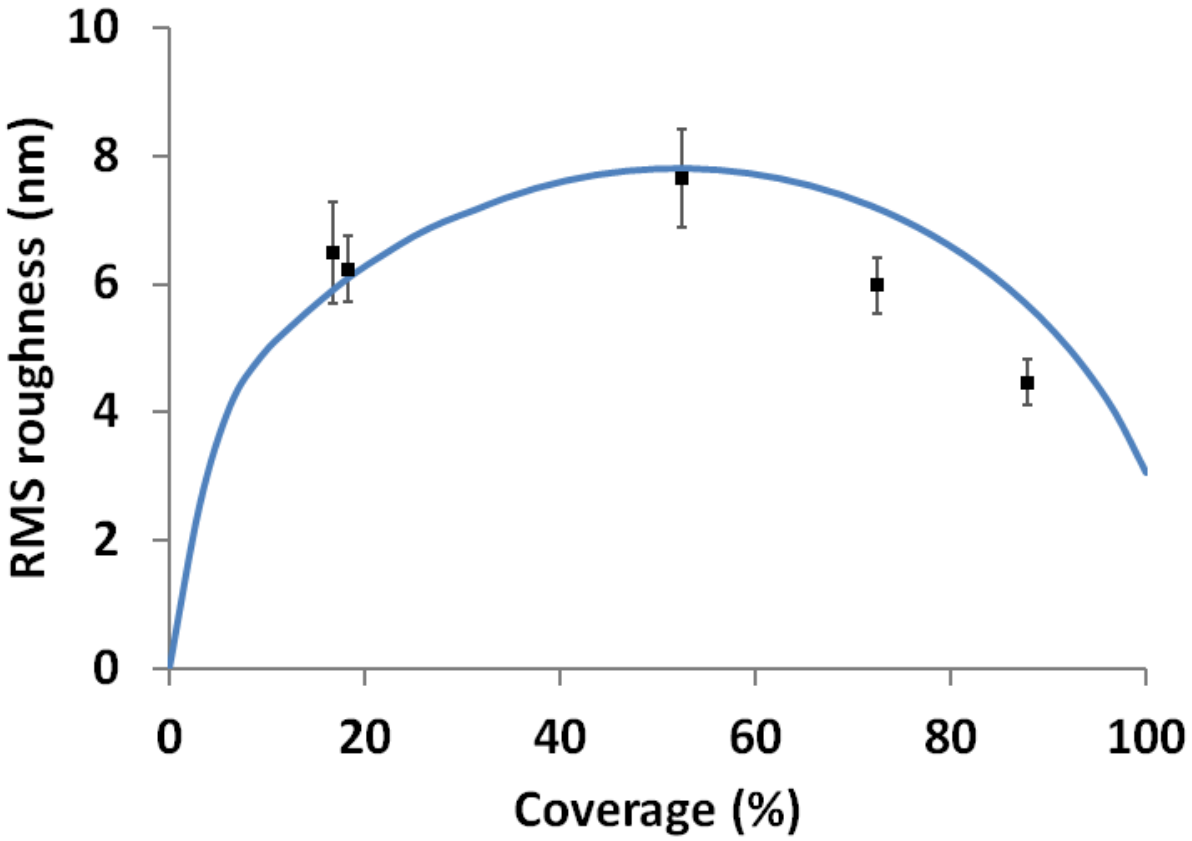

Figure 4.33. Rms roughness values vs. the surface coverage for a nanoparticle monolayer based on Figure 4.32.

For these kinds of surfaces, the analytical model we applied on previous nanoparticle films is no longer suitable. The key issue is that the surface analysis model is based on the Greenwood-Williamson (GW) model. One of the most important assumptions in the GW model is that the surface height follows a Gaussian distribution, which allows the use of probability density functions (PDFs) of a standard form. The surface height distributions of a previous film and a film in this section are shown in Figure 4.34. It is clear that the surface height distribution of the first film is approximated well by a Gaussian distribution. However, the last film has a double peak distribution profile, which does not fit any existing distribution functions. The

double peak profile is caused by the step change of the height from incomplete monolayer coverage on the substrate.

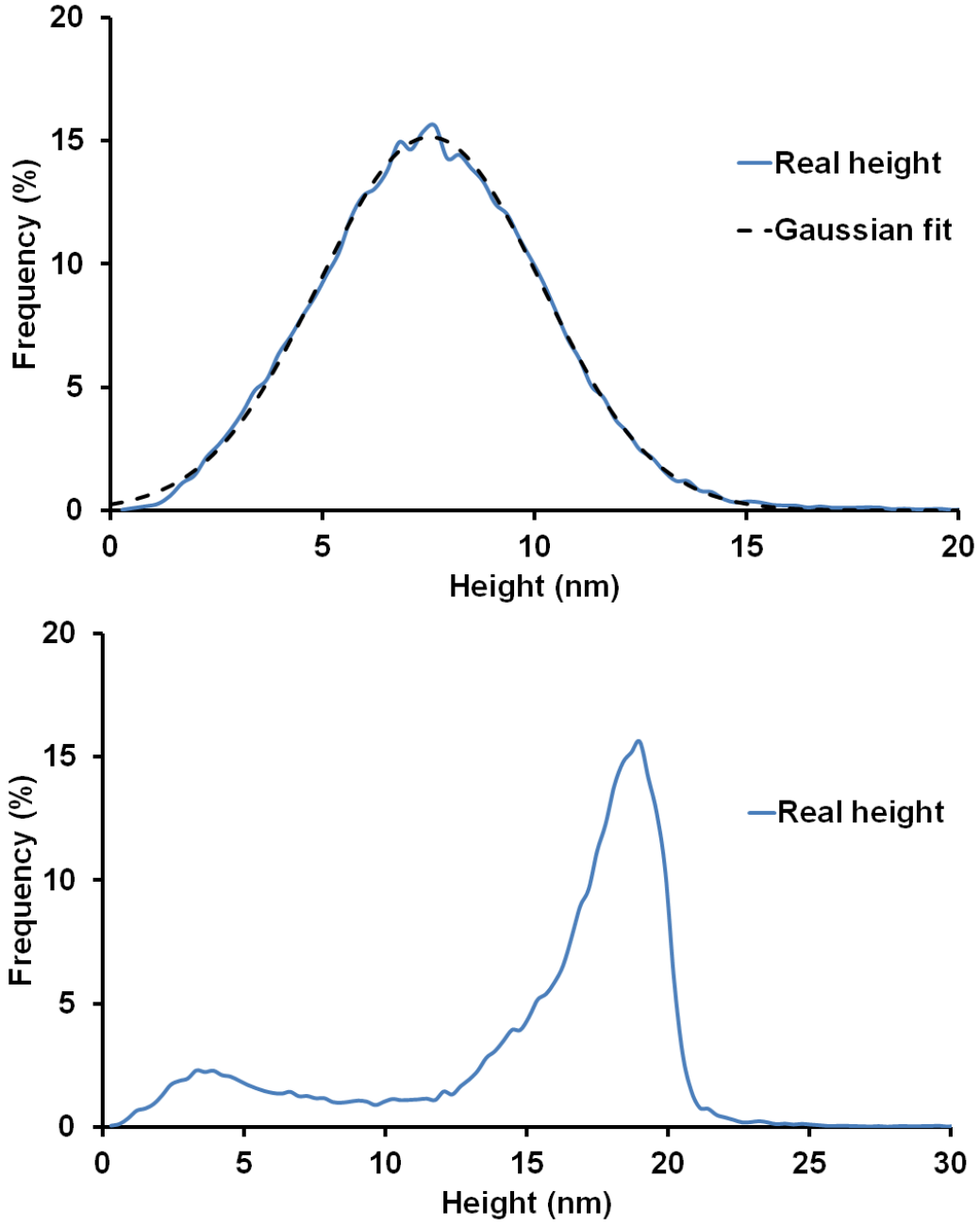

Figure 4.34. Examples of surface height distributions with a good Gaussian approximation (top), and a non-Gaussian distribution (bottom).

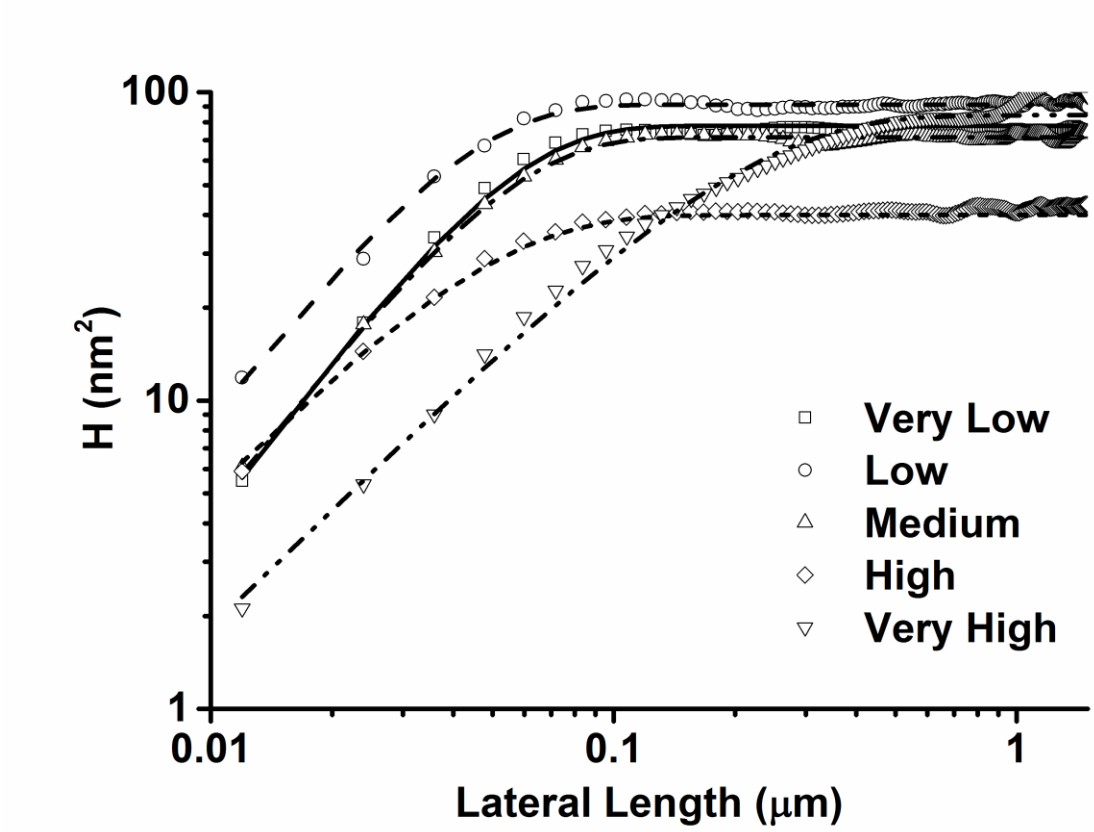

Figure 4.35. Experimental HHCF data for iron oxide nanoparticle coatings at various concentrations. Lines are the corresponding HHCF curves calculated using the proposed HHCF model fitting.

Size of NPs (nm)	rms roughness (nm)	Autocorrelation length (nm)	Roughness exponent
Mono 20 Very Low	6.24 ± 0.51	50.8 ± 4.3	0.843 ± 0.056
Mono 20 Low	7.65 ± 0.77	49.2 ± 5.1	0.822 ± 0.046
Mono 20 Medium	5.98 ± 0.43	50.1 ± 4.7	0.858 ± 0.071
Mono 20 High	4.47 ± 0.36	43.3 ± 3.8	0.683 ± 0.024
Mono 20 Very High	6.49 ± 0.79	195.3 ± 9.4	0.641 ± 0.035

Table 4.7. Surface parameters calculated from the HHCF model for iron oxide nanoparticle coatings at various concentrations.

Analysis based on HHCF can still be applied here, as the HHCF is computed as normalized histograms of the experimental height values and does not require any predetermined models. Figure 4.35 shows the experimental HHCF curves from AFM data and corresponding HHCF curves by model fitting. The rms roughness, autocorrelation lengths, and roughness component values from HHCF model are summarized in Table 4.7. All values here were calculated from the previous HHCF analysis. As shown in Table 4.7, the autocorrelation length remained approximately 50 nm for most of the surfaces except for the coating at very high concentration, which was due to the large islands formed on top of the monolayer. The small variation in autocorrelation lengths occurred because the original particle size affected the final particulate size on the surface, which derived from the particle-particle interactions during the

GXL process. The value of the roughness component decreased as the concentration, or surface coverage, increased. A higher roughness exponent reflects lower local surface asperities, and is associated with smoother short-range surface topography with fewer rough structures.

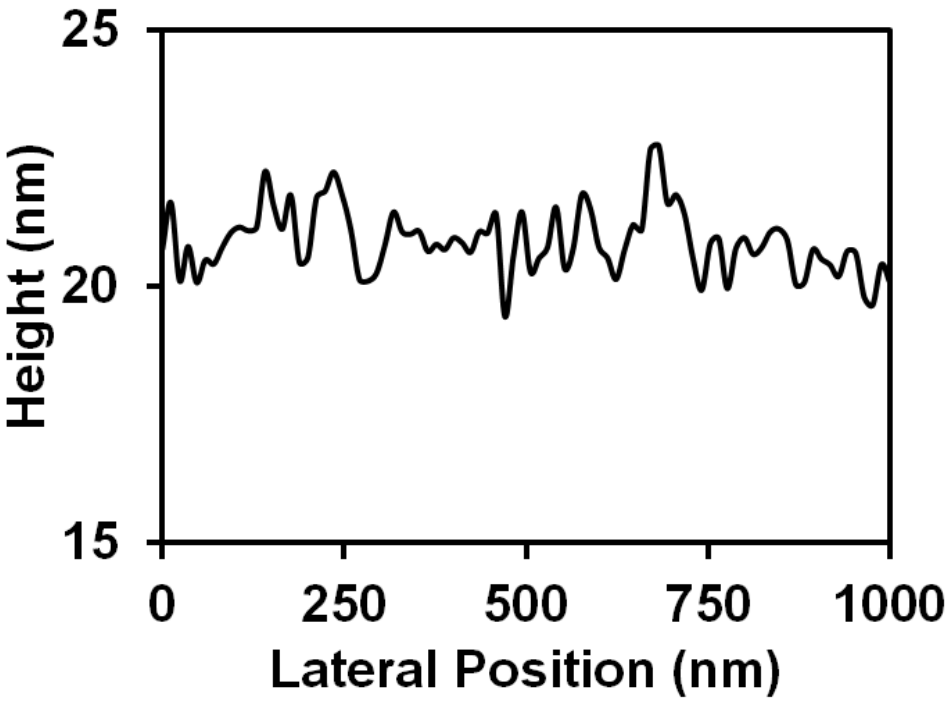

Figure 4.36. Line profile of the top layer of iron oxide nanoparticle islands.

Because the analytical model cannot be used for the surfaces obtained here, an alternative simplified model based on the surface coverage was constructed for the quantitative analysis. The interaction between the coated surfaces can be treated as van der Waals interactions between two parallel plates. Each plate included two layers: a Si substrate on the bottom, the thickness of which can be approximated as infinite, and a monolayer of iron oxide nanoparticles on top with a thickness equal to its diameter (20 nm). When the two surfaces were brought into proximity, the total adhesion was contributed by the retarded van der Waals interaction between the Si

substrate, which can be ignored, as the distance between the two Si surfaces was approximately 40 nm, and the van der Waals interaction between the iron oxide nanoparticle layers. Figure 4.36 shows the line profile of the top layer of iron oxide nanoparticle islands compared to the regular line profile with edge height change. The surface texture is relatively smooth and the height variation is only approximately 1.5 nm. Because of this short mean plane separation, the van der Waals interaction between the iron oxide nanoparticle layers became the main contribution to the adhesion. The apparent work of adhesion expressed in the van der Waals interaction between two parallel finite plates is as follows (Anandarajah et al., 1995):

$$\gamma_{NC} = \frac{A}{12\pi}\left[\frac{1}{D^2} + \frac{1}{(D+2t)^2} - \frac{2}{(D+t)^2}\right] \tag{4.17}$$

where D is the mean separation distance between two rough surfaces, t is the thickness of the coated nanostructure films, and A is the Hamaker constant.

This equation was calculated based on full surface coverage. If the unit area of the surface is covered in part with the iron oxide nanoparticle monolayer, the actual contribution of adhesion should be modified according to the surface coverage, w_s:

$$\gamma_{NCR} = w_s\gamma_{NC} = \frac{Aw_s}{12\pi}\left[\frac{1}{D^2} + \frac{1}{(D+2t)^2} - \frac{2}{(D+t)^2}\right] \tag{4.18}$$

Surface	Apparent work of adhesion (exp.) ($\mu J/m^2$)	Apparent work of adhesion (calc.) ($\mu J/m^2$)	Surface Coverage (%)
Mono 20 Very Low	369.4 ± 77.2	441.8 ± 103.5	18.3
Mono 20 Low	533.1 ± 116.4	1227.4 ± 213.7	52.2
Mono 20 Medium	570.7 ± 103.9	1718.4 ± 312.9	72.5
Mono 20 High	923.6 ± 118.2	2135.7 ± 416.6	87.9
Mono 20 Very High*	382.5 ± 176.8	410.0 ± 98.6	16.7

Table 4.8. Experimental and calculated values of apparent work of adhesion based on surface coverage. *The surface coverage of the coating at very high concentration was estimated differently (see discussion below).

Based on this equation, the calculated and experimental values of apparent work of adhesion are summarized in Table 4.8. The surface coverage here can be treated as the apparent contact area of the surface. For the coating at very high concentration, the covered area of the top layer of iron oxide nanoparticles was used to estimate surface coverage, with the assumption that the submerged layers do not contribute greatly to the total adhesion because of high D_{ave} (>40 nm). It is clear that the apparent work of adhesion decreased as the apparent contact area decreased. It should be noted that most of the calculated values were higher than the

experimental values. There are several potential reasons for this difference. It was assumed in the calculations that the partially covered surfaces were in alignment. This may not be true for real contact behavior, especially with low surface coverage, where only part of the nanoparticle films are facing each other. In this case, the retarded van der Waals interaction is lower than expected. Another possible reason is that, as the concentration of the initial nanoparticle solution increased, the sub-monolayer of iron oxide nanoparticles formed with some dispersed aggregates on top of the surface. Although these aggregates are not dominant, they will change the D_{ave}. At short mean plane separation distances, the retarded van der Waals interaction depends strongly on the D_{ave}, such that even a small change will reduce the adhesion significantly.

By altering the initial concentration of the monodispersed 20 nm iron oxide nanoparticle solutions via GXL deposition technology, the surfaces of the MEMS devices could be coated uniformly with these nanoparticles. Because of the high surface tension of the substrate, the film formation of the nanoparticles now followed the Frank-van der Merwe growth mechanism, leading to the appearance of a surface covered in part with monolayer island structures. The size of the nanoparticles still affected the reduction of adhesion; however, the contribution of adhesion now derived primarily from the van der Waals interaction between nanoparticle monolayers. Based on the experimental results and theoretical calculations, the surface coverage increased as the initial concentration increased, while the surface film growth was limited at the sub-monolayer level. This led to an increased apparent work of adhesion because of the larger interaction area when two surfaces are brought close. This proves that, under different surface topographical conditions, it is essential to reduce the total contact area to reduce adhesion, while still obtaining a sufficient long-range roughness.

4.3.5 Tribological effect of coatings based on GXL deposited gold nanorods

In previous chapters, it was demonstrated that the surfaces of MEMS devices can be coated with size-varied iron oxide nanoparticles via GXL deposition technology. Altering the summit density and radius, which are affected by the average size of the initial nanoparticles, reduced the contact area. Changing these parameters affected the total effects of normal and retarded van der Waals interactions between contacting asperities, and reduced the adhesion. As these characteristic parameters are affected by the spherical shape of nanoparticles, an alternative possibility is to use nanomaterials of various shapes, such as nanorods and nanocubes. These shapes may have a higher surface contact area compared to nanospheres, and lead to improved stability. Application of these shapes also may produce films with different contact areas and morphologies that will affect the surface tribology.

The gold nanorods used in this experiment were stabilized with dodecanethiol, which has the same stabilizing ligand as the gold nanoparticles used in Chapter 3. This ensured that the surface chemistry of the ligands did not change greatly, so that we could focus on the differences between shapes. The TEM image of the gold nanorods is shown in Figure 4.37. The SPR (surface plasmon resonance) and LSPR (localized surface plasmon resonance) peaks were measured via UV-Vis at 760 nm and 510 nm, respectively, which corresponded to the length and diameter of the gold nanorods. The TEM image shows that the average length and diameter of the gold nanorods were 30.0 ± 3.7 nm and 8.0 ± 2.1 nm, respectively.

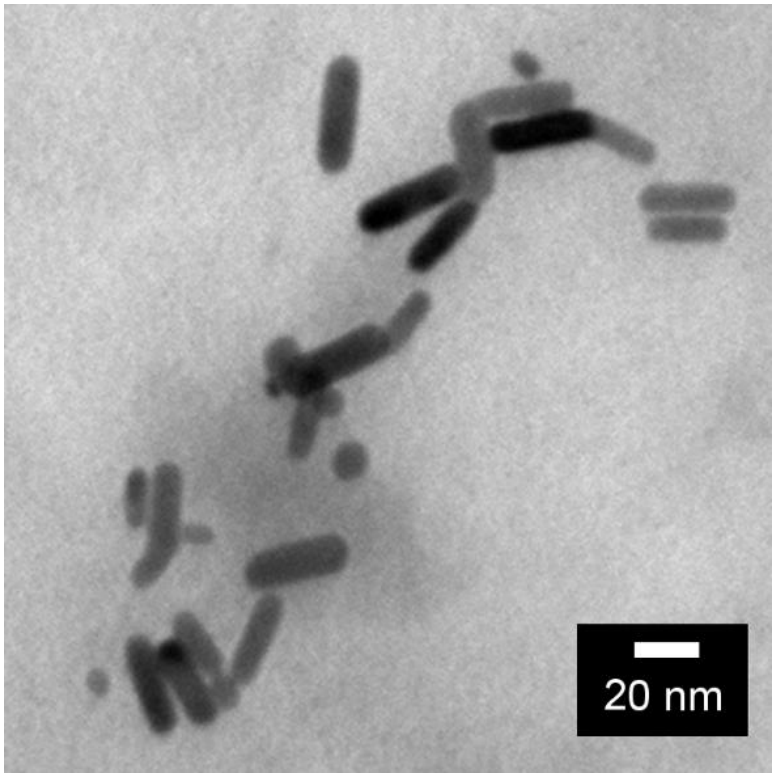

Figure 4.37. TEM image of the gold nanorods used for GXL deposition.

Preliminary tests of GXL deposition of the gold nanorods applied to a diced Si wafer were performed to check the feasibility of the surface modification. However, the results were unexpected. Rather than a relatively uniform surface morphology, the surface was covered in part with very large aggregates. Figure 4.38 shows AFM images of the surface at a scale of 30 μm. There are significant, large aggregated structures dispersed on the surface, the dimensions of which were approximately 2 μm, with a height of hundreds of nanometers. An enlarged AFM scan of the aggregate is shown in Fig 4.38 as well. The maximum height of the aggregates, consisted of rod-like asperities, was approximately 500 nm. All of these images indicate that GXL deposition of gold nanorods did not result in uniform nanostructure films such as those we obtained in previous chapters, but very large agglomerates instead, which limits the application

of such a coating to MEMS devices. As the height of these structures was 500 nm, while the space between the substrate and the device layer of the MEMS chip was only 2 µm, rather than producing a roughening effect, the aggregates may compromise the performance of the devices. Another possible issue is that the top of these aggregates may not be immobilized well, leading to structures that are bound weakly.

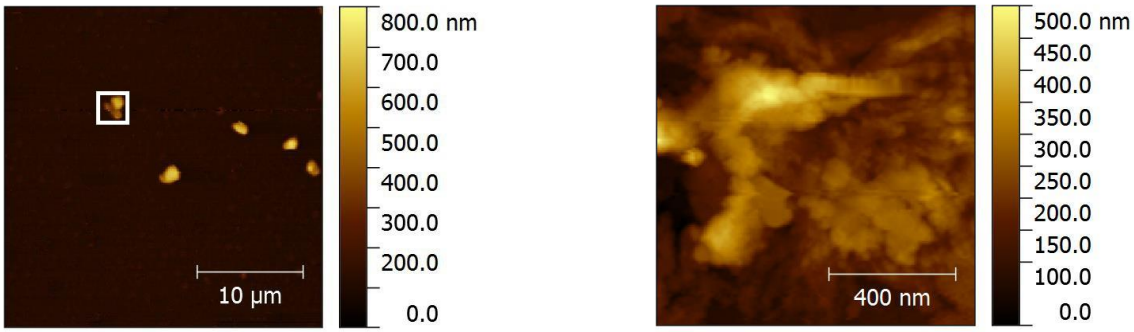

Figure 4.38. AFM images of gold nanorod-coated chip surface at a scale of 30 µm (left), and an enlarged scan of the aggregates (right). The white square indicates the enlarged area.

The assumption was that the interaction between nanorods is much greater than that of the nanoparticles controlled by the GXL process. To investigate this effect further, the conditions of the GXL process for gold nanorods were changed. In the initial nanorod solution, a concentration only 1% of that used previously was introduced to the GXL process. The initial pressure for the gas expansion was reduced to 100 psi, and the gas expansion rate was reduced by half. All of these changes were made to ensure that the gold nanorods did not precipitate from the solution too rapidly, and had sufficient time to interact with the substrate with high surface energy, which should prefer to form a uniform layer.

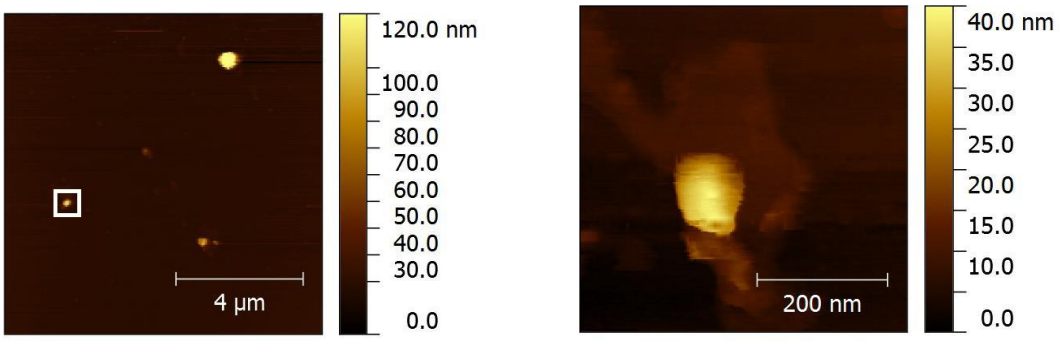

Figure 4.39. AFM images of gold nanorod-coated chip surface at a very dilute concentration on a scale of 30 µm (left), and an enlarged scan of the aggregates (right). The white square indicates the enlarged area.

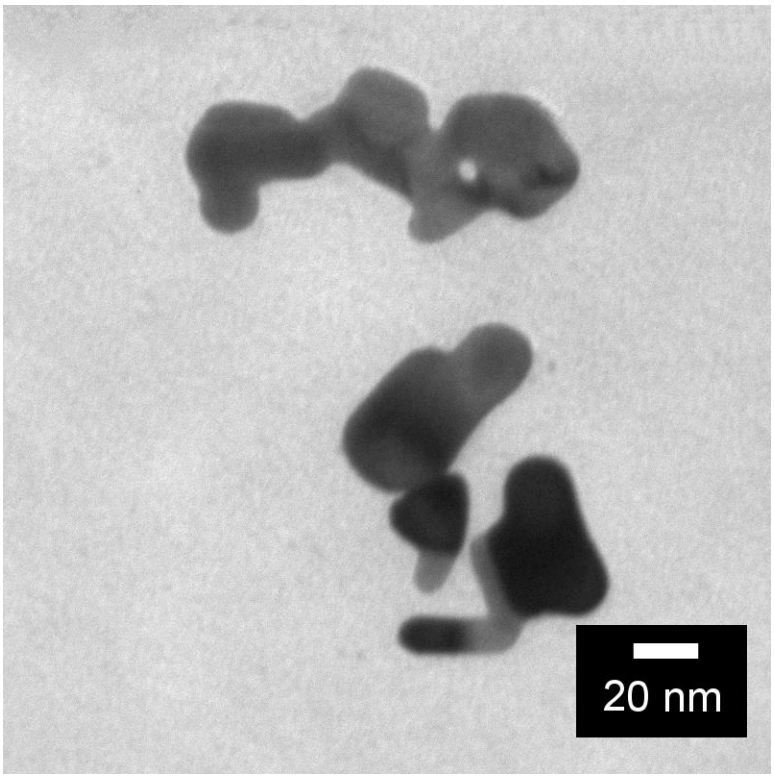

Figure 4.40. TEM image of the gold nanorods deposited on a TEM grid at a very dilute concentration.

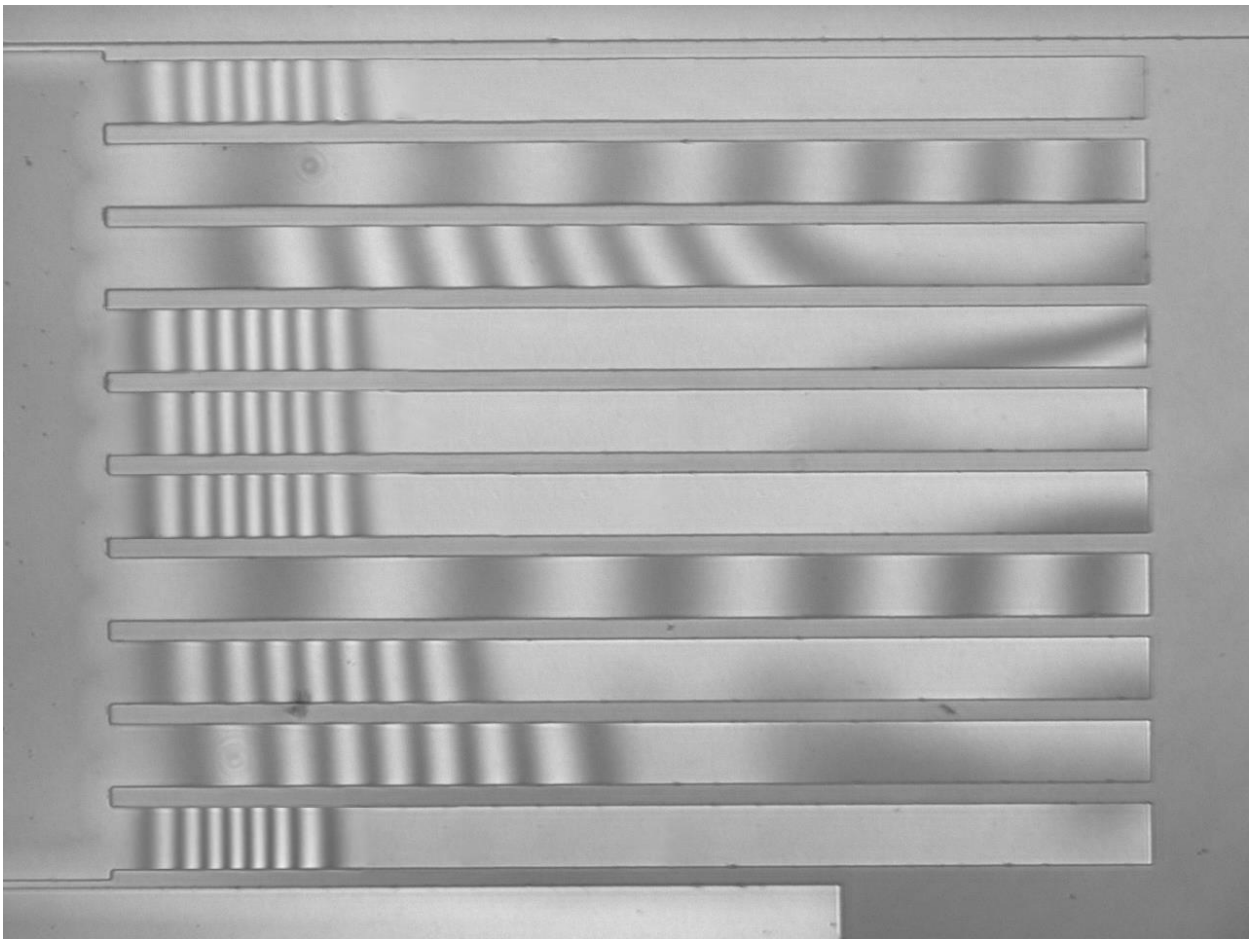

Figure 4.41. Interferogram showing an actuated cantilever beam array of the chip coated with gold nanorods.

After the experimental conditions were optimized, GXL deposition of gold nanorods was applied on the TEM grid, Si substrate, and MEMS chips. Unfortunately, we still obtained no uniform films. AFM images of the surface on a scale of 30 μm are shown in Figure 4.39. Isolated aggregates existed on the surface, while the density was significantly lower, and the maximum height also decreased to approximately 120 nm. Figure 4.39 shows an enlarged AFM scan of the aggregate, which has structures with irregular shapes. Similar results were obtained from the nanorod-deposited TEM grid, the image of which is shown in Figure 4.40. The gold nanorods

stuck to each other to form large asperities; such aggregates may not provide appropriate adhesion reduction and cause the devices to perform improperly. Gold nanorods were deposited on one MEMS chip and the interferogram of the actuated cantilever beams on the gold nanorod-coated chip is shown in Figure 4.41. It is clear that 5 out of 10 cantilever beams stuck to the surface after actuation and the crack length was quite similar to that of uncoated, clean chips, indicating no reduction in adhesion. The other 5 beams showed larger crack lengths, but they were distributed very unevenly because of the nonuniform coating on the substrate. Taken together, these observations led to the conclusion that, even under optimized conditions, gold nanorods cannot be deposited well as uniform films on various substrates, and the good reduction of adhesion expected cannot be achieved.

To understand the difference between the precipitation behaviors of nanoparticles and nanorods better, a theoretical calculation based on the interaction between various shapes during the GXL process was introduced. It has been proposed that during the GXL process, CO_2 is dissolved into hexane and both expands the volume of the liquid mixture and reduces the strength of the organic solvent effectively. This reduction in solvent strength reduces the stabilization effect of the ligands on nanoparticles. Once the solvent strength was reduced below the threshold for stabilization, the particles began to aggregate and precipitate out of solution, at which point the surface energy of the substrate affected the film formation mechanism. The substrate used in this system was a Si substrate with SiO_2 on the surface, the critical surface tension of which was approximately 140 dyn/cm. It was demonstrated in previous sections that this substrate results in the layer-by-layer mode of growth for the iron oxide nanoparticles. Therefore, the issue here was the way in which various nanoshapes tend to aggregate, which should be affected by the interaction energy of the system overall.

A total interaction energy model to correlate the solvent-ligand interaction with the maximum size of a ligand stabilized nanoparticle that can be dispersed within a given solvent system has been constructed by Shah, Kitchens and Saunders (Shah et al., 2002; Kitchens et al., 2003; Saunders et al., 2011b). The total interaction energy, Φ_{total}, is the sum of attractive and repulsive terms, including the van der Waals attractive potential, Φ_{vdW}, the osmotic repulsive potential, Φ_{osm}, and the elastic repulsive potential, Φ_{elas}.

$$\Phi_{total} = \Phi_{vdW} + \Phi_{osm} + \Phi_{elas} \tag{4.19}$$

The analysis begins with a simple situation: the total interaction energy for two nanospheres separated by a certain distance. The van der Waals attractive potential (Hamaker, 1937), a simplified form of which is given in Equation 4.20, increases with an increase in nanoparticle radius or with a decrease in the center-to-center separation distance between the nanoparticles.

$$\Phi_{vdW} = -\frac{AR}{12D} \tag{4.20}$$

where A is the Hamaker constant, R is the nanoparticle radius, and D is the surface-to-surface separation distance.

For the repulsive contribution, osmotic and elastic repulsive terms are introduced for the total interaction calculations (Vincent et al., 1980; Vincent et al., 1986). These two repulsive

terms, which originate from "soft sphere" theory, are used for the total interaction energy to balance the van der Waals forces of attraction between nanoparticles (Shah et al., 2002).

The osmotic term is related to the change in solvation of the ligand tails between nanoparticles, which depends on the free energy of the solvent-ligand tail interactions. This interaction is calculated based on the ligand tail length and the surface-to-surface distance (Equations 4.21 and 4.22).

$$\Phi_{osm} = \frac{4\pi R k_B T_e}{v_{solv}/N_A}\phi^2\left(\frac{1}{2}-\chi\right)\left(l-\frac{D}{2}\right)^2 \qquad for\ l < D < 2l \qquad (4.21)$$

$$\Phi_{osm} = \frac{4\pi R k_B T_e}{v_{solv}/N_A}\beta\phi^2\left(\frac{1}{2}-\chi\right)\left[l^2\left(\frac{D}{2l}-\frac{1}{4}-\ln(D/l)\right)\right] \qquad for\ D < l \qquad (4.22)$$

where v_{solv} is the molar volume of the solvent, l is the ligand length, φ is the ligand volume fraction, and χ is the Flory-Huggins interaction parameter.

The ligand volume fraction, φ, is defined as a function of the ligand surface coverage, Γ:

$$\phi = \Gamma\left[\frac{3R^2 l}{(R+l)^3 - R^3}\right] \qquad (4.23)$$

where the value of Γ is assumed to be 0.75 (Saunders et al., 2011b).

The Flory-Huggins interaction parameter, χ, is a function of the Hildebrand solubility parameter of the solvent and ligand:

$$\chi = \frac{v_{solv}}{R_i T_e}\left(\delta_{solv} - \delta_{lig}\right)^2 \quad (4.24)$$

where R_i is the ideal gas constant, and δ_{solv} and δ_{lig} are the Hildebrand solubility parameters of the solvent and ligand, respectively.

The elastic term results from the entropic losses from the compression of ligand tails present between two nanoparticle cores:

$$\Phi_{elas} = \frac{2\pi R k_B T_e l^2 \phi \rho}{MW}\left\{\frac{D}{l} ln\left[\frac{D}{l}\left(\frac{3 - D/l}{2}\right)^2\right] - 6ln\left(\frac{3 - D/l}{2}\right) + 3\left(1 - \frac{D}{l}\right)\right\} for\ D < l \quad (4.25)$$

where ρ is the density of the ligand (0.854 g/mL), and MW is its molecular weight (202.4 g/mol).

Based on these calculations, contributions to the total interaction energy from the attractive and repulsive terms were calculated for nanoparticles of 5 nm and 20 nm. The relative contributions of these potentials are shown in Figures 4.42 and 4.43 as a function of the surface-to-surface separation distance, D. It can be seen that nanoparticles of both sizes showed a minimum energy at 2 nm, which is twice the ligand length, and differs depending on nanoparticle size. The lower this minimum energy, the less stable the nanoparticles become, and

their tendency to precipitate is greater when the stabilization effect of the solution is reduced. As in Figures 4.42 and 4.43, the minimum energy for nanoparticles of 5 nm was -4.7k_BT, while this value was -16.9k_BT for nanoparticles of 20 nm. This indicates that nanoparticles of larger diameters tend to aggregate and precipitate when they are brought close together, which is affected by the concentration of the initial solution. This is consistent with previous results from nanoparticle coatings of AuNPs at different concentrations.

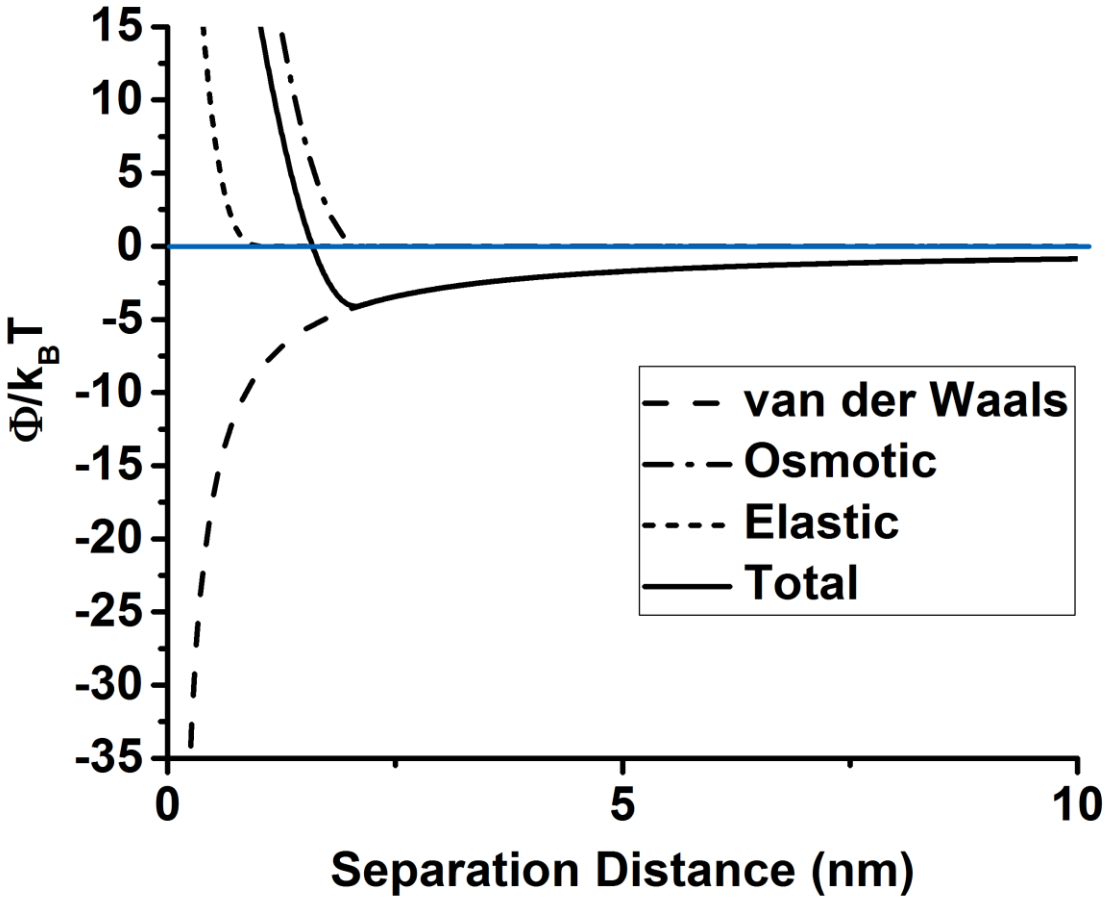

Figure 4.42. Attractive and repulsive potentials that contribute to the total interaction energy for 5 nm oleic, acid-stabilized, iron oxide nanoparticles.

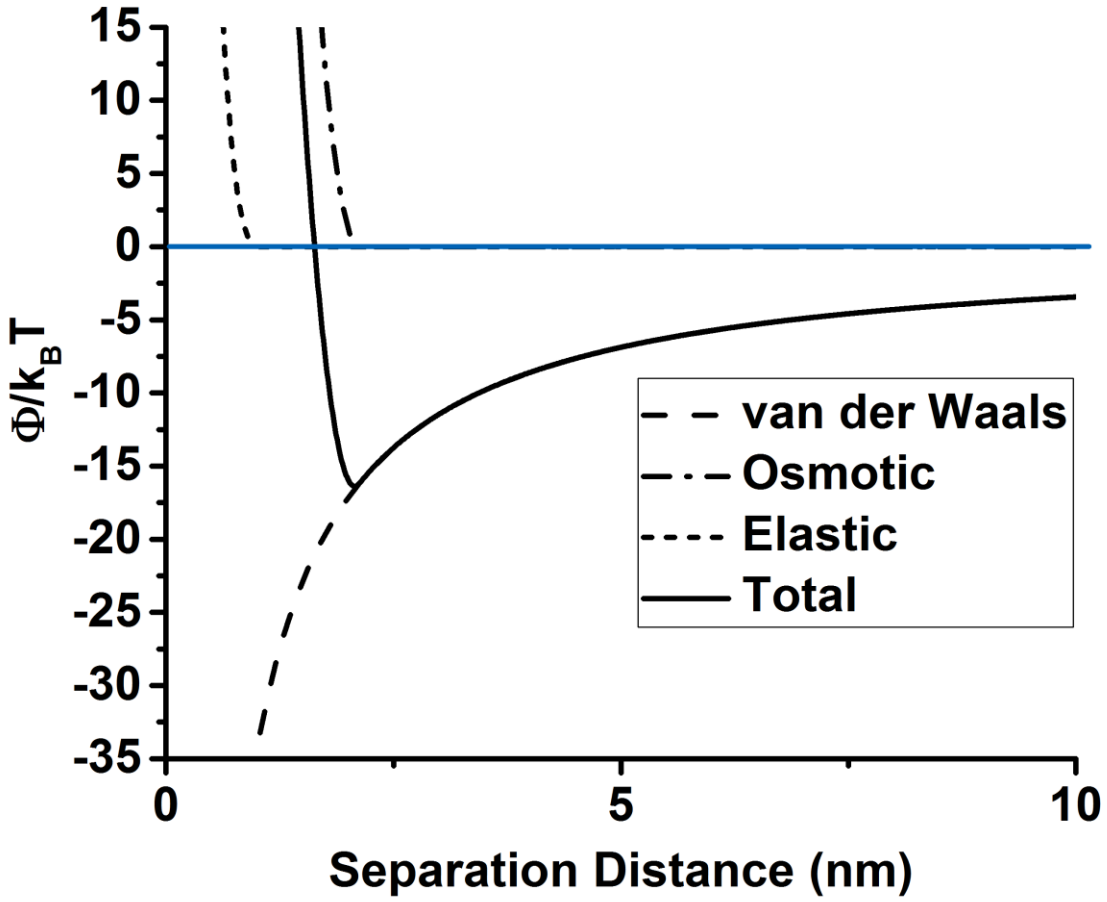

Figure 4.43. Attractive and repulsive potentials that contribute to the total interaction energy of 20 nm oleic, acid-stabilized, iron oxide nanoparticles.

Next, we considered the total interaction energy of the nanorods. Because nanorods have a nonuniform particle geometry, key parameters that influences their packing behavior, the attractive force and steric interaction, will differ from that of nanospheres. It has been reported that assembly of gold nanorods shows certain organized structures and two typical packing orientations, the end-to-end (EE) and side-to-side (SS) configurations (Figure 4.44). For these two configurations, calculation of the total interaction energy follows previous theoretical models with some assumptions. The nanorod is now treated as a superposition of a series of

spheres with the spherical center distance equal to the radius (Xie et al., 2011). The total energy calculation also is based on this superposition assumption (Figure 4.45).

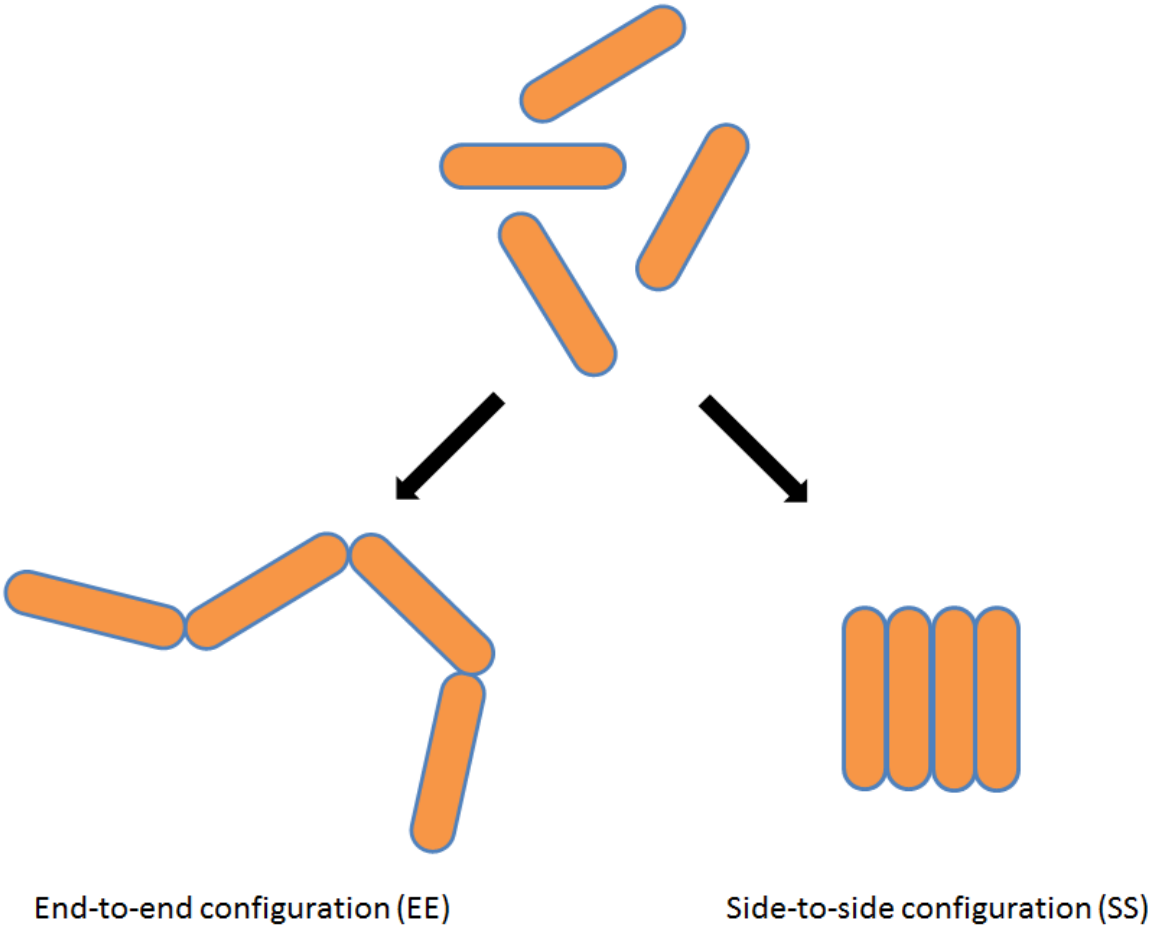

Figure 4.44 Scheme of gold nanorods assembly: end-to-end (EE) configuration and side-to-side (SS) configuration.

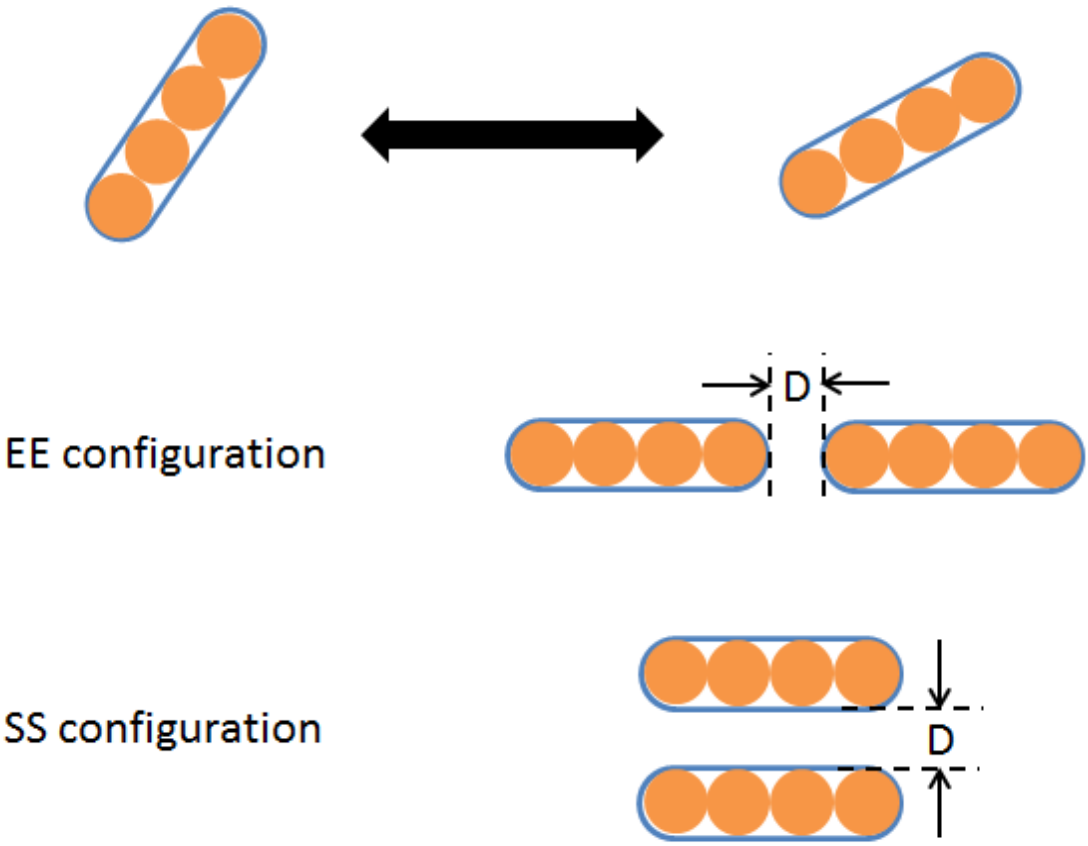

Figure 4.45. Superposition assumption used in the total energy calculation for gold nanorods.

Contributions to the total interaction energy from the attractive and repulsive terms were calculated for two gold nanorods with EE and SS assemblies, respectively, the geometric parameters of which were based on the gold nanorods used in this chapter. The relative contributions of these potentials are shown in Figures 4.46 and 4.47 as a function of the surface-to-surface separation distance, D. It can be seen that, compared to the nanoparticles, the total energy of the nanorods in both configurations is lower, indicating that the interaction between nanorods is greater. The minimum energy for the EE assembly was -6.8k_BT, while that for the SS assembly was -24.5k_BT. Such a huge difference in the total energy indicates that the SS

assembly of the gold nanorods is thermodynamically more favorable than that of the EE assembly.

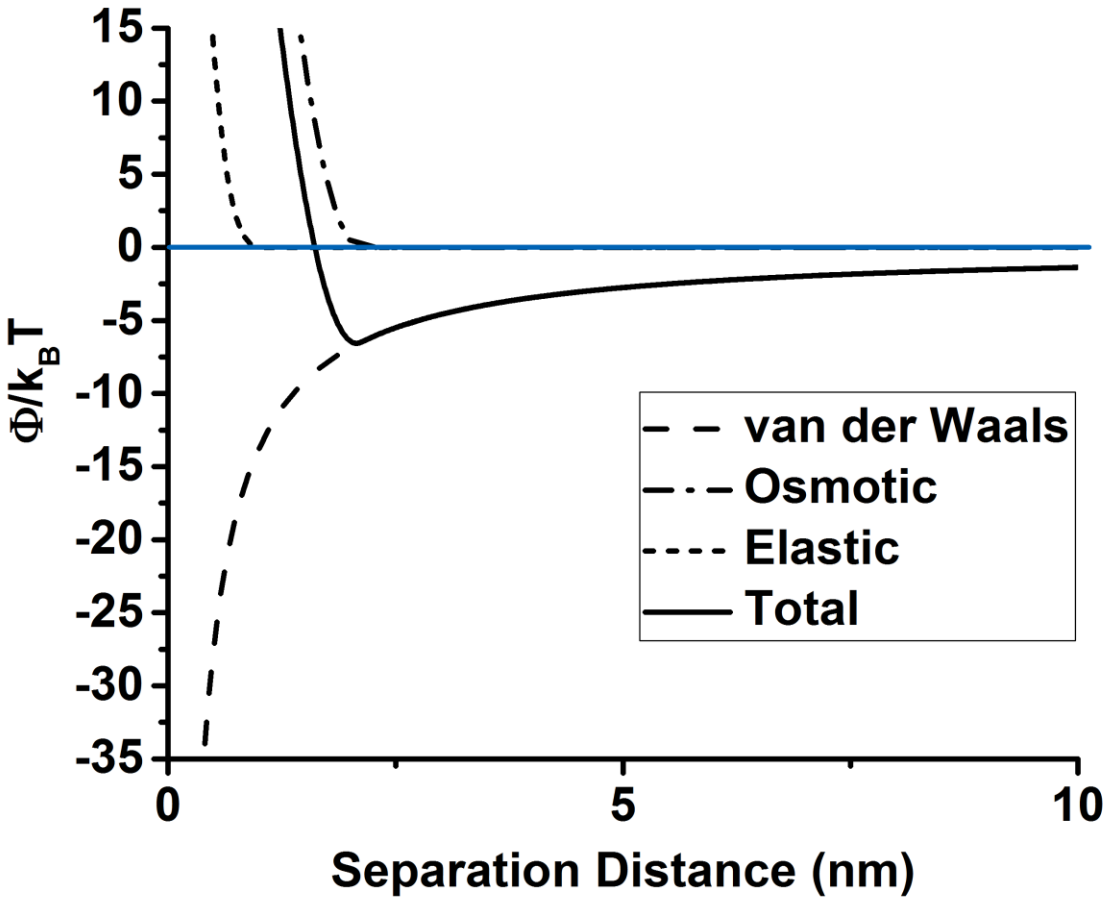

Figure 4.46. Attractive and repulsive potentials contributing to the total interaction energy for end-to-end (EE) assembly of gold nanorods.

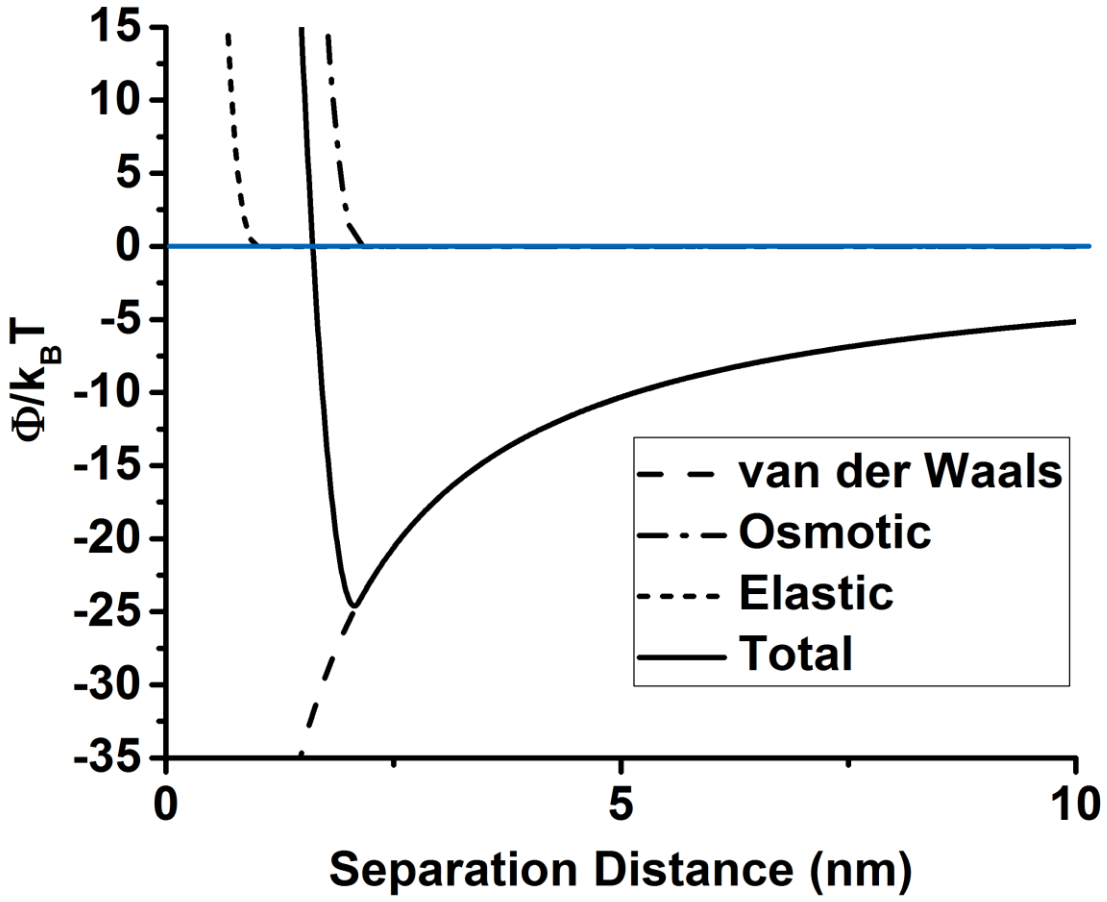

Figure 4.47. Attractive and repulsive potentials contributing to the total interaction energy for side-to-side (SS) assembly of gold nanorods.

When the nanostructure solutions were used in the GXL process and applied under various pressures of CO_2, the system became more complex. To calculate the total energy, several parameters had be changed. Gas-expanded liquids are mixtures of two solvent

components; therefore, the Hamaker constant should be calculated based on a three-component system, which is affected by the volume fraction of each component in the solvent mixture. A more important change is the nature of the interaction between the ligand tails and the solvent. It has been shown that adding an antisolvent decreases the solvent strength and reduces the solvent-ligand interaction. The Limited Ligand Length Solvation Model (LLLSM) was considered, which describes the reduction of ligand-solvent interaction, where the effective ligand length decreases with an increase in the CO_2 concentration because the weaker solvent mixture is unable to solvate the ligand tails completely (Saunders et al., 2011b). This extends the total ligand length, but only part of it interacts with the solvent because only a portion of its length contacts the solvent. This change does not affect the van der Waals interaction, but has a significant effect on the osmotic and elastic repulsive terms.

The total interaction energy of various nanoshapes in pure solution and under GXL conditions (an applied CO_2 pressure of 500 psi) is plotted in Figures 4.48 to 4.51. For all nanoshapes used in this system, the total energy had a lower shift after the GXL process was applied, and the threshold separation distance at which there is minimum interaction energy decreased due to the reduction of ligand length by the LLLSM assumption. From the plots, it is clear that, as the overall size increased, the change in the minimum interaction energy became more significant, leading to the conclusion that larger nanoshapes become unstable more easily when the particle-solvent and particle-particle interactions are affected. For the comparison of nanorods, the SS configuration had the largest energy gap between the pure solvent and GXL process, at approximately $16.9k_BT$. The SS assembly and aggregation of gold nanorods can be attributed to the balance of the van der Waals attraction and the short-range osmotic and elastic repulsion. The GXL process broke the balance and, because of the strong tendency to assume the

SS assembly, led to the attraction of gold nanorods, which appeared to be an isolated aggregation even at a very dilute concentration.

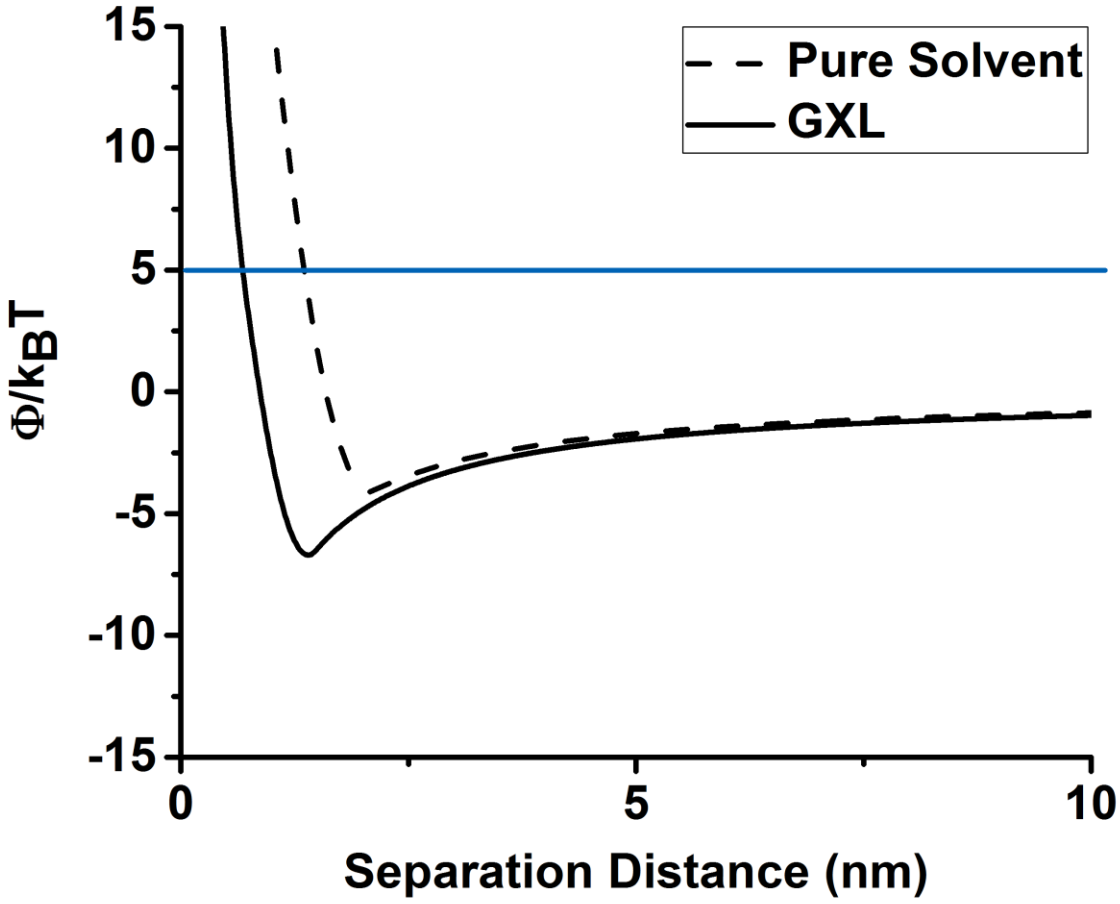

Figure 4.48. Comparison of total energies for 5 nm iron oxide nanoparticles in pure solvent and under GXL condition.

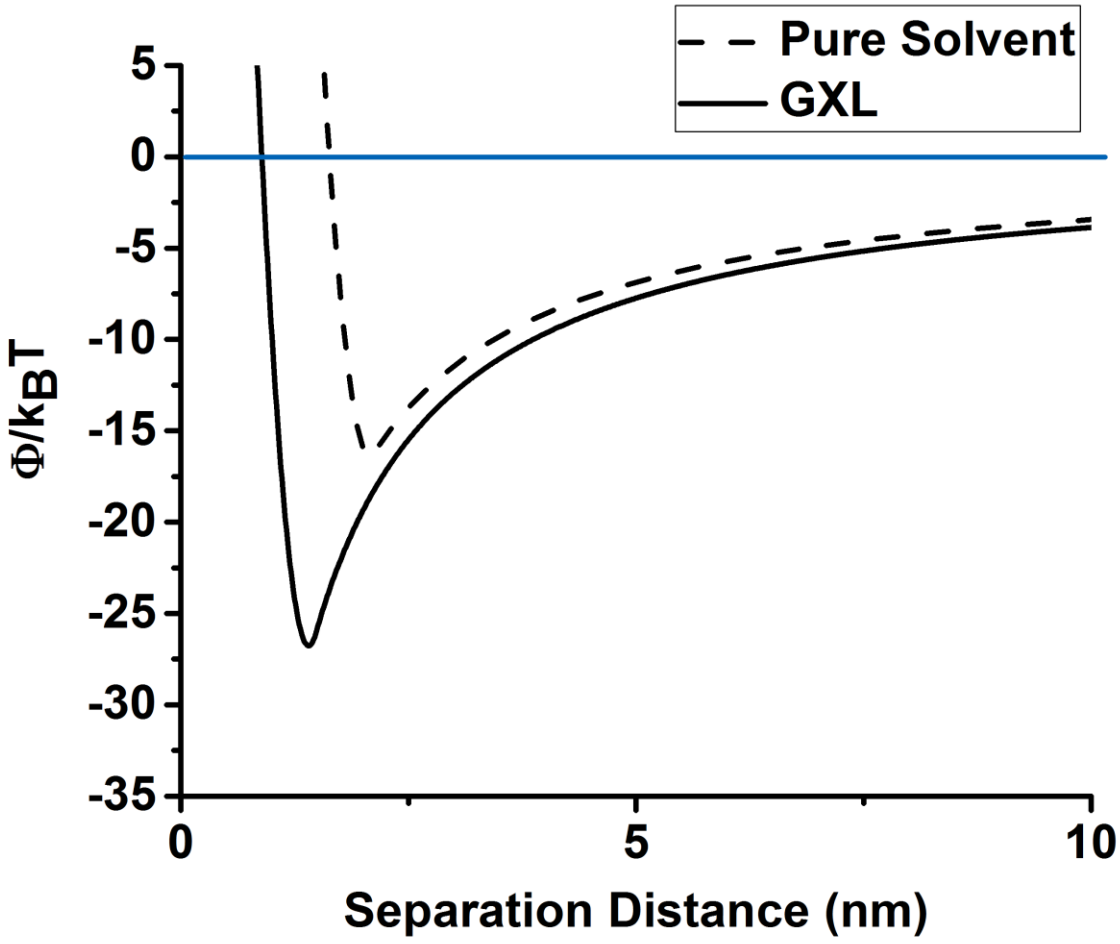

Figure 4.49. Comparison of total energies for 20 nm iron oxide nanoparticles in pure solvent and under GXL condition.

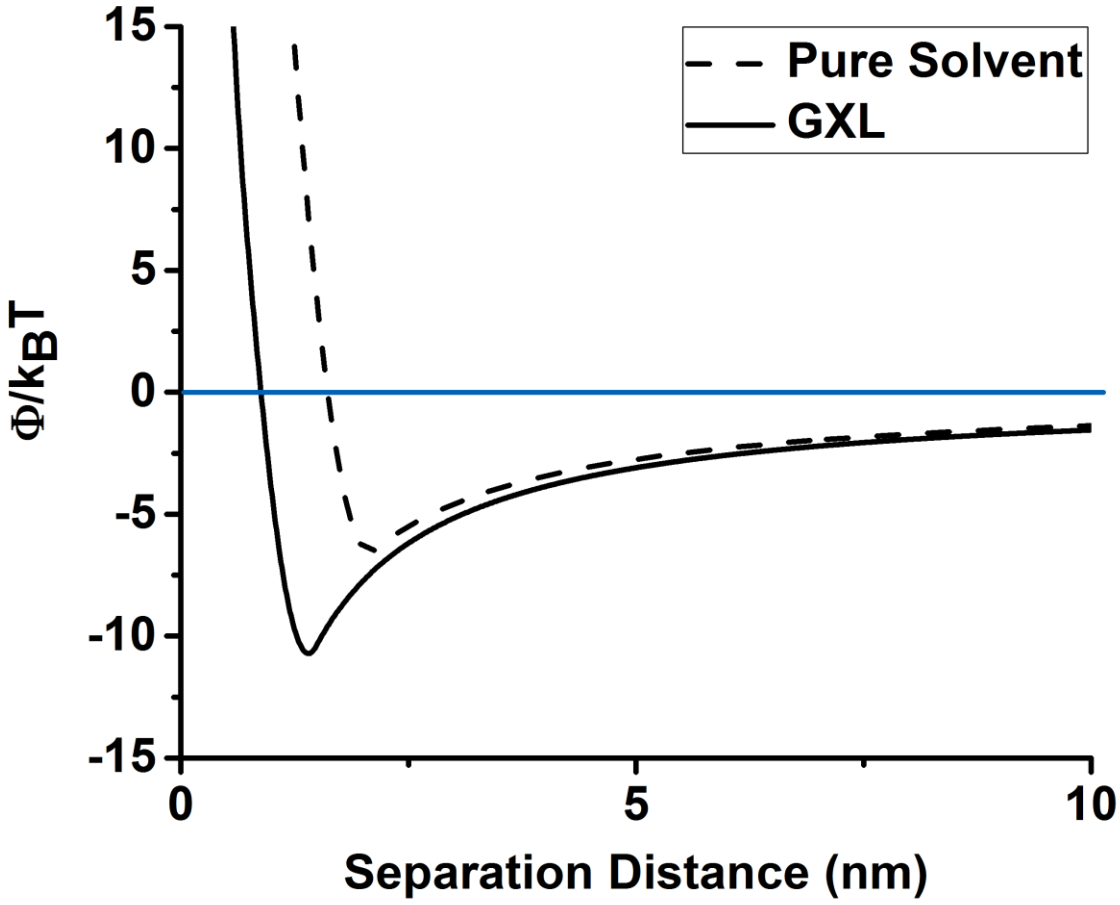

Figure 4.50. Comparison of total energies for gold nanorods with end-to-end (EE) assembly in pure solvent and under GXL condition.

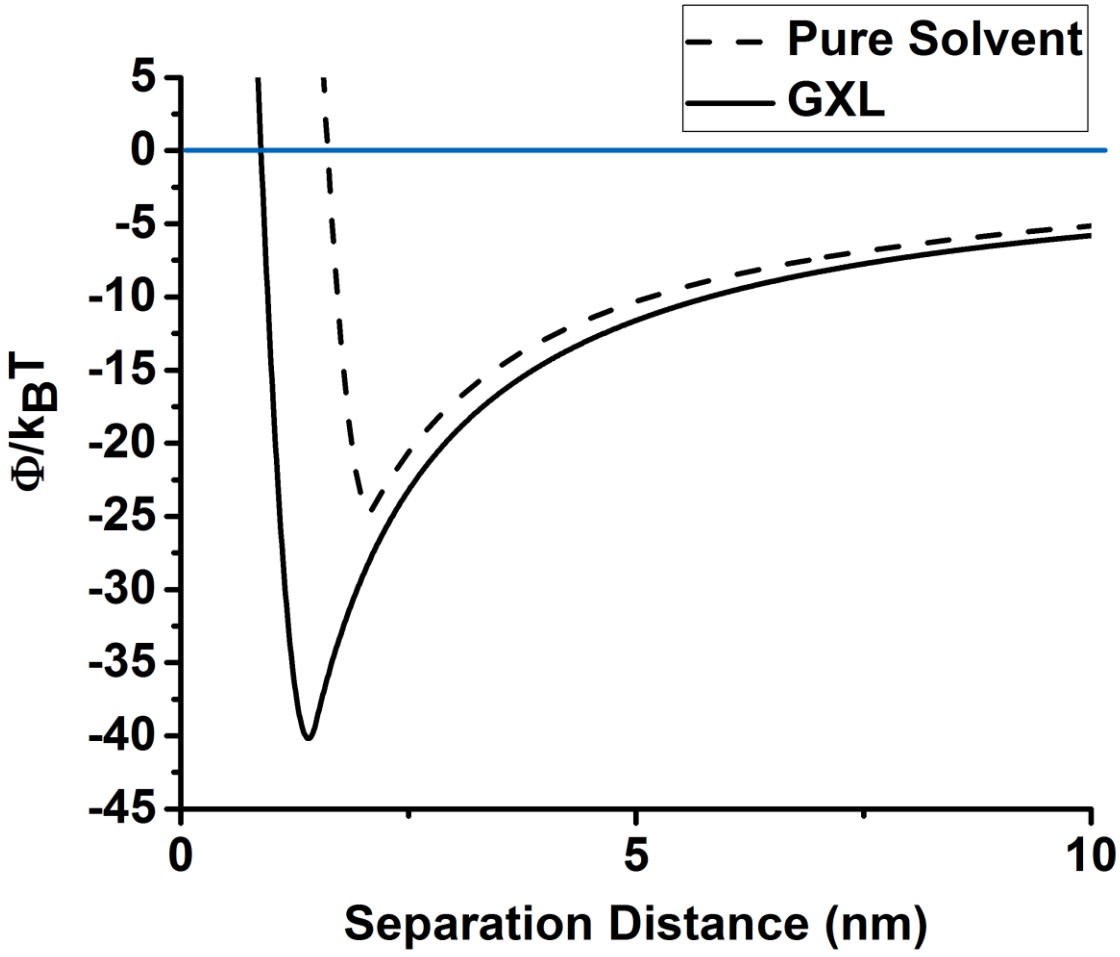

Figure 4.51. Comparison of total energies for gold nanorods with side-to-side (SS) assembly in pure solvent and under GXL condition.

Gold nanorods were used in a GXL deposition technology to coat the surfaces of MEMS devices. However, rather than the uniform nanocoatings that have been obtained with nanoparticles, only isolated aggregates existed on the surface. Test results showed that gold nanorods cannot be deposited well as uniform films on various substrates and the expected good reduction of adhesion cannot be achieved. To investigate this effect further, a total interaction

energy model was introduced to simulate the interactions between various nanoshapes and correlate the solvent-ligand interaction with the maximum size of a ligand-stabilized nanoparticle that can be dispersed within a given solvent system. The calculation results indicated that larger nanoshapes become unstable more easily when the particle-solvent and particle-particle interactions are affected. For gold nanrods, the SS configuration is more favorable when the nanorods become unstable and precipitate from the solution, leading to aggregation even at a very dilute concentration. Therefore, it is still possible to coat nanoshapes, but a better design based on the surface chemistry of the nanostructures is required.

4.4 Conclusion

The surfaces of MEMS devices were coated uniformly with size-varied iron oxide nanoparticles via GXL deposition technology. The mean plane separation distance between two surfaces in contact increased, while the contact area was reduced by altering the summit density and radius, which sdre affected by the average size of the initial nanoparticles. Based on the experimental results and theoretical calculations, the decrease in plane separation lowerdc the retarded van der Waals interaction, diminishing the non-contacting portion's contribution to adhesion; on the other hand, normal van der Waals interactions between contacting asperities sdre affected by the combination of the average summit density and radius, which plays the dominant role in adhesion. Changing these parameters affected the total effects of normal and retarded van der Waals interactions between contacting asperities, leading to reduced adhesion.

Because the apparent work of adhesion can be reduced by using iron oxide nanoparticles of larger average diameter, it is worth investigating the adhesion reduction effects that result from varying the initial concentration of monodispersed, 20 nm iron oxide nanoparticles to see whether the size and the concentration effects can be combined for better adhesion reduction. When the initial concentration of monodispersed, 20 nm iron oxide nanoparticle solutions was varied via GXL deposition technology, the surfaces of MEMS devices could be coated uniformly with these nanoparticles. Because of the high surface tension of the substrate, the film formation of the nanoparticles followed the Frank-van der Merwe growth mechanism and led to the appearance of a surface covered in part with monolayer island structures. The size effect of the nanoparticles on the reduction of adhesion still existed; however, the contribution of adhesion now derived primarily from the van der Waals interaction between the nanoparticle monolayers. Based on the experimental results and theoretical calculations, the surface coverage increased as the initial concentration increased, while the surface film growth was limited at the sub-monolayer level; this led to an increase of the apparent work of adhesion, which derived from the greater interaction area when two surfaces were brought close. This proved that under different surface topographical conditions, it is essential to reduce the total contact area to reduce adhesion and maintain sufficient long-range roughness.

Gold nanorods also were used via GXL deposition technology to coat the surfaces of MEMS devices. However, rather than the uniform nanocoatings that have been obtained with nanoparticles, only isolated aggregates formed on the surface. Test results showed that gold nanorods cannot be deposited well as uniform films on various substrates and the good reduction in adhesion expected cannot be achieved. To understand this effect better, a total interaction energy model was introduced to simulate the interactions between various nanoshapes and

correlate the solvent-ligand interaction with the maximum size of a ligand-stabilized nanoparticle that can be dispersed within a given solvent system. The results indicated that larger nanoshapes become unstable more easily when the particle-solvent and particle-particle interactions are affected. For gold nanorods, the SS assembly is more favorable when the nanorods become unstable and precipitate from the solution, leading to aggregation even at very dilute concentrations. Therefore, while it is still possible to coat nanoshapes, a better design based on the surface chemistry of the nanostructures must be considered.

Chapter 5

Durable commercial nanoparticle-based composite coatings

5.1 Introduction

Technologies such as CVD and ALD enable nanoparticle film deposition with good uniformity and precise control. Their primary scientific merits include maintaining film quality and improving the efficiency of the process. In addition, chemical stability and failure mechanisms must be determined. Potential improvements in the CVD process include introducing varying functional end-group terminated silanes to increase the reactivity of the CVD precursors. The modified VPD apparatus is able to produce aluminum oxide nanoparticles from a gas phase reaction that can then be anchored and coated by SiO_2 and hydrophobic layers. Superhydrophobic coatings have the potential to revolutionize not only the MEMS industry, but the consumer electronics industry as well. To achieve those goals, fundamental material characterizations of an optimal target structure and morphology are required. Because different application environments emphasize corresponding film properties, VPD-coated substrates are characterized by their durability, water-resistance, electrical and thermal properties, and other functions based on the requirements from customers. Atomic force microscopy, Fourier transform infrared spectroscopy, and other analysis techniques were used to assess the fundamental mechanisms of film formation and failure. The potential results will satisfy the commercial use of, and economic interest in such coatings in the market.

5.2 Experimental section

5.2.1 Nanoparticle film deposition

5.2.1.1 Coating substrate preparation

Small Si wafers were prepared by cutting large Si wafers into 1 cm square dies with a dicing blade. The Si wafers were ultrasonicated in acetone for 10 min, followed by isopropanol for 10 min, and then dried under a nitrogen stream. The wafers were etched for 10 min in concentrated HF to remove the native oxide layer, rinsed in excess deionized water, and then dried under a nitrogen stream. Next, the wafers were placed in a Novascan PSD-UVT UV Ozone Cleaner and cleaned via exposure to ultraviolet light and ozone for 15 min at ambient temperature. The wafers were then loaded into a custom-built vacuum deposition system, the design of which is described elsewhere (Anderson et al., 2008). Figure 5.1 shows a schematic diagram of the system used in this work, which consists of a rotary vane pump connected to a glass reaction chamber that contains electrodes to create in-situ, capacitively-coupled radio frequency (RF) plasma (13.56 MHz). This plasma is required for plasma cleaning and plasma-enhanced deposition. The glass reaction chamber also is connected to a vapor delivery system that allows the vapors of various volatile precursors to be introduced to the glass reaction chamber for future coating. MKS Baratron capacitance manometers monitor the system pressure.

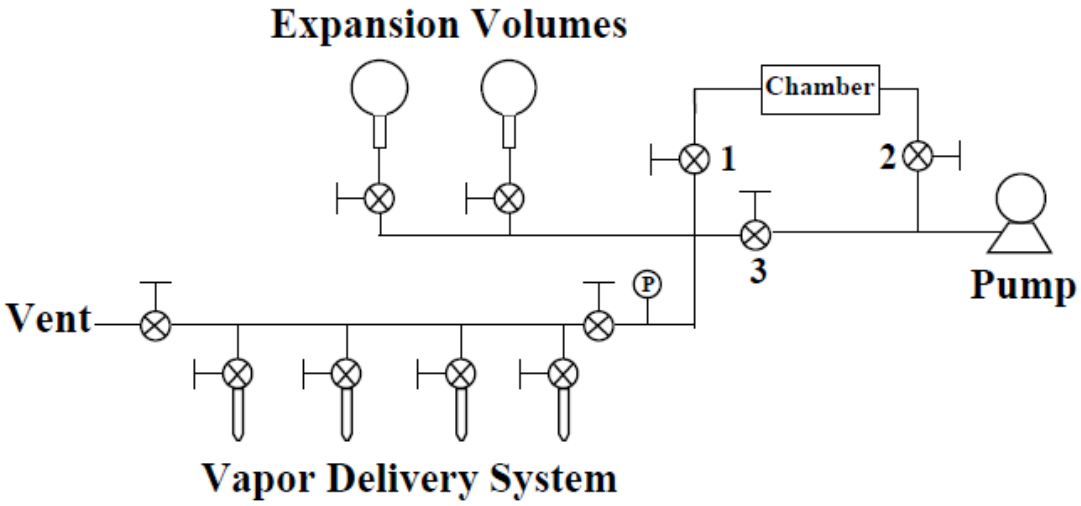

Figure 5.1. Schematic diagram of the chemical vapor deposition system (Anderson et al., 2008).

The wafer surface treatment was comprised of two steps, the first using air plasma, followed by water plasma. The air plasma treatment was used to reform the surface dioxide layer. The water plasma treatment is known to leave the surface hydroxyl group (-OH) terminated. The wafers were placed on an aluminum sample holder positioned within the chamber, underneath the lower (ground) perforated electrode. First, the pressure in the vacuum system was reduced to less than 30 mTorr. An air-gas background was created by performing purge cycles with air. Then, air was allowed to flow into the chamber. When the chamber pressure reached 1 Torr, the air flow was stopped and the pressure in the vacuum system was reduced to approximately 300 mTorr. Next, plasma was struck to the perforated electrodes; these conditions were maintained for 10 min. After the air plasma treatment was completed, the pressure of the entire system was returned to base pressure and the chamber was dosed with water vapor from the vapor delivery system to replace the air. A similar water plasma treatment was conducted for 10 min. Plasma treatment of wafers results in clean, flat surfaces free from

organic contaminants. This cleaning method was repeated until inspection via contact angle measurement indicated that the water contact angle was less than 5°. Typically, two iterations were sufficient. AFM analysis of the cleaned Si (100) wafer dies showed no significant height variation. Combined with the contact angle results, this indicated that a relatively clean, smooth, silica surface had been prepared. Ellipsometry measurement showed that a silica layer of approximately 20 Å formed on the Si (100) wafer dies.

5.2.1.2 Preparation of fumed silica support

Cellulose cotton balls were used as support templates. A silica layer was deposited onto the cotton balls using the vacuum system described above. Deionized water and tetrachlorosilane were loaded into clean glass vials and then connected to the vapor delivery system. The precursors were degassed via three freeze-pump-thaw cycles using liquid nitrogen. The cotton balls were then loaded into the vacuum deposition system and cleaned with the plasma treatment process described previously. After the plasma treatment, the pressure in the chamber was again reduced to less than 30 mTorr. Water vapor was allowed to flow into the chamber until it reached approximately 4 Torr. Tetrachlorosilane was admitted into the chamber to increase the total pressure to approximately 8 Torr, and the reaction was allowed to proceed for 10 min. This water-tetrachlorosilane reaction completed one silica layer coating cycle. For the best results, ten cycles were completed before the cotton balls were removed from the vacuum chamber. The resulting silica-layer thickness was approximately 1 μm, as measured via ellipsometry on a reference Si wafer. After removal from the vacuum system, the silica-coated cotton balls were

loaded into a furnace and heated to 700 °C in air; this temperature was maintained for 4 h. This heat treatment removed the cellulose template, leaving a thin, white, fibrous material that constituted the fumed silica support. Figure 5.2 shows a picture of a cellulose cotton ball before treatment and the fumed silica support after removal of the cellulose.

Figure 5.2. Cellulose cotton ball before treatment (left) and silica support following cellulose removal (right).

Thermal treatment of silica surfaces at this temperature causes adjacent surface silanols to bridge bond and form new Si-O-Si bonds, leading to lower reactivity of the silica surface in response to silane deposition. To reverse this effect, the fumed silica support was placed in the vacuum deposition chamber and treated with an additional silica layer coating cycle, followed by

the essential plasma treatment to reactivate the surface with available surface silanols. Figure 5.3 shows a scanning electron microscopy (SEM) image of the silica support surface after treatment. The support is a fibrous-like material with a low degree of curvature, an average fiber width of approximately 10 μm, and a length on the scale of hundreds of micrometers.

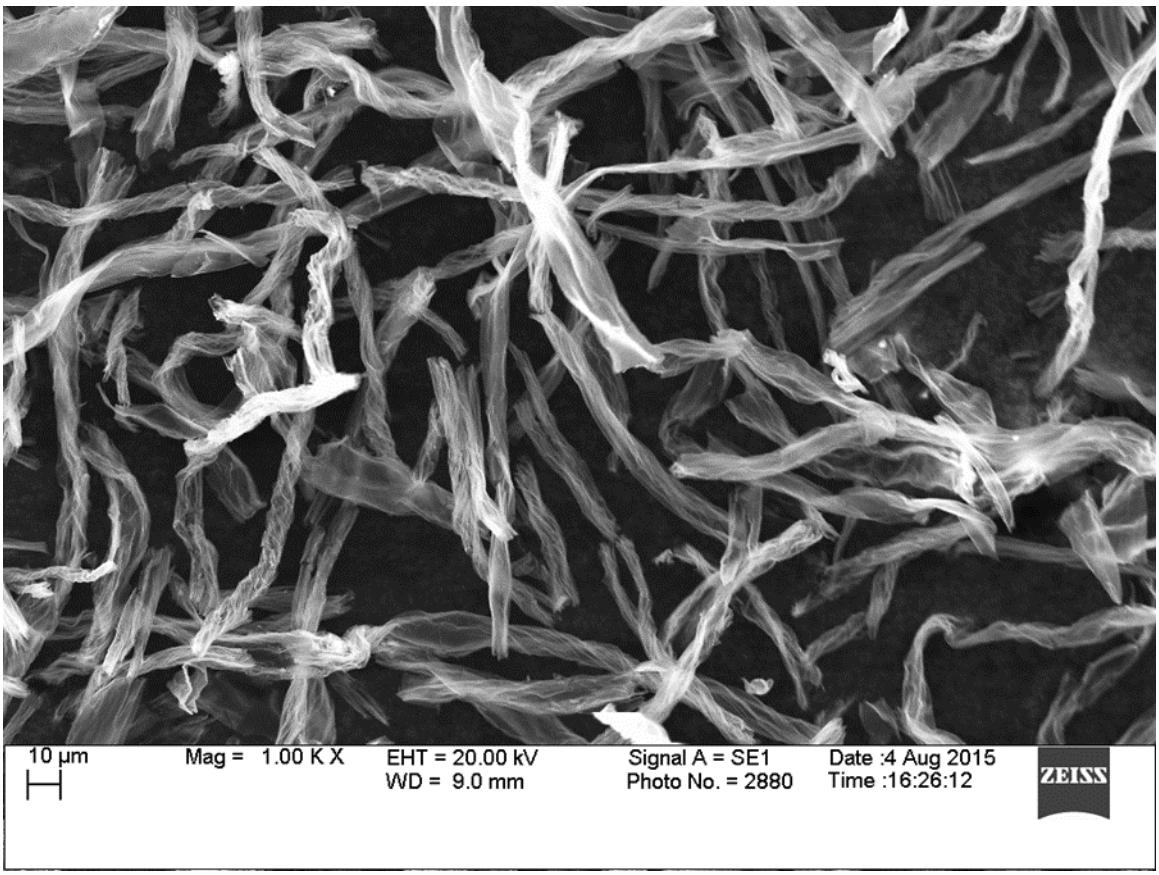

Figure 5.3. SEM image of silica support after treatment.

5.2.1.3 Vapor deposition of self-assembled monolayers

The silane coating was deposited via a similar procedure to that mentioned in the previous subsection. After the clean Si wafer or fumed silica support was loaded into the chamber, the chamber pressure was reduced to less than 30 mTorr. Excess water and precursor gases were preloaded to the expansion volume. The water gas was first allowed to flow into the chamber until the pressure exceeded 5 Torr. Then, the chamber was evacuated until the water pressure desired was reached (the required pressure varied for different precursors), and isolated from the pump. Next, the precursor gas was introduced from the expansion volume to the chamber. The reaction was conducted for 10 min before the chamber was evacuated via pumping, and purged with air. The coated samples were removed from the chamber and were then ready for testing. The coating conditions for the precursors employed in this study are listed in Table 5.1.

Precursor	Precursor pressure in expansion chamber (mTorr)	Water pressure in main chamber (mTorr)
C8-OTS	1000 ± 100	2000 ± 200
FOTS	500 ± 100	1000 ± 100
DDMS	1000 ± 100	2000 ± 200

Table 5.1. Coating conditions for SAM precursors.

For comparison, a liquid-based DDMS coating was also deposited onto a clean Si wafer via a method similar to that for other chlorosilanes. A 1 mM solution of DDMS in hexane was prepared and then set aside for 30 min to allow the silane to hydrolyze. After hydrolysis, the clean Si wafers were immersed in the solution for 45 min. Then, the coated Si wafers were rinsed several times and ultrasonicated in hexane to remove any precursor adsorbed physically. Following all substrate rinsing procedures, the coated wafers were dried under a nitrogen stream.

5.2.1.4 Commercial VPD coating

For commercial coating practices, a system called Beta is used, the commercial name of which is the RPX-540 Vapor Deposition System (Figure 5.4). The nanoparticle composite film used in this study was created using a hybrid atomic layer deposition (ALD)/chemical vapor deposition (CVD) treatment. During this process, the organic precursor was oxidized to form nanoparticles that were deposited on the substrate in the vapor phase. Subsequently, the nanoparticle films were encapsulated in a cross-linked matrix to improve their durability. The film structure is shown in Figure 5.5.

Figure 5.4. Beta system for CVD/VPD nanoparticle coating.

The system deposits customized nano-composite structures through a hybrid VPD/CVD process. Up to 5 precursors can be applied sequentially to create a variety of specialty films for specific applications. Vapors from heated precursors are controlled precisely and metered uniquely by injector valves. The system runs procedures similar to the lab-level chemical vapor system. It is controlled by a LabView-based software system with automatic process operation.

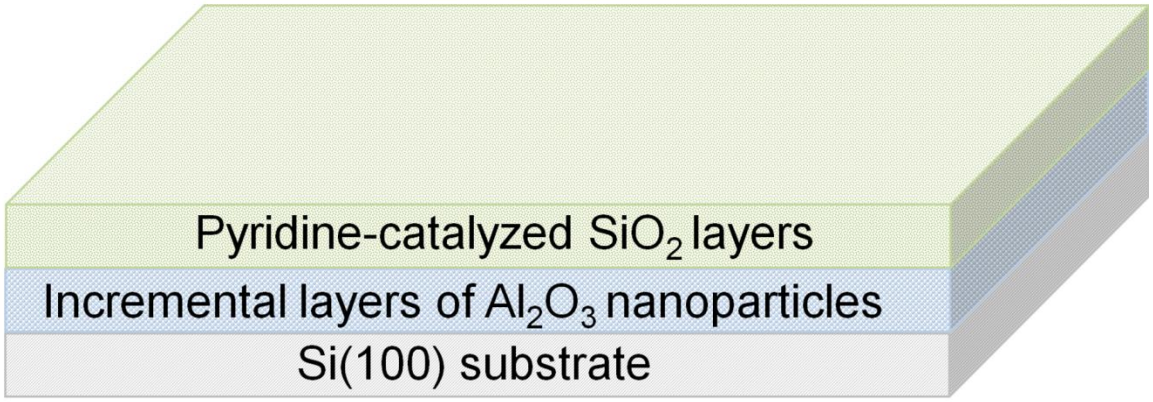

Figure 5.5. Structure of VPD-based commercial nanoparticle film.

5.2.2 Water durability test of superhydrophobic nanofilms

Figure 5.6 shows the experimental setup of the water erosion test apparatus. Tap water was used directly and the water stream was allowed to impinge on the samples, which were positioned at an angle of 45°. The flow rate of the water was changed for different samples. The distance between the nozzle and sample was fixed at 30 cm.

The test procedure was as follows. Because tap water was used, the flow rate had to be kept constant across different tests. Thus, before the test, how much of a beaker could be filled over a ten-second period was determined to ensure that the water flow rate always remained consistent; this process was performed before every run of the water erosion test. Each sample underwent an initial contact angle measurement using the Ramé-Hart Contact Angle Measurement System. Next, the surface of each sample was characterized with a Pacific Nanotechnology AFM. After all preparations, the sample was placed on the apparatus to begin

the water erosion test, which lasted 30 mins. The sample was then dried with nitrogen or helium gas. This characterization-erosion cycle was repeated several times until a total of 2 hours of water erosion was completed. After 2 hours, the water erosion time was increased to 1 hour and the entire process continued until either the sample failed (contact angle lower than 90º) or the total water erosion time reached 8 hours. A sample was considered stable if it could remain hydrophobic (contact angle greater than 90º) after 8 hours of water erosion.

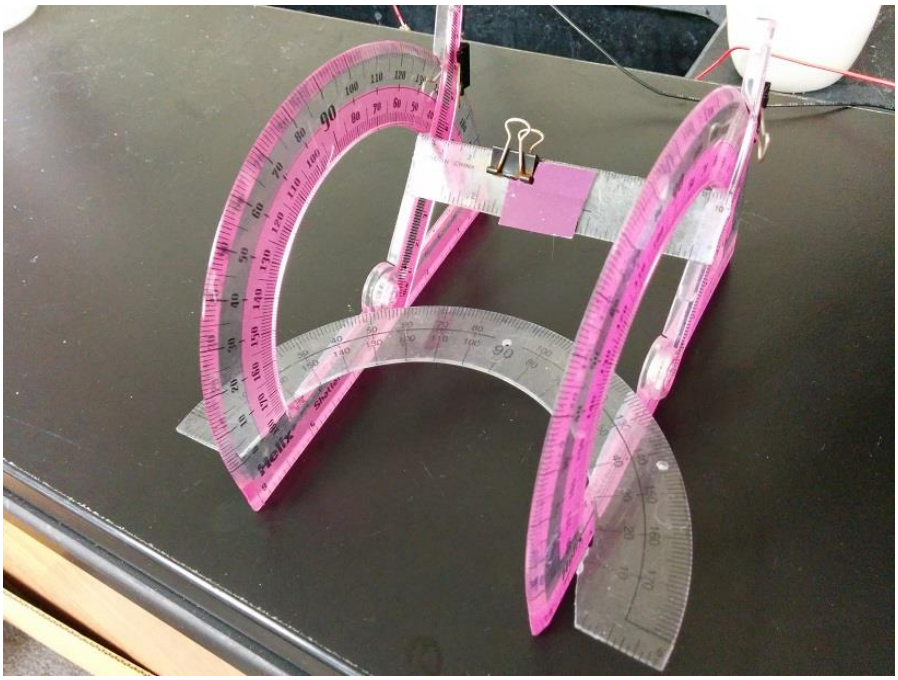

Figure 5.6. Experimental setup for water erosion test.

5.2.3 Heat stability test of superhydrophobic nanofilms

Four samples were chosen for testing: a cleaned, uncoated Si wafer, a sample with DDMS coating, a sample with FOTS coating, and a sample with C8-OTS coating. All SAM

coatings were deposited on a Si wafer. The sample substrates were kept in an oven under certain temperatures for 5 min. Then, they were removed from the oven and cooled, and the contact angle values were measured. The test was initiated at 100 °C and terminated at 600 °C, with the temperature increasing in increments of 25 °C.

A sample with SAM coating on a fumed silica support was prepared and subjected to TGA. The deposition process is described in the previous section. A Q50 TGA device (TA Instruments, DE) was used and, after deposition, the monolayer/silica support was placed in the TGA system in different environments (air or N2). The typical amount loaded was 10-12 mg of the OTS/fibrous silica support. The temperature was increased subsequently from 100 °C to 600 °C with a ramp rate of 10 °C /min and the thermal weight loss events were monitored.

The water contact angle values were measured using the sessile drop method, with a ramé-hart model 200 automated goniometer (ramé-hart, Inc., Mountain Lakes, NJ) and DROPimage Standard software. The measurement error of this system is specified as ±2°.

AFM images were collected on a commercial atomic force microscope (Nano-R AFM, Pacific Nanotechnology, Santa Clara, CA) in noncontact mode using silicon AFM tips with aluminum backside coating (NSC35/Al BS, MikroMasch, Wilsonville, OR). The typical resonant frequency was 155 kHz and the force constant was within the 1.7–14 N/m range. Images were collected at a 1 Hz scan rate and a sample rate of 512 pixels per line. The Gwyddion software package was used to process the images and acquire the parameters.

XPS data were collected using AXIS Ultra Delay Lines Detector X-ray photoelectron spectrometer (Kratos Analytical Ltd.). Samples were placed in load lock under 10^{-8} Torr vacuum, and then entered the analysis chamber, where they were analyzed under 10^{-9} Torr vacuum. A monochromatic Al Ka X-ray source was used as the photon source and the x-rays were at 90° relative to the analyzer. Broad survey spectra were collected for all samples. High-resolution spectra were collected for C 1s, O 1s, F 1s, Al 2p, and Si 2p using a passing energy of 20 eV. The analyzed core-level line shift from the surface charging was corrected using the reference C 1s level at 284.6 eV. The high-resolution, core-level elemental signals were analyzed using mixed Gaussian-Lorentzian functions with a fixed Lorentzian ratio of 20%. For quantitative analysis, relative sensitivity factors (R.S.F.) for corresponding elements were obtained from the AXIS Ultra document (C 1s: 0.296, O 1s: 0.711, Si 2p: 0.283, Al 2p: 0.234, Wanger et al., 1979).

Film thickness was measured on a Rudolph AutoEL III ellipsometer (Rudolph Research, Fairfield, NJ) equipped with a He-Ne laser (λ = 632.8 nm) at a 70° angle of incidence relative to the plain surface. The values used in the analysis were the averages of three measurements taken at three different positions on each sample.

5.2.4 Tin whisker growth test of superhydrophobic nanofilms

With the help of Dr. Bozack in the Department of Physics at Auburn University, Sn whiskers were coated on untreated substrates before our superhydrophobic nanocoating was applied. The Sn whiskers were grown on brass using a standard magnetron sputtering system that operated with various gas pressures of Ar, as reported elsewhere (Bozack et al., 2010). After the

tin whisker growth, both uncoated and coated samples were stored at atmospheric pressure and ambient temperature for months and then they were characterized by SEM.

5.2.5 Electromigration test of boards protected by superhydrophobic nanofilms

Our superhydrophibic coatings can be applied to devices for the commercial market. To test their practical performance in protecting boards, particularly for their effect on electromigration, an automatic 8-way board test system was designed.

The test system used a Raspberry Pi Model B with a Broadcom BCM2835 system-on chip that runs Linux as the main control. A GWInstek Multioutput Programmable Linear DC Power Supply GPD-2303S was used to control power output. For data acquisition, TI ADS1115 analog-to-digital converter (ADC) chips with 16 bits of resolution were used. To make it sufficiently flexible to test several boards simultaneously, an 8-channel DC 5V relay module also was integrated into the system. A schematic of the design and photo of the actual system are shown in Figures 5.7 and 5.8. Python scripts that run on the Raspberry Pi control the power supply output and relay switch while reading data from ADC chips, which provides various test environments for different boards.

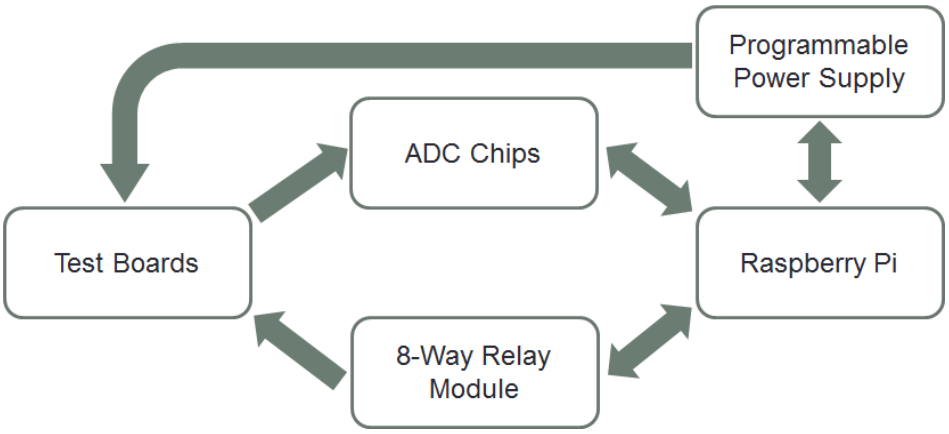

Figure 5.7. Schematic of the test system design.

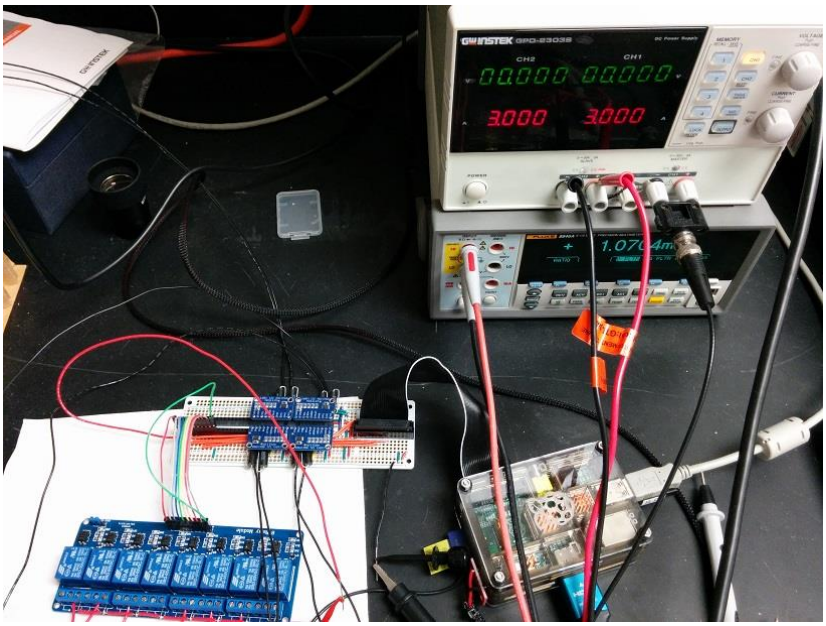

Figure 5.8. Photo of the actual test system.

The experimental process is as below. Simple electrical boards with special pattern designs were used throughout the test. Figure 5.9 shows a typical 25-mil pitch board design. 7-mil, 15-mil, and 25-mil pitch boards were all used to simulate actual designs. These boards were either uncoated or coated with our superhydrophobic coatings. The test was conducted by the automated data-collecting system based on Raspberry-Pi with DAQ chips. The board was

immersed under deionized water or other solutions and different voltage profiles can be applied on the board (constant voltage, step-increase voltage or linear-increase voltage). The test started at 0 V then a certain voltage profile was applied and kept for 90 minutes. The current values vs. time were recorded. The images of the board were automatically captured every 30 seconds by an Amscope MD800E Optical Microscope. The tested boards were further characterized by SEM.

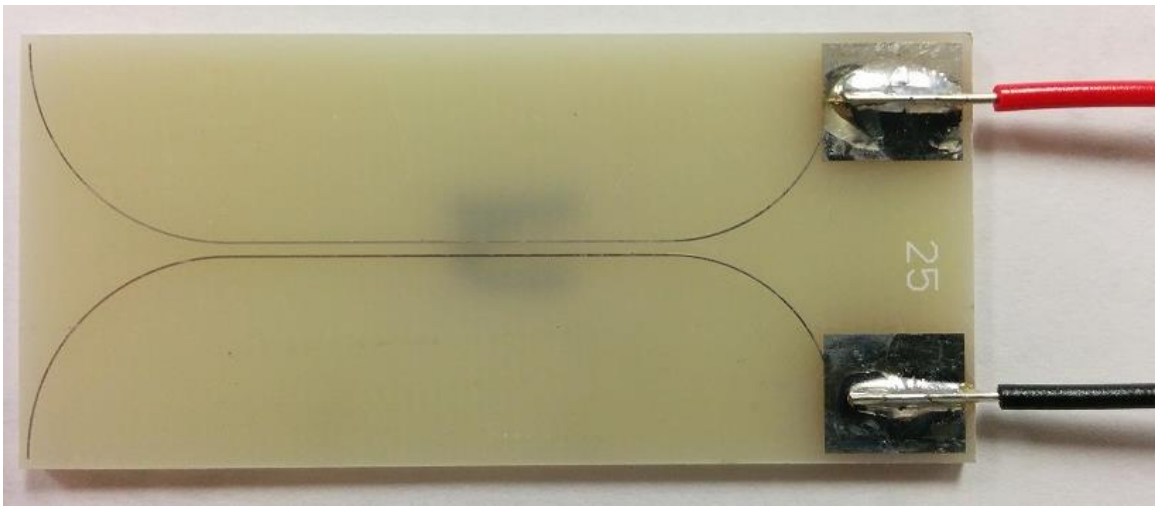

Figure 5.9. A test board with 25-mil pitch between two parallel metal lines in the middle.

5.3 Results and discussions

5.3.1 Nanoparticle films deposited by VPD system

Our superhydrophobic coatings were applied to either Si substrates or actual boards. Figure 5.10 shows a photo of uncoated and coated Si substrates.

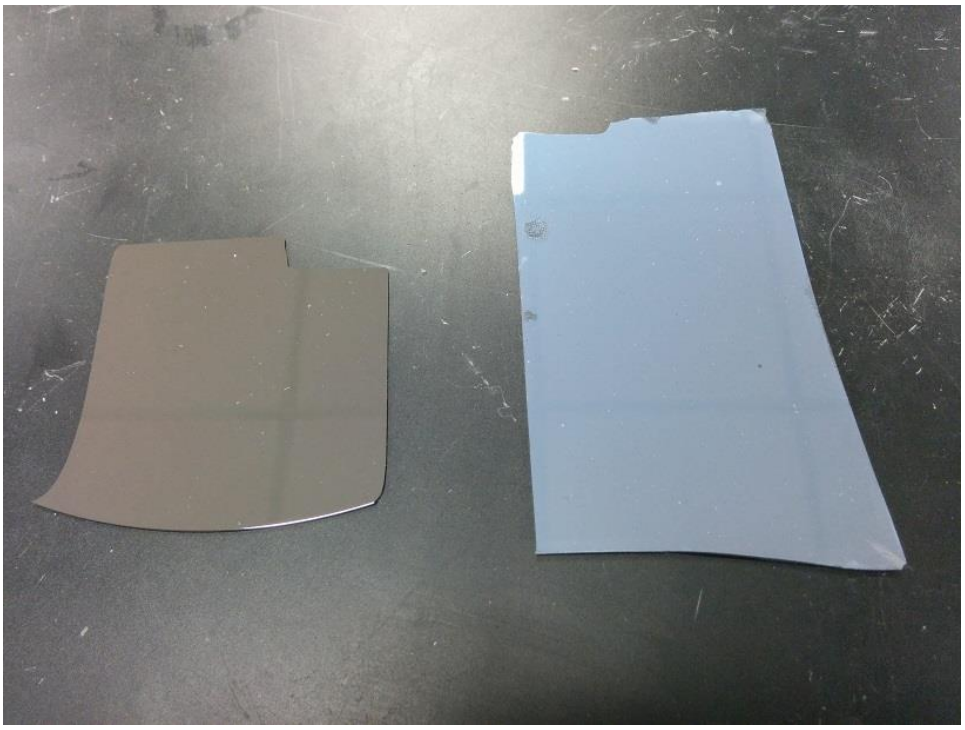

Figure 5.10. Uncoated Si substrate (left) and superhydrophobic coating deposited on Si substrate (right).

Figure 5.11 shows SEM and AFM images of a typical coating, which illustrate that the surface was relatively smooth at the macroscale. The peak height was several microns, and the surface roughness value was approximately 310 nm.

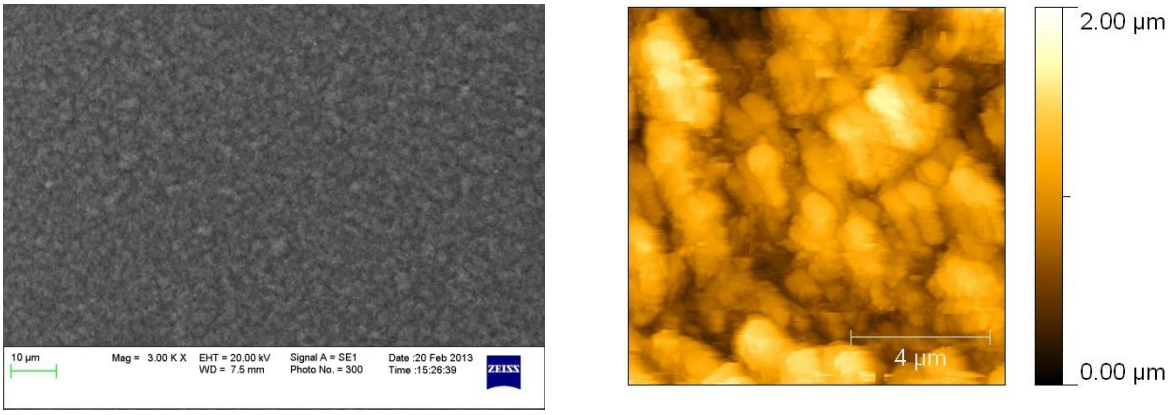

Figure 5.11. SEM and AFM images of the superhydrophobic coating.

Tests of the performance of the coatings will be discussed in the sections that follow; however, one property of the coatings should be mentioned here: their optical transparency. The more layers of film deposited on the surface, the better it will be protected. However, more layers reduce light transmittance through the coating, as shown in Fig 3.7, where the coated sample exhibits a significant color change compared to the uncoated one. The change in optical properties may be a potential disadvantage for applications, especially for coatings on optical-sensitive devices, such as cameras and lenses. Although the way in which the coatings affect the optical properties is straightforward and can be seen with the naked eye, a quantitative measurement should be introduced.

Therefore, the UV-Vis spectra of the coatings were measured to assess optical transparency. Transparent plastic cuvettes were coated with different nanocoatings and UV-Vis spectra were collected. Figure 5.12 shows the UV-Vis spectra of coatings with different numbers of layers. It is clear that as the number of layers increased, the transparency decreased, but it nonetheless remained at a relatively acceptable level within the visible light range (400-700 nm).

Therefore, whether a transparent film is needed depends on the customer's requirements. Under most circumstances, the performance of the film itself is the focus.

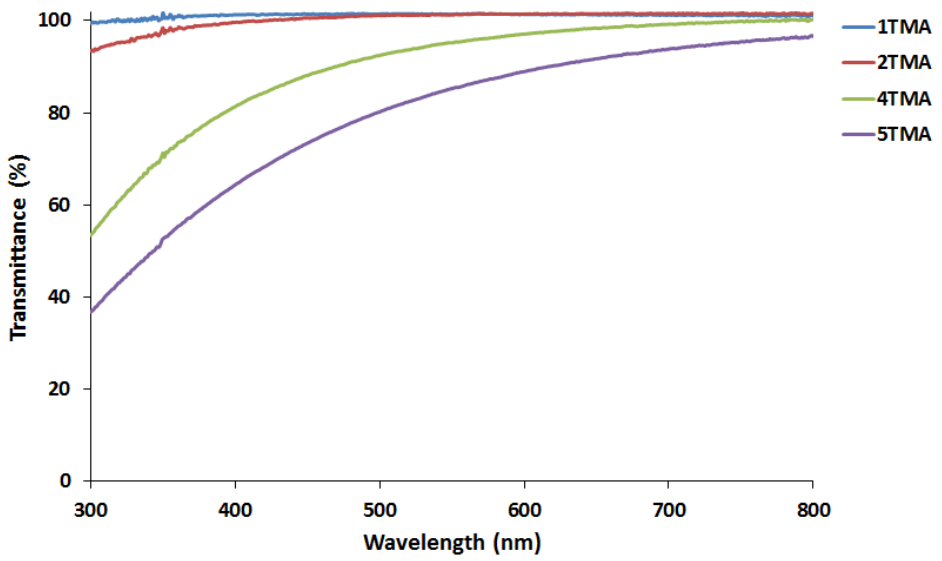

Figure 5.12. UV-Vis spectra of nanoparticle coatings of different numbers of layers. The number of layers increases from top to bottom.

5.3.2 Water durability of superhydrophobic nanofilms

A hydrophobic nanofilm is one in which the surface has a contact angle greater than 90º. Several different batches of samples with different coating recipes were evaluated for their water durability. The first batch of samples was a TMA-Amine-Gycidoxy series. This set of samples was tested under a very high flow rate, and all samples failed in less than 20 minutes. The total time that elapsed before each sample failed and the contact angle values are summarized in Table 5.2. The results show that, as the number of TMA cycles increased, durability increased as well.

This can be explained by the fact that layers formed by TMA are the main surface protection structures. Therefore, the more TMA cycles a sample has, the longer the sample can withstand the water flow.

Sample Label	Time to Fail (Minutes)	Contact Angle Values (°)	
		Original	After Test
0.5TMA + Amine + Gycidoxy + FDTS	1.0	>160	95
1TMA + Amine + Gycidoxy + FDTS	2.0	158	90
2TMA + Amine + Gycidoxy + FDTS	7.0	>160	93
3TMA + Amine + Gycidoxy + FDTS	18	>160	94

Table 5.2. Results of water durability test for TMA-Amine-Gycidoxy samples.

The second batch of samples tested was the TMA-Linker-Pyridine series, for which a low water flow rate was used. Detailed sample information and the total time elapsed before the samples failed are summarized in Table 5.3. In this case, the test results showed that samples with more layers of deposited nanoparticles became relatively less durable than those with fewer layers. This is perplexing, as one would expect that a larger number of layers would make the sample more durable.

To increase the superhydrophobicity, certain fluorocarbon-based self-assembly layers, such as FOTS, were introduced to the VPD process (Figure 5.13). It is possible that the problem with a larger number of layers is that there is less coverage with FOTS per layer. The FOTS is

essential to maintain the sample's superhydrophobicity, and once the layer containing FOTS is eroded away, the contact angle will decrease drastically.

Sample Label	Time to Fail (Hours)	Contact Angle Values (°)	
		Original	After Test
2TMA + Linker @ 50	>8	>160	123
2TMA + Linker @ 100	>8	145	119
3TMA + Linker @ 50	>8	147	127
3TMA + Linker @ 100	>8	142	117
4TMA + Linker @ 50	7.5	>160	95
4TMA + Linker @ 100	6.5	148	91

Table 5.3. Water durability test results for TMA-Linker-Pyridine samples. The number after the sample label indicates the partial pressure of pyridine used during the VPD process.

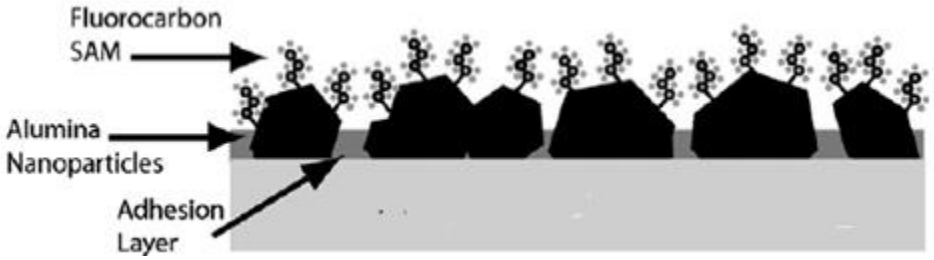

Figure 5.13. Use of fluorocarbon SAMs for superhydrophobicity.

The effect of pyridine also should be mentioned. A 4TMA sample with 100 mTorr was less durable than that with 50 mTorr. It has been reported that pyridine is a favorable catalyst for hydrolysis, because it promotes the formation of surface layers (Du et al., 2007). However, because of the reduced failure time, it is possible that a pyridine residue in the sample may have produced certain negative effects. Therefore, further research is needed to determine the way in which pyridine works in this system.

Sample Label	Time to Fail (Hours)	RMS Surface Roughness (nm)	
		Original	After Test
2TMA + Linker @ 50	>8	523	437
2TMA + Linker @ 100	>8	439	332
3TMA + Linker @ 50	>8	482	395
3TMA + Linker @ 100	>8	511	546
4TMA + Linker @ 50	7.5	118	35.6
4TMA + Linker @ 100	6.5	276	122

Table 5.4. Surface roughness values for TMA-Linker-Pyridine samples. The number after the sample label indicates the partial pressure of pyridine used during the VPD process.

Some reports have indicated that the wetting behavior of microstructured hydrophobic surfaces is affected by surface roughness (Lee et al., 2010). To understand the surface change better, AFM images of the samples were obtained to trace the change in the surface structure.

The RMS roughness values of the samples in their original state and after failure are summarized in Table 5.4.

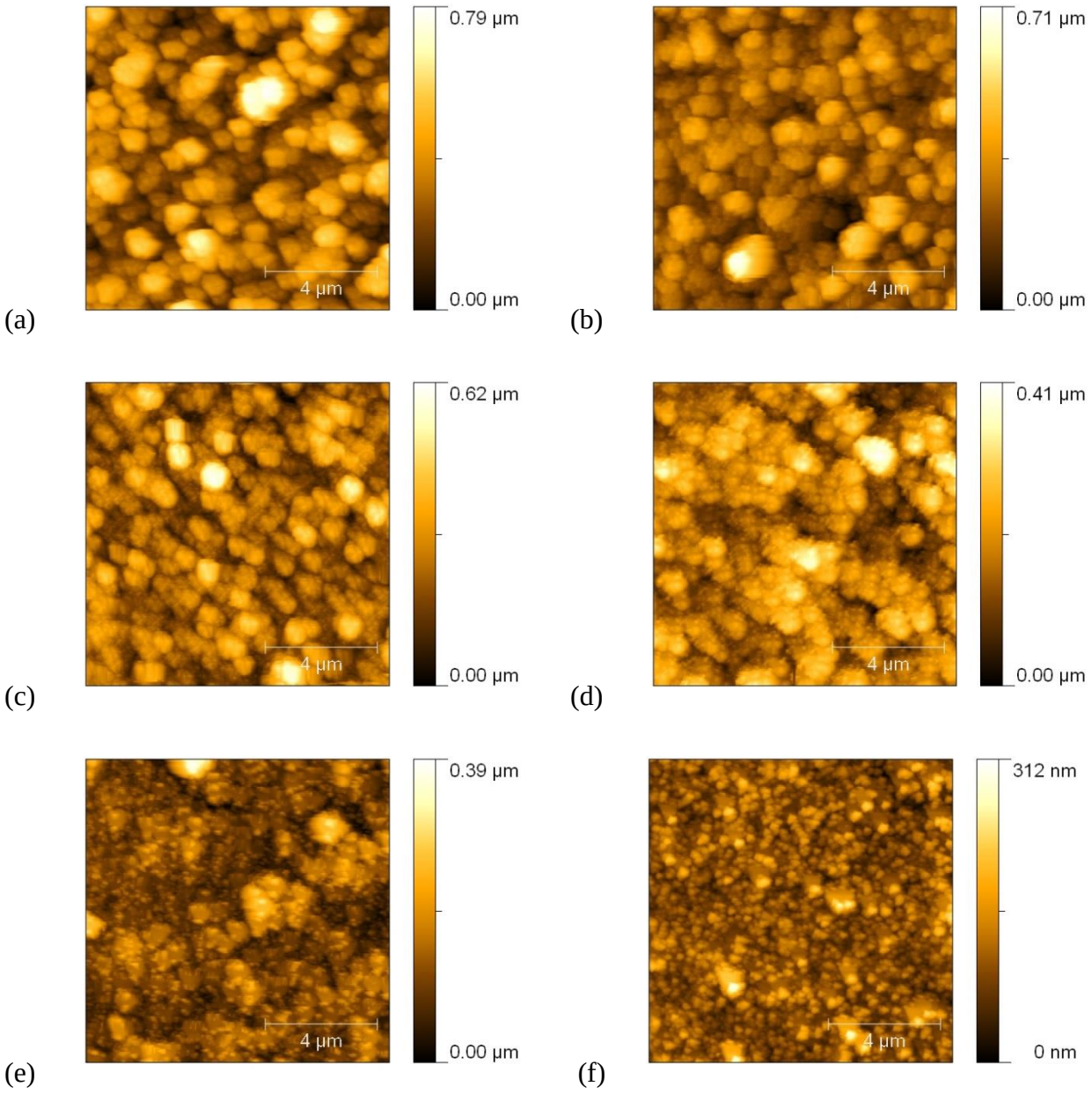

Figure 5.14. AFM images of 4TMA + Linker @ 100 sample. The images were taken: (a) before test, (b) after 1 hour, (c) after 2 hours, (d) after 4 hours, (e) after 6 hours, and (f) after test.

Compared to the original samples, the surface roughness values decreased after failure in most of the samples. This also was confirmed in AFM images of one sample throughout the test (Figure 5.14), which showed that many rough nanostructures disappeared after water erosion. Therefore, from a microscopic perspective, the nanostructures should produce better durability.

For perfectly smooth surfaces, the contact angle is determined by surface energy. However, unlike ideal surfaces, real surfaces are not perfectly smooth. To produce a superhydrophobic surface, two key features are required: low surface energy of the material, and a surface morphology with a certain roughness on the nano- and microscale.

The Cassie-Baxter and Wenzel models are those used commonly to describe the effect of surface roughness on superhydrophobicity. In the Cassie-Baxter model, the droplet base contacts only the tips of the roughness elements. Consequently, the bottom of the droplet is in contact both with air and the tops of the protruding elements on the solid substrate. On the other hand, the Wenzel model shows that the droplet wets the roughness elements completely and is in intimate contact with the solid substrate. (Figure 5.15)

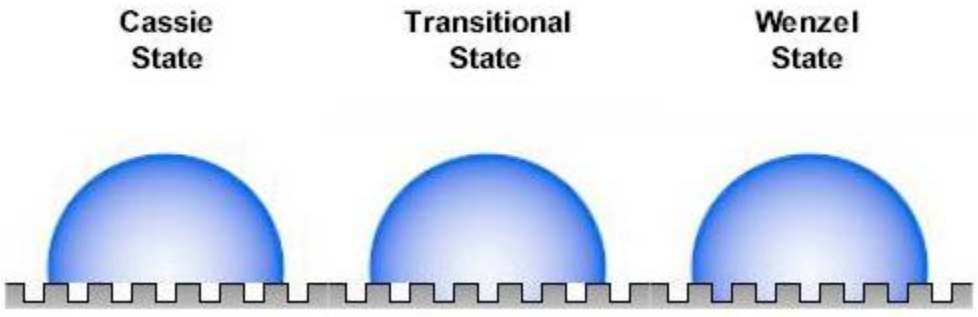

Figure 5.15. The state of Cassie-Baxter model, Wenzel model and the transitional state.

To maintain superhydrophobicity, it is necessary to prevent the drop from being impaled on the surface structure by maintaining the Cassie-Baxter state. However, when the surface topology changes, the Cassie-Baxter state begins to compel with the Wenzel state, in which the contact angle value is usually lower. Therefore, when the Cassie-Wenzel transition occurs, it is usually described as the loss of superhydrophobicity. Previous reports have shown that the state of droplet wetting changes from the Cassie to the Wenzel state by increasing the spacing on the surface, which results in a decrease of surface roughness and the density of structures with peak height (Lee et al., 2010). During the transition, the water droplets remain inside the groove formed by the rough structures and the liquid meniscus moves downward because of the balance between the gravitational and capillary forces. Our AFM images and corresponding surface roughness values were consistent with this explanation.

5.3.3 Heat stability of superhydrophobic nanofilms

SAM coatings were deposited via a vapor-phase process using DDMS, FOTS, and C8-OTS precursors. For DDMS coatings, both liquid-deposited films (LDDMS) and vapor-deposited films (VDDMS) were tested. Contact-angle measurements, ellipsometry, and AFM were used to assess the quality of the coatings deposited to determine the layer thickness and surface roughness. The water contact angle, film thickness, and rms surface roughness results for the SAM coatings are presented in Table 5.5. Data for clean SiO_2 also are shown for comparison. The contact angle values agree with those in other reports (Ashurst et al., 2001b; Ashurst et al., 2003), which indicates that the hydrophobic coatings of different precursors were deposited

successfully on the Si wafers and that the surface coverage was acceptable. No film thickness data are provided for the SiO_2 layer, as it is considered the substrate.

Coating	Water contact angle (°)		Film thickness (Å)	RMS roughness (nm)
	Measured	Reported		
C8-OTS	102 ± 3	105	13.8 ± 1.2	0.34 ± 0.05
FOTS	104 ± 3	110	12.7 ± 1.0	0.26 ± 0.04
VDDMS	100 ± 2	103	6.9 ± 0.6	0.23 ± 0.04
LDDMS	102 ± 2	103	7.4 ± 0.7	0.33 ± 0.06
SiO_2	<5	0-30	-	0.09 ± 0.02

Table 5.5. Contact angle values, film thickness, and rms surface roughness values of SAM coatings.

Self-assembled multilayer structures of these precursor molecules may develop during a conventional liquid-based deposition process, through additional adsorption and oligomerization of precursors in the solution. The thickness data of all three precursors showed that monolayer coating was achieved. With respect to the properties of these films (such as thermal stability), the bonding strength and the ordering or structure of the film are key parameters that cannot be determined directly with the information given in Table 5.5. It has been reported that both perfluoroalkyl and alkyl chains exhibit some order packing during film formation, and that a decrease in the tilt angle of the perfluoroalkyl chains with respect to the surface occurs when both the film coverage of the substrate and the packing density of the deposited film increase

(Gao et al., 1997). Therefore, an improved monolayer film yields a more dense structure, which may enhance thermal stability.

From the data shown in Table 5.5, it is apparent that the coatings have characteristics that are comparable with those in other published results, which indicates that the vapor coating process was effective. To compare the liquid- and vapor-based coatings, DDMS films were produced both via a solution and vapor-phase method. AFM images of the liquid- and vapor-phase deposited films are shown in Figure 5.16. A scan of a clean Si wafer is also shown as a reference. Although the contact angle values show that the DDMS films produced by both processes have similar surface hydrophobicity, the AFM scans reveal some differences between the results of the two methods. Visible aggregates are apparent on the surface of the liquid-deposited film, while the vapor-phase deposited film exhibits significantly fewer aggregates. Reduced aggregation would be an advantage in the application of such coatings on real devices, especially for systems involving multiple parts on the micro- or nanoscale.

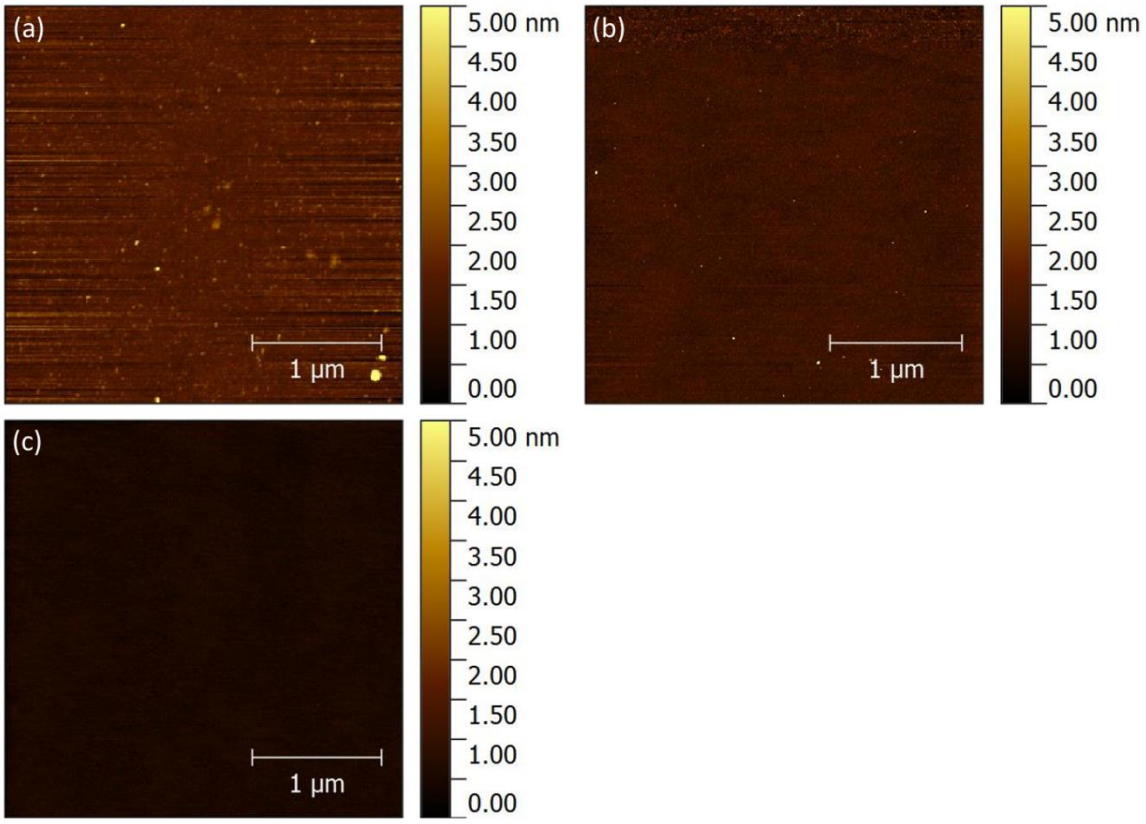

Figure 5.16. AFM images of (a) liquid- and (b) vapor-based DDMS films, and (c) AFM image of clean Si wafer shown as a reference.

Exposure to high temperatures (>300 °C) typically has a negative effect on the properties of nanoparticle films, for example, their superhydrophobicity. In order to maintain superhydrophobicity at high temperatures, which may be useful in certain commercial applications, the thermal stabilities of the SAMs prepared in this study were characterized.

A thermal stability test was conducted based on changes in the contact angle in response to temperature variations, and the contact angle vs. temperature data are shown in Figures 5.17 and 5.18. Note that, in Figure 5.17, all the SAMs were coated on a clean Si wafer. The sample with the DDMS coating retained a high contact angle value at temperatures up to 400 °C, which

began to decrease (indicating a loss in hydrophobicity) at 450 °C. The sample with the FOTS coating exhibited similar behavior. Note that these results are consistent with other reports for such systems (Ashurst et al., 2001b). On the other hand, the sample with the C8-OTS coating began to decompose at 200 °C. The following mechanism for the alkyl silanes is proposed to explain this behavior. The decomposition first occurs via cleavage of the C-C bonds of the alkyl chains, together with β-hydride elimination, resulting in a reduction in chain length (Kluth et al., 1998). The Si-C bond of the surface-adsorbed methyl group, however, is very strong and can remain at the surface at a higher temperature (Faucheux et al., 2006). Therefore, for OTS, the alkyl chain oxidizes and decomposes upon heating. DDMS, which has only methyl groups at the surface, is immune to the effects of the graduated C-C bond cleavage, which helps this precursor maintain its stability at high temperatures (Kluth et al., 1997). FOTS follows a decomposition mechanism similar to that of OTS; however, as the F atoms on the alkyl chain replace the majority of the H atoms, β-hydride elimination during thermal decomposition is prohibited (Kluth et al., 1997). At higher temperatures, disorders in orientation and conformation appear, rather than massive C-C bond breakage, which is still limited by the dense packing of the tail groups; the the C-F bonds protect the C-C chains at lower temperatures, before chain scission occurs at high temperatures.

To test the compatibility of these SAMs with practical device protection layers, the Repellix commercial nanocomposite coating was used as a reference. Figure 5.18 shows a plot of the thermal stability test results for SAMs with this commercial coating. The results demonstrated that all the SAMs had reasonably good thermal stability from the beginning to approximately 300 °C, which again demonstrates the importance of the superhydrophobic coating as a protective layer.

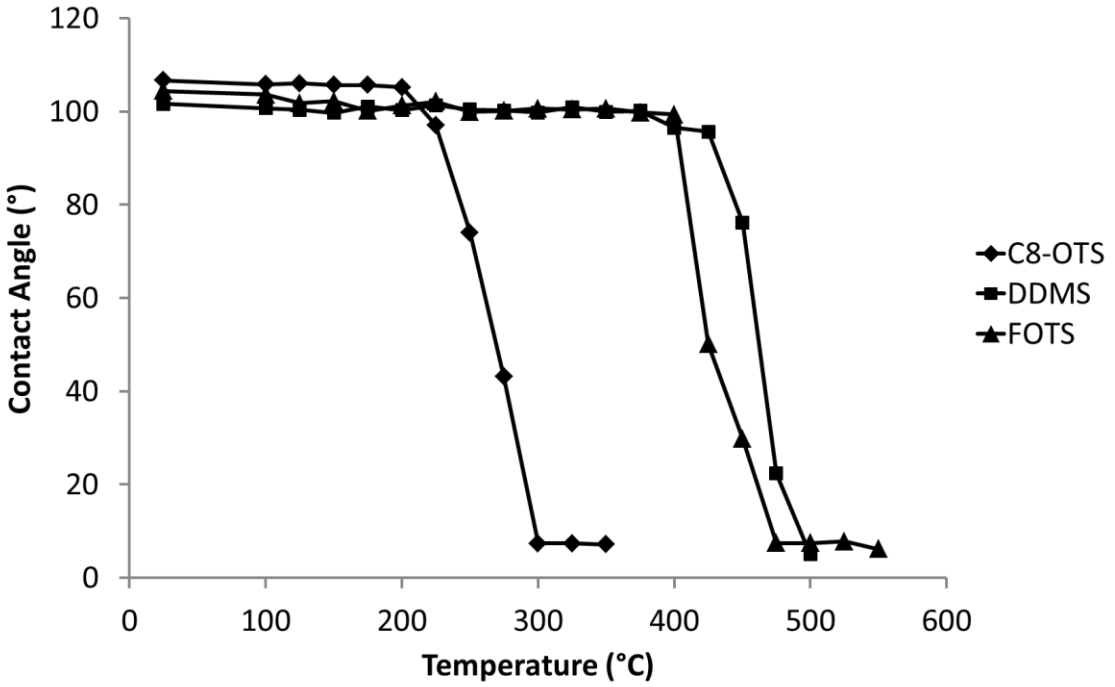

Figure 5.17. Contact angle values vs. temperature for SAMs on clean Si wafer.

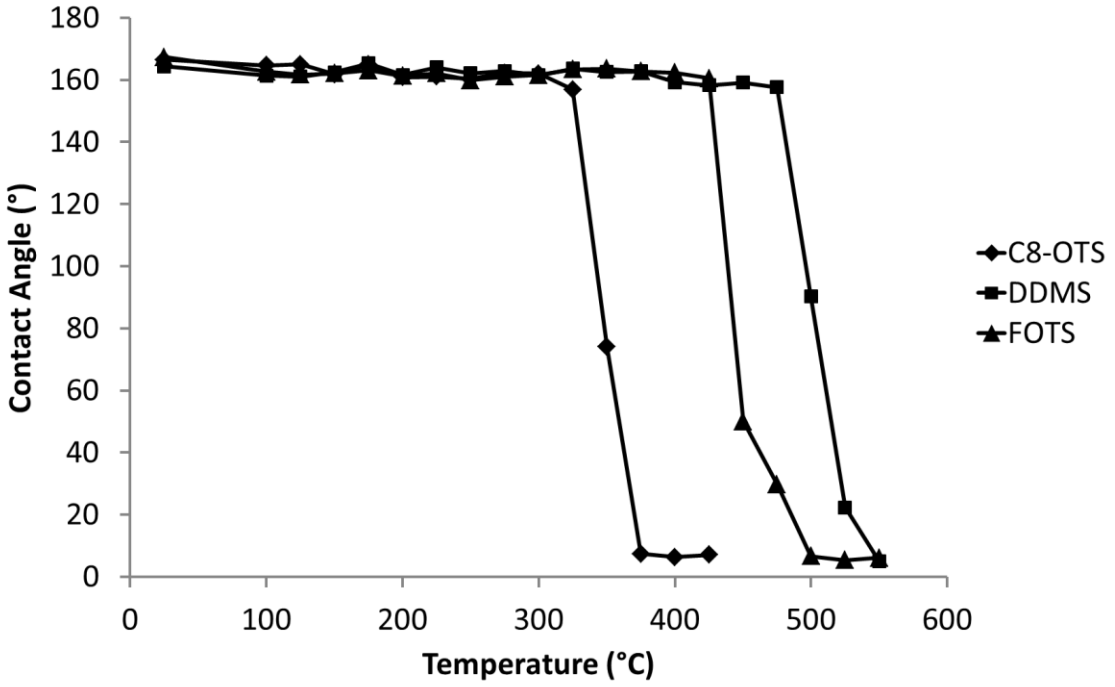

Figure 5.18. Contact angle values vs. temperature for SAMs on commercial Repellix coating.

Conventionally, coating failure is defined as the contact angle dropping below 90°. From the plot in Figure 5.18, it is apparent that the C8-OTS coating began to fail at 350 °C, and the contact angle decreased to less than 10° at 375 °C. The FOTS coating maintained its efficacy until 425 °C, at which point it also failed. The DDMS coating exhibited the best performance, as those samples could be heated to 500 °C and the contact angle remained larger than 160°. However, it then began to fail, and the contact angle decreased to less than 10° at 550 °C.

It is worth noting that the thermal stability test results demonstrated similar trends for SAMs on both the Si wafer and nanocomposite coating; however, some differences were apparent. Specifically, the initial contact angle values of the SAMs on the commercial coating (~160°) were larger than those of the SAMs on the Si wafer (~100°). Further, the SAMs on the commercial coating had higher film-failure temperatures. This indicates that, from a microscopic perspective, the surface nanostructures may be responsible for the superior thermal stability test results.

For smooth surfaces, such as a Si wafer, the surface energy determines the SAM properties in part, which the properties of the SAM molecules affect as well. However, unlike ideal surfaces, real surfaces are not perfectly smooth, and to produce a superhydrophobic surface, two key features are required: a low surface energy and a surface morphology with a certain roughness on the micro- or nanoscale. The commercial nanocomposite coating is designed to satisfy both of these requirements.

When the surface is rough, the change in the contact angle (or the hydrophobicity) is affected not only by the surface chemical properties, but is also heavily dependent on the surface

microstructures; this dependency can be described by the classic Cassie-Baxter and Wenzel models (Kluth et al., 1997). In the Cassie-Baxter model, the droplet base remains only on the tips of the roughness elements. Consequently, the bottom of the droplet is in combined contact with air and the peaks of the protruding asperities on the solid substrate. On the other hand, the Wenzel model shows that the droplet wets the roughness elements completely and is in intimate contact with the solid substrate.

Thus, we considered the effect of the surface roughness on the thermal behavior of the SAMs. On a smooth surface, the SAM molecules bond to the surface and are packed tightly via the van der Waals interactions between the tail's functional groups. As described previously, when the coated surface is heated, the tail group begins to degrade. This affects the surface behavior (such as hydrophobicity) significantly, as changes in the SAM functional groups are the only source of variations in the surface properties. On the other hand, when the SAMs are applied to a rough surface, the hydrophobicity achieved is enhanced through a combination of both morphological and chemical factors that yield a superhydrophobic surface (contact angle > 150°).

From the test results, the FOTS and DDMS on the Si wafer failed at similar temperatures; however, DDMS showed better results on nanocomposite coating than did FOTS. It is proposed that vapor-phase silane oligomerization may take place in the DDMS and water vapor mixture. This reaction between DDMS and water may produce a type of oligomer that appears as a viscous liquid. This type of liquid can be deposited on the substrate in part as a very thin film that cannot be seen directly and has a much higher thermal stability than does the SAM itself. As reported previously, the contact angle of this thin film is approximately 104°-106° and severe

adhesion results are obtained during the application of DDMS coating on MEMS devices when the coating condition is not optimized properly (Ashurst et al., 2003). Therefore, when DDMS is applied to surfaces with rough microscale structures, this oligomer liquid will condense at the point where there is confined capillary space with respect to its surroundings, such as the rough structures. This capillary condensation may have an important effect on the thermal stability of DDMS on synthetic microstructures, as the DDMS oligomer liquid will be adsorbed inside the structures and withstand high ambient temperature.

To improve our understanding of the thermal stability, SAMs were coated on a fumed silica support and TGA was conducted. TGA is another technique that can provide information about the monolayer formation and degradation mechanisms. The TGA of a SAM-coated Si substrate is limited, because the changes in the mass are so small compared to the overall film loading on flat substrates. High-surface-area support materials are used often to provide the relatively high loadings necessary for experimental resolution when examining thin films using TGA. However, the fumed silica supports employed in this study were produced via a template-based technique and had a typical weight of 10-12 mg, which is sufficient for TGA sensitivity.

TGA data for fumed silica supports with no SAM coatings are shown in Figure 5.19. The thermal analysis was conducted within the 100–650 °C temperature range in air, and a total weight loss of approximately 2.0% was apparent over the entire temperature range. The initial weight loss that occurred up to temperatures of approximately 200 °C can be associated with loss of the hydrogen bonded water network and residual solvent. The further weight loss at high temperatures may be associated with desorption of the water generated by free silanol

condensation. These data served as a good baseline for comparison of surface modification approaches.

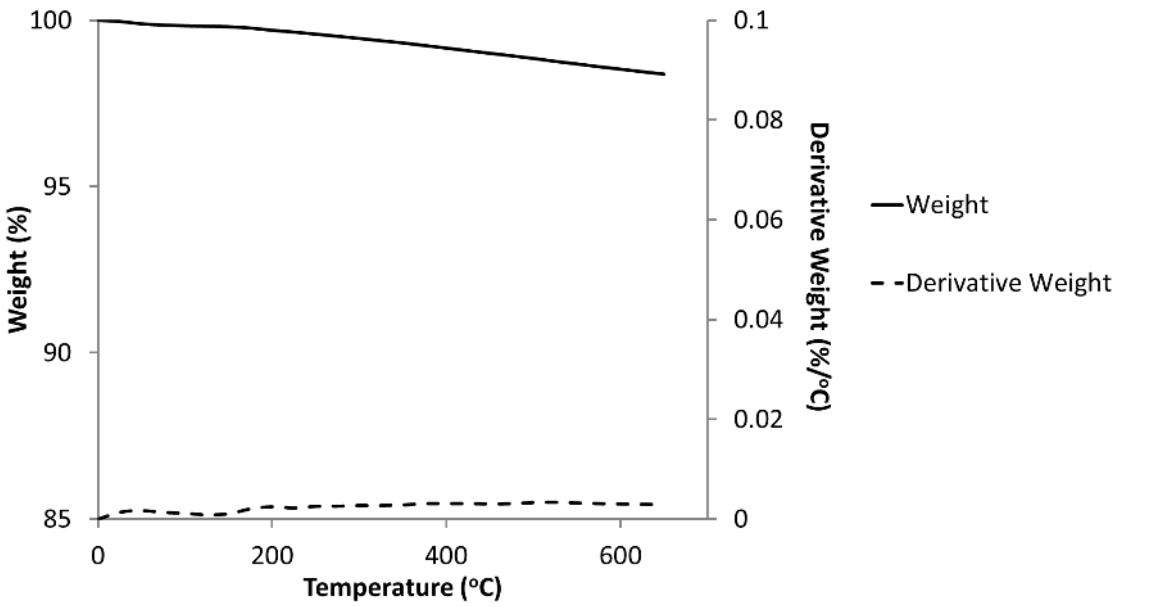

Figure 5.19. Weight loss and derivative weight loss curves of fumed silica support.

Different SAMs were coated on the silica supports and the TGA results for the coated silica supports in either air or nitrogen are shown in Figures 5.20-5.25. For three SAM coatings, i.e., C8-OTS, FOTS, and DDMS, similar weight-loss trends were obtained, and several clear weight-loss events were apparent in all the TGA curves. However, the weight derivative curve provides more detailed information on the thermal events. For all samples examined, the first event occurred between room temperature and 200 °C. When the temperature began to increase above room temperature, the residual solvent and water from the coating and post-treatment process was removed. As the temperature increased, neighboring crosslinked Si-OH moieties eliminated water, thereby resulting in gradual weight loss. The next event was the thermal

decomposition of the coated SAM molecules. Note that this temperature range varied for the different SAMs.

TGA data for C8-OTS-coated samples in air and nitrogen are shown in Figures 5.20 and 5.21, respectively. For the OTS, clear mass loss occurred at 200 and 250 °C in air and nitrogen, respectively. These values are consistent with the contact angle measurements. Thermal decomposition of SAMs may occur at lower temperatures in air, as air can induce thermal degradation through cleavage of the C-C bonds of the alkyl chains, together with β-hydride elimination, as described above. The C8-OTS molecule has a long alkyl chain and is a vulnerable molecule at high temperature. Thus, the significant mass loss from 350 to 500 ^{0}C can be attributed to the decomposition of the C8-OTS molecule.

TGA data for FOTS-coated samples in air and nitrogen are shown in Figures 5.22 and 5.23. As a SAM that is used commonly, it is apparent that FOTS was very stable and did not exhibit significant mass loss until 400 °C, which is again consistent with previous contact angle measurements. After the FOTS began to decompose, rapid mass loss occurred from 450 to 550 °C. Comparing the FOTS with the C8-OTS case, no significant thermal decomposition occurred between 200 °C and 400 °C. This again supports the notion that the F atoms protect the alkyl chains of FOTS, and that β-hydride elimination during thermal decomposition is prohibited before the entire functional group becomes unstable at high temperature.

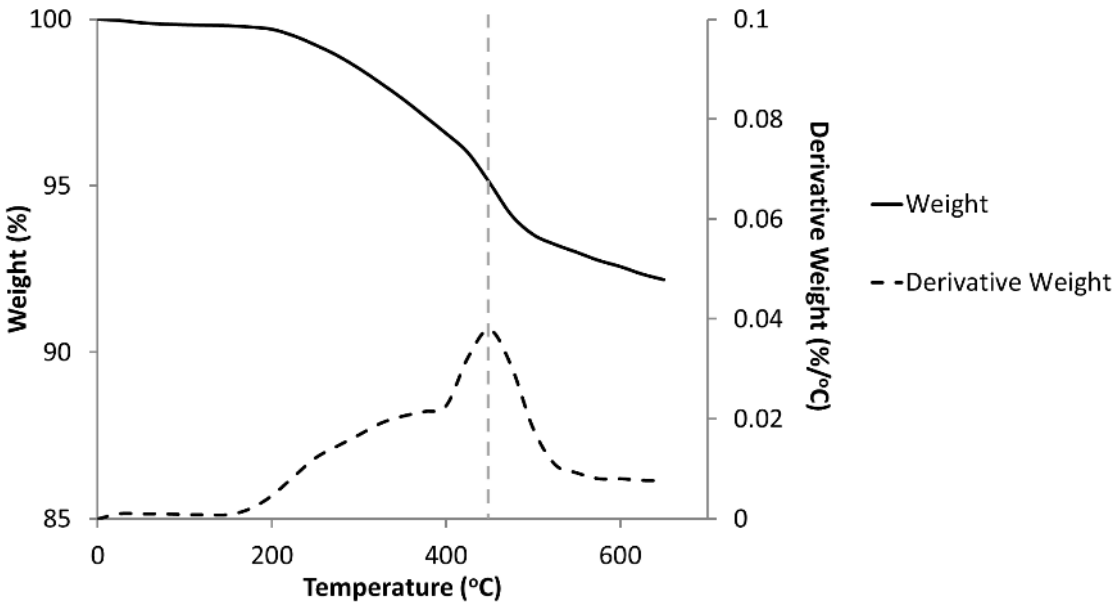

Figure 5.20. Weight loss and derivative weight loss curves of C8-OTS in air. The dashed line indicates the peak mass loss temperature.

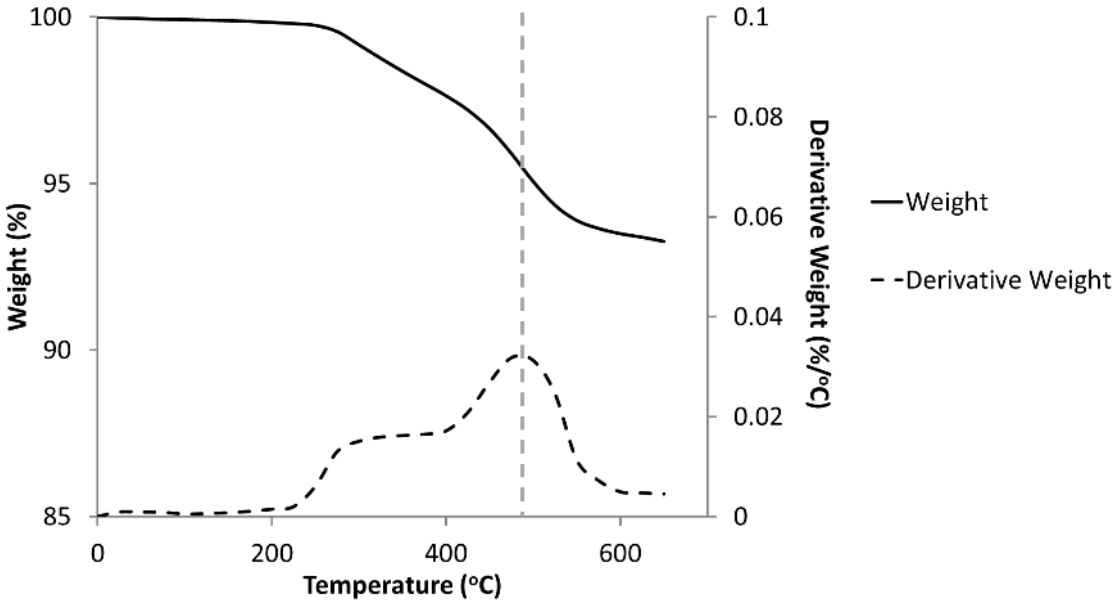

Figure 5.21. Weight loss and derivative weight loss curves of C8-OTS in nitrogen. The dashed line indicates the peak mass loss temperature.

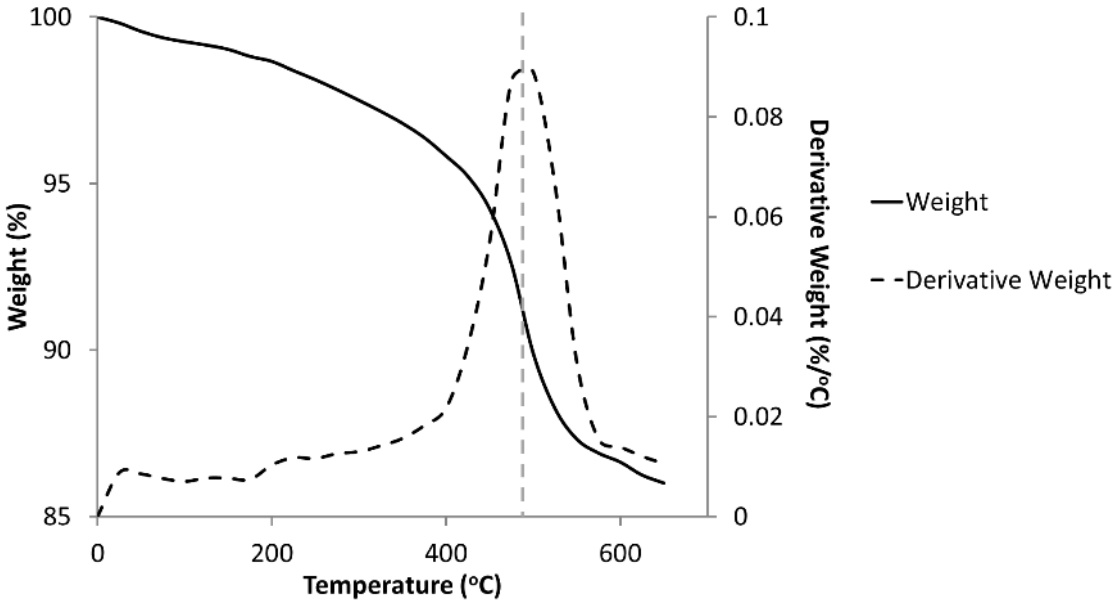

Figure 5.22. Weight loss and derivative weight loss curves of FOTS in air. The dashed line indicates the peak mass loss temperature.

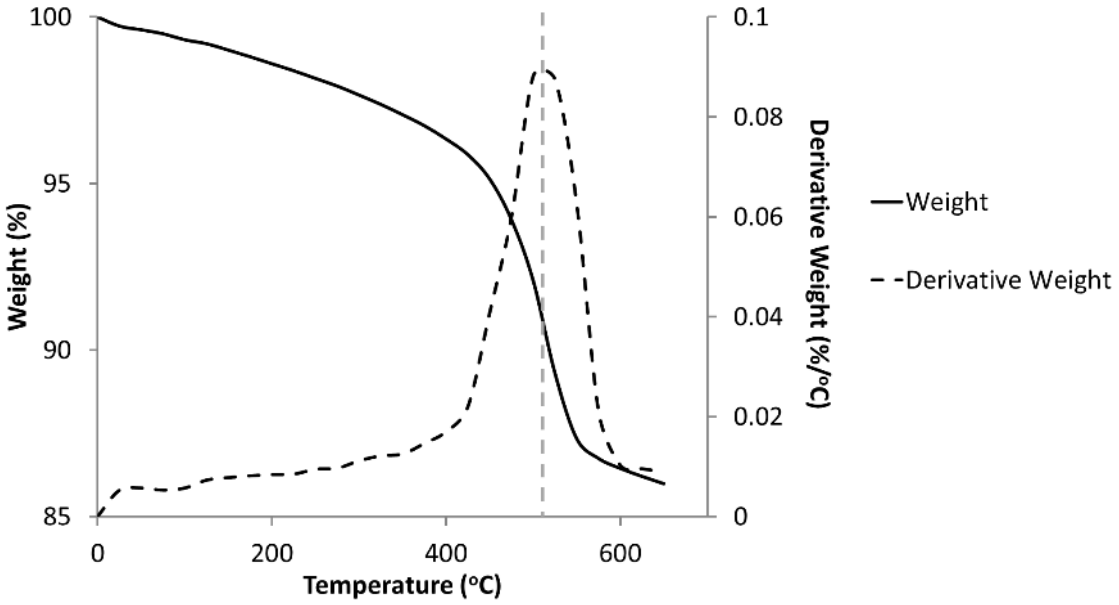

Figure 5.23. Weight loss and derivative weight loss curves of FOTS in nitrogen. The dashed line indicates the peak mass loss temperature.

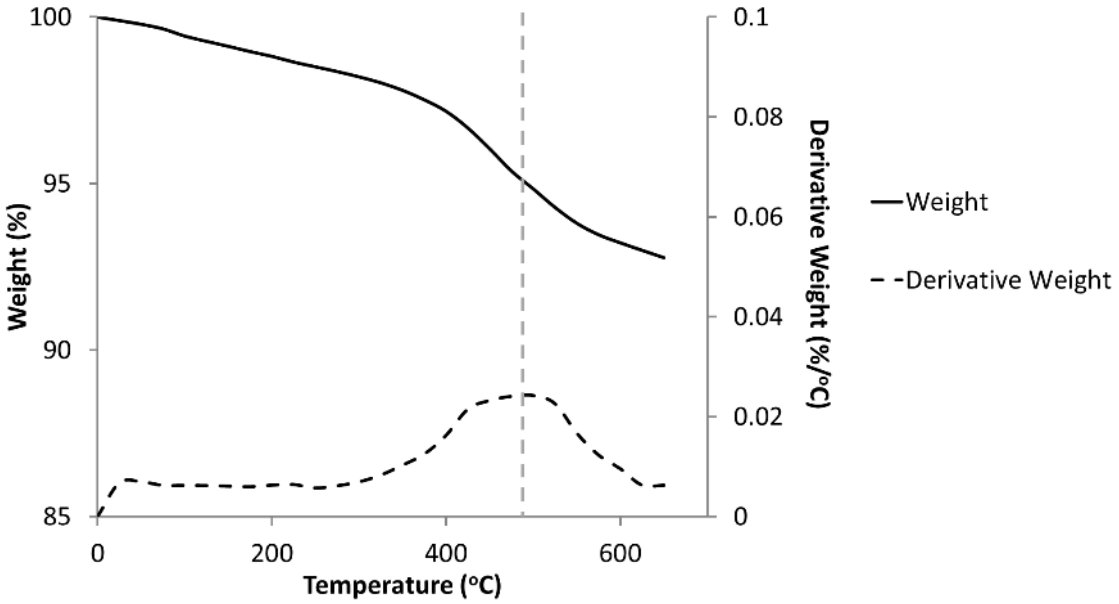

Figure 5.24. Weight loss and derivative weight loss curves of DDMS in air. The dashed line indicates the peak mass loss temperature.

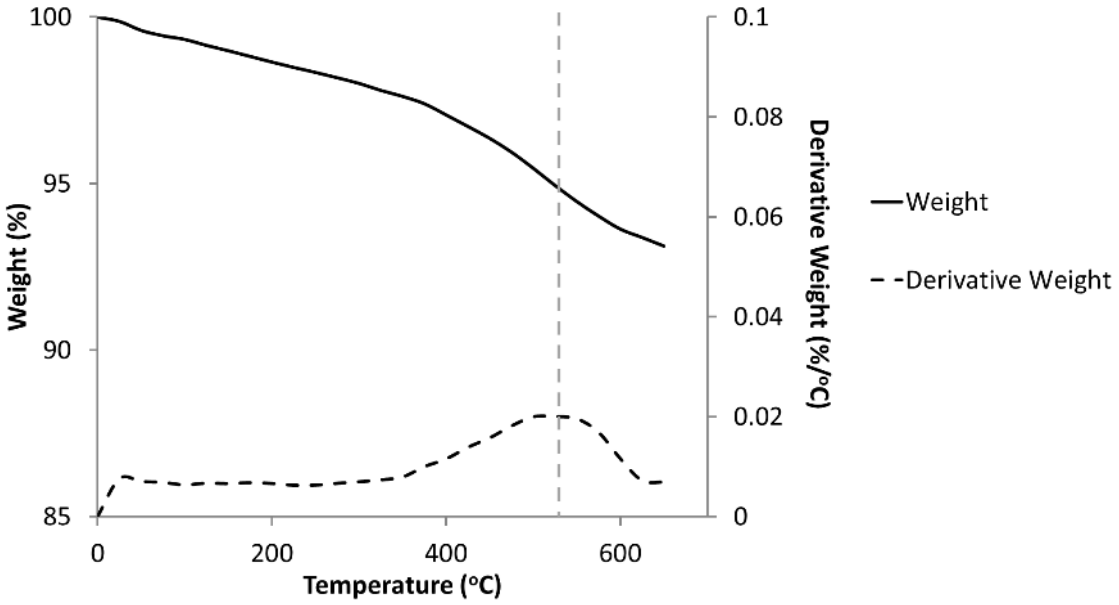

Figure 5.25. Weight loss and derivative weight loss curves of DDMS in nitrogen. The dashed line indicates the peak mass loss temperature.

Figures 5.24 and 5.25 show TGA data for DDMS-coated samples in air and nitrogen. In the case of DDMS, it was difficult to identify the point on the weight curve at which the actual thermal decomposition began. However, it is apparent from the weight derivative curve that a distinctive mass loss occurred from 350 to 600 °C. Therefore, the thermal behavior of the DDMS features a combination of the behaviors exhibited by the C8-OTS and FOTS. The thermal decomposition is gradual and occurs over a broad temperature range, but DDMS can still withstand a higher temperature.

Based on the TGA data, the results were consistent with the contact-angle measurements on Si wafers. Further, the TGA data provided more detail about the thermal behavior. Hence, it is apparent that C8-OTS decomposes at lower temperatures, but FOTS and DDMS remain stable at higher temperatures. On the other hand, the FOTS film exhibits a rapid decomposition process, while the DDMS film decomposes slowly over a broad temperature range. This finding may be important for practical applications, as the DDMS-coated surface retains its properties in part if sufficient surface coverage remains, even if some of the coating has suffered thermal damage.

In both the contact angle test and TGA results, DDMS exhibited better thermal stability on a nanocomposite coating than C8-OTS and FOTS. To understand the surface properties at the molecular bonding level better, X-ray photoelectron spectroscopy (XPS) was introduced in the coating analysis. XPS has been used widely in both qualitative and quantitative characterizations of the chemical state changes of various elements and the composition of SAM-coated substrates before and after thermal treatment.

XPS survey spectra of a clean Si substrate and commercial vapor-deposition-based nanocomposite coating is shown in Figure 5.26. Table 5.6 shows the binding energies and corresponding elemental information (Wanger et al., 1979).

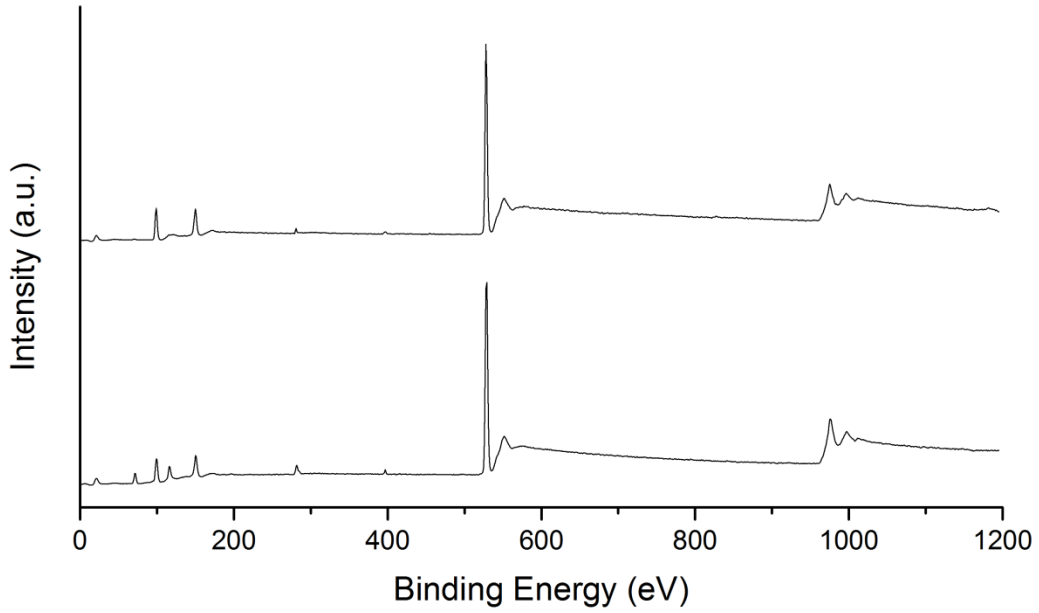

Figure 5.26. XPS survey spectra of a clean Si substrate (top) and commercial vapor-deposition-based nanocomposite coating (bottom).

Elemental components	O 2s	Al 2p	Si 2p	Al 2s	Si 2s	C 1s	N 1s	O 1s
Binding energy (eV)	23.0	74.4	103.3	120.8	150.9	284.6	398.1	531.0

Table 5.6. Binding energies and the corresponding elemental components of substrates.

A survey spectrum of the silicon substrate revealed that the main elements that exist on the surface are Si and O, and the Si peak corresponded to the surface layer of SiO_2. The O peak

derived primarily from the SiO_2 as well, while there was a tiny shoulder that could be deconvoluted to a peak at 531.5 eV, and corresponded to -OH species on the surface. Trace amounts of C and N that are attributable to surface impurities were also confirmed from the spectrum. A survey spectrum of the commercial vapor-deposition-based nanocomposite coating showed that, compared to the silicon substrate, significant Al peaks appeared as the indicator of one of the main elements that exists on the surface. Al and O elements derive from the incremental layers of Al_2O_3 nanoparticles, while Si and O elements are in the protection layers. Peaks also indicated the existence of moderate amounts of C and N, the source of which can be attributed to the use of pyridine as the catalyst for SiO_2 layer formation.

High-resolution spectra of O 1s, Si 2p, and Al 2p for both substrates are shown in Figures 5.27 and 5.28. Because there was no Al on the clean Si substrate, the main elemental components, Si and O, had only one oxidation state. One synthetic peak was applied for high-resolution spectra of both O 1s and Si 2p. Oxygen on the commercial vapor-deposition-based nanocomposite coating now had two components: oxygen in -Si-O-Si- and in -Al-O-Al-. These two components are required for a suitable fit for the core-level O 1s peak. The previous one had a binding energy of 532.6 eV and corresponded to the oxygen bonding with silicon (-Si-O-Si-), while the other had a binding energy of 531.2 eV and corresponded to the oxygen bonding with aluminum (-Al-O-Al-). After the peaks were fitted, the relative sensitivity factors of the corresponding elements were taken into account, and the atomic ratios calculated are summarized in Table 5.7. For the clean Si substrate, the O/Si ratio calculated was 2.26:1. For the commercial vapor-deposition-based nanocomposite coating, the O/Si ratio calculated was 2.22:1, and the O/Al ratio was 1.72:1. These calculated values were similar to, but slightly higher than the theoretical ratios (O/Si = 2:1 and O/Al = 1.5:1). This is probably due to the oxygen in the

impurities and surface silanols. Spectra of both substrates showed clear characteristic peaks of the main elements and appropriate elemental compositions; therefore, they can be used as a reference for further coating analysis.

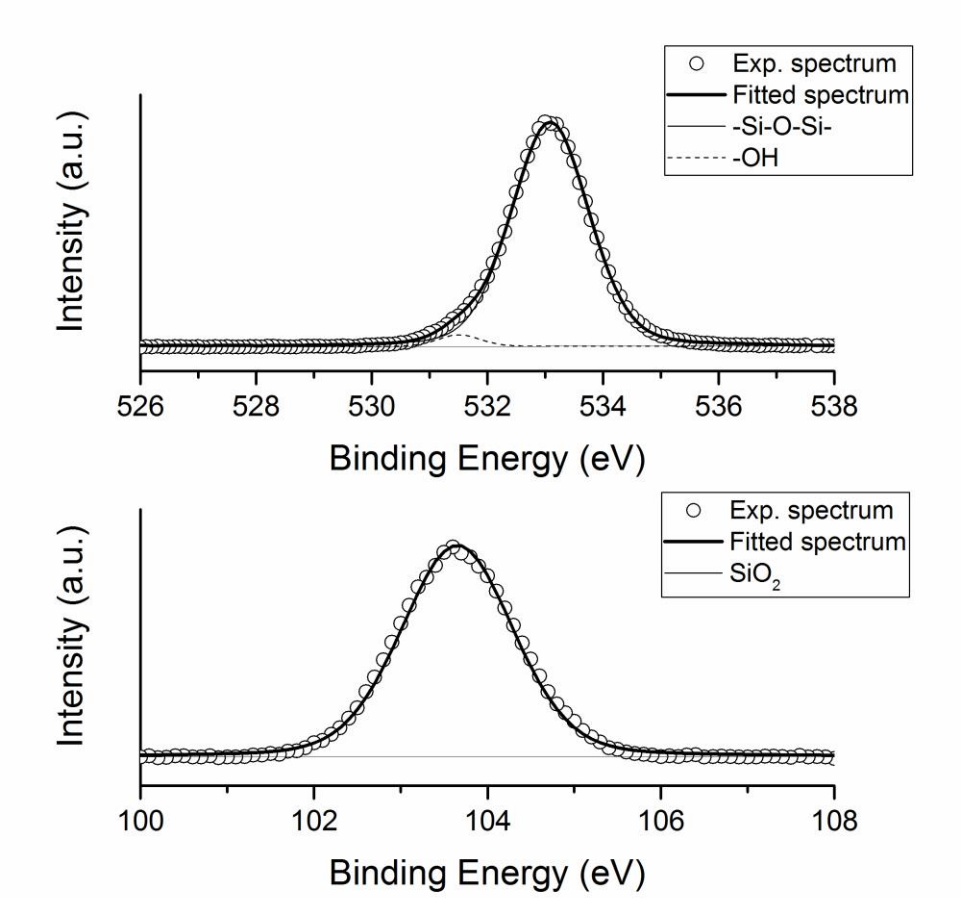

Figure 5.27. High-resolution spectra of O 1s (top) and Si 2p (bottom) of a clean Si substrate.

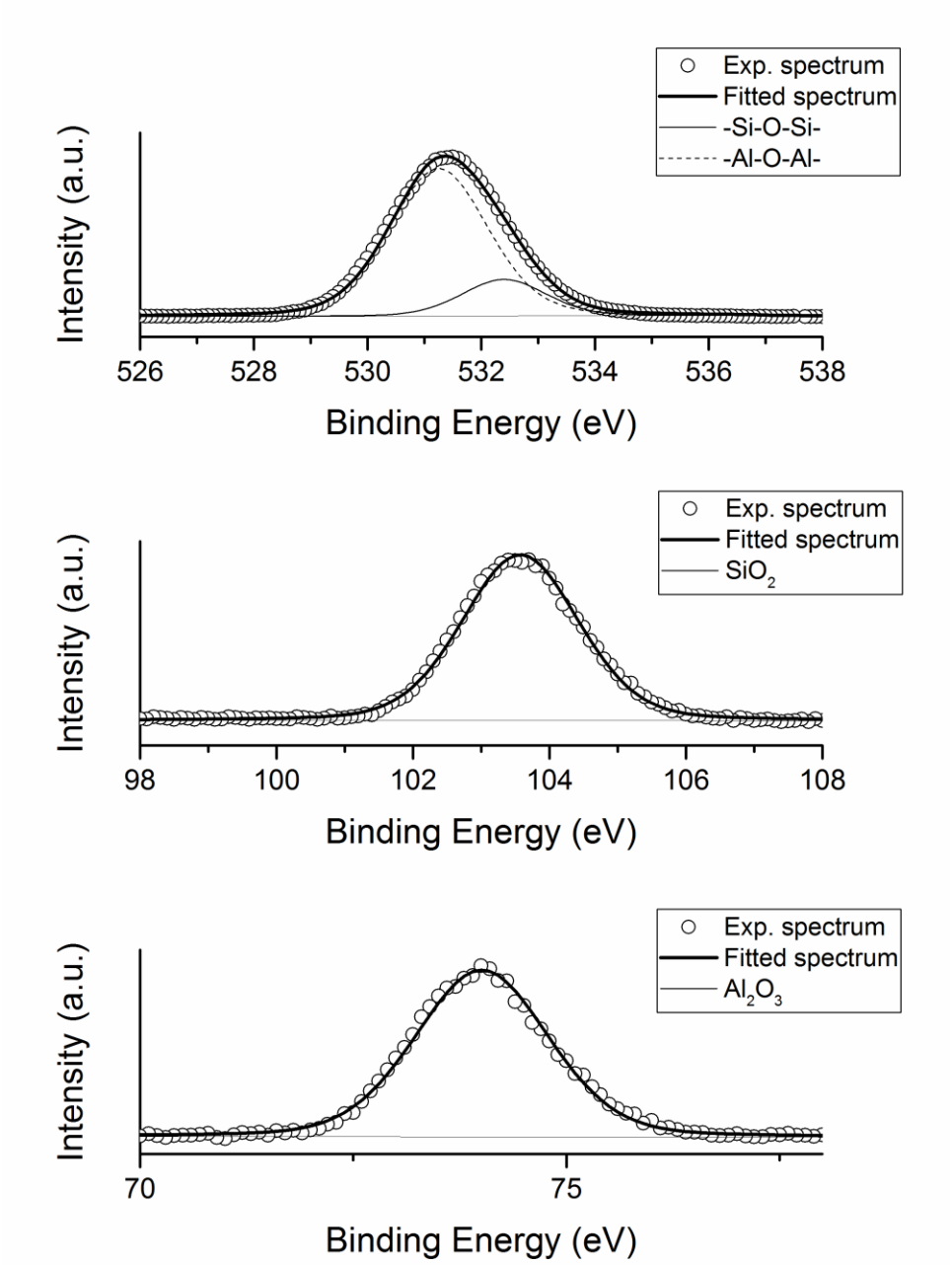

Figure 5.28. High-resolution spectra of O 1s (top), Si 2p (middle), and Al 2p (bottom) of a commercial nanocomposite substrate.

Substrate	Peak area (fitted from experimental data)				Atomic ratio	
	O(Si)	O(Al)	Si	Al	O(Si)/Si	O(Al)/Al
Clean Si substrate	52508 ± 1870	-	9209 ± 124	-	2.26 ± 0.08	-
Commercial nanocomposite	50566 ± 1129	19273 ± 192	9026 ± 149	3679 ± 121	2.22 ± 0.06	1.72 ± 0.06

Table 5.7. Quantitative analysis of elemental components of substrates.

XPS survey spectra of the Si substrate coated with DDMS at various temperatures are shown in Figure 5.29. Compared to the uncoated Si substrate, the spectrum of the coated sample without heat treatment showed a clear C 1s peak, indicating the coating of the DDMS monolayer. As the samples were heated to 450 °C, the intensity ratio of C 1s and Si 2p decreased significantly because of the loss of alkyl chains of DDMS. When the sample was heated to 500 °C, the spectrum was very similar to that of the uncoated clean Si substrate, which indicates that the DDMS coating had decomposed, leaving only the hydrophilic SiO_2 surface. This is consistent with the results of the contact angle and TGA analyses.

High-resolution spectra of C 1s, Si 2p, and O 1s of the DDMS-coated Si substrate are shown in Figures 5.30, 5.31 and 5.32. In the C 1s spectra, the original DDMS-coated sample showed a single C 1s peak, which corresponded to the carbon in -Si-CH_3. After the sample was heat treated, the overall intensity of the C 1s peak decreased, and a shoulder appeared in the spectra at 450 and 500 °C. After the peak deconvolution, the binding energy of this shoulder peak was approximately 287.0 eV and derived from the carbon-oxygen bonds. Because this peak did not exist on the DDMS coating without heat treatment, it can be attributed to the oxidized carbon species, either from the methyl chain of the DDMS or from the residues on the surface.

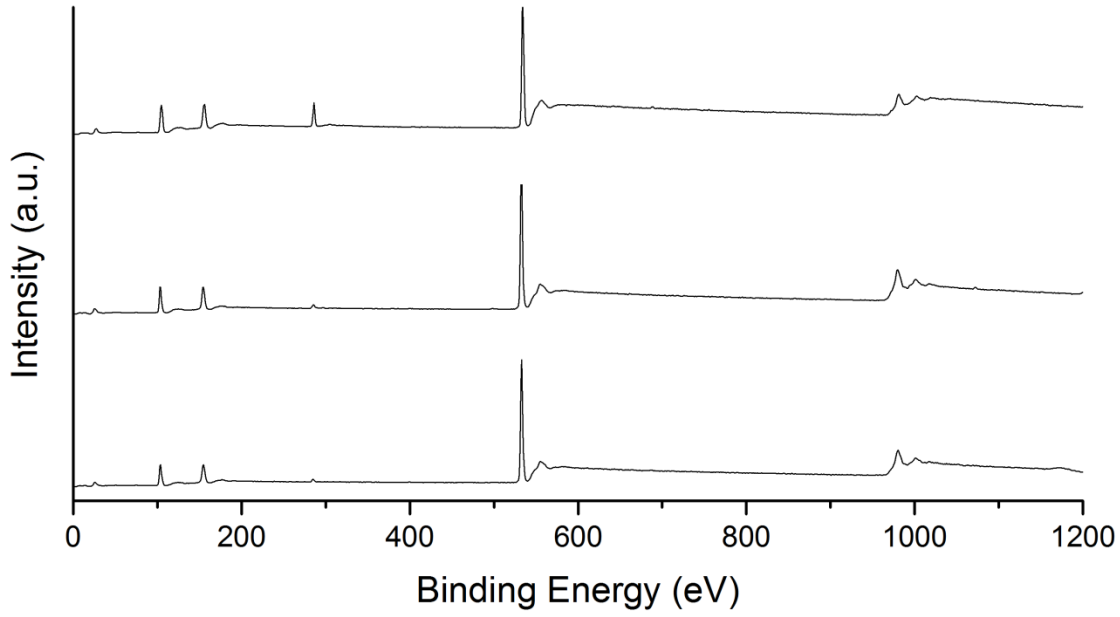

Figure 5.29. XPS survey spectra of DDMS-coated Si substrate: original (top), heated to 450 °C (middle), and 500 °C (bottom).

The high-resolution Si 2p spectrum for the original DDMS-coated Si substrate can be deconvoluted into two components: silicon in SiO_2 and in -Si-CH_3. The first had a binding energy of 103.5 eV and corresponded to the silicon bonding in SiO_2 (-Si-O-Si-), while the second had a binding energy of 101.2 eV and corresponded to the silicon bonding from silane (-Si-CH_3). After the sample was heated to 450 °C, no effective deconvolution of the Si 2p spectrum could be achieved, suggesting that after the alkyl chain has decomposed, the Si from silane derived from a silica-like structure on the surface, and the chemical environment cannot be distinguished clearly from the existing silica layer.

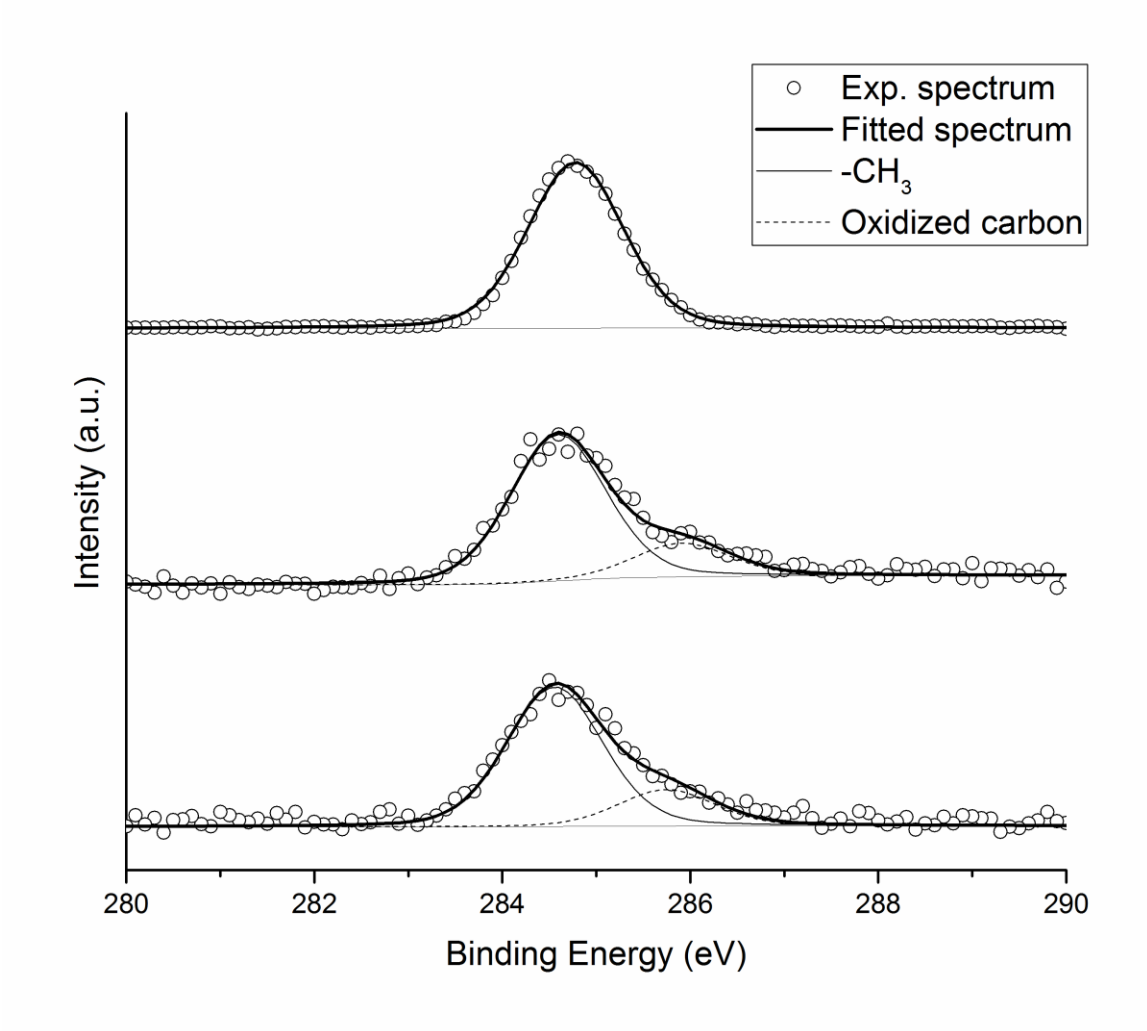

Figure 5.30. High-resolution spectra of C 1s of DDMS-coated Si substrate: original (top), heated to 450 °C (middle), and 500 °C (bottom).

The O 1s spectra of all samples showed a single broad peak. The oxygen atoms in silane and in silica have very similar binding energy values (532.5 eV vs. 533.0 eV). Therefore, deconvolution of these two peaks is unreliable. A quantitative analysis can still be conducted based on the single peak information, which will be discussed later.

Based on the information from the high-resolution spectra of C 1s, Si 2p, and O 1s, we concluded that the decomposition of the DDMS coating derived primarily from the oxidation of the methyl chain. Because there are no C-C bonds in DDMS, the cleavage of the Si-C bond of the methyl group is very strong and can persist at a higher temperature.

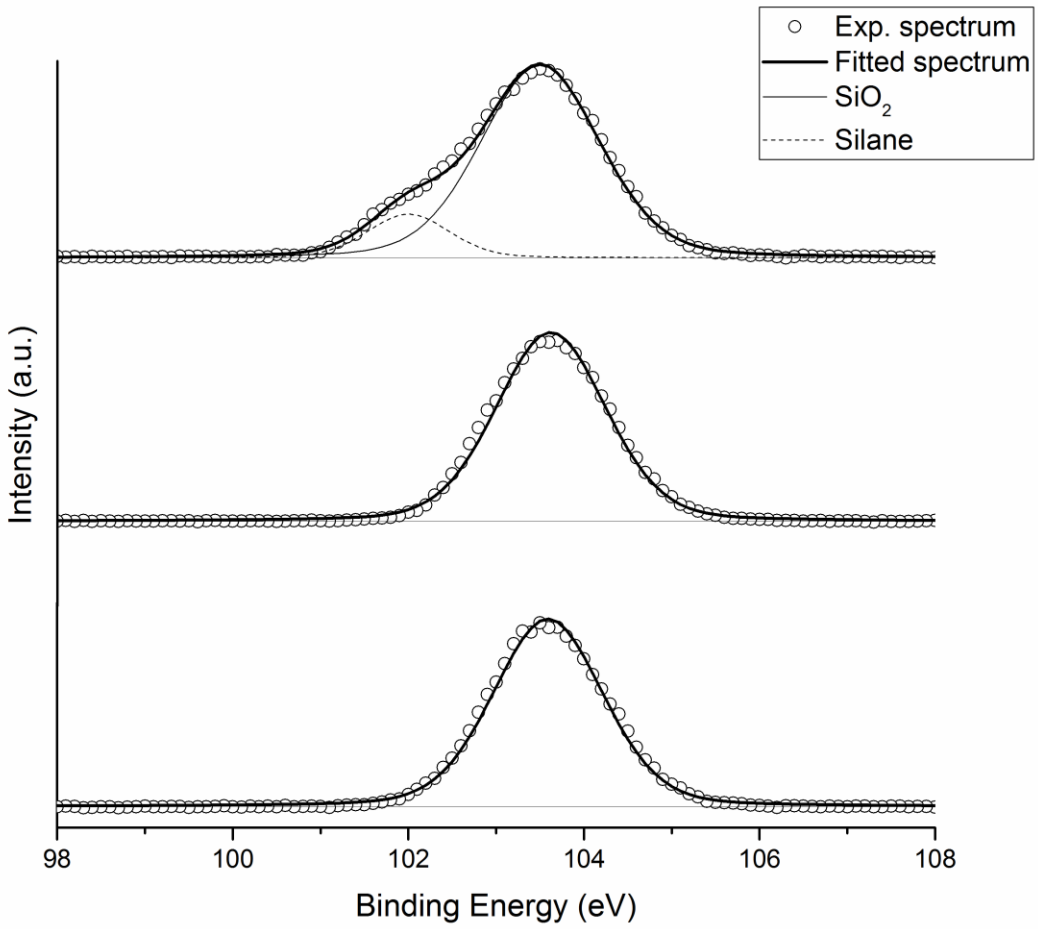

Figure 5.31. High-resolution spectra of Si 2p of DDMS-coated Si substrate: original (top), heated to 450 °C (middle), and 500 °C (bottom).

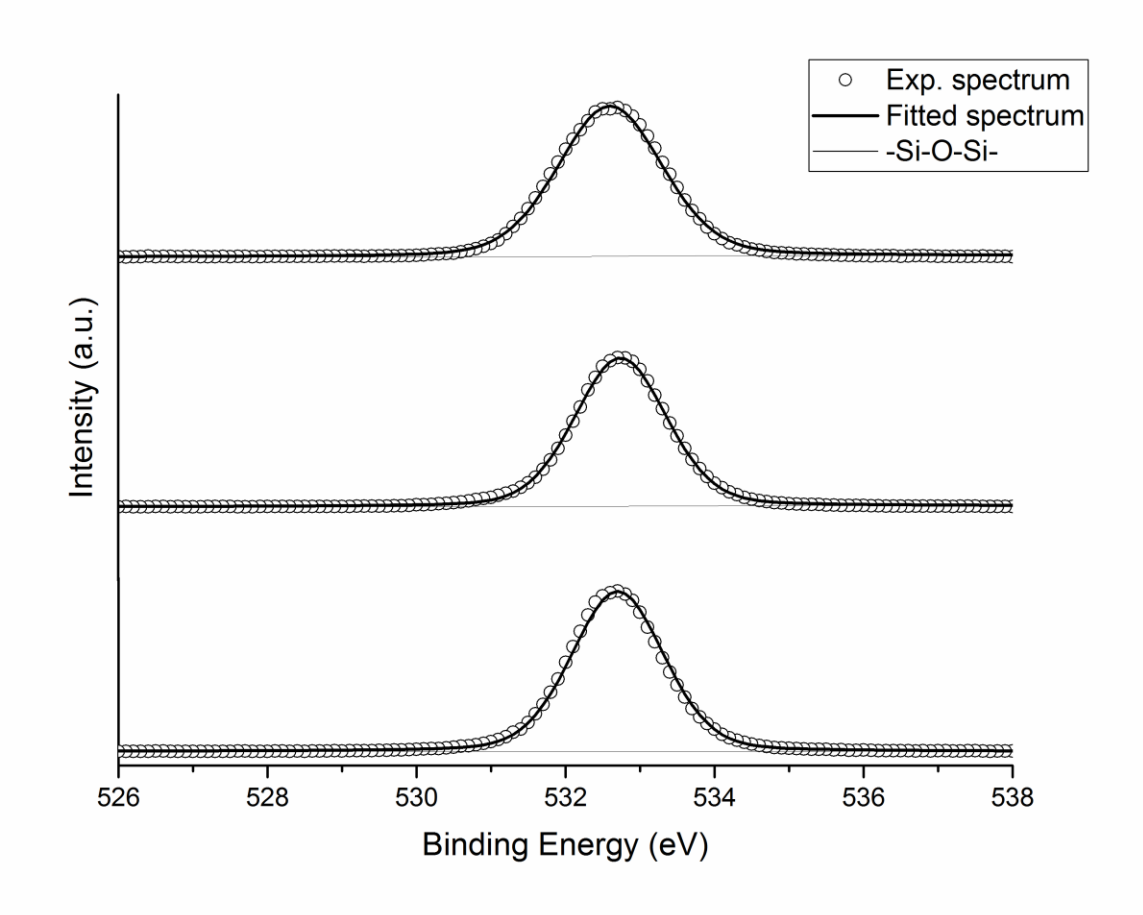

Figure 5.32. High-resolution spectra of O 1s of the DDMS-coated Si substrate: original (top), heated to 450 °C (middle), and 500 °C (bottom).

Figure 5.33 shows XPS survey spectra of a commercial nanocomposite substrate coated with DDMS at various temperatures. The C 1s peak was present in all spectra, and did not change significantly, although the intensity ratio of C 1s to Si 2p was still higher than that of the uncoated substrate, indicating the coating of DDMS. Further investigation of core-level spectra of different elements is required to analyze the DDMS decomposition.

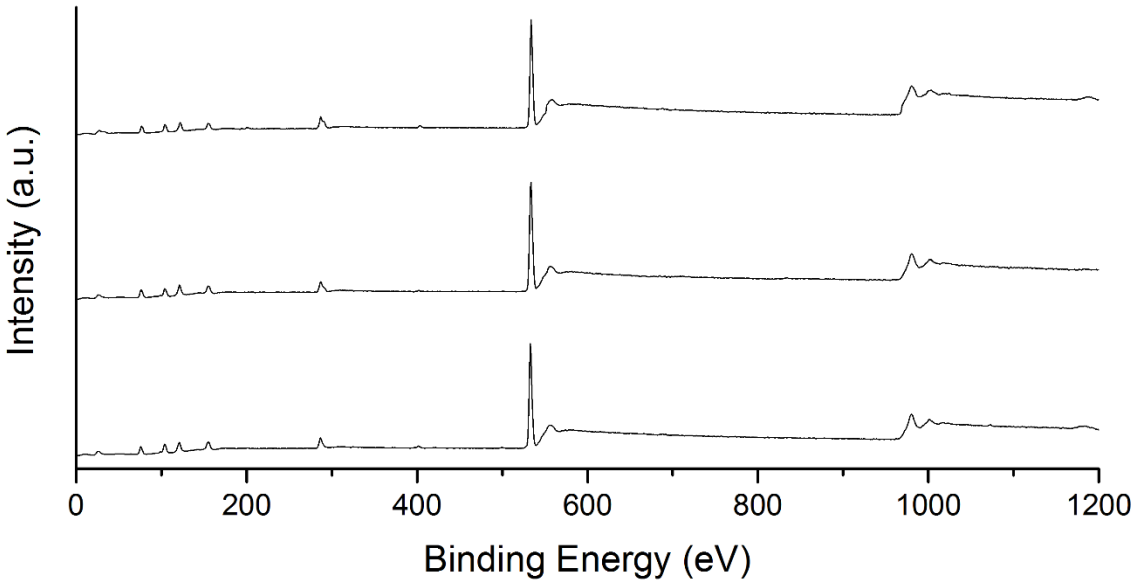

Figure 5.33. XPS survey spectra of DDMS-coated commercial nanocomposite substrate: original (top), heated to 500 °C (middle), and 550 °C (bottom).

Figures 5.34 through 5.36 show high-resolution spectra of C 1s, Si 2p, and O 1s of a DDMS-coated commercial nanocomposite substrate. The C 1s peaks obtained were very similar to those of the DDMS-coated Si substrate. The original DDMS-coated sample did not show multiple C 1s peaks, while the samples treated at higher temperatures began to show shoulder peaks. The binding energy of this shoulder peak also was approximately 287.0 eV, and derived from the carbon-oxygen bonds in the oxidized carbon species.

The Si 2p spectra for the DDMS-coated commercial nanocomposite substrate also can be deconvoluted into two components: silicon in SiO_2 (103.5 eV) and in -Si-CH_3 (102.0 eV). In this case, for the DDMS coating on this substrate, even after the sample was heated to 550 °C, deconvolution of the Si 2p spectrum could still be achieved, indicating that not all of the alkyl chains had decomposed. The ratio of the Si peak area from silane to that from silica was higher

compared to that in the DDMS-coated Si substrate. This ratio decreased as the treatment temperature increased, and the Si peak could be distinguished in all samples. This suggests that more silane structures remained on the surface of the DDMS coating on the commercial substrate after heat treatment, which is likely the reason for its better thermal stability.

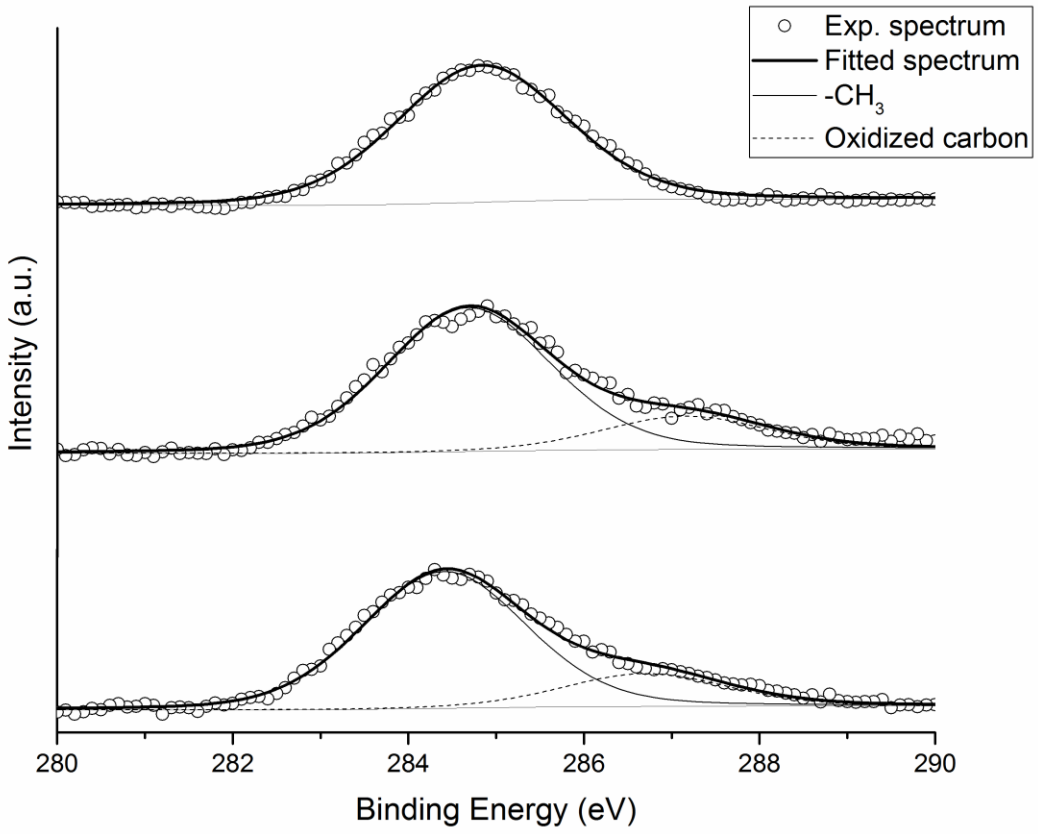

Figure 5.34. High-resolution spectra of C 1s of DDMS-coated commercial nanocomposite substrate: original (top), heated to 500 °C (middle), and 550 °C (bottom).

As discussed earlier, the O 1s spectra of the DDMS-coated commercial nanocomposite substrate have two components: oxygen in -Si-O-Si- (531.2 eV) and in -Al-O-Al- (532.6 eV). The ratio of the peak area from these two kinds of oxygen did not change greatly before and after heat treatment, which indicates that the silane structure remained on the surface. However, within the Si-O band range, deconvolution of the peaks for O from silane and from silica still were not available.

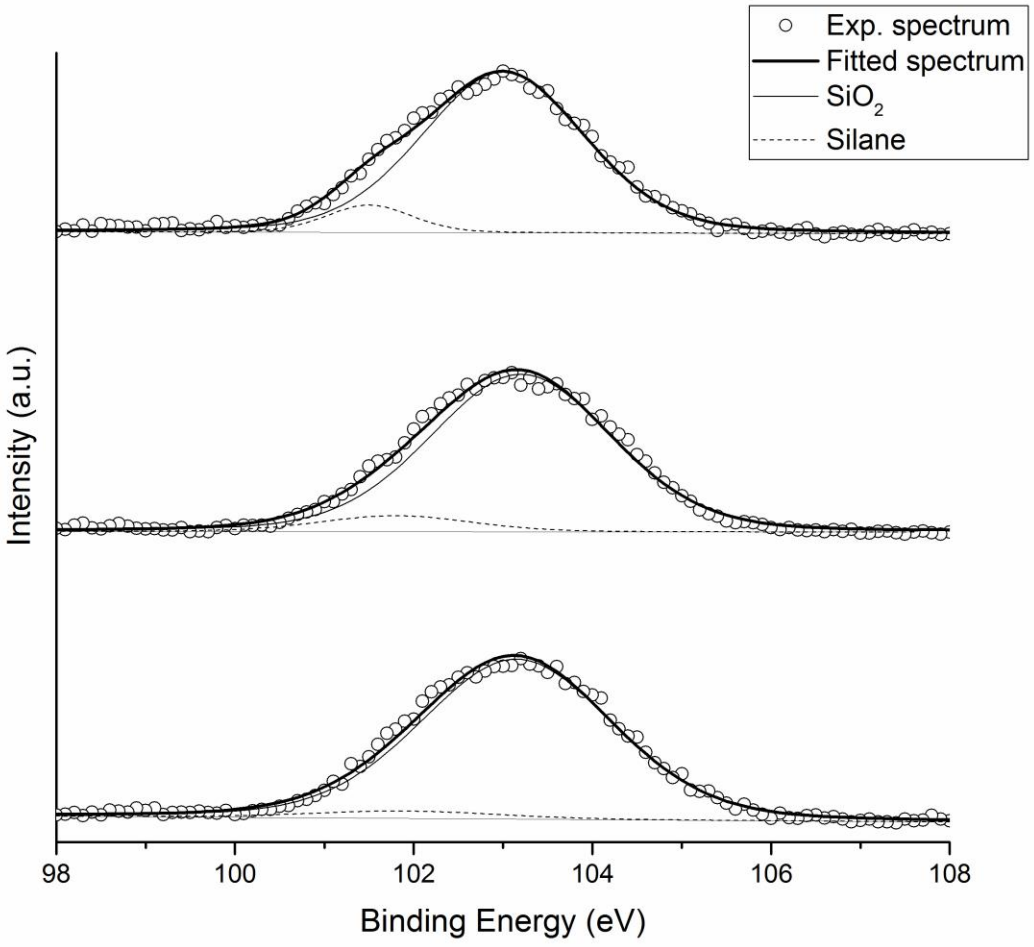

Figure 5.35. High-resolution spectra of Si 2p of the DDMS-coated commercial nanocomposite substrate: original (top), heated to 500 °C (middle), and 550 °C (bottom).

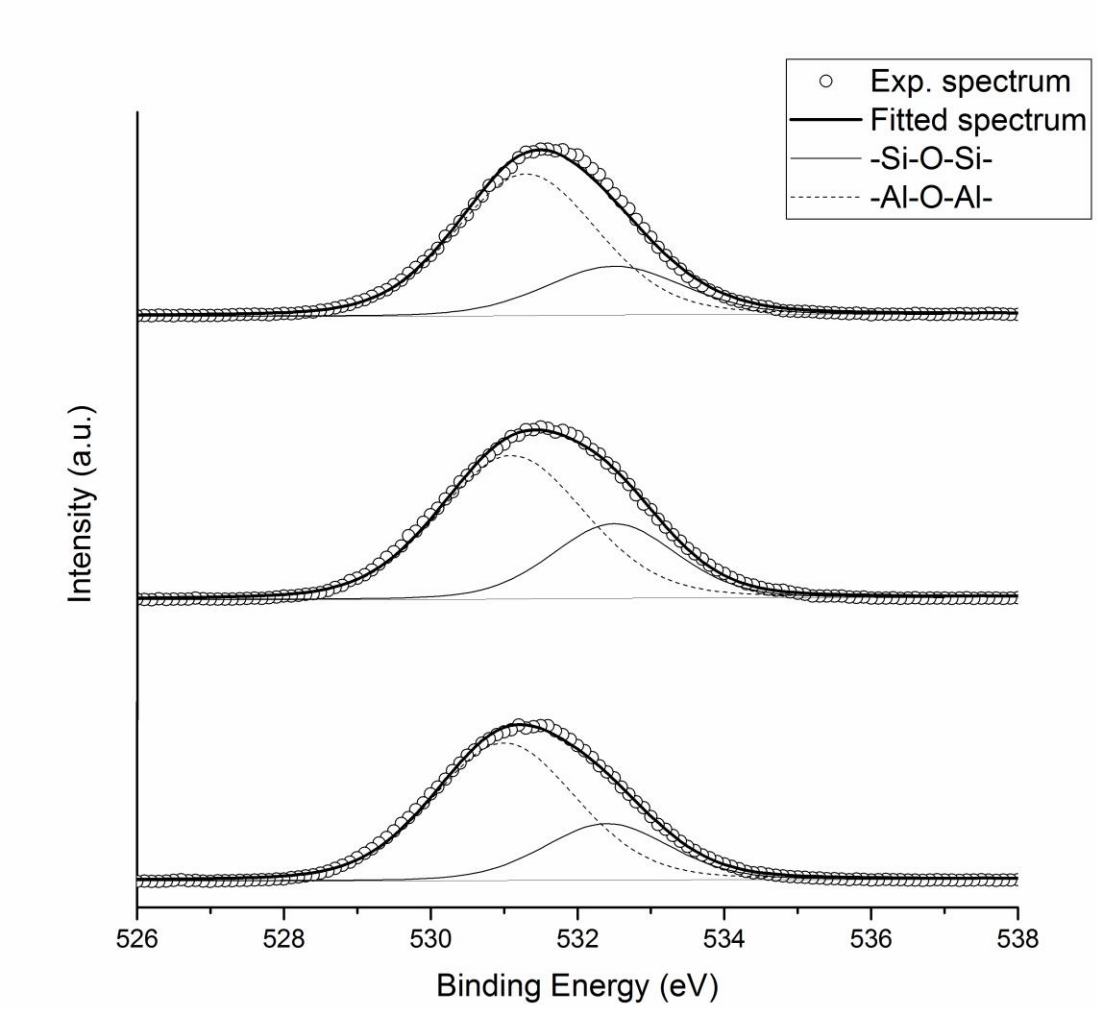

Figure 5.36. High-resolution spectra of O 1s of the DDMS-coated commercial nanocomposite substrate: original (top), heated to 500 °C (middle), and 550 °C (bottom).

Based on the high-resolution spectra information for C 1s, Si 2p, and O 1s, it can be concluded that the DDMS coating on the commercial nanocomposite substrate decomposes through oxidation of the methyl chain. The improved thermal stability is attributable to the higher stability of the silane structure, as confirmed by the Si 2p spectra.

To obtain a better understanding of the way in which the silane structure improves thermal stability, a quantitative analysis was performed for the Si and O atoms. It was discussed previously that vapor-phase silane oligomerization may take place in the DDMS and water vapor mixture. This reaction may produce a type of oligomer that appears as a viscous liquid and condenses on rough structures where the capillary space is confined with respect to its surroundings. Similar reactions have been reported for several alkyltrichlorosilanes (Fadeev et al., 2000). If DDMS is polymerized, polydimethylsiloxane (PDMS) oligomer may be achieved. A schematic of DDMS- and PDMS-coated surfaces is shown in Figure 5.37.

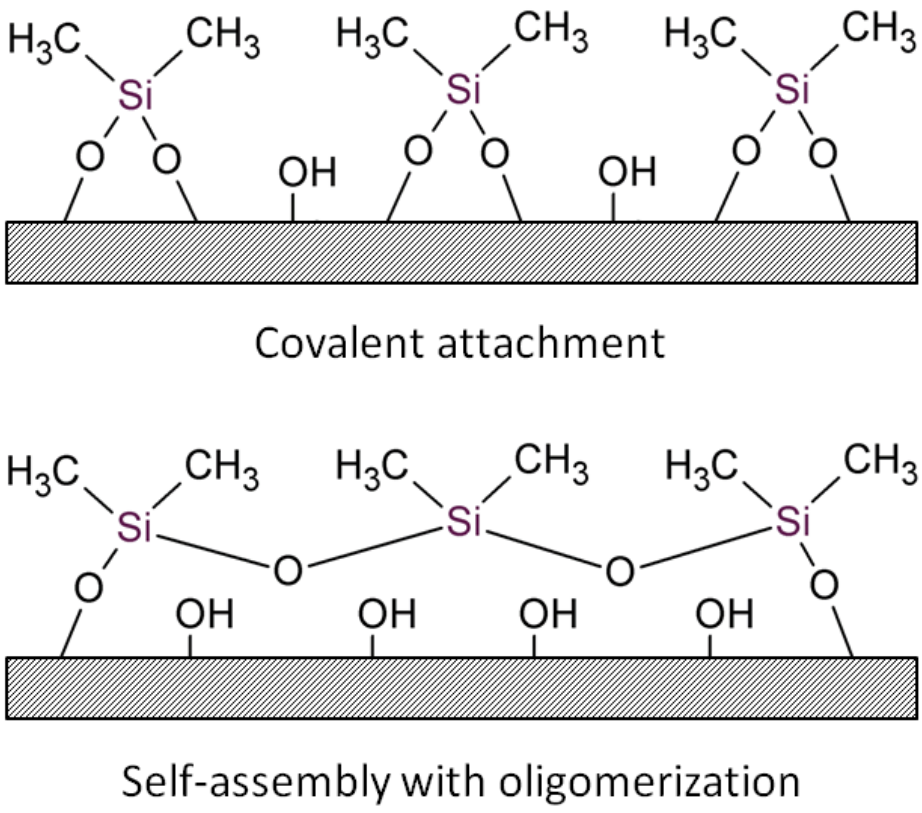

Figure 5.37. Chemical structures of covalent DDMS bonding (top), and PDMS oligomer bonding (bottom) on Si substrate.

From the chemical structures, it can be seen that, compared to the DDMS-coated surface, the PDMS coating had a lower O/Si ratio because of the H_2O loss during the polymerization between silane molecules. Quantitative analysis of Si 2p and O 1s for both DDMS-coated substrates was evaluated and the results are shown in Tables 5.8 and 5.9.

Substrate	Peak area (fitted from experimental data)				Atomic ratio	
	O(Si)	Si(total)	Si(silane)	Si(SiO_2)	O(Si)/ Si(total)	Si(silane)/ Si(SiO_2)
Original	63387 ± 1241	12449 ± 188	1171 ± 15	11278 ± 187	2.03 ± 0.05	0.10 ± 0.003
Heated to 500 ℃	55233 ± 1649	10040 ± 150	-	10040 ± 150	2.20 ± 0.07	-
Heated to 550 ℃	58737 ± 1083	10052 ± 115	-	10052 ± 115	2.32 ± 0.05	-

Table 5.8. Quantitative analysis of Si and O elements of DDMS-coated Si substrates.

Substrate	Peak area (fitted from experimental data)				Atomic ratio	
	O(Si)	Si(total)	Si(silane)	Si(SiO_2)	O(Si)/ Si(total)	Si(silane)/ Si(SiO_2)
Original	18946 ± 179	3636 ± 48	353 ± 6	3511 ± 48	1.95 ± 0.03	0.09 ± 0.002
Heated to 500 ℃	27797 ± 185	5989 ± 79	469 ± 9	5520 ± 78	1.88 ± 0.03	0.08 ± 0.002
Heated to 550 ℃	19179 ± 231	3379 ± 64	156 ± 4	3223 ± 64	2.26 ± 0.05	0.04 ± 0.001

Table 5.9. Quantitative analysis of Si and O elements of DDMS-coated commercial nanocomposite substrates.

The O/Si ratios calculated for the clean Si substrate and commercial vapor-deposition-based nanocomposite substrate were 2.26:1 and 2.22:1, respectively (Table 5.7). Table 5.8 shows that the O(Si)/Si(total) ratio for the original DDMS-coated Si substrates remained approximately 2.10 compared to the uncoated substrate (O/Si = 2.22). This indicated that the DDMS coating on the surface not only involved direct covalent bonding, but also oligomerization of dichlorosilane into polydimethylsiloxane in the presence of water with vapor-phase deposition, which resulted in a decreased O/Si ratio. This ratio increased after heat treatment together with the absence of the Si peak from silane, which derived from the decomposition of silane and oxygen introduced by surface oxidation. For the DDMS-coated commercial nanocomposite substrates, the O(Si)/Si(total) ratio decreased by 15% compared to the uncoated substrate before the substrates were heated to 550 °C. The decrease in the O(Si)/Si(total) ratio can be attributed to the PDMS oligomer coating, which had a lower O/Si ratio than that of the DDMS coating, and consequently showed better thermal stability and decomposed at higher temperatures. When the PDMS oligomer began to decompose, the coated surface lost its superhydrophobicity, and PDMS oligomer oxidation in air produced a silica-like structure in the condensed phase (Camino et al., 2001). The O/Si ratio of the surface increased again to approximately 2:1 because of oxidation and the formation of silica.

XPS results of the DDMS-coated substrate before and after heat treatment showed that the thermal decomposition of the DDMS coating was attributable to the oxidation of the methyl chain and the conversion from silane to SiO_2-like structures. Compared to the DDMS-coated Si substrate, more silane structures remained on the surface of the DDMS coating on the commercial substrate after heat treatment, which resulted in better thermal stability. Quantitative analysis showed that polymerized DDMS, or PDMS oligomer, may exist on the surface of the

rough commercial substrate and can contribute to the stable silane structures. This explains the different thermal stability of the DDMS-coated Si substrate and the commercial nanocomposite substrate. The rough morphology of the substrate plays an important role and could be a potential for future applications.

5.3.4 Tin whisker growth test of superhydrophobic nanofilms

Metallic whiskers have been a concern in electronics for a long while, as they cause short circuits in condenser plates (Smetana, 2007). The potential growth of whiskers on tin and tin alloys has attracted great interest in electronics because they are the primary finish for most electronic devices. Alloying Sn with a small percent of Pb was found to reduce tin whisker growth greatly, and this has become a common practice in the electronics industry since.

Under normal conditions, tin whisker growth may take several months or even years. With the help from Dr. Bozack in the Department of Physics, Auburn University, we achieved tin whisker growth on our coated and uncoated samples within a few months. His technology uses various background Ar pressures during sputter deposition, which changes the stress state of the thin film deposited. Attempts to grow whiskers using a relatively low background pressure of background Ar gas have been conducted (Bozack et al., 2010). Figure 5.38 shows a typical SEM image of a tin whisker growing on the substrate.

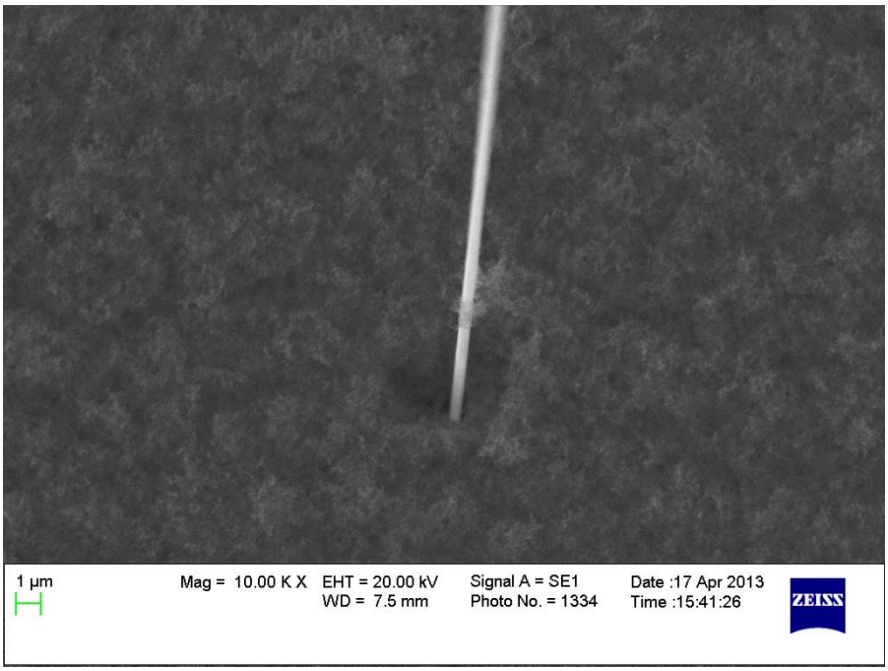

Figure 5.38. A tin whisker growing on the substrate.

SEM images of samples before and after tin whisker growth are shown in Figure 5.39. One can see that on the uncoated samples, several long tin whiskers grew on the surface after tin whisker treatment, while no tin whiskers appeared on the surface of the coated samples. This indicates that the coating offers some protection against tin whisker growth.

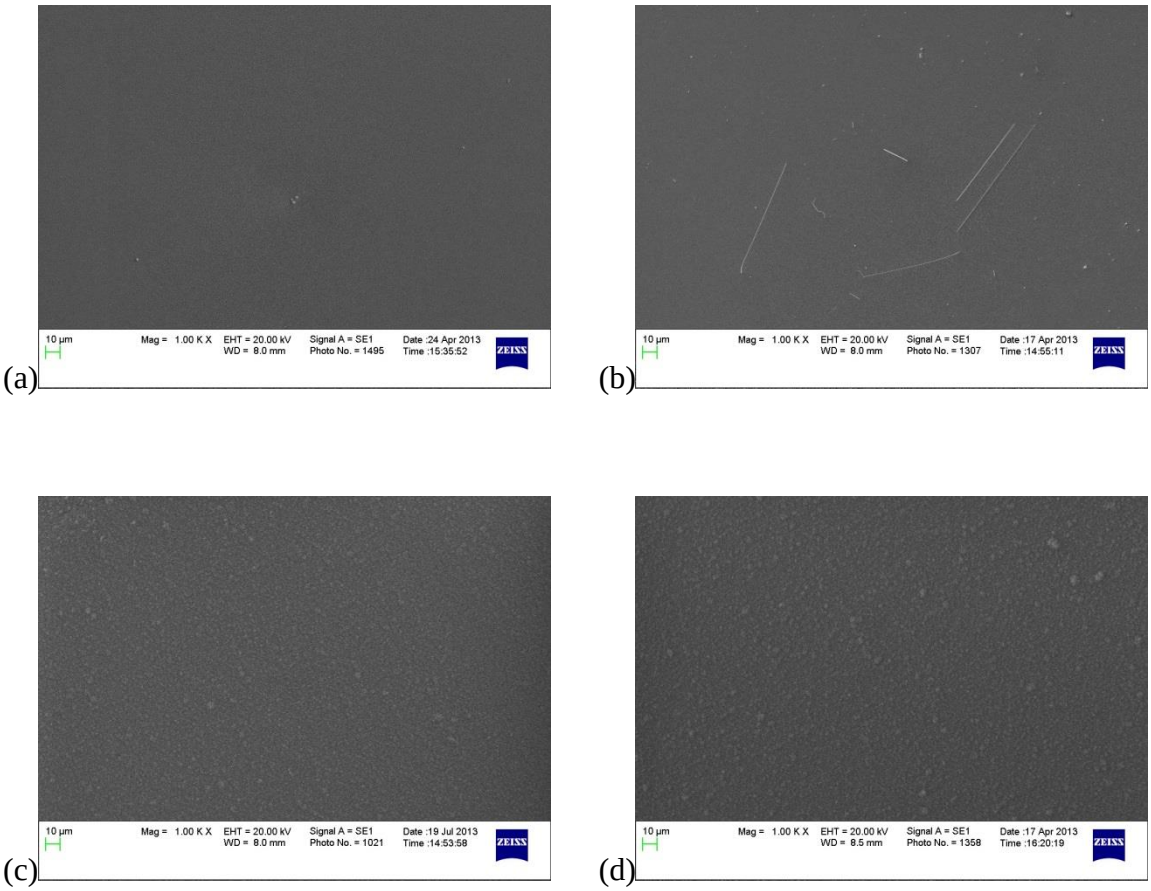

Figure 5.39. SEM images of samples with tin whisker treatment. The samples are: (a) uncoated before treatment, (b) uncoated after treatment, (c) coated before treatment, and (d) coated after treatment.

The mechanism of the growth of tin whiskers is still not understood well. There have been many theoretical assumptions, and many papers have disputed existing theories. The theory accepted most commonly now is that the driving force in tin whisker growth is compressive stress in the tin films. Oblique grain boundaries near the surface of the bulk tin produce lower stress states in the whisker grain boundary relative to the vertical grain boundaries. The movement of atoms from the grain boundary into the whisker grain results in open sites, to

which Sn atoms can then move by diffusion and provide the driving force for tin whisker growth (Figure 5.40, Smetana, 2007).

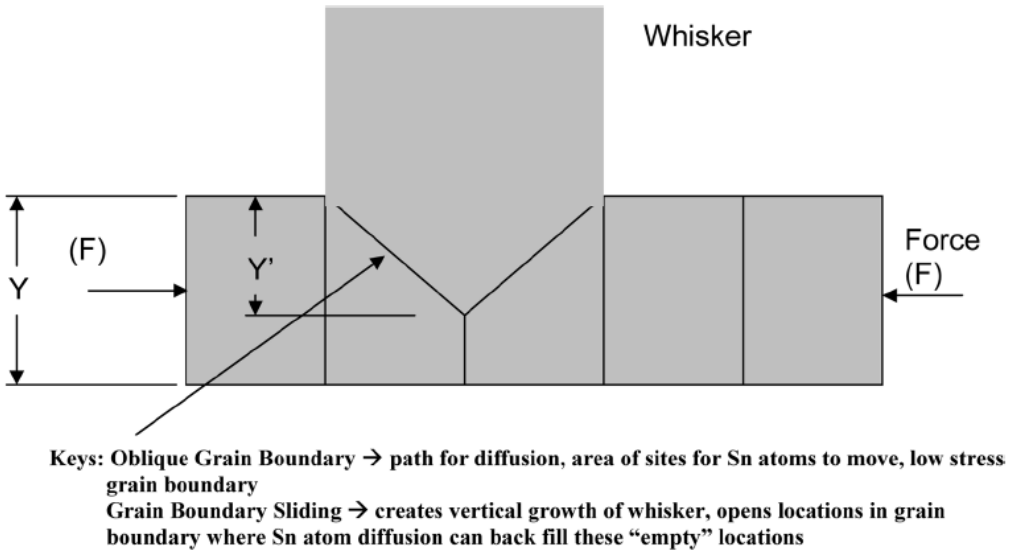

Figure 5.40. Possible mechanism of tin whisker growth (Smetana, 2007).

One possibility is that with the VPD nanoparticle coating available now, some of the defects on the surface can be filled with alumina particles, which reduces the boundary sliding and diffusion. This could reduce the boundary stress state between the grains and help the boundaries pin to each other.

5.3.5 Electromigration test of superhydrophobic nanofilms

The original definition of electromigration derives from research on metal films, and indicates the transport of material caused by the gradual movement of the ions in a conductor via

momentum transfer between conducting electrons and diffusing metal atoms. This usually occurs in the solid state and requires high temperature and current density (Tan et al., 2007).

However, in our research, we defined electromigration as metallic electromigration, or electrolytic electromigration, as this form of electromigration is an electrochemical phenomenon that takes place primarily at normal ambient conditions where the local temperatures and current densities are low enough to allow water on the surface. It involves metal migration, corrosion, and electrolysis, which has a significant influence on the performance and reliability of devices coated with superhydrophobic films.

The test procedure has been described before. A certain voltage is applied to the test board throughout the test. If this applied voltage is too low, any change requires a significant amount of time. In contrast, if the voltage is too high, nearly all of the boards will fail within one minute, which makes the comparison among different boards meaningless. Therefore, to determine an acceptable voltage range for the test, boards with different pitches were tested with a linearly-increasing voltage profile to assess their performance. The curves obtained are shown in Figure 5.41. The current began to rise at approximately 3V for all of the boards, which corresponds to an electric field of 5000-20000 V/m depending on the pitch width. Electric field strengths of such values are a good point for the electromigration to appear.

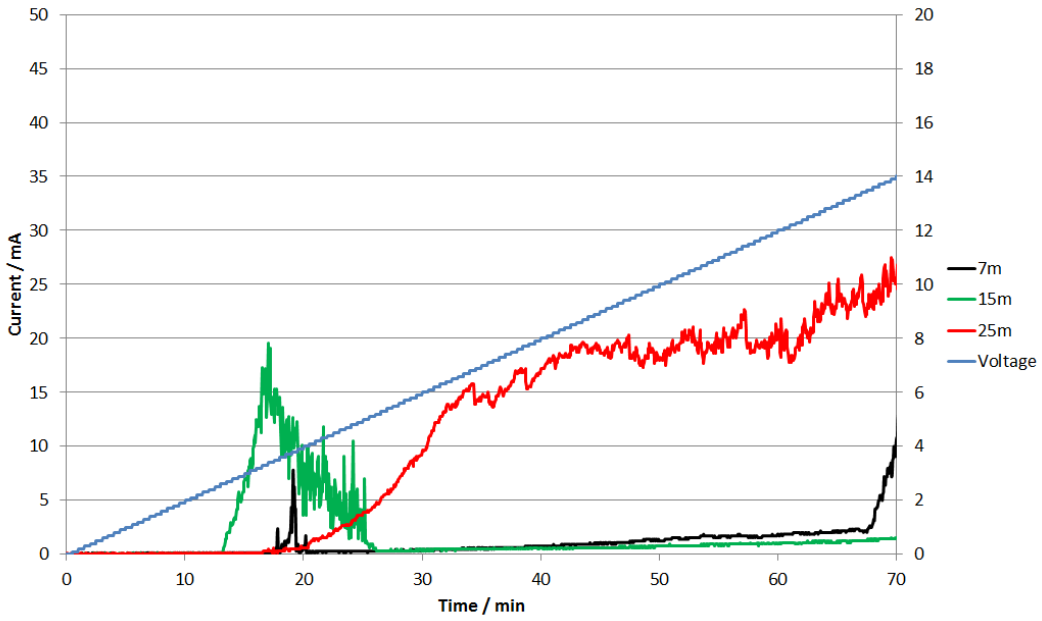

Figure 5.41. Current vs. time curves for uncoated boards with varying pitches under a linear voltage profile.

Figure 5.42 shows a typical test result curve, which illustrates the performance differences between uncoated and coated boards very clearly. Here, two key parameters were introduced to characterize the coating performance: the break time (t_b), which indicates when the current first exceeds 0.2mA, and the maximum current (I_{max}) throughout the test. The break time indicates how long the board can run properly before it fails. The maximum current describes how seriously the electromigration phenomenon, or the dendrite growth, affects the board's performance. Therefore, these parameters can be compared between uncoated and coated boards under different conditions.

Tables 5.10 and 5.11 summarize the break times and maximum current values for both uncoated and coated boards at different voltages. From the table, it can be seen that the break time for the coated board was longer than that for the uncoated board for all boards with varying

pitch widths, which demonstrated that the coating protected against electromigration before the board began to fail. Even after electromigration began, the maximum current reached by the coated board was significantly lower than that for the uncoated boards. The coating also reduced the density of dendrites growing on the surface of the board, which can be seen in the pictures of the boards after the test (Figure 5.43).

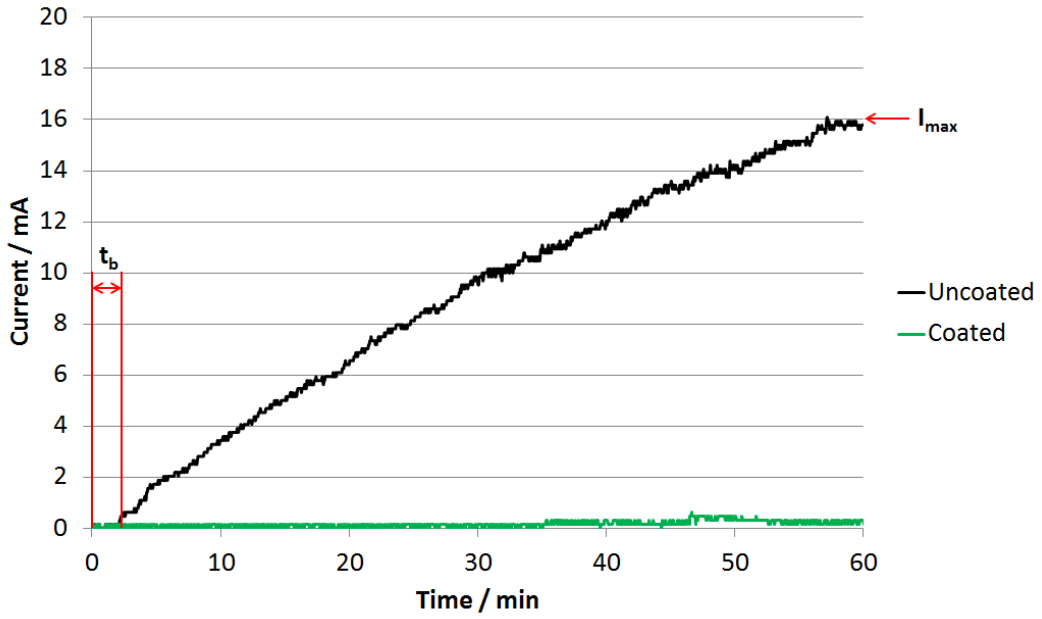

Figure 5.42. Current vs. time curves for uncoated and coated boards with 25-mil pitch at 3V.

	Uncoated			Coated		
Pitch (mil)	7	15	25	7	15	25
Break time (min)	2.2	38	80	50	>90	>90
Maximum current (mA)	16	2.1	0.6	0.3	<0.2	<0.2

Table 5.10. Break times and maximum current values of uncoated and coated boards at 2V.

	Uncoated			Coated		
Pitch (mil)	7	15	25	7	15	25
Break time (min)	0.4	3.4	14	0.9	80	>90
Maximum current (mA)	104	19	3.0	5.9	0.3	<0.2

Table 5.11. Break time and maximum current values of uncoated and coated boards at 3V.

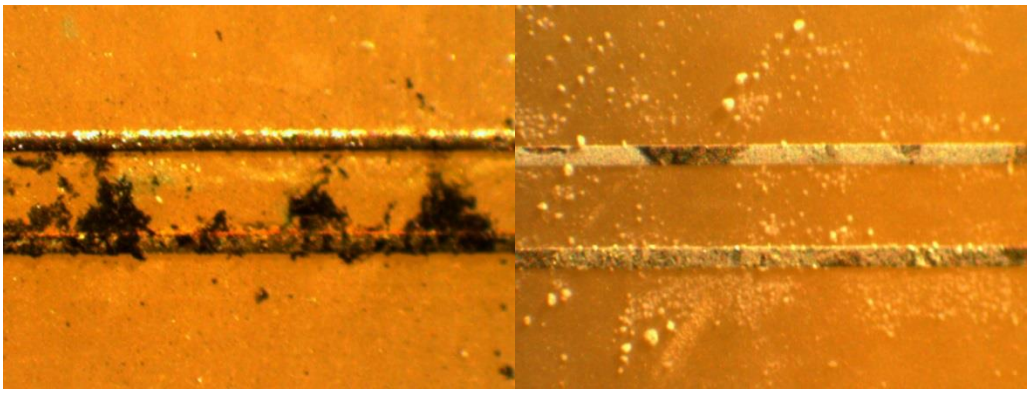

Figure 5.43. Uncoated (left) and coated boards (right) with 25-mil pitch after test at 3V.

Thus, we demonstrated that our superhydrophobic coatings provided effective protection against the electromigration phenomenon. It is important to achieve a better understanding of the dendrite growth process, which is very complex and still not explained well.

The electromigration process includes three main phenomena: electrolysis, corrosion, and dendrite growth. The reactions associated with each phenomenon are listed below.

The theoretical electrolysis voltage of water is 1.23 V. During the initial period of voltage application, H^+ and OH^- ions from water gather around the electrodes quickly and thus, the current flows rapidly. This can be demonstrated by the change in pH near the electrodes because of the electrolysis of water. At the anode, the pH is approximately 3, while at the cathode, a pH of approximately 10 has been reported (Yu et al., 2006). Therefore the electrolysis reactions are:

H^+ at anode: $2H_2O \rightarrow 4H^+ + O_2 + 4e^-$

H^+ at cathode: $2H^+ + 2e^- \rightarrow H_2$

OH^- at anode: $4OH^- \rightarrow O_2 + 2H_2O + 4e^-$

OH^- at cathode: $2H_2O + 2e^- \rightarrow H_2 + 2OH^-$

The electrolysis reactions have the following effects on the electromigration process. First, it produces H^+ and OH^- ions in the solution, which act as electrolytes between the metal wires under the electric fields applied. Second, the H_2 and O_2 gas generated will either remain or come out from the solution. As these bubbles flow, the environment around the electrodes will become unstable (Figure 5.44).

At the same time as the electrolysis, the metal corrodes, and will dissolve in solution at the anode; the corresponding standard electrode potentials are:

Sn at anode: $Sn \rightarrow Sn^{2+} + 2e^-$ Standard electrode potential: -0.136V

Pb at anode: $Pb \rightarrow Pb^{2+} + 2e^-$ Standard electrode potential: -0.126V

Both Sn and Pb follow a similar procedure, and thus, Sn is used as an example here. The Sn ion elution occurs under applied voltages. However, Sn^{2+} is not stable in the solution, and instead binds with OH^- to form $Sn(OH)_2$ according to the following equilibrium:

$Sn^{2+} + 2OH^- \leftrightarrow Sn(OH)_2$

Some of the $Sn(OH)_2$ will precipitate from the water solution and cause corrosion on the electrode (Fig 3.22), while some remains in the solution, but at very low solubility, and moves to the cathode under the electric field, where electrochemical deposition, or dendrite growth, occurs.

Sn at cathode: $Sn^{2+} + 2e^- \rightarrow Sn$

The metallic deposition at the cathode forms dendrites that grow towards the anode and cause a short when the two electrodes connect.

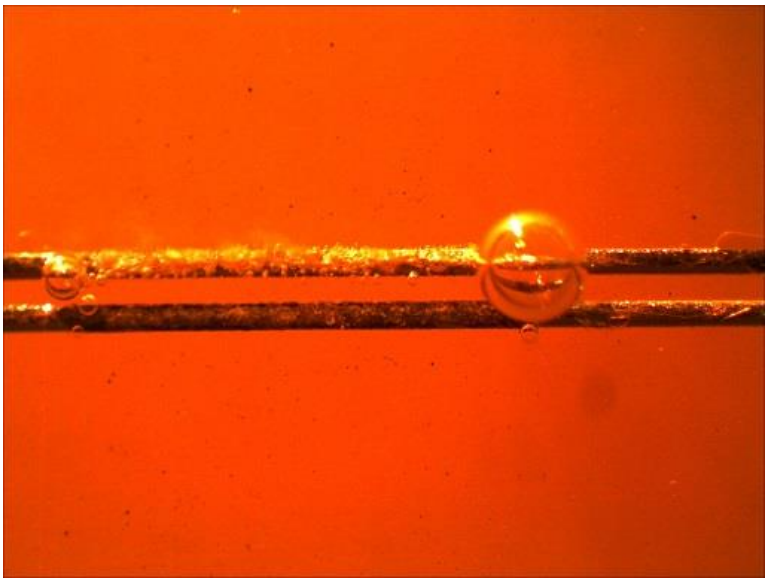

Figure 5.44. Bubbles and corrosion layer deposited on the wire.

Based on the discussion above, the general process for electromigration can be summarized as follows:

Precipitates are produced by metal ions formed by anodic corrosion, by either direct electrochemical dissolution or a multistep electrochemical process. Thereafter, these metal ions begin to migrate through the electrolyte toward the cathode under the electrical field. Metal ions deposit at the cathode and form dendrites or dendrite-like structures that grow toward the anode and may result in short circuit bridges.

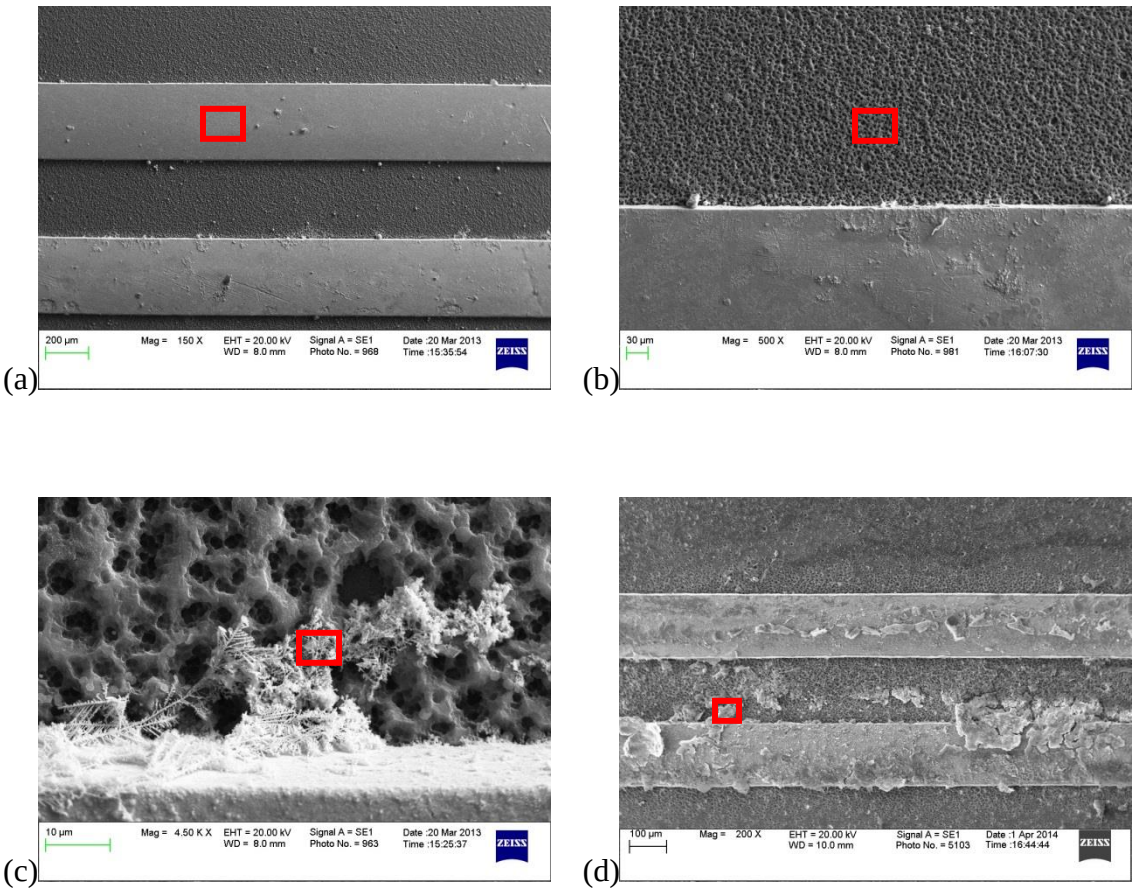

Figure 5.45. SEM images of (a) metal wires, (b) superhydrophobic coating, (c) dendrites coming from uncoated boards, and (d) dendrite-like structures coming from coated boards. The red rectangles indicate EDS scanning areas.

Therefore, superhydrophobicity plays an important role here. It keeps water away from the metal wire directly, which reduces the hydrolysis and solvation of metal ions into solution. This increases the break time of the coated boards significantly, and thereby allows them to stand longer before they begin to fail.

When electromigration begins, it is worth noting whether the superhydrophobic coating is involved in the progress. Energy-dispersive X-ray spectroscopy with SEM was used to check the composition of different areas on the board before and after the test. The original metal wires and coatings, and the dendrite grown on uncoated coated boards, were analyzed to determine their elemental compositions. Figure 5.45 shows the SEM images of selected areas.

Areas	Elemental Compositions (wt %)			
	Sn	Pb	Al	Si
Uncoated Metal Wire	66.71	33.29	0	0
Coating	4.78	4.83	59.86	30.53
Dendrite (Uncoated)	38.81	61.19	0	0
Dendrite (Coated)	27.74	61.83	5.51	4.92

Table 5.12. Elemental compositions of different areas of uncoated and coated boards.

The elemental compositions are summarized in Table 5.12. It is clear that there was a larger amount of Sn on the original metal wire. However, Pb was the main element in the

dendrites. This change is related to metals' susceptibility to corrosion, which is determined by their standard electrode potential. Another important aspect is ion mobility, as metal ions have to move across the insulator bridge before they are reduced to metal. It has been reported that the ion transport is related closely to the solubility product of $Me(OH)_x$, where Me indicates the metal ions. If the solubility is quite low, the time required for the ions' transport will be considerably longer, and the metal hydroxides will have a greater tendency to precipitate on the electrode just after formation (Yu et al., 2006). Table 5.13 shows the difference in solubility among metal ions. According to these data, the primary reason that Pb is a main part of the dendrites is due to the higher solubility product of its hydroxides.

Compound	Solubility product constant (K_{sp})	Ionic species	Solubility (S)
Ag(OH)	2.0×10^{-8}	Ag^{+}	1.4×10^{-4}
$Pb(OH)_2$	1.2×10^{-15}	Pb^{2+}	6.7×10^{-6}
$Zn(OH)_2$	1.2×10^{-17}	Zn^{2+}	1.4×10^{-6}
Cu(OH)	1.0×10^{-14}	Cu^{+}	1.0×10^{-7}
$Sn(OH)_2$	1.0×10^{-28}	Sn^{2+}	3.0×10^{-9}

Table 5.13. Comparison of the solubility of the slightly soluble precipitate, and the relative solubility of the metal ions (Yu et al., 2006).

The elemental analysis showed that some Al and Si existed in the dendrites from coated boards. This can be attributed to the coating beneath. Another possibility is that some of the Al_2O_3 dissolved into the solution and formed Al hydroxides that integrated with the dendrites. Al hydroxide is a bad conductor that will increase the resistivity of the dendrite bridge significantly and reduce the current that can pass.

5.4 Conclusion

VPD-based durable superhydrophobic nanoparticle coatings were achieved and applied to actual boards. Fundamental material characterizations for an optimal target structure and morphology were developed. Because different application environments emphasize corresponding film properties, VPD-coated substrates were characterized for their durability, water-resistance, electrical and thermal properties, and other functions based on customers' requirements.

The coatings were subjected to a water erosion test to assess the durability of superhydrophobicity. The results showed that our coating afforded good protection against water erosion. The layers of coatings deposited and the catalyst during the coating process had certain effects on the final performance. The mechanism of the superhydrophobicity was the transition from the Cassie-Baxter to Wenzel state. Increased spacing on the surface resulted in a decrease of surface roughness and the density of structures with peak height. AFM images and corresponding changes in surface roughness were consistent with this transition.

Self-assembled monolayers were applied to our coatings to improve their ability to withstand higher temperatures. Samples were heated in either a furnace or using TGA, and the corresponding results were used to analyze the coatings' heat stability. The application of SAMs increased the temperature at which the film began to fail and the contact angle value dropped. The differences between results from the furnace and TGA derived from the desorption mechanism of the monolayers. XPS results of the DDMS-coated substrate before and after heat treatment showed that the thermal decomposition of the DDMS coating was attributable to oxidation of the methyl chain and the conversion from silane to SiO_2-like structures. Quantitative analysis showed that polymerized DDMS, or the PDMS oligomer, may exist on the surface of rough commercial substrates and can contribute to stable silane structures. This explained the difference in thermal stability between the DDMS-coated Si substrate and the commercial nanocomposite substrate. The rough morphology of the substrate played an important role and could have potential in future applications.

Metallic whiskers have been a significant concern in electronics, and our coating showed the potential to serve as a protective layer against tin whisker growth. Although the tin whisker growth mechanism is still not known well, it is often related to compressive stress in the tin films. Our explanation is that with the VPD nanoparticle coating, some of the surface defects may be filled with alumina particles that reduce the boundary sliding and diffusion, which also could reduce the boundary stress state between the grains and help the boundaries pin to each other.

The VPD nanoparticle coatings were applied to electric boards and tested underwater to ensure that they are applicable for the commercial market. One of the main problems in actual

devices is electromigration, which derives from the migration of metal ions in solution and the reduction of ions into metal deposition. The superhydrophobic coating played an important role here, in that it kept water away from the metal wire directly, which reduced the hydrolysis and solvation of metal ions into solution. Another possibility is that some of the VPD nanoparticle layers dissolved into the solution and formed Al hydroxides that integrated with the dendrites, making the dendrite bridge less conductive and reducing the current flow.

Chapter 6

Conclusions and avenues for future work

6.1 Films of size-varied gold nanoparticles via GXL deposition on silicon substrates

To study the way in which deposition conditions affect film formation and how to achieve better control of the surface chemistry and morphology of the deposited film, we can deposit various self-assembled monolayers in liquid phase onto substrates prior to nanoparticle deposition by combining the SAM and GXL technologies to provide both a low energy surface and a rough nanoparticle coating. Thus, self-assembled monolayers (SAMs) were applied to Si substrates and characterized. The contact angle and thickness values of these SAMs were consistent with the measured and calculated values in other reports, which proved that smooth and uniform monolayers formed on the Si substrate, which is very important in the deposition of nanoparticles.

Film growth, which is affected by the critical surface tension of the SAMs, indicated an alternation between layer-by-layer deposition and agglomeration formation, which also changed the surface roughness. On the other hand, the surface chemistry of the AuNPs, which is affected by the stabilizing ligands on the nanoparticles, also had some effect on film deposition. By using the combination of dodecanethiol-stabilized AuNPs and APhTS-caoted Si substrates, we confirmed that the deposited nanoparticle films followed the Stranski-Krastanov mechanism. The morphology changes induced by the concentration of the nanoparticle solution emphasizes

the importance of the number of nanoparticles involved in film deposition and demonstrated the possibility to achieve better control of the films formed.

A calculation based on the GW model was applied to the surface topographies from AFM data presented and used as a quantitative assessment method to compare various coatings. The variation in concentration of the initial nanoparticle solution helps us observe the growth process. When nanoparticles of different sizes were deposited on a SAM-coated substrate at varying concentrations, the surface morphology and roughness were affected at multiple length scales. Changing the concentration had a major effect on the long-range roughness parameters, such as the rms surface roughness and standard deviation of summit height distribution. The average size of the nanoparticles affected short-range roughness parameters, such as autocorrelation length and roughness exponents. Particle and grain clustering dictated the dimensions of local agglomerations and this effect was independent of the initial concentration. The size variation in the nanoparticles allowed the opportunity to achieve better control of several important surface parameters, such as the ratio of true to apparent contact area, which is critical to minimize adhesion and friction in real applications.

The results discussed in this work indicated that the morphology of nanoparticle films can be engineered for specific surfaces to provide potential improvements in interfacial applications by altering certain deposition conditions.

6.2 Nanoparticle films based on nanomaterials of different sizes and shapes and their effect on microtribology control for MEMS devices

By using size-varied iron oxide nanoparticles via a GXL deposition technology, the surfaces of MEMS devices were coated uniformly with these nanoparticles. The mean plane separation distance between two contacting surfaces was increased, while the contact area was reduced by altering the summit density and radius, which are affected by the average size of the initial nanoparticles. Based on the experimental results and theoretical calculations, the decreased plane separation reduced the retarded van der Waals interaction and diminished the non-contacting portion's contribution to adhesion. On the other hand, normal van der Waals interactions between contacting asperities were affected by the combination of average summit density and summit radius, which plays the dominant role in adhesion. Changing these parameters affected the total effects of normal and retarded van der Waals interactions between contacting asperities, leading to reduced adhesion.

Because the apparent work of adhesion can be reduced by using iron oxide nanoparticles of larger average diameter, it was worth investigating the adhesion reduction effects by varying the initial concentration of monodispersed 20 nm iron oxide nanoparticles to see whether the size and concentration effects could be combined to reduce adhesion even more. When the initial concentration of monodispersed 20 nm iron oxide nanoparticle solutions was varied via a GXL deposition technology, the surfaces of MEMS devices could be coated uniformly with these nanoparticles. Because of the high surface tension of the substrate, the film formation of the nanoparticles then followed the Frank-van der Merwe growth mechanism, and led to the appearance of a surface covered in part with monolayer island structures. The size effect of the

nanoparticles on the reduction of adhesion still existed; however, the contribution of adhesion now derived primarily from the van der Waals interaction between nanoparticle monolayers. Based on the experimental results and theoretical calculations, the surface coverage increased as the initial concentration increased, while the surface film growth was limited at the sub-monolayer level. This led to an increase of the apparent work of adhesion, which derived from the higher interacting area when two surfaces are brought close. This demonstrated that under different surface topographical conditions, a reduction in the total contact area is essential to reduce adhesion and obtain sufficient long-range roughness.

Gold nanorods were used via a GXL deposition technology to coat the surfaces of MEMS devices. However, rather than the uniform nanocoatings that are obtained with nanoparticles, only isolated aggregates existed on the surface. Test results showed that gold nanorods cannot be deposited well as uniform films on various substrates, and the expected good reduction of adhesion cannot be achieved. To understand this effect further, a total interaction energy model was introduced to simulate the interactions between various nanoshapes and correlate the solvent-ligand interaction with the maximum size of a ligand-stabilized nanoparticle that can be dispersed within a given solvent system. Results of the calculations indicated that larger nanoshapes become unstable more easily when the particle-solvent and particle-particle interactions are affected. For gold nanorods, the side-to-side (SS) configuration was more favorable when the nanorods became unstable and precipitated from the solution, leading to aggregation even at very dilute concentrations. Therefore, the possibility to coat nanoshapes still exists, but a better design based on the surface chemistry of the nanostructures must be developed.

6.3 Durable commercial nanoparticle-based composite coatings

VPD-based, durable superhydrophobic nanoparticle coatings were achieved and applied on actual boards, and fundamental material characterizations for an optimal target structure and morphology were developed. As different application environments emphasize corresponding film properties, VPD-coated substrates were tested for their durability, water-resistance, electrical and thermal properties, and other functions based on customers' requirements.

The coatings were subjected to a water erosion test to determine the durability of superhydrophobicity, and the results showed that our coating offered good protection against water erosion. The layers of coatings deposited and the catalyst used in the coating process had certain effects on the final performance. The mechanism of the superhydrophobicity was the transition from the Cassie-Baxter to Wenzel state. Increased spacing on the surface resulted in decreased surface roughness and the density of structures with peak height. AFM images and corresponding changes in surface roughness values were consistent with this transition.

Self-assembly monolayers were applied to our coatings to increase their ability to withstand higher temperatures. Samples were heated in either a furnace or TGA and the corresponding results were used to analyze the coatings' heat stability. The application of SAMs increased the temperature at which the film began to fail and the contact angle value dropped. The differences between furnace and TGA results were attributable to the desorption mechanism of monolayers. XPS results of the DDMS-coated substrate before and after heat treatment showed that the thermal decomposition of the DDMS coating derived from the oxidation of the methyl chain and the conversion from silane to SiO_2-like structures. Quantitative analysis

showed that polymerized DDMS, or PDMS oligomer, may exist on the surface of rough commercial substrates and can contribute to the stable silane structures. This explains the difference in thermal stability between the DDMS-coated Si substrate and the commercial nanocomposite substrate. The rough morphology of the substrate plays an important role and could have potential for future applications.

Metallic whiskers are a concern in electronics and our coating showed the potential to provide a protective layer against tin whisker growth. Although the tin whisker growth mechanism is still not understood well, it is often related to compressive stress in the tin films. Our explanation of the effects obtained is that with the VPD nanoparticle coating, some of the defects on the surface may be filled in with alumina particles, which reduce the boundary sliding and diffusion. This could reduce the boundary stress state between the grains and help the boundaries pin to each other.

The VPD nanoparticle coatings were applied to electric boards and tested underwater to ensure that they are applicable to the commercial market. One of the primary problems for actual devices is electromigration, which derives from the migration of metal ions in solution and reduction of ions into metal deposition. The superhydrophobic coating played an important role here, as it kept the water away from the metal wire directly, which reduced the hydrolysis and solvation of metal ions into solution. Another possibility is that some of the VPD nanoparticle layers dissolved into the solution and formed Al hydroxides that integrated with the dendrites, making the dendrite bridge less conductive and reducing the current flow.

The durable, superhydrophobic nanocomposite coating developed can be applied as a conformal vapor deposited film, offering good surface coverage that can overcome issues with solution techniques, as well as various improvements in performance that will qualify this new material for practical applications. The potential results will satisfy the commercial use of, and economic interest in such coatings in the market.

6.4 Ideas for future work

In addition to the current progress described in previous chapters with respect to the engineering of thin film deposition and morphology, there are several possibilities for future work in the synthesis and applications of nanoparticle-based thin films for MEMS and superhydrophobicity.

One of the plans during my preliminary defense was to integrate the use of various nanoshapes into thin films to control tribology. An attempt with gold nanorods was described in Chapter 4; however, only isolated aggregates were obtained. The test results showed that gold nanorods cannot be deposited well as uniform films on various substrates and good reductions in adhesion cannot be achieved. There are some possible reasons for this result. One is the strong tendency for side-to-side attraction of the gold nanorods, which led to severe aggregation confirmed by the total energy calculations. Another issue is the nanorods' surface chemistry. Because of their rod-like shape, most gold nanorods thus far are synthesized in an aqueous medium. To disperse them well in an organic solvent for the GXL process, a phase transfer process must be introduced that includes ligand exchange. This exchange process destabilizes the

nanorods, as the ligand coverage is in doubt. Usually, thiol-stabilized gold nanorods only remain well dispersed for a few weeks to months in an aqueous medium, in contrast to which, thiol-stabilized gold nanoparticles remain stable for years in organic solvent. Therefore, the possibility to coat nanoshapes still exists, but will require a better design based on the surface chemistry of the nanostructures.

Another idea is to focus on the substrate itself. In this work, the coating substrate was either clean Si or SAM-coated Si. A uniform surface layer is expected to provide control of the morphology of nanoparticle films. On the other hand, patterning techniques can be applied on the substrate to make certain "grow-from" structures on the surface as the base morphology of nanoparticle coating. Thereafter, the nanoparticle coatings can be deposited on the substrate to form the morphologies designated. Previous reports have indicated that patterning on a standard Si wafer has been achieved (Kim et al., 2001; Byun et al., 2014); however, because the sacrificial layer etching is the last step in microinstrument fabrication, making the patterning available on the substrate of a SOI wafer revealed after etching would be a challenge. Therefore, it is worth investigating the way in which the patterning process can be integrated with the existing MEMS fabrication procedure.

For commercial nanocomposite superhydrophobic coatings, the films' durability remains the key issue. Water has been used extensively to simulate a real environment. However, during our daily life, other liquids, such as sports beverages, may be spilled on phones or laptops. These liquids contain large amounts of electrolytes, which could be fatal to the performance of these films. For example, we tested a board protected by the superhydrophobic coating in salt water (which contains electrolytes) rather than tap water, and it failed within 30 seconds after the

voltage was applied. This implies that the film should have a denser structure, which requires the combination of other deposition techniques, such as plasma-enhanced vapor deposition.

References

Adamson, A. W., Gast, A. P. *Physical Chemistry of Surfaces, 6th Edition*, 1990, New York, NY: John Wiley & Sons, Inc.

Anand, M., McLeod, M. C., Bell, P. W., Roberts, C. B. Tunable solvation effects on the size-selective fractionation of metal nanoparticles in CO_2 gas-expanded liquids. *Journal of Physical Chemistry B*, 2005, **109**, 22852-22859.

Anderson, A., Ashurst, W. R. Investigation of a vapor deposited thin silica film as a novel substrate for *in situ* Fourier transform infrared spectroscopy, *Journal of Vacuum Science & Technology A*, 2008, **26**, 1357-1361.

Ansari, N. Understanding the effect of surface topography on stiction and friction in MEMS. Ph.D. Dissertation, Auburn University, 2011.

Alivisatos, A. P. Perspectives on the physical chemistry of semiconductor nanocrystals. *Journal of Physical Chemistry*, 1996, **100**, 13226-13239

Anandarajah, A., Chen, J. Single correction function for computing retarded van der Waals attraction. *Journal of Colloid and Interface Science*, 1995, **176**, 293-200.

Ashurst, W. R., Yau, C., Carraro, C., Howe, R. T., Maboudian, R. Alkene based monolayer films as anti-stiction coatings for polysilicon MEMS. *Sensors and Actuators A*, 2001a, **91**, 239-248.

Ashurst, W. R., Yau, C., Carraro, C., Howe, R. T., Maboudian, R., Dugger, M. T. Dichlorodimethylsilane as an anti-stiction monolayer for MEMS. *Journal of Microelectromechanical Systems*, 2001b, **10**, 41-49.

Ashurst, W. R., Carraro, C., Maboudian, R., Frey, W. Wafer level anti-stiction coatings for MEMS. *Sensors and Actuators A: Physical*, 2003, **104**, 213-221.

Bellino, M. G., Calvo, E. J., Gordillo, G. Adsorption kinetics of charged thiols on gold nanoparticles. *Physical Chemistry, Chemical Physics*, 2004, **6**, 424-428.

Bhushan, B. *Introduction to Tribology, 2nd Edition*. 2002, New York, NY: John Wiley & Sons, Inc.

Birdi, K. S. *Surface Chemistry Essentials*. 2013, Boca Raton, FL: CRC Press.

Bozack, M. J., Crandall, E. R., Rodekohr, C. L., Dean, R. N., Flowers, G. T., Suhling, J. C. High lateral resolution Auger Electron Spectroscopic (AES) measurements for Sn whiskers on brass. *IEEE Transactions on Electronics Packaging Manufacturing*, 2010, **33**, 198-204.

Brown, K. R., Natan, M. J. Hydroxylamine seeding of colloidal Au nanoparticles in solution and on surfaces. *Langmuir*, 1998, **14**, 726-728.

Brust, M., Walker, M., Bethell, D., Schiffrin, D. J., Whyman, R. Synthesis of thiol-derivatised gold nanoparticles in a two-phase liquid–liquid system. *Journal of the Chemical Society, Chemical Communications*, 1994, 801-802.

Bush, A. W., Gibson, R. D., Keogh, G. P. The limit of elastic deformation in the contact of rough surfaces. *Mechanics Research Communications*, 1976, **3**, 169-174.

Byun, I., Coleman, A. W., Kim, B. SAM meets MEMS: Reliable fabrication of stable Au-patterns embedded in PDMS using dry peel-off process. *Microsystem Technologies*, 2014, **20**, 1783-1789.

Camino, G., Lomakin, S. M., Lazzaria, M. Polydimethylsiloxane thermal degradation Part 1. Kinetic aspects. *Polymer*, 2001, **42**, 2395-2402.

Carpick, R. W., Flater, E. E., VanLangendon, J. R., de Boer, M. P. Friction in MEMS: From single to multiple asperity contact. *SEM Annual Conference & Exposition on Experimental and Applied Mechanics*, 2002, location.

Choi, J., Kawaguchi, M., Kato, T. Spreading of perfluoropolyethers on FDTS-coated amorphous carbon surfaces. *IEEE Transactions on Magnetics*, 2004, **40**, 3189-3191.

Choy, K. L. Chemical vapour deposition of coatings. *Progress in Materials Science*, 2003, **48**, 57-170.

Chumpitaz, L. D. A., Coutinho, L. F., Meirelles, A. J. A. Surface tension of fatty acids and triglycerides. *Journal of the American Oil Chemists' Society*, 1999, **76**, 379-382.

Clarke, N. Z., Waters, C., Johnson, K. A., Satherley, J., Schiffrin, D. J. Size-dependent solubility of thiol-derivatized gold nanoparticles in supercritical ethane. *Langmuir*, 2001, **17**, 6048-6050.

Cliffel, D. E., Zamborini, F. P., Gross, S. M., Murray, R. W. Mercaptoammonium-monolayer-protected, water-soluble gold, silver, and palladium clusters. *Langmuir*, 2000, **16**, 9699-9702.

Comeau, K. D., Meli, M. V. Effect of alkanethiol chain length on gold nanoparticle monolayers at the air-water interface. *Langmuir*, 2012, **28**, 377-381.

de Boer, M. P., Michalske, T. A. Accurate method for determining adhesion of cantilever beams. *Journal of Applied Physics*, 1999, **86**, 817-827.

de Boer, M. P., Knapp, J. A., Michalske, T. A., Srinivasan, U., Maboudian, R., Adhesion hysteresis of silane coated microcantilevers. *Acta Materialia*, 2000, **48**, 4531-4541.

DelRio, F. W., de Boer, M. P., Knapp, J. A., Reedy, E. D., Clews, P. J., Dunn, M. L. The role of van der Waals forces in adhesion of micromachined surfaces. *Nature Materials*, 2005, **4**, 629-634.

DelRio, F. W., Dunn, M. L., Boyce, B. L., Corwin, A. D., de Boer, M. P. The effect of nanoparticles on rough surface adhesion. *Journal of Applied Physics*, 2006, **99**, 104304.

Doms, M., Feindt, H., Kuipers, W. J., Shewtanasoontorn, D., Matar, A. S., Brinkhues, S., Welton, R. H., Mueller, J. Hydrophobic coatings for MEMS applications. *Journal of Micromechanics and Microengineering*, 2008, **18**, 055030.

Du, Y., Du, X., George, S. M. Mechanism of pyridine-catalyzed SiO_2 atomic layer deposition studied by Fourier transform infrared spectroscopy. *The Journal of Physical Chemistry C*, 2007, **111**, 219-226.

Fadeev, A. Y., McCarthy, T. J. Self-assembly is not the only reaction possible between alkyltrichlorosilanes and surfaces: Monomolecular and oligomeric covalently attached layers of dichloro- and trichloroalkylsilanes on silicon. *Langmuir*, 2000, **16**, 7268-7274.

Faucheux, A., Yang, F., Allongue, P., Henry de Villeneuve, C., Ozanam, F., Chazalviel, J. N. Thermal decomposition of alkyl monolayers covalently grafted on (111) silicon. *Applied Physics Letters*, 2006, **88**, 193123.

Feynman, R. There's plenty of room at the bottom. *A Talk at an American Physical Society Meeting*, 1959.

Frechette, J., Maboudian, R., Carraro, C. Thermal behavior of perfluoroalkylsiloxane monolayers on the oxidized Si(100) surface. *Langmuir*, 2006, **22**, 2726-2730.

Friedrich, T., Raudzis C., Muller-Fiedler, R. Experimental study of in-plane and out-of-plane adhesions in microelectromechanical systems. *Journal of Microelectromechanical Systems*, 2009, **18**, 1326-1334.

Gad-el-Hak, M. *MEMS: Introduction and Fundamentals*. 2006, Boca Raton, FL: CRC Press

Gandhi, D. D., Ganesan, P. G., Chandrasekar, V., Gan, Z., Mhaisalkar, S. G., Li, H., Ramanath, G. Molecular-nanolayer-induced suppression of in-plane Cu transport at Cu-silica interfaces. *Applied Physics Letters*, 2007, **90**, 163507.

Gao, W., Dickinson, L., Grozinger, C., Morin, F. G., Reven, L. Order-disorder transitions in self-assembled monolayers: A ^{13}C solid-state NMR study. *Langmuir*, 1997, **13**, 115-118.

Greenwood, J. A. Contact of Rough Surfaces in *Fundamentals of Friction: Macroscopic and Microscopic Processes*. 1992, Netherlands: Springer Verlag.

Greenwood, J. A., Williamson, J. B. P. Contact of nominally flat surfaces. *Proceedings of the Royal Society A: Mathematical, Physical, and Engineering Sciences*, 1966, **295**, 300-319.

Groner, M. D., Fabreguette, F. H., Elam, J. W., George, S. M. Low-temperature Al_2O_3 atomic layer deposition. *Chemistry of Materials*, 2004, **16**, 639-645.

Hamaker, H. C. The London-van der Waals attraction between spherical particles. *Physica*, 1937, **4**, 1058-1072.

Hariharan, P., Oreb, B. F., Eiju, T. Digital phase-shifting interferometry: A simple error-compensating phase calculation algorithm. *Applied Optics*, 1987, **26**, 2504-2506.

Herrmann, C. F., DelRio, F. W., Bright, V. M., George, S. M. Conformal hydrophobic coatings prepared using atomic layer deposition seed layers and non-chlorinated hydrophobic precursors. *Journal of Micromechanics and Microengineering*, 2005, **15**, 984-992.

Hoffman, R. W. Stress distributions and thin film mechanical properties. *Surface and Interface Analysis*, 1981, **3**, 62-66.

Hoivika, N. D., Elamb, J.W., Lindermana, R. J., Brighta, V. M., Georgeb, S. M., Lee, Y. C. Atomic layer deposited protective coatings for micro-electromechanical systems. *Sensors and Actuators A: Physical*, 2003, **103**, 100-108.

Hong, H. G., Sackett, D. D., Mallouk, T. E. Adsorption of well-ordered zirconium phosphonate multilayer films on high surface area silica. *Chemistry of Materials*, 1991, **3**, 521-527.

Huang, Y. H., Vasan, A. S., Doraiswami, R., Osterman, M., Pecht, M. MEMS reliability review. *IEEE Transactions on Device and Materials Reliability*, 2012, **12**, 482-493

Hurst, K. M., Roberts, C. B., Ashurst, W. R. A gas-expanded liquid nanoparticle deposition technique for reducing the adhesion of silicon microstructures. *Nanotechnology*, 2009, **20**, 185303.

Hurst, K. M., Roberts, C. B., Ashurst, W. R. Characterization of gas-expanded liquid-deposited gold nanoparticle films on substrates of varying surface energy. *Langmuir*, 2011, **27**, 651-655.

Ingram, D. R., Kotsmar, C., Yoon, K. Y., Shao, S., Huh, C., Bryant, S. L., Milner, T. E., Johnston, K. P. Superparamagnetic nanoclusters coated with oleic acid bilayers for stabilization of emulsions of water and oil at low concentration. *Journal of Colloid and Interface Science*, 2010, **351**, 225-232.

Israelachvili, J. N. *Intermolecular and Surface Forcesforces, 2nd ed. 1992*, London, UK: Academic Press.

Jain, T. K., Morales, M., Sahoo, S. K., Leslie-Pelecky, D. L., Labhasetwar, V. Iron oxide nanoparticles for sustained delivery of anticancer agents. *Molecular Pharmaceutics*, 2005, **2**, 194-205.

Jessop, P. G., Subramaniam, B. Gas-expanded liquids. *Chemical Reviews*, 2007, **107**, 2666-2694.

Johnson, K. L. *Contact Mechanics*. 2003, Cambridge, UK: Cambridge University Press.

Jost, H. P. Tribology: How a word was coined 40 years ago. *Tribology & Lubrication Technology*, 2006, **62**, 24-29.

Kim, B. J., Kim, G. M., Liebau, M., Huskens, J., Reinhoudt, D. N., Brugger, J. "SAMs meet MEMS": Surface modification with self-assembled monolayers for the dry-demolding of photoplastic MEMS/NEMS. Paper presented at the *14th IEEE International Conference on Micro Electro Mechanical Systems*, 2001, location.

Kim, H. J., Lee, H., Maeng, W. J. Applications of atomic layer deposition to nanofabrication and emerging nanodevices. *Thin Solid Films*, 2009, **517**, 2563-2580.

Kim, S., Sohn, H., Boo, J. H., Lee, J. Significantly improved stability of n-octadecyl-trichlorosilane self-assembled monolayer by plasma pretreatment on mica. *Thin Solid Films*, 2008, **516**, 940-947.

Kitchens, C. L., McLeod, M. C., Roberts, C. B. Solvent effects on the growth and steric stabilization of copper metallic nanoparticles in AOT reverse micelle systems. *Journal of Physical Chemistry B*, 2003, **107**, 11331-11338.

Kluth, G. J., Sander, M., Sung, M. M., Maboudian, R. Study of the desorption mechanism of alkylsiloxane self-assembled monolayers through isotopic labeling and high resolution

electron energy-loss spectroscopy experiments. *Journal of Vacuum Science & Technology A*, 1998, **16**, 932-936.

Kluth, G. J., Sung, M. M., Maboudian, R. Thermal behavior of alkylsiloxane self-assembled monolayers on the oxidized Si(100) surface. *Langmuir*, 1997, **13**, 3775-3780.

Krim, J., Indekeu, J. O. Roughness exponents: A paradox resolved. *Physical Review E*, 1993, **48**, 1576-1578.

Laurent, S., Forge, D., Port, M., Roch, A., Robic, C., Vander Elst, L., Muller, R. N. Magnetic iron oxide nanoparticles: Synthesis, stabilization, vectorization, physicochemical characterizations, and biological applications. *Chemical Reviews*, 2008, **108**, 2064-2110.

Lee, J. B., Gwon, H. R., Lee, S. H., Cho, M. Wetting transition characteristics on microstructured hydrophobic surfaces. *Materials Transactions*, 2010, **51**, 1709-1711.

Lee, K., Jur, J. S., Kim, D. H., Parsons, G. N. Mechanisms for hydrophilic/hydrophobic wetting transitions on cellulose cotton fibers coated using Al_2O_3 atomic layer deposition. *Journal of Vacuum Science & Technology A*, 2012, **30**, 01A163.

Liu, J., Anand, M., Roberts, C. B. Synthesis and extraction of D-glucosestabilized Au nanoparticles processed into low-defect, wide-area thin films and ordered arrays using CO_2-expanded liquids. *Langmuir*, 2006, **22**, 3964-3971.

Liu, J., Sutton, J., Roberts, C. B. Synthesis and extraction of monodispersed sodium carboxymethylcellulose-stabilized platinum nanoparticles for the self-assembly of ordered arrays. *Journal of Physical Chemistry C*, 2007a, **111**, 11566-11576.

Liu, X., Atwater, M., Wang, J., Huo, Q. Extinction coefficient of gold nanoparticles with different sizes and different capping ligands. *Colloids and Surfaces B: Biointerfaces*, 2007b, **58**, 3-7.

Maboudian, R., Ashurst, W. R., Carraro, C. Self-assembled monolayers as anti-stiction coatings for MEMS: Characteristics and recent developments. *Sensors and Actuators*, 2000, **82**, 219-223.

Maboudian, R., Howe, R. T. Critical review: Adhesion in surface micromechanical structures. *Journal of Vacuum Science & Technology B*, 1997, **15**, 1-20.

Mastrangelo, C. H., Hsu, C. H. A simple experimental technique for the measurement of the work of adhesion of microstructures. *Solid-State Sensor and Actuator Workshop, 5th Technical Digest*, 1992, vol. #, 208-212.

McCool, J. I. Comparison of models for the contact of rough surfaces. *Wear*, 1986, **107**, 37-60.

McLeod, M. C., Anand, M., Kitchens, C. L., Roberts, C. B. Precise and rapid size selection and targeted deposition of nanoparticle populations using CO_2 gas expanded liquids. *Nano Letters*, 2005, **5**, 461-465.

Nayak, P. R. Random process model of rough surfaces in plastic contact. *Wear*, 1973, **26**, 305-333.

Neouze, M. A. Nanoparticle assemblies: Main synthesis pathways and brief overview on some important applications. *Journal of Materials Science*, 2013, **48**, 7321-7349.

Ohring, M. *Materials Science of Thin Films: Deposition & Structure, 2nd Edition*. 2002, San Diego, CA: Academic Press.

Persson, B. N. J. Theory of rubber friction and contact mechanics. *Journal of Chemical Physics*, 2001, **115**, 3840-3861.

Poda, A., Anderson, A., Ashurst, W. R. Self-assembled octadecyltrichlorosilane monolayer formation on a highly hydrated silica film. *Applied Surface Science*, 2010, **256**, 6805-6813.

Ramezani, A., Alasty, A., Akbari, J. Closed-form approximation and numerical validation of the influence of van der Waals force on electrostatic cantilevers at nano-scale separations. *Nanotechnology*, 2008, **19**, 015501.

Rao, C. N. R., Kulkarni, G. U., Thomas, P. J., Edwards, P. P. Size-dependent chemistry: Properties of nanocrystals. *Chemistry-A European Journal*, 2002, **8**, 28-35.

Rao, C. N. R., Muller, A., Cheetham, A. K. *The Chemistry of Nanomaterials: Synthesis, Properties and Applications*. 2004, Weinheim, Germany: WILEY-VCH Verlag GmbH & Co.

Rhee, H., Kwon, H., Kim, C. K., Kim, H., Yoo, J., Kim, Y. W. Comparison of deep silicon etching using SF6/C4F8 and SF6/C4F6 plasmas in the Bosch process. *Journal of Vacuum Science & Technology B*, 2008, **26**, 576-581.

Sau, T. K., Murphy, C. J. Room temperature, high-yield synthesis of multiple shapes of gold nanoparticles in aqueous solution. *Journal of the American Chemical Society*, 2004, **126**, 8648-8649.

Saunders, S. R. Use of gas-expanded liquids as tunable solvents for the preparation of well-defined nanomaterials. Ph.D. dissertation, Auburn University, 2011a.

Saunders, S. R., Eden, M. R., Roberts, C. B. Modeling the dispersability of polydisperse nanoparticles in gas-expanded liquids. *Journal of Physical Chemistry C*, 2011b, **115**, 4603-4610.

Saunders, S. R., Roberts, C. B. Tuning the precipitation and fractionation of nanoparticles in gas-expanded liquid mixtures. *Journal of Physical Chemistry C*, 2011c, **115**, 9984-9992.

Saunders, S. R., Roberts, C. B. Nanoparticle separation and deposition processing using gas expanded liquid technology. *Current Opinion in Chemical Engineering*, 2012, **1**, 91-101.

Santalla, S. N., Kanyinda-Malu, C., de la Cruz, R. M. Stranski–Krastanov growth mode in Ge/Si (0 0 1) self-assembled quantum dots. *Journal of Crystal Growth*, 2003, **253**, 190-197.

Shah, P. S., Holmes, J. D., Johnston, K. P., Korgel, B. A. Size-selective dispersion of dodecanethiol-coated nanocrystals in liquid and supercritical ethane by density tuning. *Journal of Physical Chemistry B*, 2002, **106**, 2545-2551.

Shah, P. S., Hanrath, T., Johnston, K. P., Korgel, B. A. Nanocrystal and nanowire synthesis and dispersibility in supercritical fluids. *Journal of Physical Chemistry B*, 2004, **108**, 9574-9587.

Shon, Y. S., Wuelfing, W. P., Murray, R. W. Water-soluble, sulfonic acid-functionalized, monolayer-protected nanoparticles and an ionically conductive molten salt containing them. *Langmuir*, 2001, **17**, 1255-1261.

Sinha, S. K., Sirota, E. B., Garoff, S., Stanley, H. B. X-ray and neutron scattering from rough surfaces. *Physical Review B*, 1988, **38**, 2297-2311.

Smetana, J.Theory of tin whisker growth: The end game. *IEEE Transactions on Electronics Packaging Manufacturing*, 2007, **30**, 11-22.

Srinivasana, U., Houston, M. R., Howe, R. T., Maboudian, R. Self-assembled fluorocarbon films for enhanced stiction reduction. *International Conference on Solid-State Sensors and Actuators*, 1997, **2**, 1399-1402.

Tan, M. C., Roy, A. Electromigration in ULSI interconnects. *Materials Science and Engineering: R: Reports*, 2007, **58**, 1-75.

Underwood, S., Mulvaney, P. Effect of the solution refractive index on the color of gold colloids. *Langmuir*, 1994, **10**, 3427-3430.

Venables, J. A., Spiller, G. D. T., Hanbucken, M. Nucleation and growth of thin films. *Reports on Progress in Physics*, 1984, **47**, 399-459.

Vengsarkar, P. S., Xu, R., Roberts, C. B. Deposition of iron oxide nanoparticles onto an oxidic support using a novel gas-expanded liquid process to produce functional Fischer−Tropsch synthesis catalysts. *Industrial & Engineering Chemistry Research*, 2015, **54**, 11814-11824.

Vincent, B., Luckham, P. F., Waite, F. A. The effect of free polymer on the stability of sterically stabilized dispersions. *Journal of Colloid and Interface Science*, 1980, **73**, 508-521.

Vincent, B., Edwards, J., Emmett, S., Jones, A. Depletion flocculation in dispersions of sterically-stabilised particles ("soft spheres"). *Colloids and Surfaces*, 1986, **18**, 261-281.

Wanger, C. D., Riggs, W. M., Davis, L. E., Moulder, J. F., Muilenberg, G. E. *Handbook of X-ray Photoelectron Spectroscopy*. MN: Perkin-Elmer Corp., Physical Electronics Division, 1979.

Williams, D. P., Satherley, J. Size-selective separation of polydisperse gold nanoparticles in supercritical ethane. *Langmuir*, 2009, **25**, 3743.

Xiao, X., Qian, L. Investigation of humidity-dependent capillary force. *Langmuir*, 2000, **16**, 8153-8158.

Xie, Y., Guo, S., Ji, Y., Guo, C., Liu, X., Chen, Z., Wu, X., Liu, Q. Self-assembly of gold nanorods into symmetric superlattices directed by OH-terminated hexa(ethylene glycol) alkanethiol. *Langmuir*, 2011, **27**, 11394-11400.

Yamada, Y., Tsung, C. K., Huang, W., Huo, Z., Habas, S. E., Soejima, T., Aliaga, C. E., Somorjai, G. A., Yang, P. Nanocrystal bilayer for tandem catalysis. *Nature Chemistry*, 2011, **3**, 372-376.

Yamanoi, Y., Yonezawa, T., Shirahata, N., Nishihara, H. Immobilization of gold nanoparticles onto silicon surfaces by Si-C covalent bonds. *Langmuir*, 2004, **20**, 1054-1056.

Yao, H., Momozawa, O., Hamatani, T., and Kimura, K. Stepwise size-selective extraction of caroxylate-modified gold nanoparticles from an aqueous suspension into toluene with tetraoctylammonium cations. *Chemistry of Materials*, 2001, **13**, 4692-4697.

Yonezawa, T., Toshima, N. Polymer-stabilized metal nanoparticles. *Advanced Functional Molecules and Polymers*. 2001, London, UK: Gordon and Breach.

Yu, D. Q., Jillek, W., Schmitt, E. Electrochemical migration of Sn-Pb and lead free solder alloys under distilled water. *Journal of Materials Science: Materials in Electronics*, 2006, **17**, 219-227.

Zhao, P. X., Li, N., Astruc, D. State of the art in gold nanoparticle synthesis. *Coordination Chemistry Reviews*, 2013, **257**, 638-665.